1-1-2005

The remote continuous structural health monitoring of the East 12th Street Bridge

Derek Jay Hemphill
Iowa State University

The remote continuous structural health monitoring of the East 12th Street Bridge

by

Derek Jay Hemphill

A thesis submitted to the graduate faculty

in partial fulfillment of the requirements for the degree of

MASTER OF SCIENCE

Major: Civil Engineering (Structural Engineering)

Program of Study Committee:
Terry J. Wipf, Co-major Professor
Brent M. Phares, Co-major Professor
Lowell F. Greimann
Loren W. Zachary

Iowa State University

Ames, Iowa

2005

Graduate College
Iowa State University

This is to certify that the master's thesis of

Derek Jay Hemphill

has met the thesis requirements of Iowa State University

Signatures have been redacted for privacy

TABLE OF CONTENTS

LIST OF FIGURES

LIST OF TABLES

1. INTRODUCTION

1.1 Background

In early 2004, the Iowa Department of Transportation (Iowa DOT) completed construction of Iowa's first High Performance Steel (HPS) bridge, the East 12th St. Bridge (hereafter referred to as the E. 12th St. Bridge or the bridge) over I-235 in Des Moines, IA, with funding from the Federal Highway Administration's (FHWA) Innovative Bridge Research and Construction (IBRC) program. When compared with conventional steels, HPS, developed in the mid-1990's, has improved weldability, weathering, and fracture toughness characteristics. As the replacement of bridges in Iowa, and nationwide, becomes more prevalent, the advantages of HPS make its use potentially very appealing. Specifically, the advantages of improved weathering and fracture toughness characteristics have long-term benefits which could not only reduce maintenance costs but also extend the useful life of the structure.

The E. 12th St. Bridge, constructed using HPS girders, shown in Fig. 1.1, replaced a concrete box girder bridge. The replacement is part of a renovation of the I-235 corridor through Des Moines and the surrounding metro area. The two-span bridge runs nearly North and South. Providing one lane of traffic in each direction, the bridge connects the state capital area on the South to a residential area including East High School on the North.

Figure 1.1. East 12th Street Bridge over I-235 in Des Moines, IA.

The IBRC program, which provides funding to design and construct innovative bridge solutions, required that the performance of the HPS bridge be evaluated and documented over a two-year period. With the ongoing success of bridge monitoring in Iowa, it was decided to further develop and deploy a continuous Structural Health Monitoring (SHM) system for this evaluation. With this system, the bridge performance could be evaluated at any point in time as well as with respect to time. This report documents the design and construction of the bridge, summarizes the monitoring system in place, describes the data management system, and documents the structural performance of the bridge.

1.2 Objectives

The main objectives of the work summarized herein are:

- **Monitor and document the construction of Iowa's first HPS bridge** - Since the E. 12th St. Bridge is the Iowa DOT's first use of HPS girders in bridge construction, it was important to document how the use of HPS alters typical bridge construction practices.
- **Evaluate the use of HPS in bridge applications** - With the ever aging infrastructure system in the state, it is necessary to identify viable options for rehabilitating the transportation system. The general structural performance of the bridge was studied to substantiate the further use of HPS in Iowa.
- **Use innovative structural health monitoring techniques to continuously monitor the bridge performance** - SHM offers a distinct advantage over conventional visual inspection in that bridge condition can be monitored continuously without being subjective. At any point in time, the overall condition of the bridge can be evaluated without the need to inspect the bridge, thus eliminating the need for traffic control typically required for field inspections.
- **Develop initial concepts for monitoring bridge deterioration over time and develop a baseline record for identifying structural performance changes** - Another aspect of SHM is the potential for quantifying the rate at which bridges deteriorate. Until recently, the technologies used to evaluate structures were inadequate to accurately monitor structures for an extended period of time. With the technologies developed and deployed in this project, it is possible to monitor structures over a long period of time without data drift, degradation, or error. With proper algorithms (similar to those developed as part of this project), reliable SHM systems can provide the information required to predict bridge deterioration over time; such information would present opportunities to predict the remaining life of a structure by knowing the current state of the bridge.
- **Conduct a fatigue evaluation with specific interest in the impact of design features associated with HPS** - Several typical and atypical fatigue sensitive details were included in the bridge design. These details include the web gap detailing, stiffeners welded to the tension flanges, and weld concentrations at web and flange plate splices. These specific details were being evaluated because of Iowa's continued interest in their long-term performance.
- **Continue developing expertise in the broad field of SHM in the state of Iowa** - The state of Iowa has long been a leader in innovative bridge research and construction. As a state with an extensive network of bridges and infrastructure but limited resources, it is important

to continue to work toward finding ways in which the infrastructure can be monitored to extend the life of the structures without compromising the safety of the general public, damaging the surrounding environment, and paralyzing the important transportation network that links not only the state together but surrounding states as well.

1.3 Scope

The research summarized herein consists of several components. Initially the work consisted of observing and documenting the construction of the bridge. Concurrently, an innovative remote continuous SHM system (the first of its type in Iowa) was developed using available hardware to further advance the practice of installing reliable long-term SHM systems on the bridge infrastructure. A data management system, including custom developed software, was also developed to use the obtained data to evaluate both the long-term and short-term performance of the bridge. Early in the project it was decided that it was important to develop a system that could separate the long-term transient effects (such as temperature) from live load effects. Several techniques were investigated for accomplishing this. Ultimately, a behavior-based technique was developed that reliably separates these effects. Through the developed data management and interpretation system, the performance of the HPS girders was assessed, and a baseline record of the bridge's structural performance established. An evaluation of the typical and atypical fatigue sensitive details was also conducted to provide information on their general performance over time.

1.4 Report Organization

A literature review documenting the differences in HPS from ordinary structural steel, existing SHM technologies and needs, and stress cycle counting techniques is given in Chapter 2. The bridge description and a general construction overview are summarized in Chapter 3. Chapter 4 provides details on the monitoring and data management systems deployed on the HPS bridge. Chapter 5 presents the performance of the bridge both over time and during a controlled load test. Observations and conclusions are given in Chapter 6.

2. LITERATURE REVIEW

In order to fully understand how the HPS girders used in the E. 12th St. Bridge are unique compared to other bridges in Iowa, a review of the characteristics of HPS was performed. SHM technologies and systems were also reviewed to provide the research team with an understanding of the current state-of-the-art SHM systems, what their strengths and weaknesses were, and how the practice of SHM could be improved through this project. To facilitate the quantification of stress cycles that the bridge was exposed to, cycle counting techniques were also reviewed. The review of these topics allowed the project team to adequately document the construction of the subject bridge, to design and install a SHM system, and to evaluate the performance of the subject bridge while at the same time advancing the state of SHM.

2.1 High Performance Steel

Through a joint research program, the FHWA, the U.S. Navy, and the American Iron and Steel Institute (AISI) joined together in 1994 to develop HPS. This program was charged with improving the weldability characteristics, increasing the facture toughness characteristics, and providing increased corrosion resistance over ordinary steel to thereby create HPS. Since its creation, numerous bridges using HPS girders have been constructed with many being shown to have been economically built.

In specifications, HPS is differentiated from traditional steel by placing the letters "HPS" before the specified minimum yield strength of the steel in kips per square inch (ksi). In most cases the yield strength is also followed by the letter "W" which indicates that the steel must meet the ASTM G101 specification for weathering steel properties [1]. HPS is commonly available in three design yield strengths, 50 ksi (HPS 50W), 70 ksi (HPS 70W), and 100 ksi (HPS 100W).

2.1.1 Chemistry

To achieve the desired properties of HPS, an unique alloy combination was developed. For comparison, a portion of the chemical composition of HPS 50W and 70W as well as conventional steels are shown in Table 2.1 [2] (note, only the unique element levels are shown for clarity and thus, the total does not equal 100%). The reduced Carbon content in HPS improves the weldability of the steel, while the unique combination of Chromium, Copper, Nickel, and Molybdenum provides the enhanced corrosion resistance characteristics. The reduction in Sulfur content over traditional steels

improved the toughness of the steel and the combination of other elements ensures that the strength requirements are met [3].

Table 2.1. Chemical composition of conventional and High Performance Steels [2].

		Carbon (%)	Manganese (%)	Phosphorus (%)	Sulfur (%)	Silicon (%)	Copper (%)	Nickel (%)	Chromium (%)	Molybdenum (%)	Vanadium (%)	Aluminum (%)	Nitrogen (%)
70W	Minimum	0.0	0.80	0.0	0.0	0.25	0.20	0.0	0.40	0.0	0.02	0.0	0.0
	Maximum	0.19	1.35	0.04	0.04	0.65	0.40	0.50	0.70	0.0	0.10	0.0	0.0
HPS 50W & HPS 70W	Minimum	0.0	1.10	0.0	0.0	0.30	0.25	0.25	0.45	0.02	0.04	0.01	0.0
	Maximum	0.11	1.35	0.02	0.01	0.50	0.40	0.40	0.70	0.08	0.08	0.04	0.02

2.1.2 Advantages of HPS

As previously stated, during the development of HPS specific goals were set to improve the attributes of available steels. This was done in an attempt to reduce overall life-cycle costs, improve safety, and to ensure that steel remains competitive with other materials.

- Weathering - As with ordinary Weathering Steel, HPS does not have to be painted to prevent corrosion under normal atmospheric conditions. This has the potential of reducing maintenance costs.
- Fracture Toughness – HPS is more ductile at low temperatures than ordinary steel and has a higher crack tolerance. The higher crack tolerance increases the safety of the bridge by allowing more time for detecting and repairing cracks.
- Weldability - Lower preheat temperatures, less heat input control, and less post-weld treatment are needed to eliminate hydrogen-induced cracking in HPS weldments than ordinary steel weldments. This eases the fabrication process which can lead to lower initial fabrication costs.

2.1.3 Mechanical Properties of HPS

One of the goals with the development of HPS was to increase the fracture toughness of the steel at lower temperatures. The required toughness of HPS along with the minimum yield and ultimate tensile strengths are given in Table 2.2. For reference, the charpy-vee-notch is a measure of

the toughness of the material. The higher the toughness (15 ft-lbs at 10°F for traditional steels [4]) the lower the risk of a brittle fracture which again allows more time for detecting and repairing cracks.

Table 2.2. Mechanical properties for High Performance Steel [2].

	HPS 50W Up to 4 in. As-Rolled	HPS 70W Up to 4 in. (Q&T), 2 in. (TMCP)
Minimum Yield Strength, F_y, ksi (Mpa)	50 (345)	70 (485)
Ultimate Tensile Strength, F_u ksi (Mpa)	70 (485)	85-110 (585-760)
Minimum charpy-vee-notch, longitudinal orientation	25 ft.-lbs. (41 J) @ 10°F (-12°C)	30 ft.-lbs. (48 J) @ -10°F (-23°C)

2.1.4 Costs

The cost of HPS per pound is approximately twice the cost of A709 50W. However, the advantages listed above can lead to cost savings by offsetting the additional "per pound" cost with effective utilization. In most designs, smaller sections are permitted when using HPS as compared to ordinary steel. This results in a two-fold cost-reduction. First, the dead load is reduced. This reduces the overall demand on the section (i.e., dead load plus live load plus impact, etc.) and a smaller section is required. Second, because of the improved properties, less total steel is required resulting in a savings in the basic material costs. Even further, the lighter superstructure design reduces the sub-structure needs and general construction costs (e.g. lifting needs, transportation requirements, stability demands, etc.). Given that the steel does not have to be painted to prevent corrosion, long-term maintenance costs are also reduced. With higher fracture toughness, more time is available for crack detection and repair before a crack of critical length develops [2].

2.2 Structural Health Monitoring

SHM is becoming an increasingly popular way to monitor the performance of structures. To ensure the SHM system deployed on the E. 12th St. Bridge was based on the latest technology, a literature review on SHM was performed. Areas of interest included sensors and data acquisition units with a focus on Fiber Optic (FO) sensor-based systems, data transfer technologies, and data storage options.

2.2.1 Sensors

There are several types of measurements techniques that can be used to determine the behavior of a bridge structure. Strains, displacements, and accelerations are several common measurements that can be used to characterize the performance.

Several different types of strain gages are available. The most familiar types strain gages to researchers include foil strain gages [5] and vibrating wire strain gages [6]. Wireless sensors and Fiber Optic sensors (FOS) can also be used to measure strain. Foil and vibrating wire strain gages are often categorized as conventional strain gages as they have existed and been utilized for many years. There are many advantages of foil strain gages such as their low cost and ease of installation, but there susceptibility to electromagnetic and radio interference, dependence on signal amplitude, and tendency to drift over time limit their usefulness in long-term monitoring applications. Vibrating wire strain gages, although more stable over the long-run, can not sample fast enough to adequately characterize live load effects.

With conventional sensors, as the number of sensors is increased the complexity of the system is also significantly increased due to an increased number of wires. Increasing the number of wires causes an increase in installation and material costs. To offset the increased costs and complexity of systems, wireless sensors have been developed. These sensors are usually powered with a battery of varying size and generally have a limited range to which the data can be transmitted. Generally wireless sensors are larger in size as compared to non-wireless sensors. Some types of wireless sensors are programmable to perform some limited processing of the data. Drawbacks to this type of sensor include limited power supply, limited communication distance, and higher price [7].

As stated previously displacement transducers [8] and accelerometers [9] take readings which can also be used to interpret structural behavior. These sensors measure global properties of the structure to determine bridge performance characteristics. Like foil strain gages, displacement transducers and accelerometers are vulnerable to electromagnetic and radio interference, although this does not preclude them from being used in long-term monitoring projects, because they do not drift over time or depend upon signal amplitude.

FOS are a relatively new type of structural sensor that have only recently become more widely available. FOS have many advantages that can be taken advantage of in long-term SHM where conventional sensors are deficient. FOS are available that can make many different types of

measurements (e.g. strain, temperature, acceleration, displacement, etc.) and can be manufactured in unique forms to fit different needs. These needs include sensitivity (gage length or dynamic range) and location on a structure (crack detection, embedment, localized details, etc.). The ability of some types of FOS to be multiplexed together can be a significant advantage by reducing the amount of cabling infrastructure. Since FOS, and the process through which they are read, are not affected by electric and electromagnetic fields, radio frequency, and signal amplitude, a FO based system is an attractive option for long-term monitoring [10].

FOS systems operate by sending light waves (from a laser interrogator) down a fiber optic cable. The information from the light wave, which is modified in some fashion by the sensor, is returned to the interrogator and provides the measurement basis. The different techniques that are used to read the different types of information from the light wave, as well as the way in which the light wave is modified, result from the different types of FOS which are available. According to Inaudi, some of the different FOS include the following. SOFO ("based on the French acronym for Surveilance d'Ouvrages par Fibres Optiques – Structural Monitoring using Optical Fibers" [11]) displacement sensors "measure the length difference between two optical fibers" installed near each other. The sensors can measure displacements over distances between 200 mm and 10m. Microbending displacement sensors use a FOS sensor with either fiber optic cables or metallic wires wrapped along its length. The cables or wires wrapped around the sensor change the properties of the sensor causing light to be lost from the fiber. The deformation of the sensor can therefore be determined from the loss information. Known problems with microbending displacement sensors make them more suitable for short-term monitoring than long-term monitoring. Bragg Gratings (also known as "Fiber Bragg Grating" {FBG}) are capable of measuring both strain and temperature. As the fiber core of the FBG changes due to either mechanical strain or temperature change, the index of refraction of the sensor changes, therefore changing the wavelength which is returned. The major advantage of FBG is their ability to be multiplexed together on a single length of fiber optic cable. Fabry-Perot sensors are capable of measuring strain. These sensors work by measuring the interference caused by an air gap between two cleaved fibers whose ends are a small distance apart within a capillary silica tube [12].

Another type of FO technique which can be used to measure strain is with a Brillouin scattering based sensor system. This method is based upon the Brillouin scattering principle in which Brillouin scattering occurs when the density of the optical fiber is changed. Through the use of

Brillouin Optical Time Domain Reflectometry (B-OTDR), the location of the density change of the fiber can be found. This application has been used for monitoring over long distances (such as gas pipe lines) [13].

Long-gage FO sensors can be used to find the strain over long distances (gage lengths between 250 mm and 10m). This type of sensor can be useful when looking at the global properties of a structure. The SOFO sensor, a long-gage sensor, was designed specifically for embedment in concrete. This sensor allows strain measurements to be used for dynamic evaluation of a structure as well as long-term monitoring [14].

2.2.2 Fiber Optic Interrogators

As previously stated FO sensing of all types is based upon light waves and interpreting information from the light waves after a sensor has changed the properties of the light band. Different interrogators use different means to extract the information from the reflected light waves. According to Todd et. al.[15], different techniques for measuring wavelength shifts from FOS are based largely upon principles involving: scanning Fabry-Perot (SFP) filter-based interrogation, tunable acousto-optic filter interrogation, wavelength division multiplexed interferometric interrogation (WDM), and prism/CCD[charged coupled device]-array techniques. Broadband light source and broadband detectors are utilized by SFP and acousto-optic (tunable filter techniques) systems. The filters are "tuned" so only one sensor per array for multiplexed sensors is read at a time. SFP filter-based interrogation finds the gratings' reflection peaks by controlling the voltage applied to the filter while acousto-optic systems change the frequency applied to the filter. WDM and CCD-array based systems use broadband source and broadband detectors along with components that can separate wavelengths to read multiple sensors at the same time. The WDM system requires the wavelengths from the sensors be in the middle of the filter's passbands, therefore large shifts in wavelengths are not permitted. This system would be best used in applications where low amplitude readings were expected. CCD-array systems do not require the wavelengths to be within a certain bandwidth and, therefore, can read larger amplitude shifts in wavelengths [15].

Mircon Optics manufactures FOS interrogators that can read up to 512 FBG sensors on four channels at speeds up to 250 Hz. The interrogator consists of a computer with a built-in color LCD display. The system can be linked to other equipment using an Ethernet cable [16].

Roctest manufactures two different types of interrogators for use with their proprietary FOS (Fabry-Perot strain gages as well as transducers which have a wide range of measuring capabilities

including strain, pressure, temperature, displacement, and force). The first system has eight channels which can be monitored at 100, 500, or 1000 Hz. A RS-232 communication port controls each channel separately. A 10-volt analog output is generated for each individual channel. The second system is a data logger which can store 50,000 data samples before needing to be downloaded. Units consisting of 16 to 32 channels are available [17].

Luna Innovations manufactures interrogators which can scan multiple types of Luna FOS including, FBG and Fabry-Perot strain sensors and FOS accelerometers. The eight sensor channels (which can be expanded to 64 channels with expansion units also offered by Luna) output data through a RS-232 connection. A backlit LCD readout allows control of the unit which can collect data at up to 100 Hz. Another FOS interrogator offered by Luna Innovations can scan up to 8 channels at 130 Hz. This unit has an USB data port available for connecting a display. [18]

Blue Road Research manufactures several different units of which the model with the largest capacity will be detailed. The unit has two modes: High Bandwidth Mode which allows for one sensor to be read per channel at speed up to 10 kHz at a 0.2 $\mu\varepsilon$ noise level or 2 MHz at a 2.0 $\mu\varepsilon$ noise level and Multi-Sensor Mode where up to 20 sensors are able to be read per channel at speeds of 50 Hz. These units are capable of reading Blue Road Reasearch's catalog of sensors, including single and dual-axis FBG strain sensors [19].

2.2.3 Data Transfer

As with any project that involves data collection, the E. 12th St. Bridge SHM system will be required to transfer data from one location to another. In general, information must typically be transferred between equipment that is located "close" to one another and to equipment that is located "far" away. For equipment "close" to one another it is most common to establish a local area network (LAN). For greater distances, the Internet is a medium through which two LANs can be connected. Communication can take place using both wired and wireless technology.

2.2.3.1 Wired Technologies

To transfer data within a LAN the computers need to be linked together. In terms of wired connections, this is usually accomplished with Ethernet cables since they are low-cost and widely available. Ethernet connections can commonly transfer data at speeds between 10 megabits per second (Mbps) to 100 Mbps [20]. A new class of Ethernet connections can transfer data at up to 1000 Mbps. Fiber-optic cables can also be used for data transfer through Fiber Distributed Data Interface (FDDI), which can transfer at speeds between 100Mbps and 2Gbps [21].

There are many different modes to connect computers to the internet. A public Switched Telephone Network (PSTN) connection to the internet uses standard telephone lines. The transfer speed using PSTN depends on many factors and is usually less than 56 Kbps at a cost of about $20 a month. Integrated Services Digital Network (ISDN) can use a single wire to carry both voice and data over the internet; speeds are usually limited to around 64 Kbps at a cost of around $30 a month with an initial equipment fee of less than $200. Digital Subscriber Line (DSL) also uses regular telephone lines to transfer data to the Internet. DSL connections can upload data at up to 640 Kbps and download data at up to 1.5 Mbps. Cost of DSL modems is usually less than $100 and service can range between $30 and $150 per month. T-Carrier technology, which is commonly used to connect large organizations to the internet, is available in two different types T-1 and T-3. T-1 connections transfer data at speeds up to 1.544 Mbps and T-3 at up to 44.736 Mbps. These types of connections are typically available only at high costs. Asynchronous Transfer Mode (ATM), which can integrate the transfer of audio, data, image, text, and video information [22], can have transfer rates between 25 Mbps and 600 Mbps but is best suited for audio and video communication [23].

2.2.3.2 Wireless Technologies

Currently, the IEEE 802.11 standard regulates the operation of wireless LAN (WLAN). Communication within a WLAN can be performed via radio frequency (direct sequence or hopping spread spectrum) or infrared frequency. The mode of communication also governs the transmission speed which can vary from 1 Mbps to 54 Mbps for radio frequency systems and up to 622 Mbps for infrared systems. WLAN can operate between point-to-point or point-to-multipoint systems.

Wireless communication within a LAN typically occurs between two types of equipment. First, wireless devices must have a wireless network adapter. These network adapters function in much the same way as a wired network adaptor. Wireless communication to the rest of the LAN occurs through a piece of equipment known as an access point. Access points can either be stand alone units or integrated into a piece of hardware with other capabilities (e.g., routing, switching, etc.). Currently, there are three types of 802.11 standards known as 802.11a, 802.11b, and 802.11g. In some cases wireless WAN can be configured with devices utilizing any of the three standards.

An emerging technology for short distance communication within a LAN is known as Bluetooth. Currently, bluetooth is most often used between computers and their components (mouse, keyboard, etc.), mobile phones, and other portable devices. Unfortunately, the same frequency band that is used by the 802.11 standard is used for Bluetooth, so interference is possible. However, newer

standards should relive some of the congestion in that frequency range. Bluetooth has a range of up to approximately 10 meters.

Broadband wireless (BW) communication is often compared to DSL as it connects local users to the internet. The transmitter and receiver must have an unobstructed path between them to transfer information. The distance over which the BW can operate is dependant upon the frequency which is used for transmission. The local multi-point distribution service (LMDS), which utilizes transmitters spaced about one mile apart, operates at a higher frequency and has a large bandwidth (capable of supporting "all the channels of direct broadcast satellite TV"). The lower bandwidth service, multi-channel multi-point distribution service (MMDS), has transmitters up to 35 miles apart, but has lower transfer rates than LMDS.

Issues that must be considered when using any wireless communication protocol include interference and security. Interference in the communication can be caused by obstacles in the direct path of communication and also by electromagnetic interference. Interference issues can generally be overcome by intelligent placement of the wireless components. Security issues can be tightened by using authentication and encryption. Authentication can be performed through allowing only certain MAC addresses to enter the network and by using a closed network with a non-advertised name. High levels of data encryption (e.g., 128 or 256 bit) can be also used to create virtual "wires" between two wireless nodes [24].

2.2.4 Data Storage

Once the data are obtained from the data acquisition system, they will need to be stored before and after any processing of the data. The storage of the data can be broken into two categories flat files (i.e. .txt and .dat files) and databases [25]. A flat file is a single table (a table which you must know the location {row and column location} of an item to find it) [26]. A database consists of a collection of multiple tables linked together. An item is found within a database by queries. A database can be thought of as an "electronic filing system" [27]. Flat files are easy to create, don't need special software, are easy to open, and use less space than data bases. Databases are more secure than flat files, make it easy to find data when the data structure is complex, and allow multiple users to access the database at the same time [25].

2.2.5 Structural Health Monitoring Systems

On the Commodore Barry Bridge, Kulcu et. al. used different gages and acquisition rates to capture different types of data. Long-term data are collected once every 15 minutes seven days a

week using vibrating wire strain gages and a Campbell Scientific data acquisition system. Short-term data (live load) are collected at approximately 100 Hz, twice a day every day for one week during two quarters of the year with foil resistance strain gages and accelerometers and an Optim MEGADAC data acquisition system. Wind data are also collected every 5 seconds from the bridge using ultrasonic wind sensors and a Handar data acquisition system. Control of the system is provided through remote applications; this connection is made through an ordinary telephone line.

The data acquisition control and data presentation of the wind data, live video, and long-term data from the Commodore Barry Bridge are performed using a Lab-View platform. The wind data are processed and saved in daily files which are stored in a database. After processing, the long-term data are stored in spreadsheets. The short-term data are also processed before being archived. Future work on that monitoring project includes redesigning the data acquisition system so it is a fully automatic web-based system and fully automating the data processing system [28].

A strengthening project on the Horsetrail Falls Bridge, in which Fiber Reinforced Plastic (FRP) wrap was used to externally strengthen two reinforced concrete beams, was evaluated over a two year period with 28 FBG sensors. Although FBG sensors usually have a gauge length around 1 cm, capillary tubes were used to mount the sensors which effectively changed the gauge lengths to 70 cm or 100 cm, depending upon the desired gauge length. FBG sensors were chosen for their qualities that are beneficial in long-term monitoring, ability to be used with long gauge lengths, and small size which was appealing since this is a historic landmark in the Columbia River Gorge [29].

ISIS Canada has used FOS to investigate the use of FRP to strengthen deteriorated concrete structures from remote locations. At the time of publication (of the reference article) 16 bridges in Canada have been monitored using FOS. The FBG utilized generally experienced a low failure rate when properly installed. The accuracy of the FOS were verified (with success) by conventional strain gages. The resilience of FOS and electric strain gages embedded in concrete were also compared. The FOS were more robust than electric strain gages when embedded in concrete. Examples of the use of FOS by ISIS Canada are presented in the following paragraph.

On the Beddington Trail Bridge in Alberta, 20 FBG sensors were embedded into the concrete girders which were prestressed with carbon fiber composite cables. Readings were taken from the sensor 6 years after they were installed and 18 were still working. The Taylor Bridge in Manitoba is "considered to be the world's largest highway bridge reinforced by FRP and monitored using FOS". Carbon fiber reinforced polymer (CFRP) was used as reinforcement in the prestressed girders and in a

portion of the deck slab. The barrier walls were reinforced with glass fiber reinforced polymer (GFRP). The FRP reinforcing bars were monitored with 63 FBG and two mulit-Bragg sensors. Temperature compensation was provided through readings taken with 22 electric-based sensors. Twenty-six electrical strain gages were placed near selected FBG to verify the readings, of which more than 60% failed, although they were properly sealed, during the steam curing of the girders [30].

2.3 Stress Cycle Counting

Bridges are loaded by vehicles of varying configurations and weights causing varying levels of stress at different locations. These stress levels can differ even more as the global boundary conditions change with environmental changes (temperature, humidity, direct sunlight, etc.) and with bridge deterioration. To characterize the magnitudes of stresses induced on details, stress cycle counting techniques are commonly used. Stress cycle counting produces a snapshot of the size and associated number of stress cycles that a bridge has been exposed to. Such data are useful in fatigue evaluations.

The first cycle counting methods to be developed were termed level-crossing counting, peak counting, and simple range counting. Although not described in detail here, these methods are generally considered inadequate because they do not take into account the sequence in which the stress cycles occur. The order in which the cycles occur is of most importance for materials with non-linear stress-strain relationships.

The rainflow counting technique, developed by Matsuishi and Endo (sometimes known as "Falling Rain" on "Pagoda Roof"), is a procedure which counts closed hysteresis loops of varying stress magnitudes. Because of its widespread acceptance, "Rainflow Counting" is a common phrase used to denote all methods that use closed hysteresis loops to identify stress cycles. Common Rainflow Counting algorithms include the original rainflow counting, range-pair counting, range-pair-range counting, Haynes method, ordered overall range counting, racetrack counting, and hysteresis loop counting. All of these methods will provide matching results if the strain-time plot begins and ends with the largest strain magnitude. In other cases, the methods will not give equal results; but the results will be similar [31].

The following is an excerpt from Bannantine, et. al in which a step by step description of the "Falling Rain" method is given:

> The first step in implementing this procedure is to draw the strain-time history so that the time axis is oriented vertically, with increasing time downward.

One could now imagine that the strain history forms a number of "pagoda roofs." Cycles are then defined by the manner in which rain is allowed to "drip" or "fall" down the roofs. (This is the previously mentioned analogy used by Matsuishi and Endo, from which the rainflow method of cycle counting received its name.) A number of rules are imposed on the dripping rain so as to identify closed hysteresis loops. The rules specifying the manner in which rain falls are as follows:

1) To eliminate the counting of half cycles, the strain-time history is drawn so as to begin and end at the strain value of greatest magnitude.
2) A flow of rain is begun at each strain reversal in the history and is allowed to continue to flow unless;
    a. The rain began at a local maximum point (peak) and falls opposite a local maximum point greater than that from which it came.
    b. The rain began at a local minimum point (valley) and falls opposite a local minimum point greater (in magnitude) than that from which it came.
    c. It encounters a previous rainflow.

The foregoing procedure can be clarified through the use of an example. [Fig. 2.1] shows a strain history and the resulting flow of rain. The following discussion describes in detail the manner in which each rainflow path was determined.

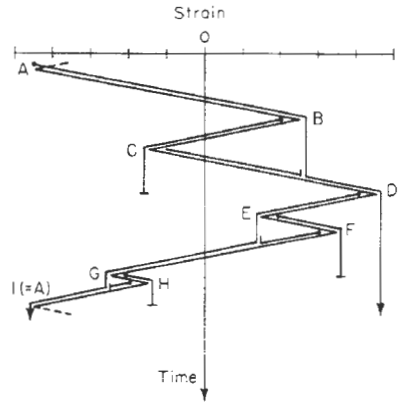

Figure 2.1. Rainflow counting ("falling rain" approach) [31].

As shown in [Fig. 2.1], the greatest strain-time history begins and ends at the strain value of greatest magnitude (point A). Rainflow is now initiated at each reversal in the strain history.

A. Rain flows from point A over points B and D and continues to the end of the history since none of the conditions for stopping rain flow are satisfied.
B. Rain flows from point B over point C and stops opposite point D, since both B and D are local maximums and the magnitude of D is greater than B (rule 2a above).
C. Rain flows from point C and must stop upon meeting the rain flow from point A (rule 2c).
D. Rain flows from point D over points E and G and continues to the end of the history since none of the conditions for stopping rain flow are satisfied.

E. Rain flows from point E over point F and stops opposite point G, since both E and G are local minimums and the magnitude of G is greater than E (rule 2b).
F. Rain flows from point F and must stop upon meeting the flow from point D (rule 2c).
G. Rain flows from point G over point H and stops opposite point A, since both G and A are local minimums and the magnitude of A is greater than G (rule 2b). Rain flows form point H and must stop upon meeting the rainflow from point D (rule 2c).

Having completed the above, we are now able to combine events to form completed cycles. In this example events A-D and D-A are combined to form a full cycle. Event B-C combines with event C-B (of strain range C-D) to form an additional cycle. Similarly, cycles are formed at E-F and G-H [31].

3. BRIDGE DESCRIPTION, DESIGN, AND CONSTRUCTION

3.1 Bridge Description

The E. 12th St. Bridge over I-235 in Des Moines, IA, shown in Fig. 1.1, is a 298 ft – 7 in. long two-span HPS girder bridge, with an 8 - in. thick cast-in-place concrete deck. The deck (constructed composite with the HPS girders) and sidewalks were constructed using High Performance Structural Concrete (HPSC) with a minimum strength of 5,000 psi. The framing plan of the bridge is shown in Fig. 3.1. The North span is 153 ft - 3 in. long and the South span is 145 ft - 4 in. long. The girders are supported at the ends with integral abutments (the North integral abutment is shown in Fig. 3.2). The driving portion of the bridge consists of two lanes with a total width of 29 ft – 6 in. The pedestrian walkways, flanking both sides of the roadway, are each 7 ft – 10 in. wide. The six girders, spaced at 8 ft – 8 in. as shown in Fig. 3.3, are constructed with HPS with each girder having three longitudinal segments. The 113 ft -6 in. long "North Region" and the 103 ft – 1 in. long "South Region" were constructed with HPS 50W steel, while the 82 ft – 0 in. long "Center Region" was constructed with HPS 70W steel. The girders in the "North Region", "Center Region", and "South Region" each have different cross-sections, the details of each are shown in Figs. 3.4 though 3.6.

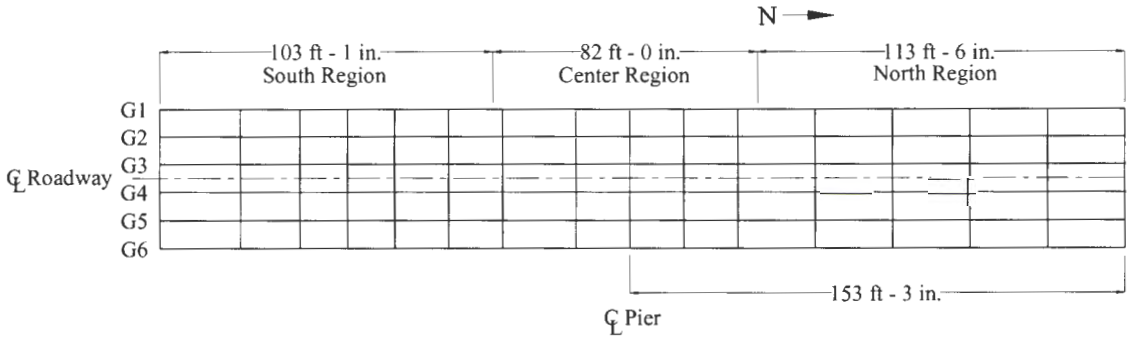

Figure 3.1. Plan view of the E. 12th St. Bridge framing system.

Figure 3.2. Photograph of typical girders and the North integral abutment.

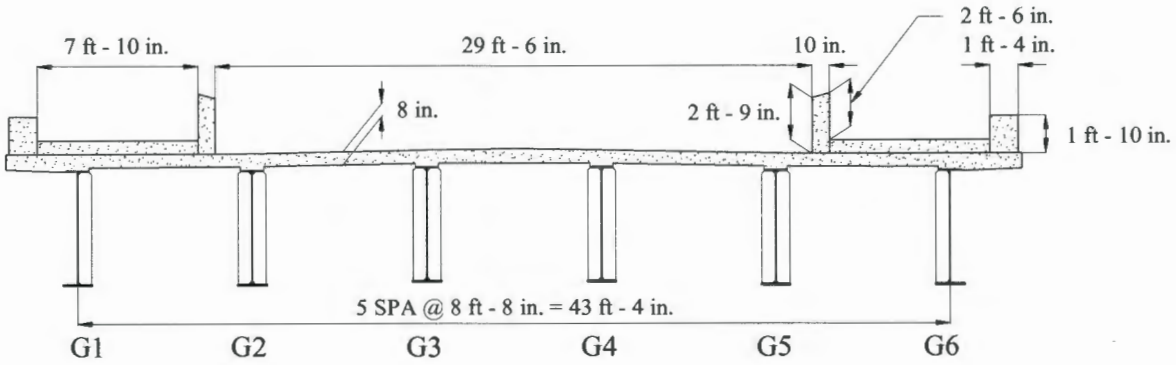

Figure 3.3. Typical cross sectional view of the E. 12th St. Bridge (looking North).

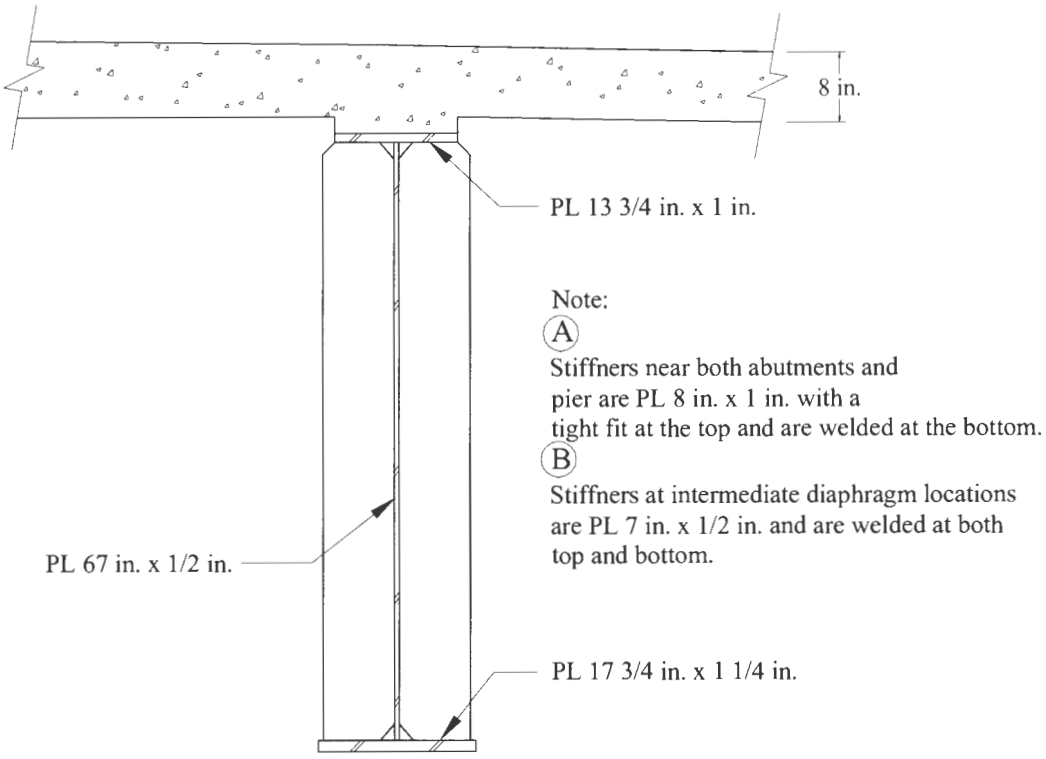

Figure 3.4. Cross section of "North Region" girders.

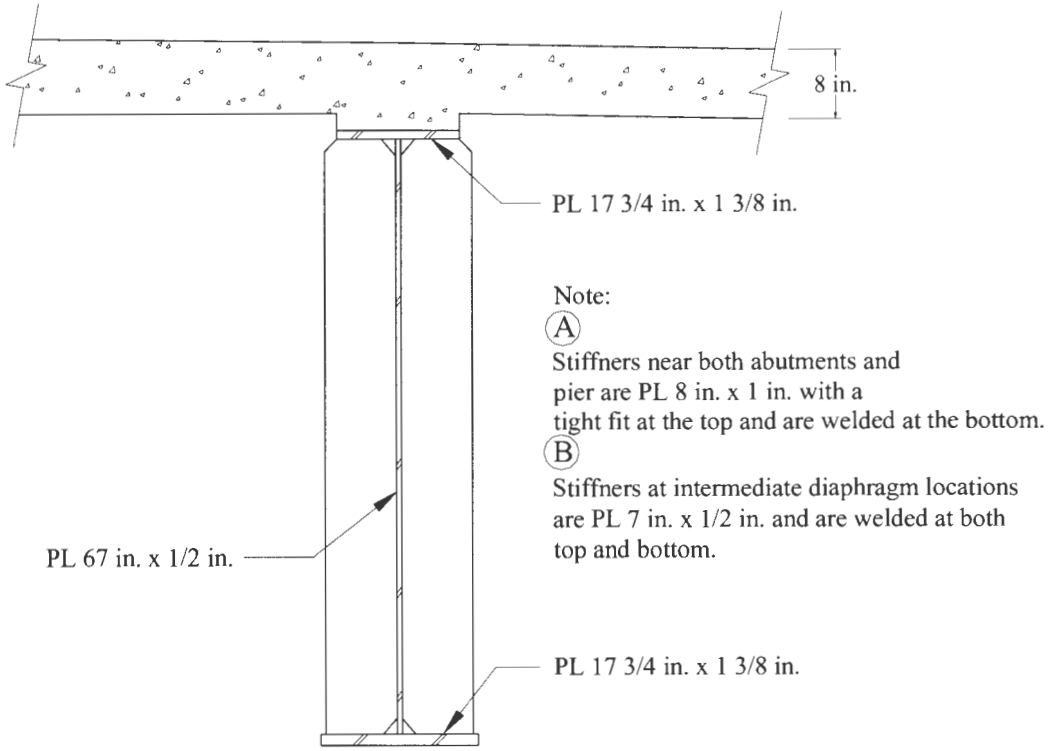

Figure 3.5. Cross section of "Center Region" girders.

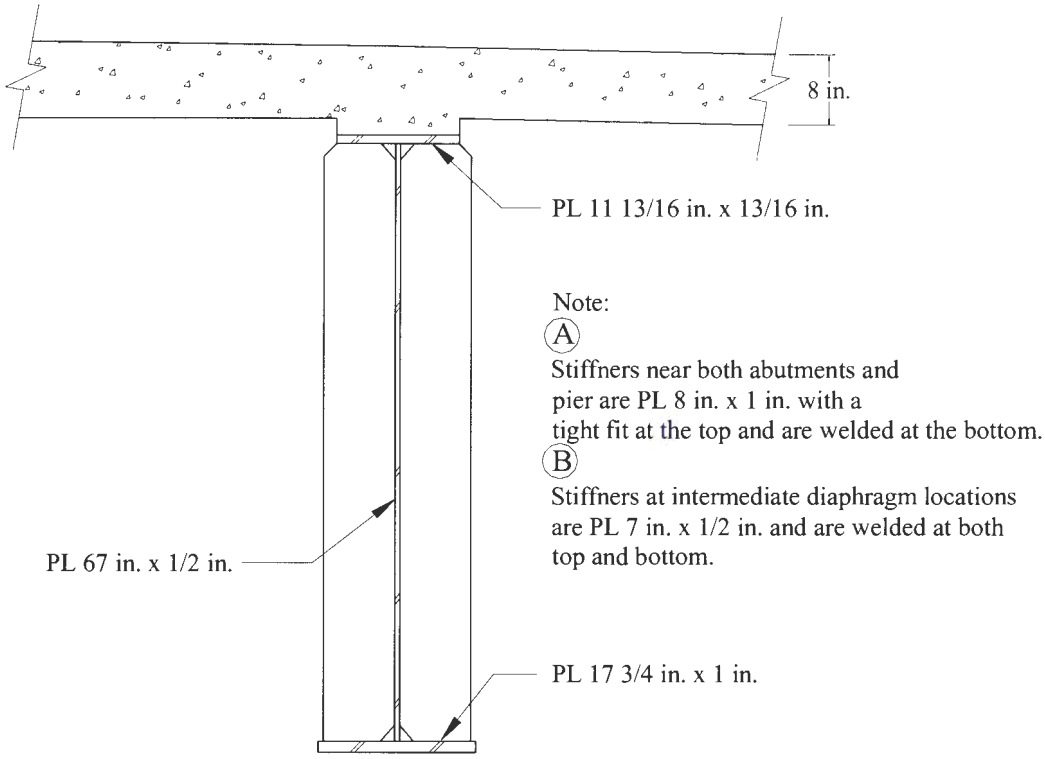

Figure 3.6. Cross section of "South Region" girders.

3.2 Bridge Design

The Iowa DOT identified the East 12th St. Bridge as an opportunity for their initial use of HPS. The IBRC Program requirements of monitoring and evaluation of the demonstration bridge for a two year period created an opportunity for the Office of Bridges and Structures to not only do a thorough evaluation of the bridge performance, but also provided an opportunity for the office to become very familiar with the design, fabrication, and construction issues associated with this relatively new structural material for future applications. The bridge was designed to take full advantage of the HPS structural properties, including material strength, toughness, and fatigue.

3.3 Bridge Construction

A challenging aspect of the construction of the subject bridge was working over the major roadway (I-235) the bridge spans. With the volume of traffic I-235 carries, the Iowa DOT mandated that I-235 not be shut down during normal work-day hours. During non-peak hours (middle of the day during the work week), one lane at-a-time could be shut down for short periods of time. The allowance for this lane closure allowed some construction operations to proceed without the need for nighttime

work. However, when construction required full closure of I-235, work had to be completed at night and typically occurred on the weekend. The contractor for the subject bridge was United Contractors, Inc. of Johnston, IA.

3.3.1 Demolition

Before construction of the new bridge could begin, the existing concrete box-girder bridge, shown in Fig. 3.7, had to be removed. Demolition began with the removal of the guardrails, light poles, and other items that could be removed without closure of I-235. On the night of Saturday, May 3rd, 2003, I-235 was closed from East 6th St. to East 15th St. to allow the majority of the demolition to take place. Most of the demolition was completed in a conventional manner using track hoes with vibrating hammers that punched holes in the bridge deck. These holes enabled track hoes with buckets to tear apart the bridge with supplemental aide from the vibrating hammer equipped track hoes (see Fig. 3.8). On the night of May 3rd, I-235 was closed to traffic at approximately 12 a.m. Saturday night and reopened to traffic 30 hours later prior to Monday morning rush hour traffic.

Figure 3.7. Photograph of original E. 12th St. Bridge.

Figure 3.8. Photograph of demolition operations - Sunday May 4th, 2003.

3.3.2 Construction

3.3.2.1 Abutment Footings

After the box girder bridge had been removed, work began by constructing new bridge abutments. As the replacement bridge has integral abutments, work started by driving H-Piles. The North abutment consists of a row of 15-HP10x42 piles with a single HP10x42 pile behind each outer pile in the row, for a total of 17 piles. The South abutment was constructed with a row of 14-HP10x42 piles with a single HP10x42 pile behind the outer pile on the West side of the abutment and 2-HP10x42 piles behind the outer pile on the East side of the abutment, for a total of 17 piles. The piles were driven to a depth where they reached the design bearing value (73 Kips). Exposed piles can be seen in Fig. 3.9 following installation. Following the piles being driven, the top of piles were encased in concrete to form the complete abutment. Figure 3.10 shows an abutment under construction.

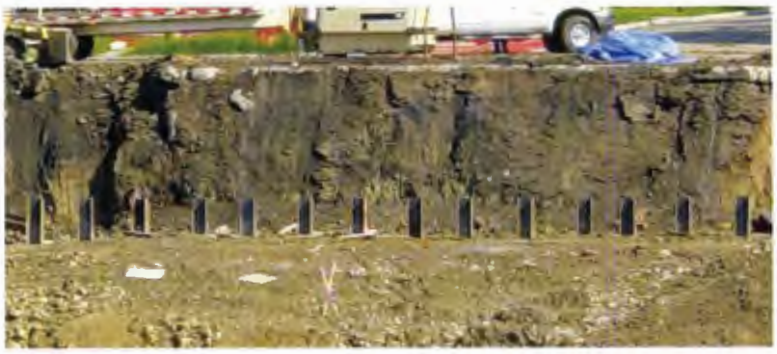

Figure 3.9. Photograph of piles at South abutment before abutment concrete was placed.

a. Front view of abutment.

b. Top view of abutment.

Figure 3.10. Photograph of South integral abutment footing before formwork was removed.

3.3.2.2 Pier

As work was progressing with the abutments, construction of the center pier was also initiated. The original bridge pier foundation was removed and a new foundation was constructed at approximately the same location. Vertical steel reinforcing bars were extended past the top of the foundation to tie the foundation and pier stem together. The reinforcing bars for the pier columns were then tied to the exposed bars, as seen in Fig. 3.11.

Due to the unique geometry of the V-Pier shown in Fig. 3.12, flat plate girder forms were used to form the North and South sides of the pier (the sides facing the abutments). Adjustable metal forms, with the ability to form radii, were used to form the curved sides of the columns. Three sides of the formwork were assembled on the ground. Specifically, one flat plate girder form was laid horizontal and the radii formwork, were set vertically upon it as seen in Fig. 3.13. This partially complete formwork was then lifted into place with the last flat plate girder form then set into position, thus completing the formwork for the pier stem and columns. The fully assembled pier formwork can be seen in Fig. 3.14.

As with the demolition of the existing bridge, the placement of the concrete for the pier stem and columns could not take occur during the day. Placement of the concrete required multiple lanes of I-235 traffic be shut down because a crane was used to lift the concrete into place and a large number of concrete trucks were needed. Together, these necessitated nighttime placement of the concrete. The completed pier stem and columns are shown in Fig. 3.15.

Figure 3.11. Photograph of reinforcing steel for the center pier.

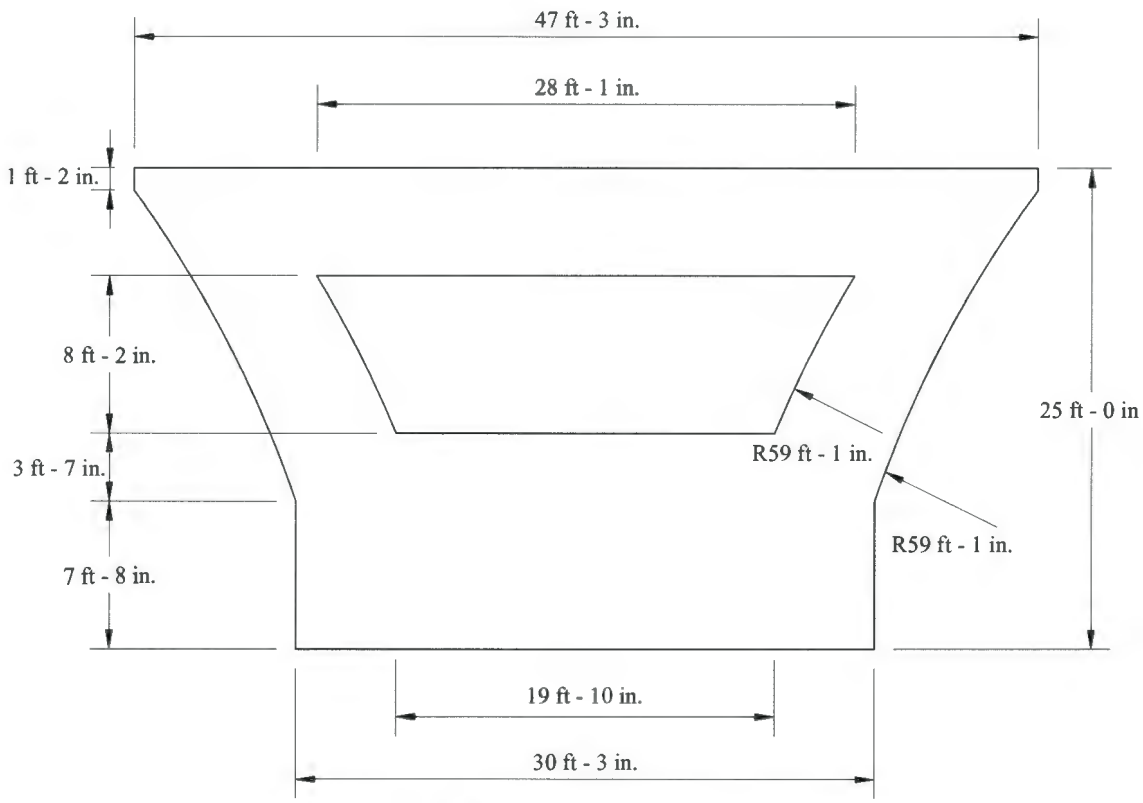

Figure 3.12. Elevation view of the center pier.

Figure 3.13. Photograph of formwork for the center pier during assembly.

Figure 3.14. Photograph of center pier formwork after assembly and placement.

Figure 3.15. Photograph of center pier after formwork was stripped and before reinforcing steel and formwork for the pier cap were constructed.

Once the pier stem and columns had gained sufficient strength, assembly of the formwork for the pier cap began. The formwork was assembled in-place; this can be seen in Fig. 3.16. Similar to the pier stem and columns, the placement of the concrete for the pier cap also took place during a nighttime shutdown of I-235. The completed pier can be seen in Fig. 3.17.

Figure 3.16. Photograph of formwork for the center pier cap being constructed.

Figure 3.17. Photograph of completed center pier.

3.3.2.3 HPS Girders

The HPS girders used in the bridge were manufactured in Illinois by Industrial Steel Construction, Inc. The girders were shipped to the site, by truck, with 3 to 4 sections of girder delivered at a time (only one section per truck). Delivery took place during non-peak daytime hours when one lane of I-235 could be closed to traffic; this lane was needed for unloading. A delivery can be seen in Fig. 3.18 and several stockpiled girders can be seen in Fig. 3.19. To facilitate construction the "North Region" and "Center Region" sections of girders were stored in the median where they were spliced together before installation. The "South Region" section of the girders were stored on the South side of I-235.

Erection of the HPS girders was also completed during a nighttime operation. The cranes used to set sections of the girders were temporarily moved directly on the I-235 roadway and the girders were hoisted over the roadway. Setting all the sections and cross-frames of the six girders occurred during three night time operations. During the first night, the "North Region" and "Center Region" of all six girders were set, as shown in Fig. 3. 20. The cross-frames between the set sections of the girders were also installed during the first night.

The "South Region" of four of the six girders (G3, G4, G5, and G6) and the corresponding cross-frames were placed during the second night. This is shown in Fig. 3.21. During the third night, the remaining regions of the two girders were installed along with the cross-frames between these sections. The completed framework of girders and cross-frames is shown in Figs. 3.22. A false deck sitting on the bottom flange of the girders was also constructed during the nighttime operations; the false deck can be seen in Fig. 3.23. This false deck served as both a work platform in regions directly over I-235 and prevented construction assemblies or debris from falling on I-235 below.

Figure 3.18. Photograph of HPS girder being unloaded following delivery.

Figure 3.19. Photograph of stock piled HPS girders located on South side of I-235.

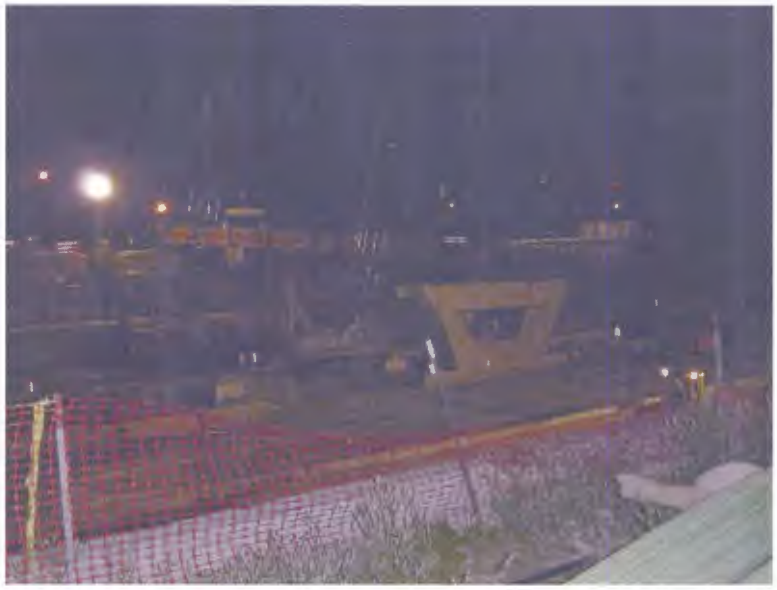

Figure 3.20. Photograph of HPS girder being set during the first of three night time operations.

Figure 3.21. Photograph of girders installed after the second night of girder setting operations.

a. Side view of bridge.

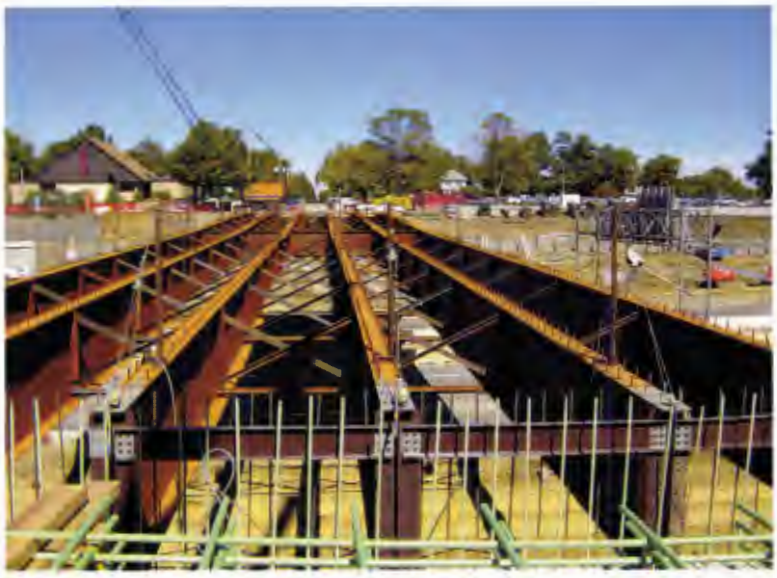

b. End view of bridge.

Figure 3.22. Photograph of bridge after all girders have been erected.

Figure 3.23. Photograph of work platform resting on the bottom flange of the girders over the I-235 roadway.

3.3.2.4 Reinforced Concrete Deck

After the formwork and reinforcing bars had been installed for the deck and the integral abutment cap, the first of two sequenced concrete placements took place. In Fig. 3.24 the deck formwork stringers can be seen along with several intermediate cross-frames. The Northern positive moment region and abutment and the Southern positive moment region and abutment were the first placement. After the second placement, consisting of the center negative moment region, had cured to sufficient strength, the pedestrian walkways and the barrier rails were placed. The concrete covered for insulation during curing can be seen in Fig. 3.25. The barrier rails (two on each side, one to guard the edge of the bridge and one to separate pedestrians from traffic) were constructed using a continuous slip forming technique. The completed slip formed barriers can be seen in Fig. 3.26.

3.3.2.5 Opening

The bridge was opened to traffic on March 23, 2004, 10 months and 20 days after the original bridge was closed for replacement. The total cost of the demotion of the original bridge and construction of the new bridge was $13,037,674.60. The completed bridge is shown in Fig. 3.27.

Figure 3.24. Photograph of intermediate cross-frames and deck formwork stringers.

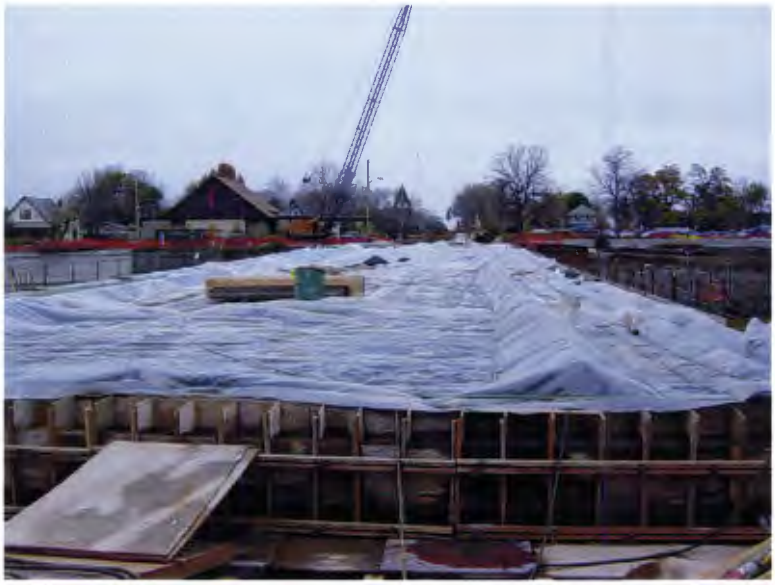

Figure 3.25. Photograph of bridge deck covered after concrete placement.

Figure 3.26. Photograph of bridge after slip forming of barriers.

Figure 3.27. Photograph of completed bridge open to traffic.

4. MONITORING SYSTEM

4.1 Introduction

The SHM System deployed on the E. 12th St. Bridge was designed to achieve the objectives listed in Chapter 1. In addition, it was decided to use off-the-shelf and readily available technologies, when possible, in an effort to minimize development time.

The SHM System developed for, and installed on, the bridge can generally be divided into three sub-systems: the Data Acquisition Sub-System (DASS), the Gateway Sub-System (GSS), and the Data Storage/Processing Sub-System (DS/PSS). A schematic of the SHM system can be seen in Fig. 4.1.

The flowchart shown in Fig. 4.2 summarizes the data "flow" from their origin at the sensors to its final format. The primary sub-systems previously mentioned, the hardware components of each sub-system, and software programs within them are shown in the flowchart. This chapter is organized in a manner similar to the organization of the Fig. 4.2 flowchart.

4.2 Data Acquisition Sub-System (DASS)

The DASS, located at the bridge, collects raw data from strain sensors strategically located on the bridge and transfers the information to the GSS, which is located at a nearby secure facility. Components of the DASS include (manufacturing company given in parentheses):

- Strain Sensing Equipment
  40 Fiber Bragg Grating (FBG) Sensors (Avensys, Inc./Bragg Photonics & LxSix)
  Si425-500 Swept Laser Interrogator (Micron Optics, Inc.)
- Communication Equipment
  2.4 GHz Wireless-802. 11g Access Point (Linksys)

4.2.1 Fiber Bragg Grating Sensors

FBG sensors are sensors "written" to a piece of conventional fiber optic. Each FBG reflects a specific wavelength of light depending on the mechanical strain induced on the sensor or changes in sensor temperature. Thus, changes in the reflection wavelength are directly related to a change in strain or temperature. As was mentioned previously, because the FBG measurements are not dependent upon signal amplitude (only upon reflected wavelength), they are more stable over time. Also, this type of sensor is not affected by electromagnetic interference, radio frequency interference, or electric currents which generally cause traditional sensors to "drift" with time and also introduce

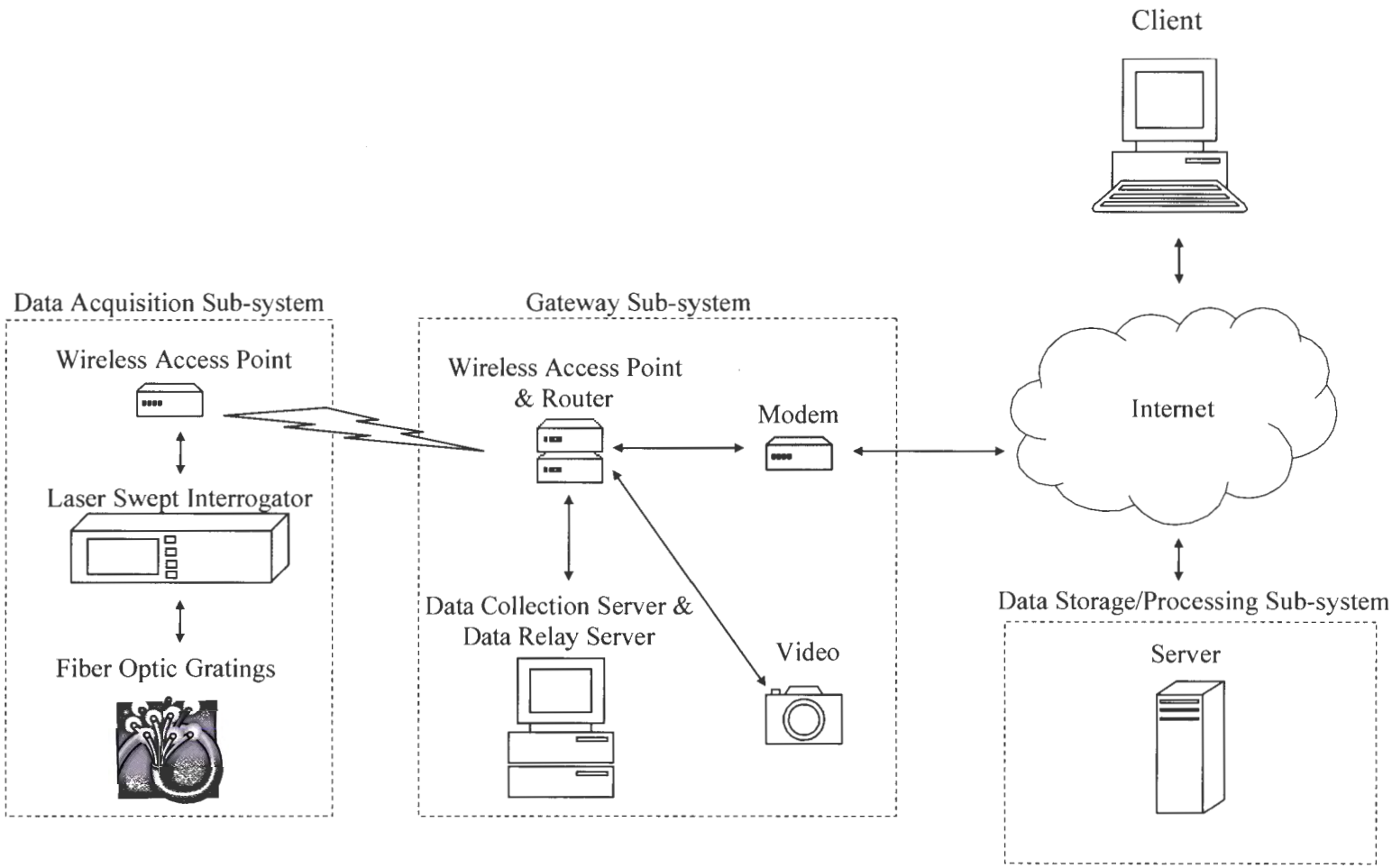

Figure 4.1. Schematic of the East 12th Street Bridge SHM system.

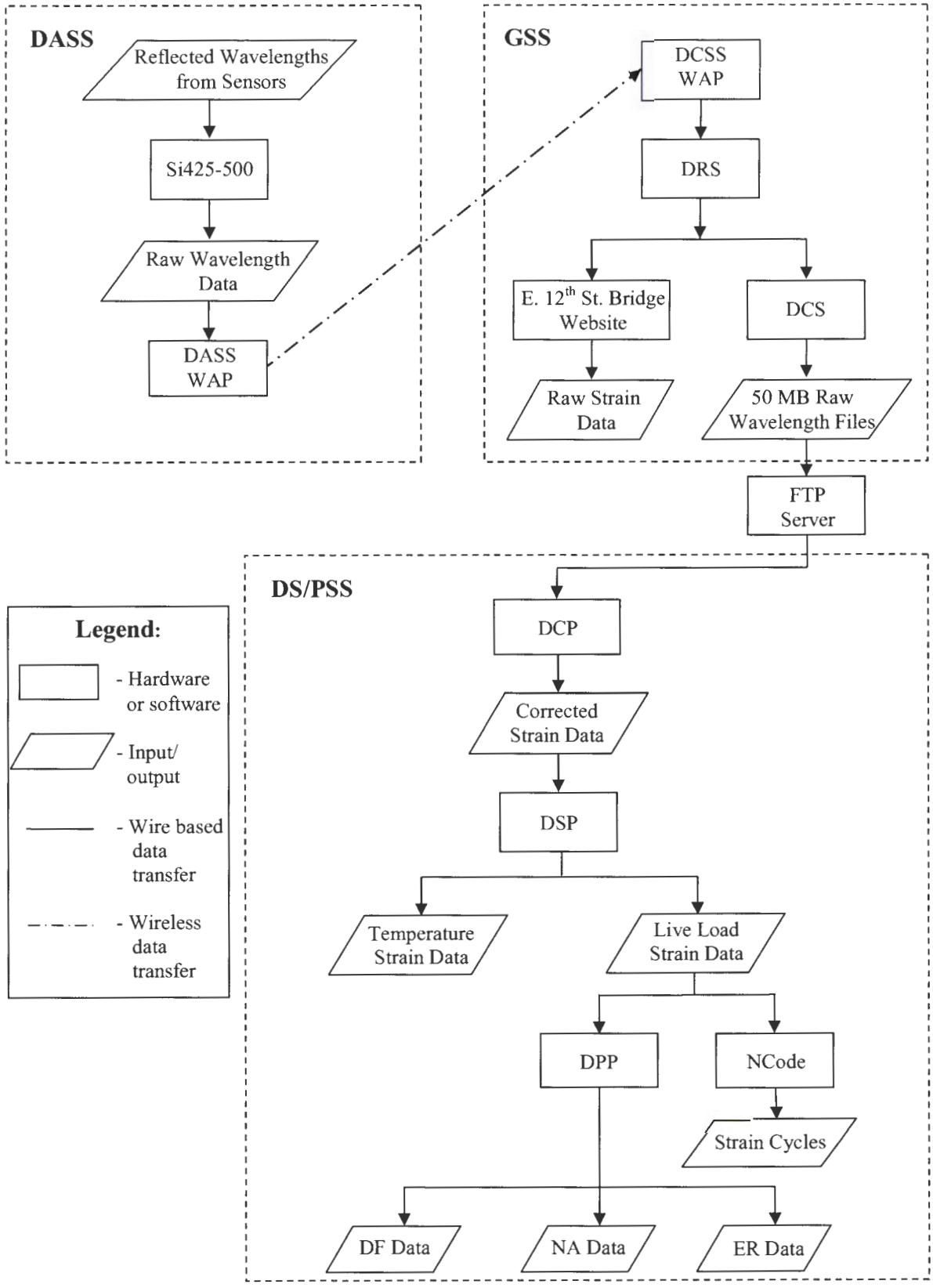

Figure 4.2. Data acquisition and processing flowchart.

random noise. In addition, multiple FBG sensors can be multiplexed on a single optical fiber which reduces lead wire lengths and numbers.

4.2.1.1 Sensor Locations

The FBG sensors installed on the subject bridge are located at strategic points on the bridge such that both the global and local performance of the bridge could be assessed. The sensors are located at the nine cross-sections (i.e., CS A through CS I) shown in Fig. 4.3. The global performance is monitored with FBG sensors placed on the bottom flanges of all the girders and select top flanges (shown in Table 4.1 and Fig. 4.4) near midspan of both the North and South spans (Cross-Sections B and I, respectively). Top and bottom flange sensors were also placed near the North abutment on several girders (Cross-Section A) and two girders were monitored with bottom flange sensors near the bridge pier (Cross-Section D).

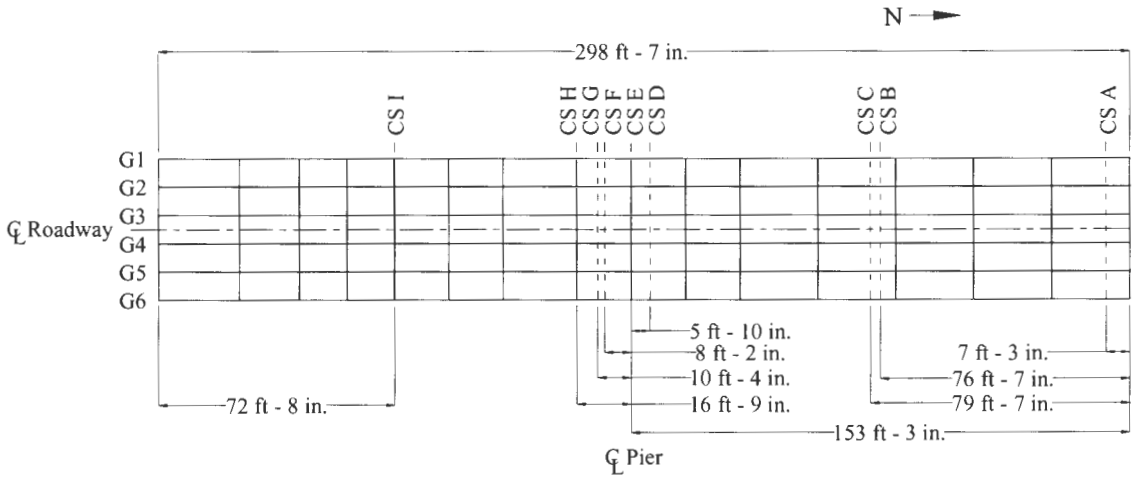

Figure 4.3. Plan view of the E. 12th St. Bridge showing the cross-sections where sensors were installed.

Localized strains near fatigue sensitive details were monitored at several locations. The web gap regions of two girders were instrumented in the negative moment region near the pier. The web gap region was monitored with two different sensor configurations; a flange tipping configuration and a web gap bending configuration (exact placements described subsequently). Two girders at Cross-Section E were equipped with web gap sensors and two girders at Cross-Section H had both flange tipping and web gap sensors installed. Stress concentrations at both a flange (Cross-Section G) and web (Cross-Section F) welded splice were also monitored in the negative moment region near the pier.

FBG sensors were also placed at three locations on the bridge to measure the steel temperature, thereafter referred to as "temperature sensors". Unlike all of the previously described sensors, these sensors were not physically attached to the bridge. Therefore, the "temperature sensors" are isolated from mechanical strain, and shifts in their reflected wavelengths are related to temperature changes only. A final FBG sensor was placed in the protective cabinet, discussed subsequently, that houses the data collection hardware. This allows the temperature in the cabinet to be monitored.

As stated previously, the sensors were monitored on four different channels (each channel has multiple sensors). The channel from which each sensor is monitored depends only upon installation convenience. Channel 1 consists of Sensors 1 to 13, which are generally near the pier; Channel 2 consists of Sensors 14 to 29, which are the sensors located near midspan of the North span and the North abutment; and Channel 3 consists of Sensors 30 to 39, which are near midspan of the South span. Channel 4 consists of the single FBG sensor monitoring the temperature in the protective box located at the bridge pier.

The locations of the sensors described in the previous paragraphs are listed in Table 4.1 and are shown in Fig. 4.4. Recall that the cross-section designations are shown in Fig. 4.3.

Figure 4.5 illustrates the typical placement of the bottom flange (Sensors 3, 4, 14, 17, 19, 20, 22, 24, 25, 26, 28, 31, 32, 33, 35, 37, and 38) and top flange (Sensors 15, 18, 21, 23, 30, 34, 36, and 39) FBG sensors. These sensors are oriented longitudinally and centered between the face of the web and the edge of the flange. In all cases, the top flange sensors were placed on the bottom of the top flange and the bottom flange sensors were placed on the top of the bottom flange.

The typical placement of the flange tipping sensors (Sensors 8 and 9) and the web gap sensors (Sensors 1, 2, 7, and 10) are shown in Fig. 4.6. The flange tipping sensors were oriented transversly on the girder top flange along the outside edge of the stiffener to measure the out of plane strain at the stiffener-to-flange interface. The web gap sensors were placed vertically on the girder web, centered at the intersection of the bottom of the web gap and the top of the stiffener.

The typical placement of the web splice sensors (Sensors 5 and 12) and the flange splice sensors (Sensors 6 and 11) are shown in Fig. 4.7. The splice sensors were oriented longitudinally along the flange-web weld at locations where either the web or flange plates were spliced with weldments.

Table 4.1. Sensor number, location, type, and channel number information.

Sensor Number	Girder Number	Cross-Section	Type	Side of Web	Channel Number
1	3	E	Web Gap	East	1
2	3	E	Web Gap	West	1
3	3	D	Bottom Flange	West	1
4	2	D	Bottom Flange	East	1
5	2	F	Web Plate Splice	East	1
6	2	G	Flange Plate Splice	East	1
7	2	H	Web Gap	West	1
8	2	H	Flange Tipping	West	1
9	1	H	Flange Tipping	East	1
10	1	H	Web Gap	East	1
11	1	G	Flange PlateSplice	East	1
12	1	F	Web Plate Splice	East	1
13	1	E	Web Gap	East	1
14	3	B	Bottom Flange	West	2
15	2	B	Top Flange	West	2
16	1	C	Bottom Flange Temperature	East	2
17	1	B	Bottom Flange	East	2
18	1	B	Top Flange	East	2
19	1	A	Bottom Flange	East	2
20	2	A	Bottom Flange	West	2
21	3	A	Top Flange	West	2
22	3	A	Bottom Flange	West	2
23	3	B	Top Flange	West	2
24	2	B	Bottom Flange	West	2
25	4	B	Bottom Flange	West	2
26	5	B	Bottom Flange	West	2
27	5	C	Bottom Flange Temperature	West	2
28	6	B	Bottom Flange	West	2
29	6	C	Bottom Flange Temperature	West	2
30	1	I	Top Flange	East	3
31	1	I	Bottom Flange	East	3
32	2	I	Bottom Flange	East	3
33	3	I	Bottom Flange	East	3
34	4	I	Top Flange	West	3
35	4	I	Bottom Flange	West	3
36	5	I	Top Flange	West	3
37	5	I	Bottom Flange	West	3
38	6	I	Bottom Flange	West	3
39	6	I	Top Flange	West	3
40	--	--	Equipment Temperature	--	4

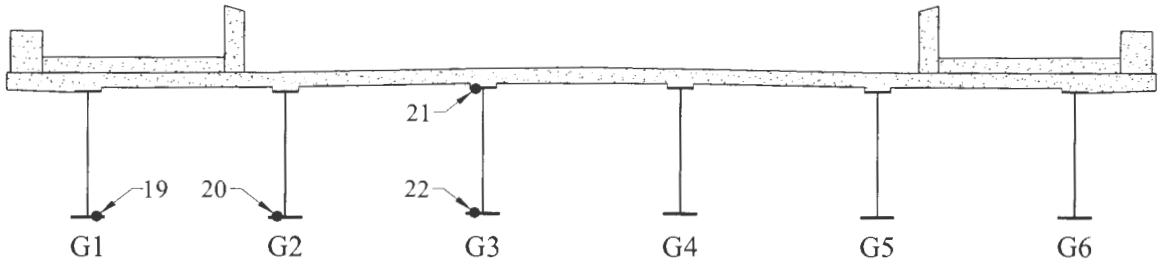

a. Cross-Section A.

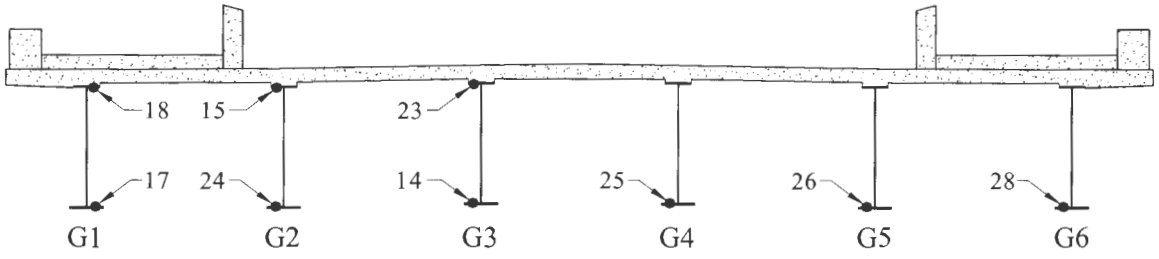

b. Cross-Section B.

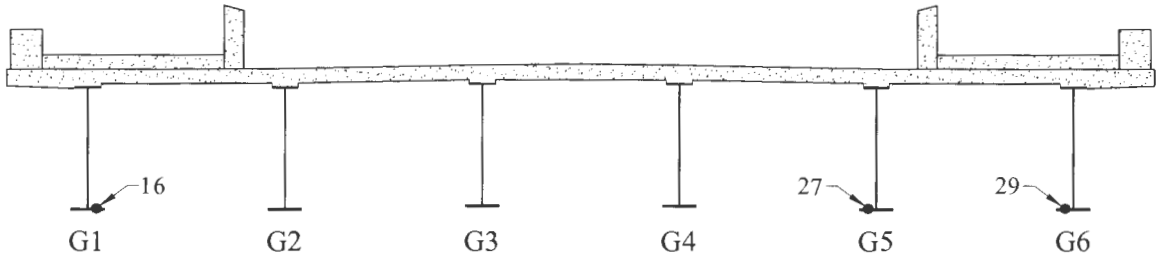

c. Cross-Section C.

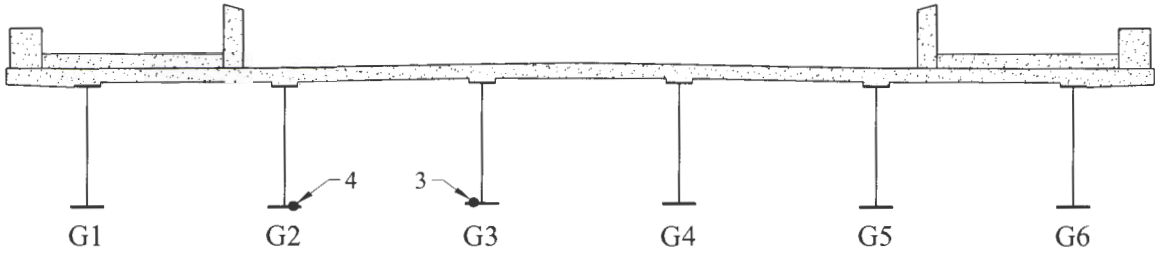

d. Cross-Section D.

Figure 4.4. Sensor locations and designations looking North.

Note: See Fig. 4.5 through 4.7 for detailed sensor location

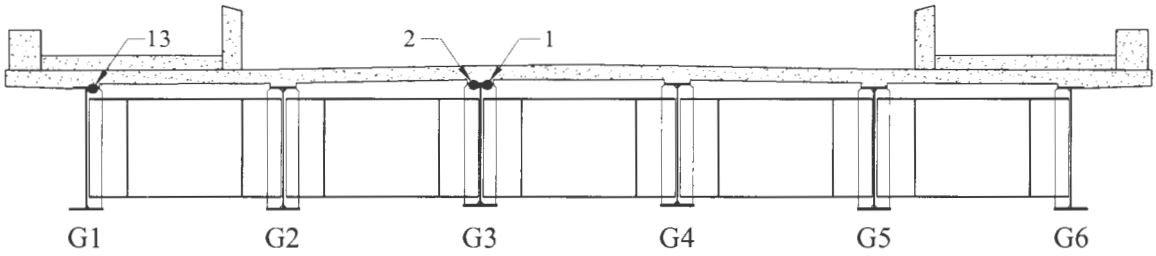

e. Cross-Section E.

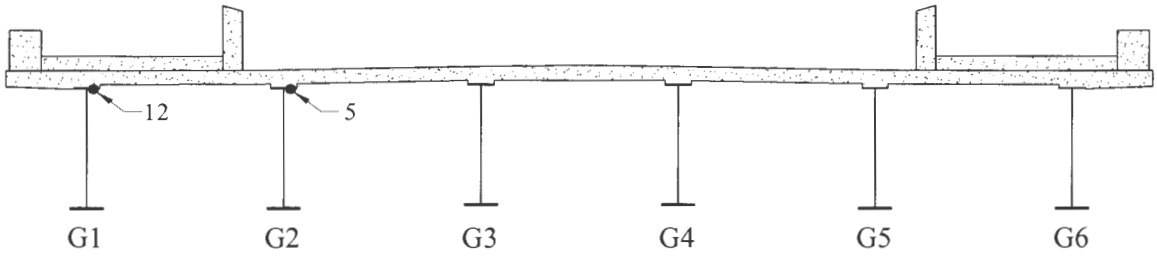

f. Cross-Section F.

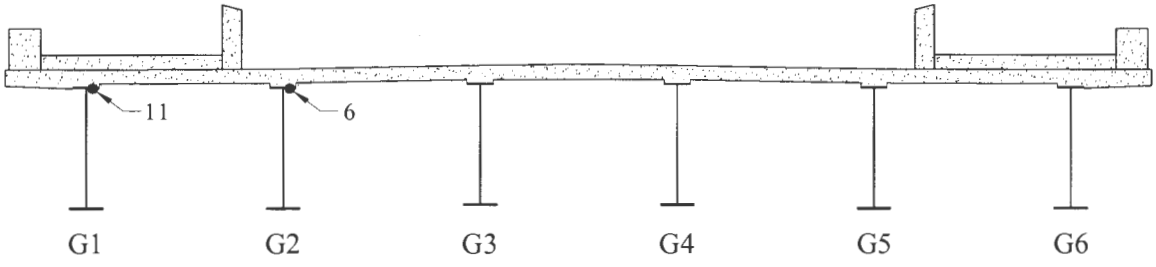

g. Cross-Section G.

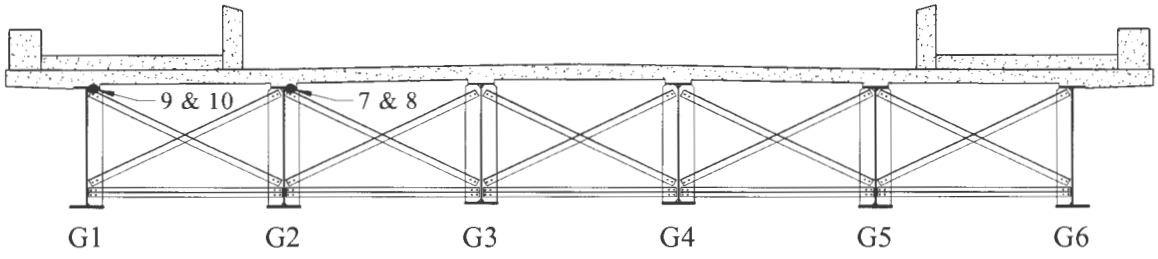

h. Cross-Section H.

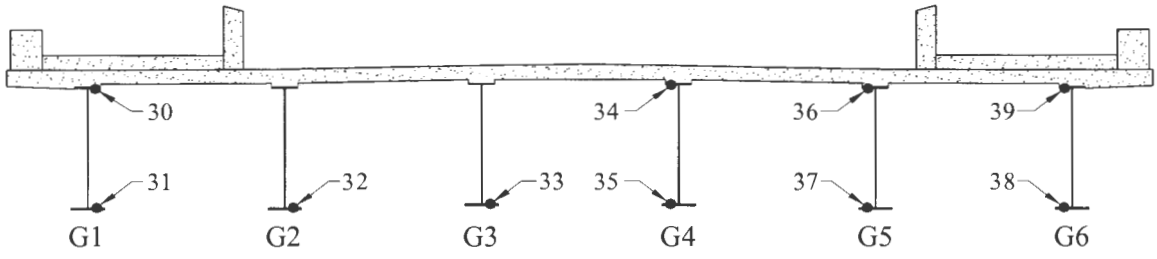

i. Cross-Section I.

Figure 4.4. Sensor locations and designations looking North (Continued).

Note: See Fig. 4.5 through 4.7 for detailed sensor location

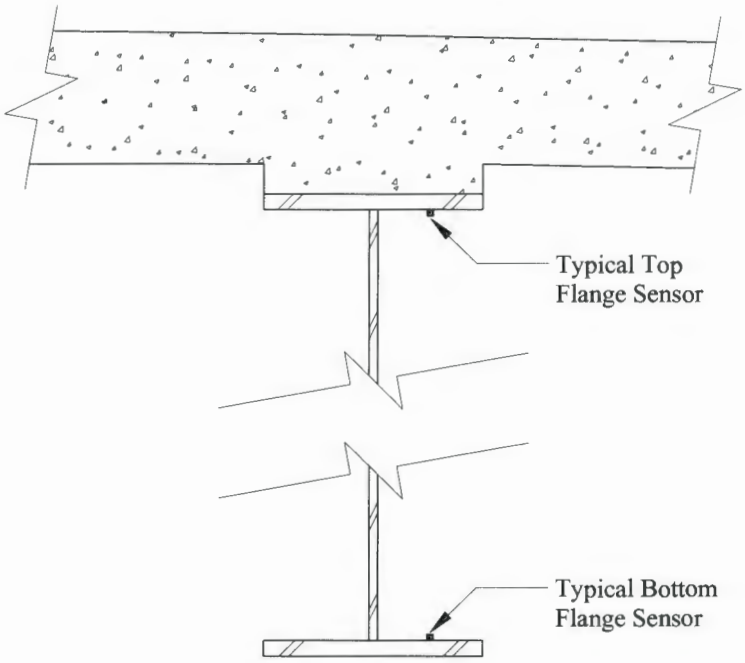

a. Typical top and bottom flange sensor placement

b. Photograph of typical top flange sensor.

c. Photograph of typical bottom flange sensor.

Figure 4.5. Typical top and bottom flange sensors.

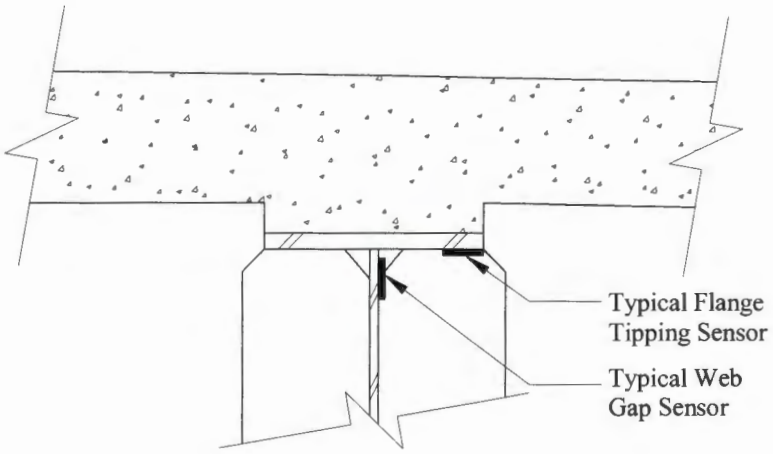

a. Typical flange tipping and web gap sensor placement.

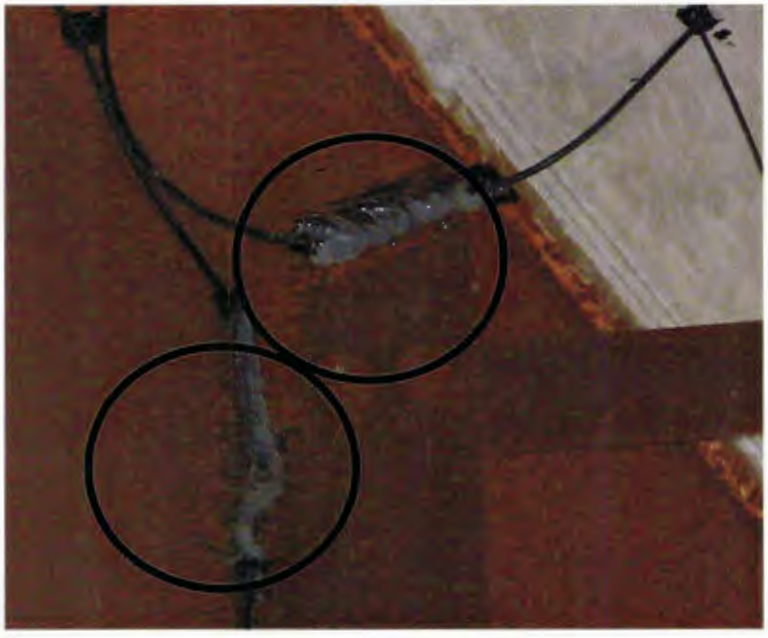

b. Photograph of typical web gap sensor (lower circle) and flange tipping sensor (upper circle).

Figure 4.6. Typical flange tipping sensor and web gap sensor.

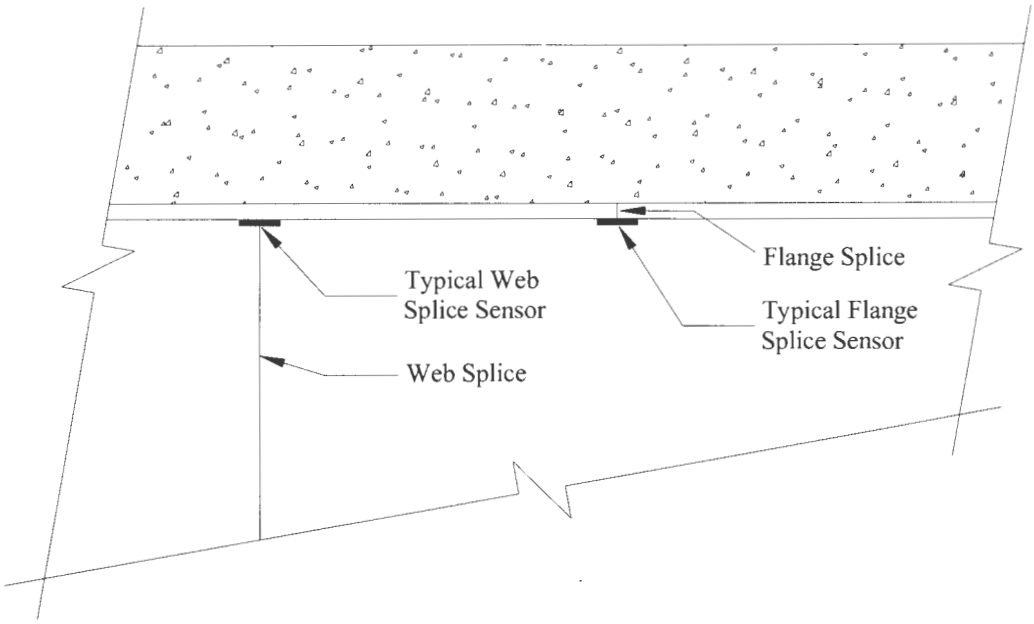

a. Typical splice sensor placement (elevation view).

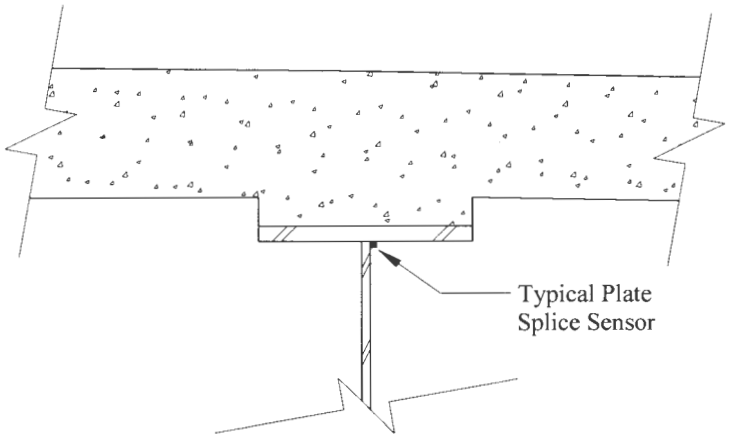

b. Typical splice sensor placement (cross-section view).
Figure 4.7. Typical plate splice sensor.

4.2.1.2 Sensor Types

Three different forms of FBG sensors were used on the E. 12th St. Bridge:

- Bare FBG
  - Single Sensors
  - Array of Sensors
- Surface-Mountable Sensor

Single bare FBGs were used for 15 of the 40 sensors. These sensors, manufactured by AVENSYS INC/Bragg Photonic Division, were written onto a SMF-28 fiber pigtail with no jacket. The pigtail distances on each side of the sensor were customized for the exact location of the sensor on the East 12th St. Bridge. A bare sensor after installation can be seen in Fig. 4.8.

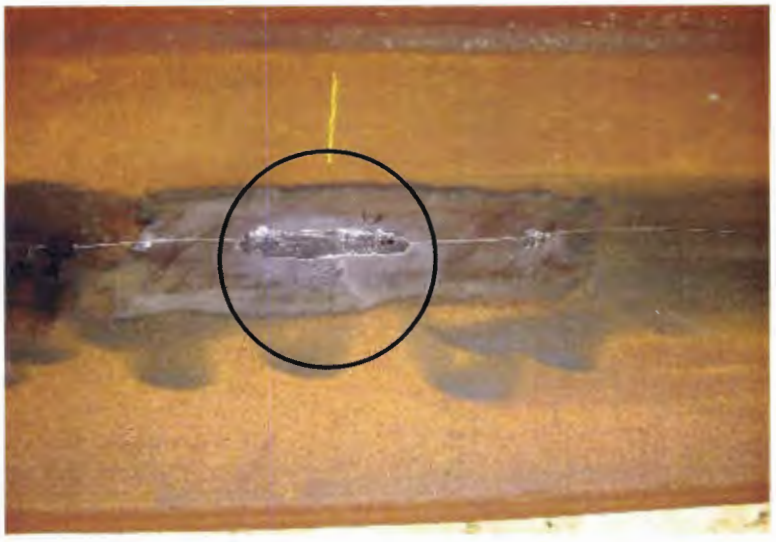

Figure 4.8. Photograph of single bare FBG after installation.

An array of FBG sensors exists when several single bare FBGs are multiplexed onto a single continuous SMF-28 fiber pigtail. This type of sensor arrangement was custom manufactured by LxSix Photonics, Inc. for this project. Specified distances between the sensors were provided by the project team. Fifteen of the sensors on the East 12th St. Bridge were installed in seven arrays of sensors. An installed single sensor multiplexed into an array looks the same as the single sensor illustrated in Fig. 4.8.

A Surface Mountable Sensor is a single FBG written into a pigtail with the sensor then embedded in an 8 in. x 3/4 in. piece of carbon fiber reinforced polymer (FRP). For the specific surface mountable sensors used in this project, FC/APC connectors were provided at the ends of the pigtails for multiplexing the sensors together. The ten surface mountable sensors used on the subject bridge (Sensors 30 to 39) were, again, manufactured by AVENSYS INC/Bragg Photonic Division. Fig 4.9 shows a typical surface mountable sensor (Note: The surface mountable sensors were received after the bare FBG sensors were installed and collection of associated data began at a later date. This will be apparent in the *Bridge Performance Indices* section.)

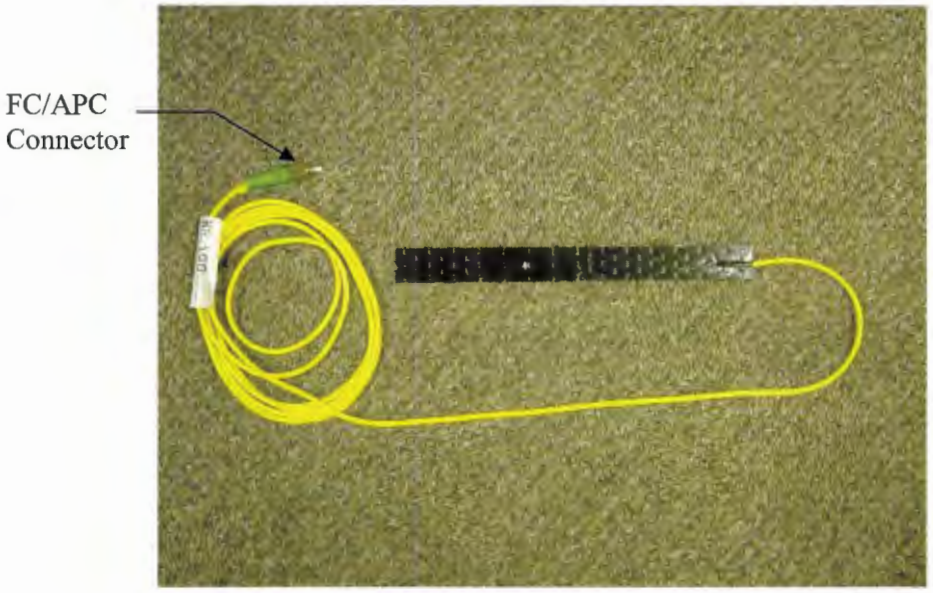

Figure 4.9. Photograph of surface mountable sensor before installation.

4.2.1.3 Jumper Cables

Fiber optic jumper cables were used to multiplex groups of FBGs separated by "longer" distances. The jumper cable used on the subject bridge consist of round duplex cable with SMF-28 fiber manufactured by Corning Cable Systems/Corning Division. Shown in Fig. 4.10 is a jumper cable that runs along the top flange of a girder to connect the Si425-500 and the first sensor on Channel 2.

4.2.1.4 Splices

Splicing was performed to join individual fibers (either containing a sensor, an array of sensors, or a jumper). Two different types of splices were used on this project.

- Fusion Splices
- Mechanical Splices

Fusion splicing consists of aligning the cores of two separate fibers and then fusing them together. A Fiber Optic Splicing Professional from Huxley Communication, located in Huxley, IA, performed the 37 fusion splices required for the project at a cost of $35 per splice. Fig. 4.11 shows two fibers being fusion spliced together.

Mechanical splices consist of the previously mentioned FC/APC connectors at the ends of the Surface Mountable Sensors and FC/APC mating sleeves. Fig. 4.12 shows a mechanical splice used on the bridge. Eleven mechanical splices were utilized during this project. To weatherize the splices

(both fusion and mechanical), silicone was used to cover the spliced region. A weatherized fusion splice is shown in Fig. 4.13.

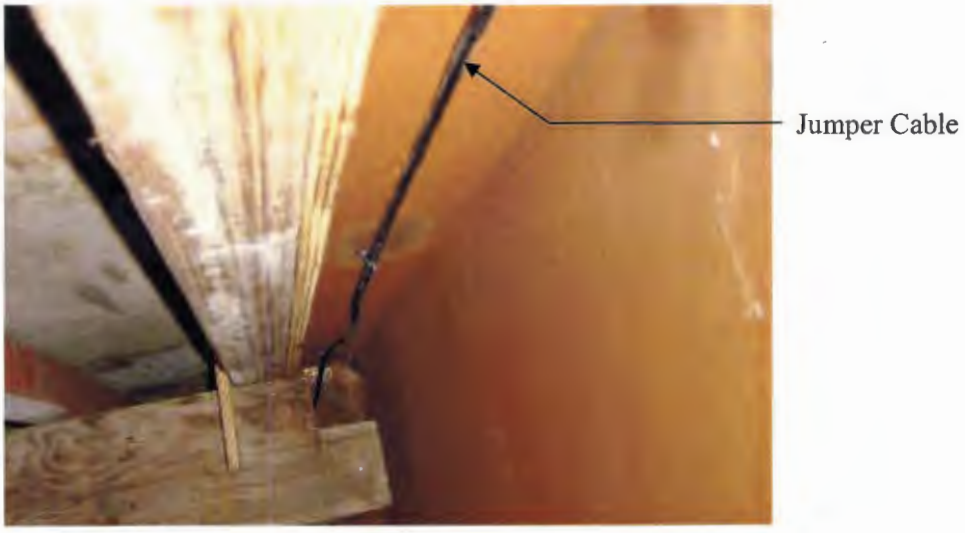

Figure 4.10. Photograph of jumper cable installed on top flange of girder.

Figure 4.11. Photograph of fusion splicing of two fibers.

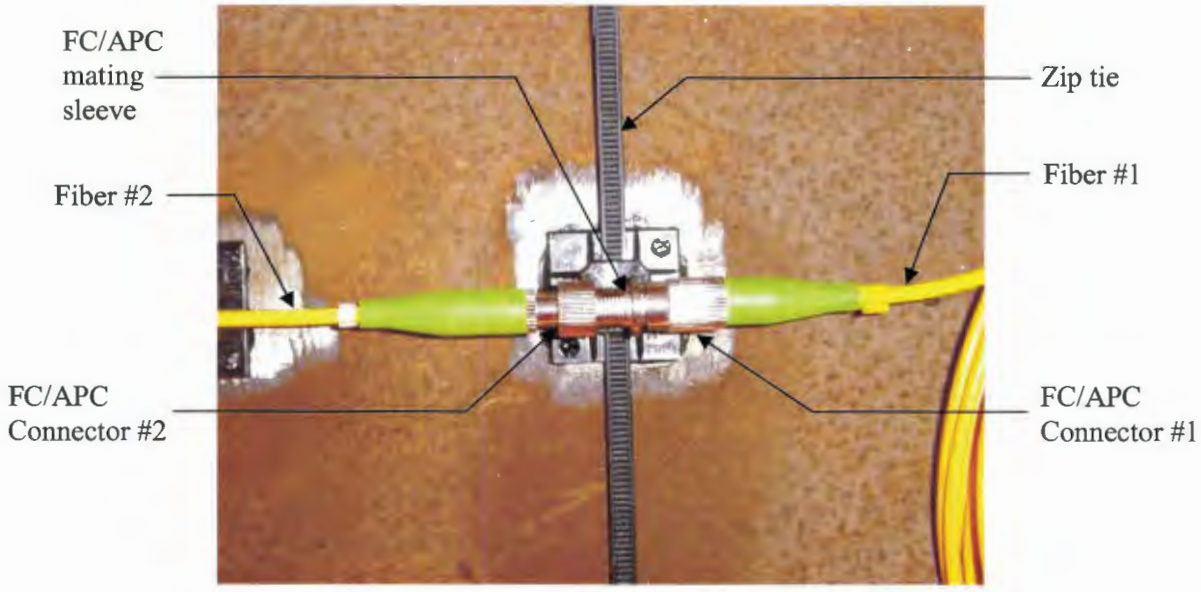

Figure 4.12. Photograph of FC/APC mating sleeve connecting two fibers.

Figure 4.13. Photograph of completed splice after silicone protection has been applied.

4.2.1.5 Sensor Installation

Installation of the individual sensors began with surface preparation. A wire wheel on a hand-held grinder was used to remove the weathering layer from the steel. A hand-held grinder with a sanding disc was then used to polish the steel to a smooth finish. The area was then cleaned with a

rag and acetone. The size of area prepared in this manner depended on which type of sensor was being installed. The bare fiber FBG sensors required approximately a 6 in. x 1 in. area while the surface mountable sensors required approximately a 10 in. x 2 in. area.

The general approach for adhering the bare FBG sensors and the Surface Mountable Sensors is generally the same, but the details for each installation procedure depend somewhat upon the sensor type. The details for each installation procedure are described in the following paragraphs.

Bare FBG Sensor: After the surface was prepared and the sensor properly aligned, a dot of epoxy was placed on the fiber optic cable approximately 1 in. away from the sensor. After the epoxy had gained sufficient strength, a line of epoxy, approximately 1/8 in. wide by 2 in. long, was then placed on the steel where the sensor was to be placed. The sensor was then placed in the line of epoxy. After the epoxy had cured, another dot of epoxy was placed on the other side of the sensor. The function of the two dots of epoxy was to ensure that stress is not placed on the sensor if the fiber is inadvertently pulled taut. Figure 4.8 shows a sensor after these steps have been performed (the dots of epoxy can be seen on each side of the sensor as well as the line of epoxy in which the sensor was placed). The epoxy used to install the bare FBG sensors was Loctite's Instant Adhesive, Clear 411. To decrease the set time, Loctite's 7452 Accelerator was used. The accelerator was misted over the epoxy following placement of the sensor. After the epoxy had fully cured, the area over and around the sensor was covered with silicone to protect it from environmental damage. A sensor covered in silicone is shown in Fig. 4.14.

Surface Mountable Sensor: After the steel surface was prepared as previously discussed, the steel surface was sprayed with Loctite's 7387 Activator. The side of the FRP sensor which was to be in contact with the steel was also sprayed with Loctite's 7387 Activator. After the activator had set, the contact side of the FRP was then coated with Loctite's Structural Adhesive - Rapid Fixture 39. The sensor was then correctly aligned and held in place for approximately 20 sec. until a bond was established. An installed surface mountable sensor is shown in Fig 4.15. After the surface mountable sensors were installed, they were also covered with silicone to protect them from damage.

Figure 4.14. Photograph of sensor covered in silicone.

Figure 4.15. Photograph of installed surface mountable sensor.

4.2.2 Interrogator

The interrogator, the instrument that interprets and outputs the readings from the FBG sensors, chosen for this project was the Si425-500 manufactured by Micron Optics, Inc. Selected for

its capabilities, size, and durability, the Si425-500 is a four channel interrogator capable of reading up to 128 FBG Sensors per channel. Maximum read rates are 250 Hz/channel for channels with less than 100 sensors and 125 Hz for channels with more than 100 sensors.

The Si425-500 Swept Laser Interrogator (shown in Fig. 4.16) is located at the hub of the DASS, which is centered on top of the bridge pier in the environmentally controlled (through the use of thermostats which control the heaters and fans) steel cabinet pictured in Fig. 4.17. The 35 pound interrogator, which is approximately 17 in. x 17 3/4 in. x 5 1/4 in., has a published operating temperature range of 50°F to 104°F. The Si425-500 operates by emitting a broadband of light from a laser through each of the four data collection channels. Each of the sensors on the fiber optic cable then reflect a single wavelength which the interrogator then registers and stores. The Si425-500 is a wavelength based interrogator which means it can not determine the location of the sensor on the fiber optic cable. Therefore, the reflected wavelength data are stored in ascending order. However, as long as one knows the initial reflected wavelength, from each sensor, one can generally associate the unspecified location data with known locations.

The Si425-500 is constantly "listening" for a "Read" command that is sent by the Data Relay Server ([DSR] - discussed subsequently). After receiving the command, the data stored in buffer by the Si425-500 are continuously transferred to the DRS in real-time until a "stop" command is given or the connection is terminated. The data are transferred from the Si425 using a static IP address and port which are assigned to the Si425-500 through a TCP/IP connection. Due to the anticipated vehicle speeds and the projected end use of the data, a scan rate of 31.25 Hz was used in this project.

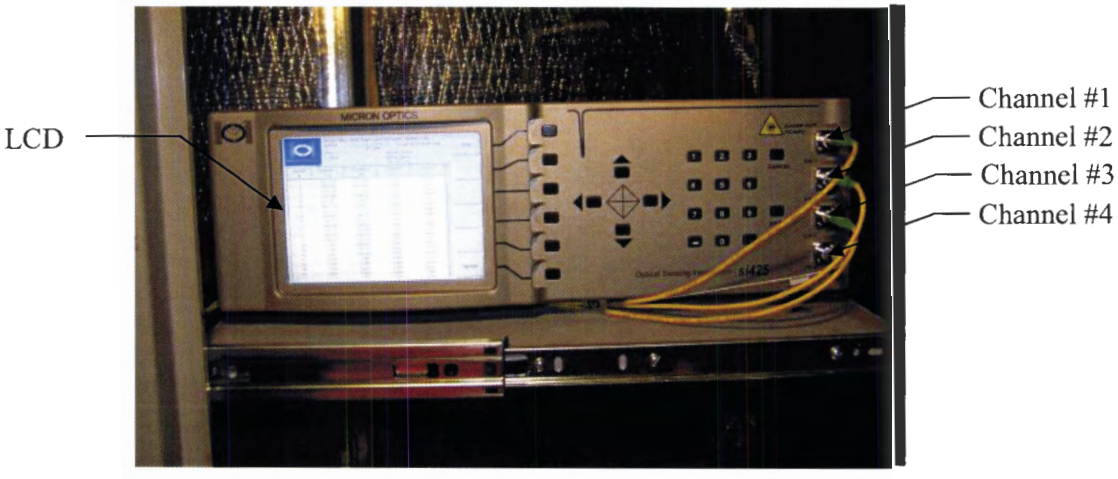

Figure 4.16. Photograph of front panel of the Si425-500 interrogator.

a. Steel cabinet.

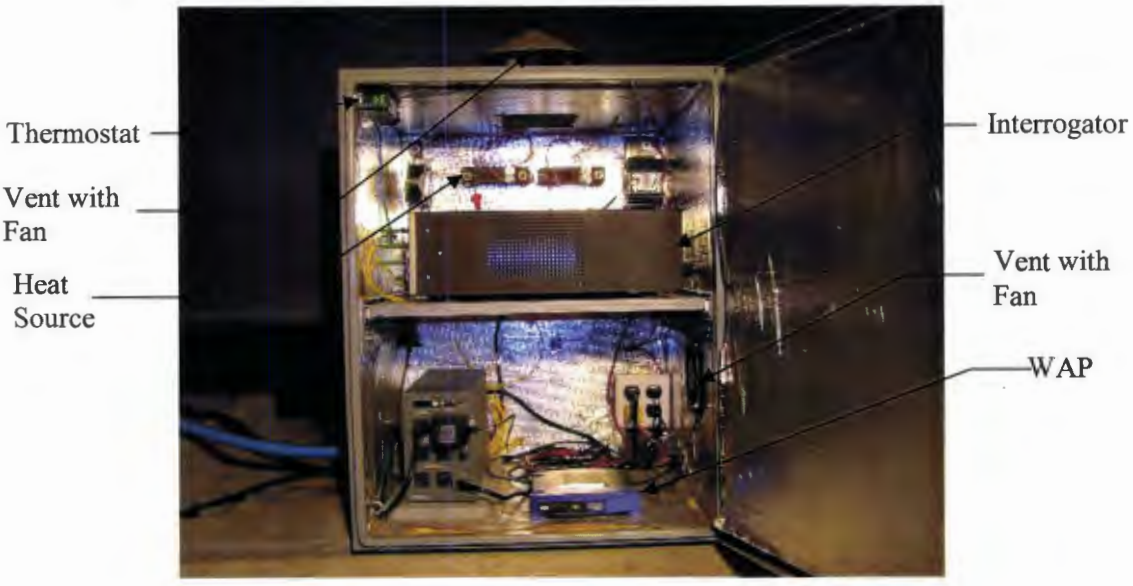

b. DASS equipment in steel cabinet.

Figure 4.17. Photograph of steel cabinet on bridge pier that houses the DASS equipment.

4.2.3 Wireless Access Point

The Si425-500 is connected to a Linksys Wireless Access Point (WAP) using an Ethernet connection, creating a LAN (the DASS LAN) between the Si425-500 and the WAP. The DASS WAP transmits the raw data, in wavelength format, from the interrogator to another WAP, that is part of the GSS, located approximately 450 ft from the bridge. Each of the WAPs have been assigned static IP and configured to operate in wireless bridge mode, thereby allowing direct communication between the DASS LAN and the GSS LAN. The wireless data transmission is protected by WEP2 (Wired Equivalent Privacy – 128 bits) and the SSID is disabled to further secure the network connection.

To ensure reliable communication between the DASS and the GSS WAPs, the antennas for the DASS WAP were placed at the east edge of the bridge pier (see Fig. 4.18) to provide line-of-sight communication between the WAPs. The use of the WAPs allowed transmission of the data between the DASS to the GSS without the need to run communications cable.

4.3 Gateway Sub-System (GSS)

The GSS, shown in Fig. 4.19 is located in a secure building approximately 450 ft from the bridge pier. Components of the GSS include (manufacturer in parentheses):

- Data Management Equipment (DME)
  - Data Relay Server (DRS)
    - Desktop Computer – 700 MHz Processor, 20.0 GB Hard Drive, 256 MB RAM (Gateway)
  - Data Collection Server (DCS)
    - Desktop Computer – 733 MHz Processor, 14.2 GB Hard Drive, 256 MB RAM (Dell)
- Communication Equipment
  - 2.4 GHz Wireless-802. 11g Access Point (Linksys)
  - 2.4 GHz Wireless-802. 11g Router (Linksys)
  - 678 DSL Modem (Cisco)
- Video Equipment
  - Canon VB-C10/VB-C10R Network Camera

The GSS WAP, DRS, DCS, DSL modem, and the video camera are all connected to one another through the Linksys router by Ethernet cables, which enable all of the GSS components to communicate with one another. All of the components were assigned a static IP address, thus creating a consistent GSS LAN. When data need to be transferred for permanent data storage (discussed subsequently) and client real-time data access, the Cisco 678 DSL Modem is used. This modem has the ability to download at 1.5 MBps and upload at 1.0 MBps.

Figure 4.18. Photograph of Data Acquisition Sub-System WAP antennas placed at the edge of bridge pier.

Figure 4.19. Photograph of Gateway Sub-System located in secure facility near bridge.

As stated previously, raw wavelength data from the Si425-500 are transmitted to the GSS via the WAP which then passes the data to the rest of the GSS via the router. The data are continuously called by the DRS from the Si425-500 using a TCP/IP connection. As the DRS is continuously collecting data, other applications can use a TCP/IP connection to the DRS to retrieve data in a similar manner to which the DRS collects the data from the Si425-500. When another application connects to the DRS (such as the DCS or the Web Line Chart Client [discussed subsequently]), the data stream is relayed to the other applications.

The DCS continuously obtains data from the DRS for processing and permanent storage. As the DCS downloads the data from the DRS, the binary data stream is parsed and converted to create ASCII text files of raw wavelength data. The ASCII files are automatically limited in size to 50 MB by a specially created data collection program; once the files reach the maximum size, they are saved and compressed. The compressed files are then automatically placed on an FTP server. The Data Storage/Processing Sub-System (DSPSS), located at the BEC and described subsequently, automatically downloads and removes the files from that FTP server.

As stated previously, a website provides live strain data along with a live video stream (http://www.ctre.iastate.edu/bec/structural_health/e12thst_dsm.cfm). When the website is accessed, the Web Line Chart Client program retrieves the live wavelength data from the DRS, converts it to strain, and transmits it to the website via a web portal. The interactive website allows the user to choose the sensor location from which the strain data is displayed. A Java application connects to the camera via a HTTP to provide the live video stream.

4.4 Data Storage/Processing Sub-System (DSPSS)

4.4.1 Data Storage/Processing Overview

The DSPSS housed at the BEC in Ames, Iowa, about 50 miles from the East 12th St Bridge, is where the data files are permanently stored and processed. DSPSS components include:

- Data Management Equipment
  Dell PowerEdge 4600 Server - 3.0 GHz Processor, 1.2 TB Hard drive, 4.0 GB RAM

After the wavelength data files are received at the BEC (via the FTP process described previously), the wavelength data are checked and, if need be, corrected to ensure problems that will be discussed subsequently did not occur and then converted to strain data. Several processes are then performed to ensure that the entire system is operating properly, eliminate temperature strain from the complete strain record, compute global behavior indices of the bridge, and count strain cycles at the various sensor locations.

Elimination of temperature effects is performed to allow the long-term effects of live load on the bridge to be assessed. After the temperature effect elimination, the global behavior of the bridge is monitored by computing distribution factors (DF), neutral axis locations (NA), and end restraint ratios (ER). By monitoring these basic structural characteristics, a conceptual understanding of the time dependent performance can be gained.

Rainflow counting is being used to count the number and magnitude of strain cycles at the various sensor locations. With sufficient data, the results from the strain cycle counting can then be used to evaluate the susceptibility of the details to failure and to possibly estimate remaining life.

4.4.2 Data Storage/Processing Sub-System Software

4.4.2.1 Data Correction Program

To alleviate problems within the raw wavelength data (discussed in future sections), a data correction program was developed by the research team. The program uses the absolute difference between the last known good wavelength reading and the incoming raw data to select which current readings correspond to previously know good readings. In the event that extra data (extra sensors columns) are present, this procedure determines which values are valid data.

The program then goes through a series of checks to check if the above process results in duplicate data entries selected for multiple sensors. Such an occurrence indicates that not enough sensor columns were present in the raw data. The application again uses the absolute difference to determine which duplicate value is correct and which is incorrect. The duplicate data entry which is incorrect is then "zeroed" resulting in a line of data referred to as the "zeroed corrected" data line. The program then repeats the procedure for the next line using the data from the "zeroed corrected" data line as the new last known good wavelength reading.

After an entire file is processed, the "zeroed" data entries are interpolated between the last and most recent valid known data for each sensor. The interpolation is performed so that abrupt discontinuities in the data are not created. The corrected wavelength data are then converted to strain data. It is important to note the data in the senor columns which has been "zeroed" and interpolated are not considered reliable data by the research team. The correction program allows the reliable data to be extracted from the data stream and relayed to the research team in a format that is compatible with the remaining data processing software.

4.4.2.2 Data Sorter Program

As stated above, the DSPSS performs several functions some of which are performed by the Data Sorter Program (DSP). The DSP performs basic checks of the data integrity; finds the minimum, maximum, and average strain value for each sensor in the file; and creates a time history of both the temperature and live load strain records.

The DSP, developed by the research team, is adaptable to any data set that has a time, buffer, and temperature column in addition to the sensor columns. As shown in Fig. 4.20, the user must enter

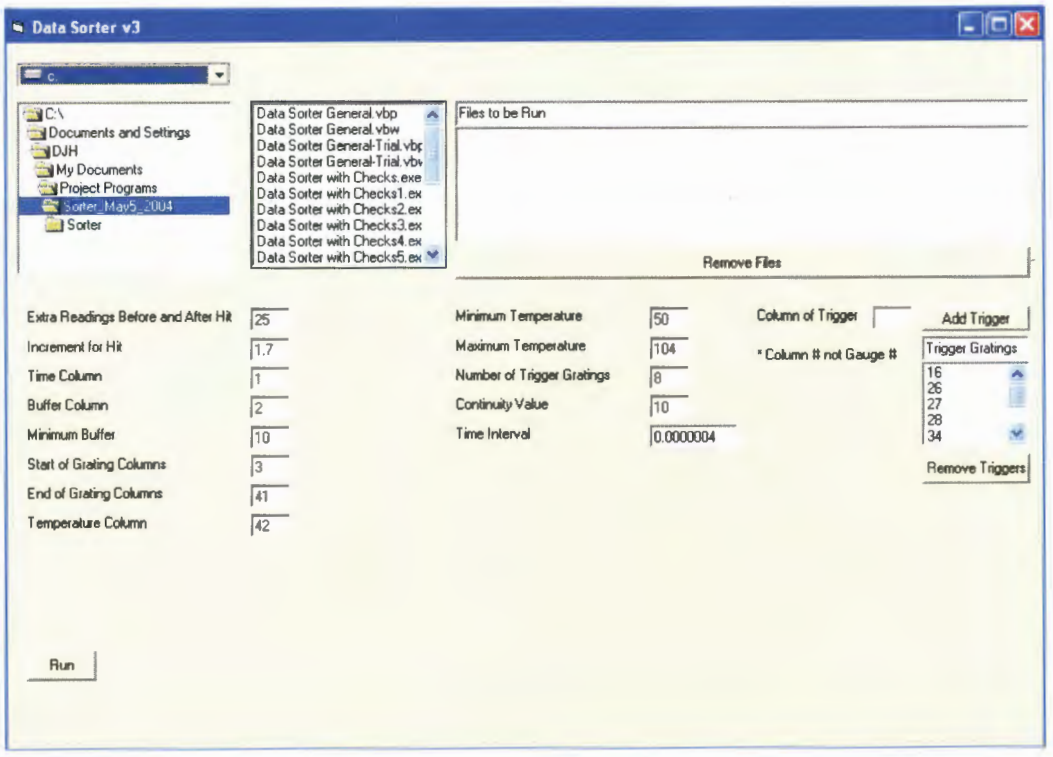

Figure 4.20. Screenshot of the DSP user interface.

the location of the time, buffer, and temperature columns along with the beginning and ending locations of the sensor columns. For the E. 12th St. Bridge the time is in Column 1, the buffer in Column 2, the sensors in Columns 3 to 41 and the temperature sensor in Column 42. Multiple files can be selected at once and the DSP will process them sequentially. The basic data integrity checks that are performed include:

- Time Gap - Determines if two consecutive time values differ by more than the specified read speed. The difference between two successive time values is found and if the difference is greater than the number entered into the Time Interval box shown in Fig. 4.20 a warning with the time of the occurrence is generated. This check is completed to ensure continuity of the data collection process and proper system operation.
- Buffer Check - Informs if the buffer (a measure of the amount of the Si425-500's internal memory being used) drops below a specified threshold. If any value in the buffer column drops below the value entered in the Minimum Buffer box shown in Fig. 4.20, a warning with the time of the occurrence is generated. The buffer check allows the research team to monitor the data collection process. If the buffer value is repeatedly dropping issues with the data collection software could be occurring.
- Continuity Check - Informs if the difference between two consecutive readings of one sensor is larger than a specified threshold. If the difference between two

consecutive readings of one sensor is larger than the threshold specified in the Continuity Value box, a notice appears at the completion of the program's operating period. The continuity check is used to indicate a malfunction of a sensor or the data acquisition system.

- Temperature Check - Informs if the steel cabinet, which contains the data acquisition equipment, drops below or rises above specified temperatures. If a value in the temperature column is less than the value entered in the Minimum Temperature box, or is greater than the value entered in the Maximum Temperature box shown in Fig. 4.20, a warning with the time of the occurrence is generated. This check ensures the environmental controls (i.e. heater, fans, vents, etc.) of the DASS protective box are functioning properly.

The DSP also creates a Minimum, Maximum, and Average file. As the name indicates, the file consists of the minimum, maximum, and average reading for each sensor within a file. This statistical information can be useful to the research team for monitoring long-term trends of the sensors.

The temperature/traffic separation routine in the DSP is based on the idea that if one knows the temperature strain time history, one can subtract that time history from the raw strain time history, to generate the live load strain time history. The algorithm that was developed for the DSP identifies traffic events based upon machine coded structural behavior concepts and removes those time periods from the raw data file. A file (called the temporary temperature file) that contains raw strains with gaps where traffic events occurred is created. Since the traffic events last a short time, the temperature effects during the traffic event are assumed to vary linearly from the beginning of the traffic event to the end. Linearly interpolated data points are then generated appropriately to complete the temperature strain file during periods when the traffic events occurred. The values in the complete temperature file are then subtracted from the values in the raw data file and a traffic file is created.

Traffic events are identified by searching for rapidly changing portions of the raw strain record. To accomplish this, the difference is raw strain between every fourth reading is computed. For example, points A and B in Fig. 4.21, and compared against the "Increment for Hit" value entered as shown in Fig. 4.20. When the difference exceeds that value, a traffic event is "identified". Comparing every fourth reading, rather than every reading, is done to reduce false call occurrence.

To reduce processing time, the DSP is designed so that a limited number of sensors can be selected as "trigger sensors". Trigger sensors are the sensors whose data the above described process

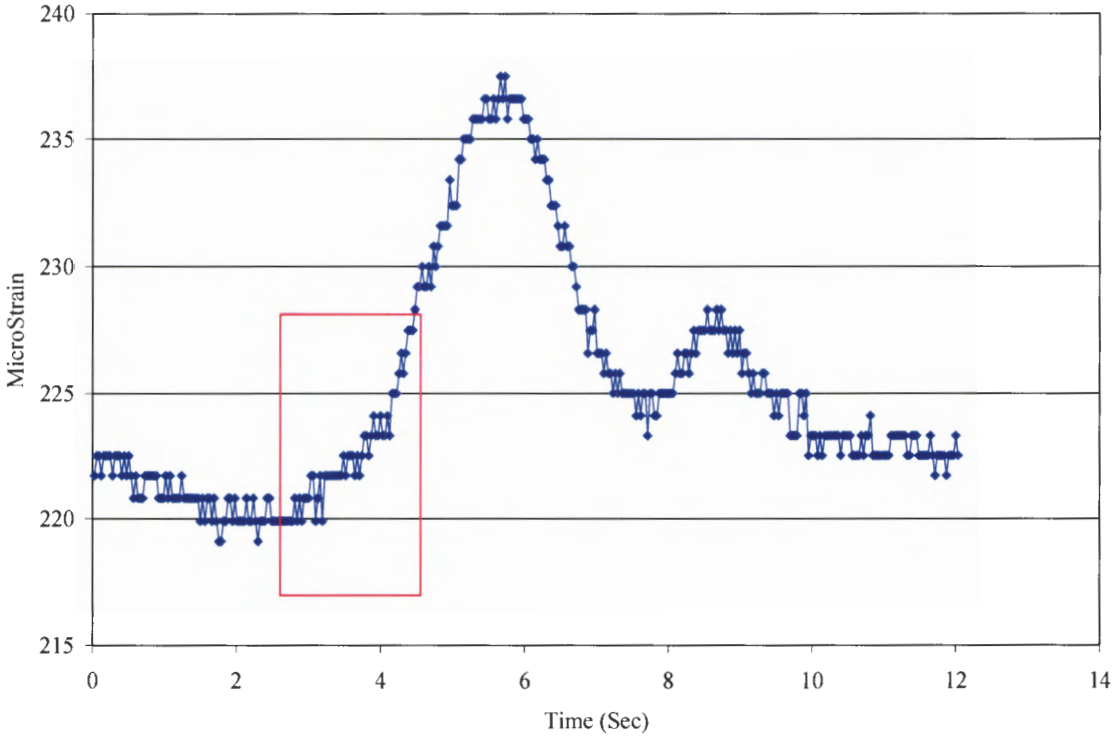

a. Traffic event in the raw strain data.

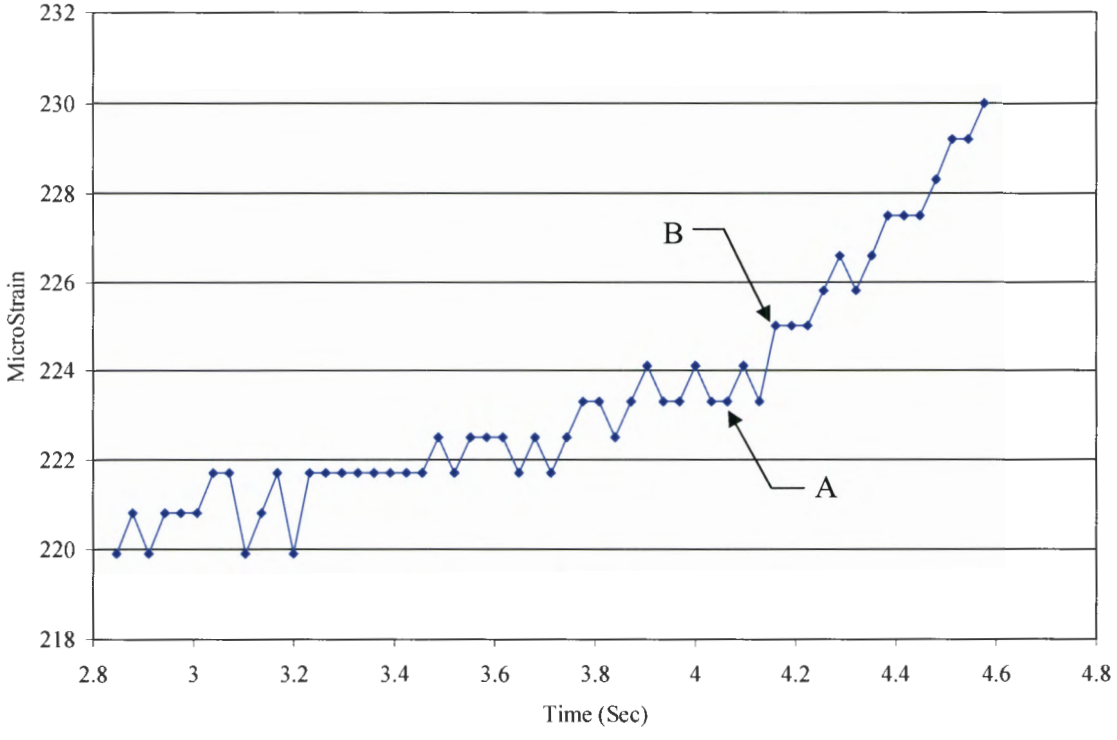

b. Strain data in box shown in part a.

Figure 4.21. Illustration of temperature/traffic separation process.

utilizes for identifying traffic events. When the data in one of the trigger columns signify an event, the row in which the event occurs and a specified number of rows before and after the event are stored as the traffic event. To ensure that the entire traffic event is captured, the user can specify an additional number of readings to be considered part of the traffic event. The number of rows to store before and after a trigger is reached is set by the DSP user through the Extra Readings Before and After Hit box shown in Fig. 4.20. The number of readings before and after the event that best obtains the whole event will depend on the location of the trigger sensors and the speed and the properties of typical passing vehicles. For the East 12th St. Bridge, 25 readings before and after a trigger event worked appropriately well.

There are several limitations to the type of bridge that the DSP developed for this project can be applied. The bridge must have a minimum number of time periods during the day during which no traffic is present. In other words enough temperature-only behavior needs to occur such that an accurate temperature strain time-history can be generated.

To illustrate the separation process described above, Fig. 4.22 shows an example of raw data that have been processed by the DSP. When the raw data for nine days are globally examined, it is immediately clear that the temperature effects for each day are larger than the live-load effects. After processing, the temperature only data (Figs. 4.22c and 4.22d) show a smoother trend without the peaks caused by the live-load effects. The traffic data (Figs. 4.22e and 4.22f) show the strains are centered near the 0.0 $\mu\varepsilon$ axis as one would expect.

4.4.2.3 Data Processor Program

The DPP calculates several engineering parameters and indices that can be used to monitor the performance of the bridge over time. The DPP was designed specifically for the E. 12th St. Bridge SHM system and is not applicable to other data sets without changing the underlying computer code. The process in which a file is selected to be run through the DPP is the same as the DSP; the DPP also allows multiple files to be selected and run in succession to one another. To compute the various indices, the appropriate check boxes must be selected. The DPP user interface is shown in Fig. 4.23.

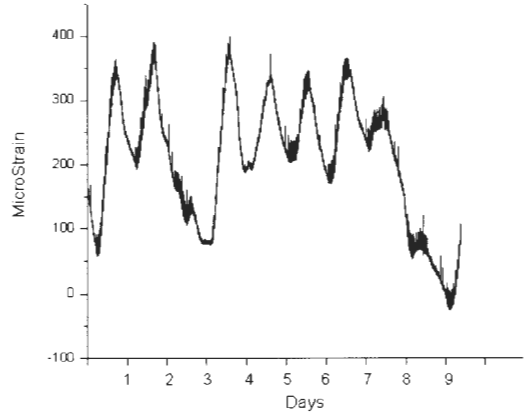

a. Raw data - 9 days.

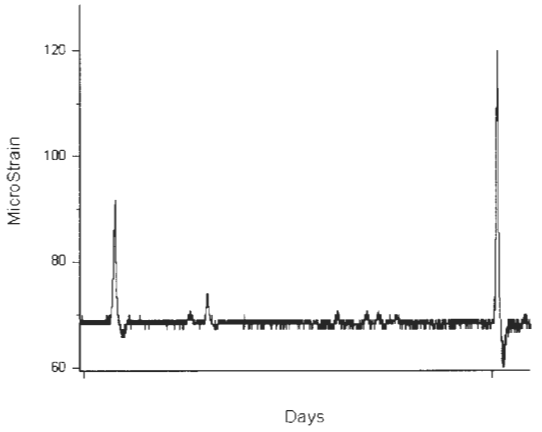

b. Raw data - 1 minute.

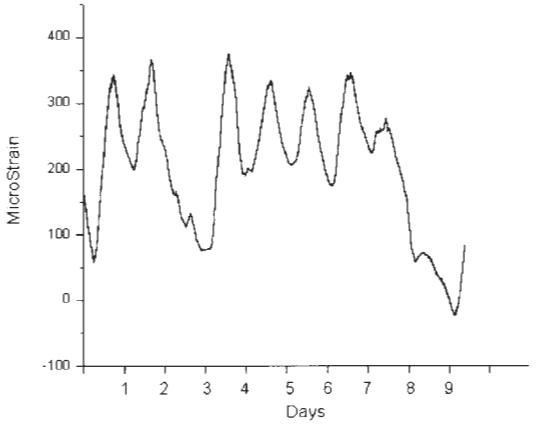

c. Temperature data - 9 days.

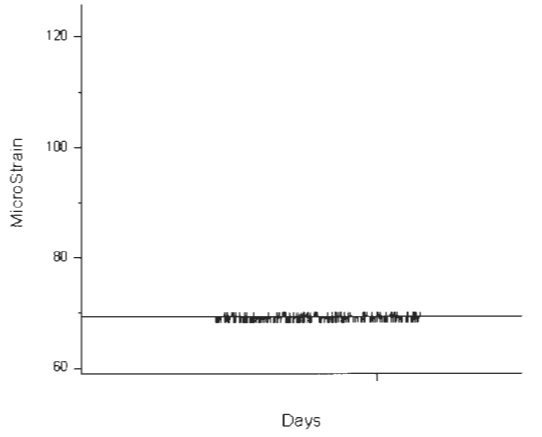

d. Temperature data - 1 minute.

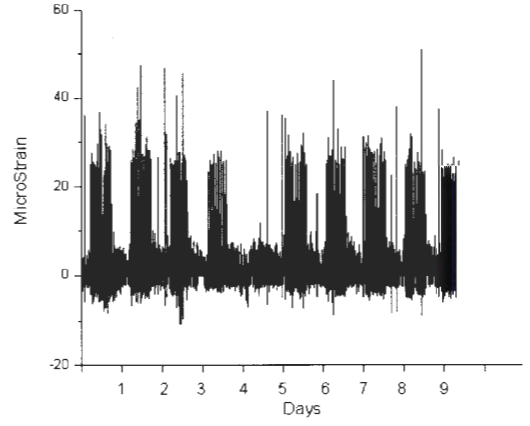

e. Traffic data - 9 days.

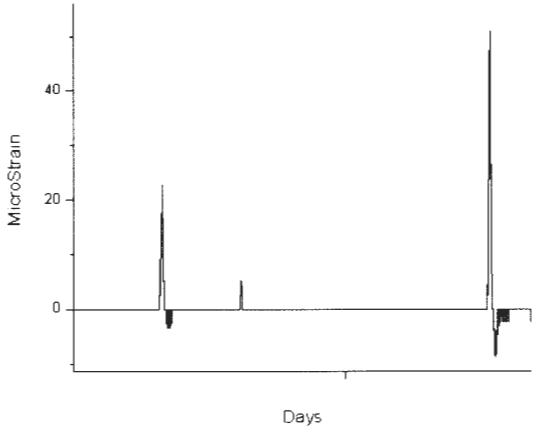

f. Traffic data - 1 minute.

Figure 4.22. Raw, temperature, and traffic data for 9 days and 1 minute.

Distribution Factor - The DF is calculated at cross-sections where there are bottom flange sensors on each girder laterally across the bridge. This occurs at the midspans of both the North and the South spans of the bridge. The DF for each girder at each midspan is found by taking the strain on the bottom flange of the particular girder at the particular cross-section and dividing it by the sum of all of the bottom flange strains at that particular cross-section.

$$DF = \frac{\varepsilon_n}{\varepsilon_1 + \varepsilon_2 + \varepsilon_3 + \varepsilon_4 + \varepsilon_5 + \varepsilon_6} \quad \text{or} \quad \frac{\varepsilon_i}{\sum_{i=1}^{n=6} \varepsilon_n} \tag{1}$$

Where: ε_n = Strain from Girder of Interest
ε_1 = Strain from Girder 1
ε_2 = Strain from Girder 2
ε_3 = Strain from Girder 3
ε_4 = Strain from Girder 4
ε_5 = Strain from Girder 5
ε_6 = Strain from Girder 6

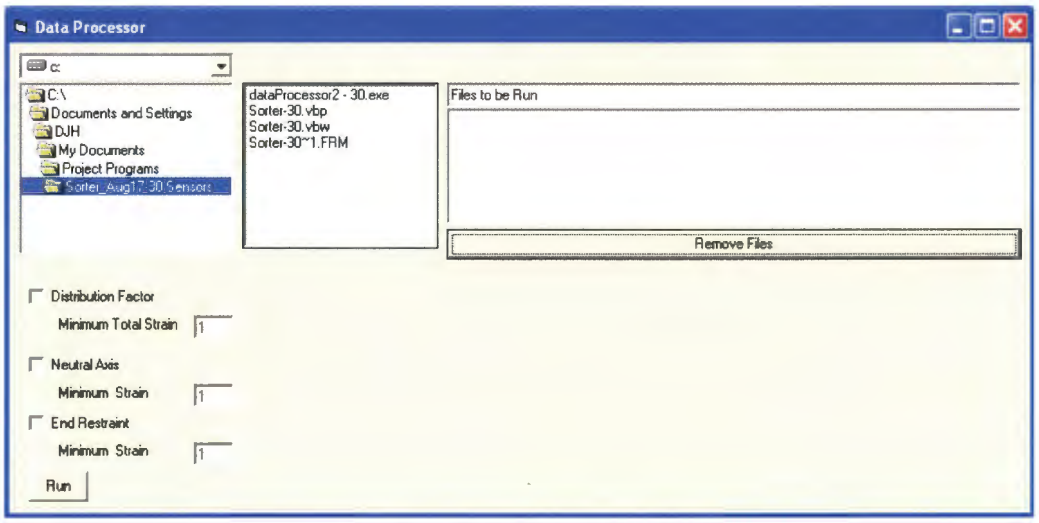

Figure 4.23. Snapshot of the DPP user interface.

The DF is only calculated when the sum of the strains is greater than the threshold entered in the box labeled Minimum Total Strain in Fig. 4.23. A DF file is created that has the DF for each girder at each cross-section. Table 4.2 summarizes the sensors that are involved in calculating the DF at each cross-section.

Table 4.2. Sensors used in the distribution factor calculation.

Description	Sensors
North Midspan DF	17, 24, 14, 25, 26, 28
South Midspan DF	31, 32, 33, 35, 37, 39

Neutral Axis - The NA is calculated at points on the bridge where there is a sensor on both the top and bottom flange of a girder at the same cross-section. The distance of the Neutral Axis from the bottom of the bottom flange is found by equation #2:

$$NA = \left(\frac{\varepsilon_{BF}}{\varepsilon_{BF} - \varepsilon_{TF}}\right) d_w + t_{BF} \quad (2)$$

Where: ε_{BF} = Bottom Flange Strain
ε_{TF} = Top Flange Strain
d_w = Web Depth
t_{BF} = Bottom Flange Thickness

The NA is only calculated when the bottom flange reading is greater than the value entered in the box labeled Minimum Strain next to the Neutral Axis check box in Fig. 4.23. A file similar to the DF file, the NA file, is created which has the NA locations listed for each time the NA is calculated. The FBG sensors used in the NA calculation are summarized in Table 4.3. The NA Position column is the designation used for identification purposes and will be used in subsequent sections.

Table 4.3. Sensors used in the neutral axis location calculation.

NA Position	Sensors
G1N	17, 18
G2N	24, 15
G3N	14, 23
G1S	31, 30
G4S	35, 34
G5S	37, 36
G6S	38, 39

End Restraint - The ER is determined for the three girders which have bottom flange sensors at the North integral abutment bridge. To monitor for changes in the longitudinal stiffness characteristics, the ratio of the strain on the bottom flange at the midspan to the strain of the bottom flange at the integral abutment is calculated as:

$$ER = \frac{\varepsilon_{MS}}{\varepsilon_{AS}} \tag{3}$$

Where: ε_{MS} = Midspan Bottom Flange Strain
ε_{AS} = Abutment Bottom Flange Strain

As with the DF and NA, the ER is only calculated when the strain at the midspan of the bottom flange of the girder is greater than the value in the Minimum Strain box next to the End Restraint check box in Fig. 4.23. Table 4.4 lists the sensors used for the ER ratio calculated by the DPP and the girder number by which the ratios are identified.

Table 4.4. Sensors used in the end restraint ratio calculation.

Girder	Sensors
1	19, 17
2	20, 24
3	22, 14

4.4.2.4 Averaging Programs

Programs were also developed to compute the average of the DF, NA, and ER files that were created (a separate program for each type of file). The programs create an Average File which has an entry for each file that is averaged. So for instance, if 30 DF files (30 days worth of data, for example) were processed by the DF average program, the output file would have 12 columns of data (two DFs for each girder, one for the North midspan and one for the South) and 30 rows (each row representing the average for one DF file). Using the average values from a single day, it is postulated that changes in the bridge performance indices might indicate changes in structural performance that could be related to damage and/or deterioration.

4.4.2.5 Rainflow Counting

The cycle counting method Rainflow Counting, is used to determine the number and magnitude of strain cycles occurring at each senor location. Rainflow Counting is performed on the traffic files only. Therefore the number of strain cycles the bridge sees due to traffic loading is computed and cyclic temperature cycles are not considered.

To prepare the files for Rainflow Counting, a program, Rainflow Extract, was created to generate a file containing only the strain data; therefore columns such as time, buffer, and the temperature columns are excluded. The output from Rainflow Extract is input into nCode's ICE-flow 2.0, which is commercial software capable of performing the Rainflow Counting procedure. ICE-flow is multifunctional software which allows the user to create many different processes using "Glyphs" which are preprogrammed common routines used in data processing (i.e., basic and advanced math and statistical functions, filtering, graphing, Rainflow Counting, etc.). For this project a process was created that performs Rainflow Counting on a data set created by Rainflow Extract Program. The "Duty Cycle" function in ICE-flow is then used to combine the tabular output (the number of cycles for the each strain range) from each file, creating one table with the total number of cycles for each strain range from all of the files entered into the Duty Cycle. The last final step is converting the Duty Cycle output, which is in an ICE-flow format, into a comma delimited file using another ICE-flow process. Figure 4.24 shows the Rainflow Counting sample results in the form of a histogram for a typical week of data from a midspan bottom flange sensor.

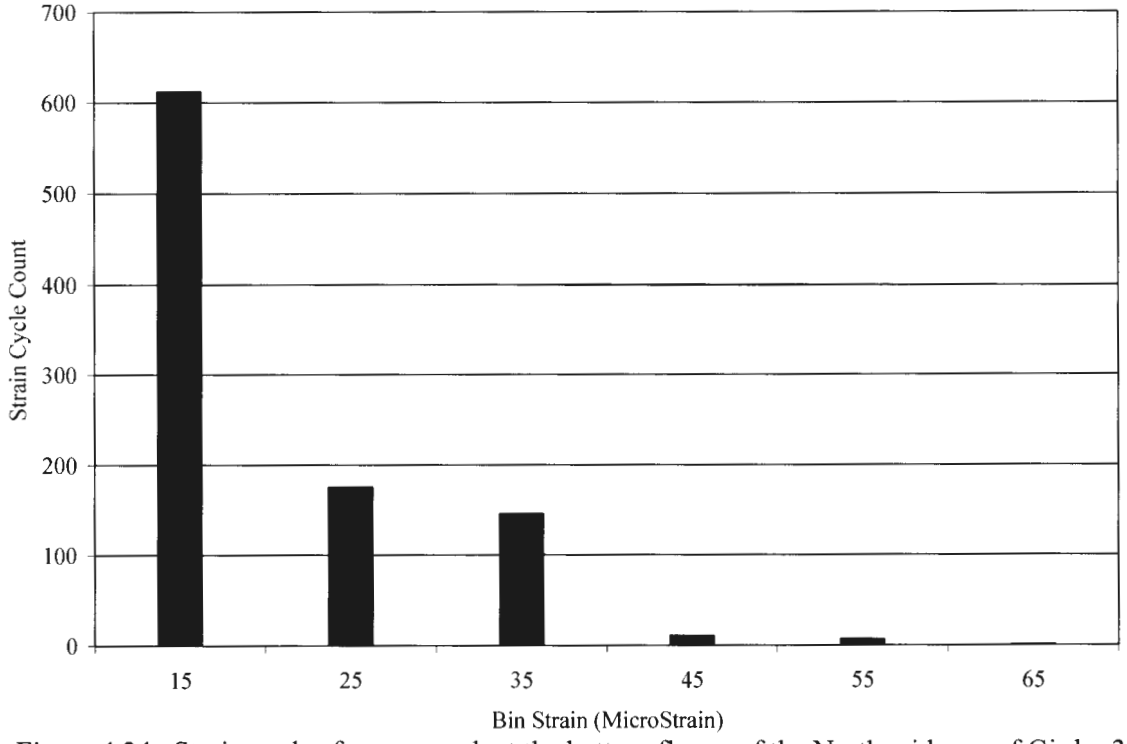

Figure 4.24. Strain cycles for one-week at the bottom flange of the North midspan of Girder 3.

5. PERFORMANCE

The performance of the E. 12th St. Bridge and the SHM for the subject bridge are evaluated through multiple techniques as discussed previously. Presented in this chapter is information from the controlled load test which was used to validate the performance of the FBG sensors. The responses of the bridge to random ambient traffic events are also evaluated. The bridge indices described in Chapter 4 are presented for the controlled load tests and also for ambient traffic for the monitored period of the bridge.

5.1 FBG Sensor Performance

To verify the accuracy of the FBG sensors during the live loading events, a controlled load test was performed. Of the 36 sensors used to measure the strain on the bridge, 23 had a Bridge Diagnostics, Inc. (BDI) strain transducers (BDI transducers used a different acquisition system for data collection) placed adjacent to them.

5.1.1 Controlled Load Test Methods

The controlled load test was performed by collecting strain data while a truck of known weight and configuration was driven across the bridge. The configuration of the load truck used in the load test is shown in Fig. 5.1. The front axle weight of the truck was 15,120 lbs. and the rear axle weight was 31,680 lbs. Table 1 gives a summary of the truck weight. The controlled load test consisted of nine runs, several runs were conducted at each location for repeatability. Runs 1 and 2 were conducted with the center of the west rear wheels 2 ft from the west barrier rail. The truck was centered on the bridge for Runs 3, 4, 7, 8, and 9. Runs 5 and 6 were conducted in a symmetrical fashion to Runs 1 and 2 on the other side of the bridge, with the East rear wheel 2 ft from the east barrier rail. The positions of the truck for the different runs of the load test are shown in Fig. 5.2. Runs 1 through 6 were performed at crawl speeds, Run 7 at 15 mph, Run 8 at 25 mph, and Run 9 was performed at 35 mph. Runs 7 through 9 were conducted to collect data for dynamic observation. All of the runs were conducted with the vehicle traveling from North to South. Photos of the truck before and during the load test are shown in Fig. 5.3.

Table 5.1. Axle weights of load truck for controlled load test (lbs).

Front Axle	Rear Axles	Total
15,120	31,680	46,800

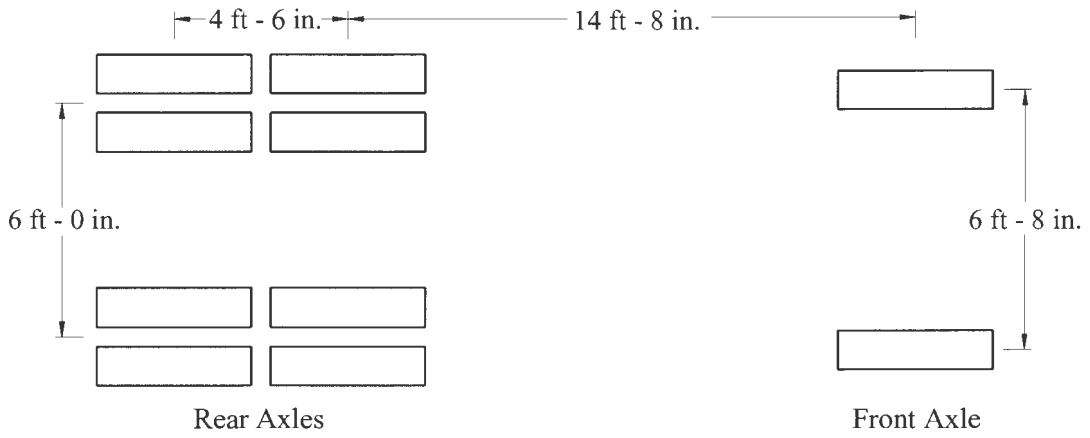

Figure 5.1. Configuration of load truck.

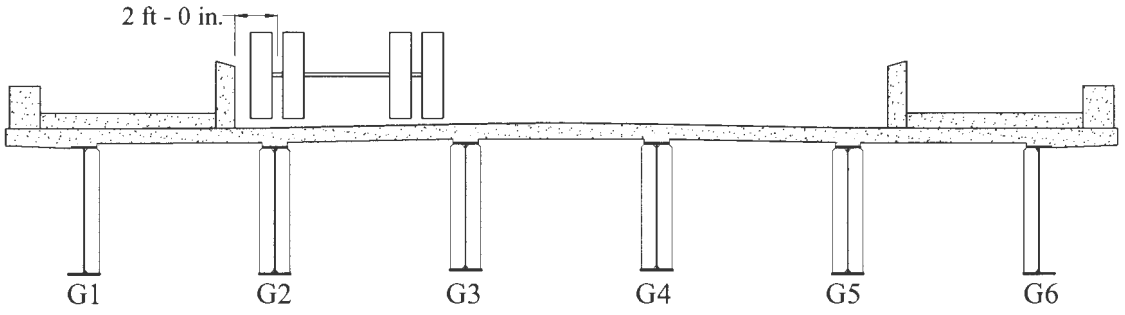

a. Runs 1 and 2

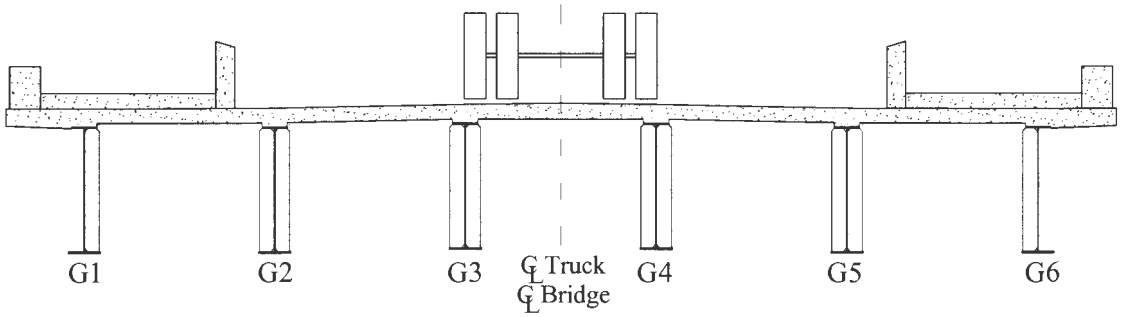

b. Runs 3, 4, 7, 8, and 9

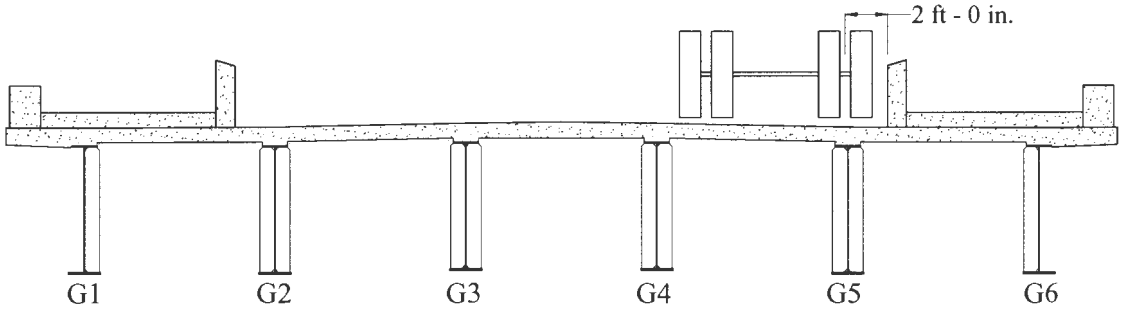

c. Runs 5 and 6

Figure 5.2. Position of load truck for the controlled load test looking North.

a. Load truck prior to controlled load test

b. Load truck during Run 2 of the controlled load test
Figure 5.3. Photos of the load truck used for the controlled load test.

The FBG strain data from the load test were processed in the same manner as the ambient traffic data, by first separating the temperature and live load traffic effects and then calculating the bridge performance indices.

5.1.2 FBG Sensor Verification

Table 5.2 compares the peak strain results from the FBG Sensors and the BDI strain transducers for Run 2 of the controlled load test, from which the comparison results are typical for all of the controlled load tests. Due to location restrictions for BDI gage installation, the comparison was

only performed for top and bottom midspan and abutment sensors. The differences in the strain from the FBG Sensors and BDI transducers are listed as well as the percent difference. The percent difference is considered no difference (ND) if the FBG reading, BDI reading, or difference between the two is less than 5 $\mu\varepsilon$. After reviewing the results of the load test comparison, only one sensor was considered unreliable under live load conditions. The Girder 1 bottom flange sensor (Sensor 19) at the abutment was consistently different than the BDI transducers.

Table 5.2. Comparison of peak strains for FBG sensors and BDI transducers from the controlled load test Run 2 (values in microstrain).

FBG Sensor #	FBG Strain	BDI Strain	Difference	% Difference
14	42	40	2	ND
15	8	8	0	ND
17	36	34	2	ND
18	1	4	-3	ND
19	-13	-28	15	54%
20	-26	-26	0	ND
21	3	2	1	ND
22	-18	-23	5	22%
23	-8	-3	-5	ND
24	48	49	-1	ND
25	20	19	1	ND
26	10	10	0	ND
28	3	3	0	ND
30	3	3	0	ND
31	39	37	2	ND
32	50	53	-3	ND
33	42	44	-2	ND
34	-3	-3	0	ND
35	22	23	-1	ND
36	-2	-1	-1	ND
37	12	13	-1	ND
38	3	3	0	ND
39	3	1	2	ND

ND – No Difference

The FBG sensors and the BDI transducers were also compared by looking at the strain time history from the controlled load test. Typical results from Runs 3 and 6 are presented here. Generally the time histories compare very well. The exception to this is the Girder 1 bottom flange abutment sensor as discussed previously and shown in Fig. 5.4 (the BDI strain does not return to zero likely due to slippage of the epoxy between the BDI transducer and the steel). Figure 5.5 shows the strain plots from a midspan bottom flange sensor with a relatively large strain magnitude in which the sensors follow the same profile with similar magnitudes. A bottom flange location with a lower strain magnitude is shown in Fig. 5.6 with fairly good accuracy between the two sensors. A top flange location with very small strain magnitude, which also includes several localized strain spikes, is shown in Fig. 5.7, and illustrates very good correlation. Notice that even with high levels of oscillations (from "noise") shown in Fig. 5.8, the different sensors behave similarly. Also shown in these figures is the difference in the magnitude of the noise band between the different types of sensors. The information presented in Table 5.2 and Figs. 5.4 to 5.8 confirms that the majority of the FBG sensors are performing accurately under short-term loading conditions.

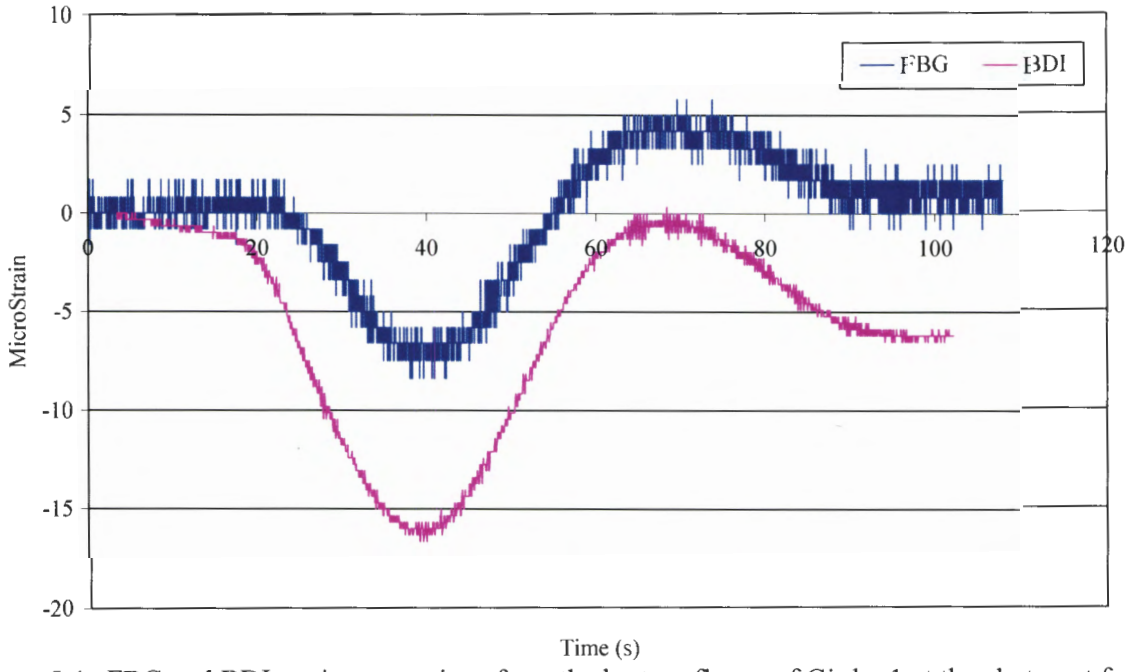

Figure 5.4. FBG and BDI strain comparison from the bottom flange of Girder 1 at the abutment from the controlled load test Run 3.

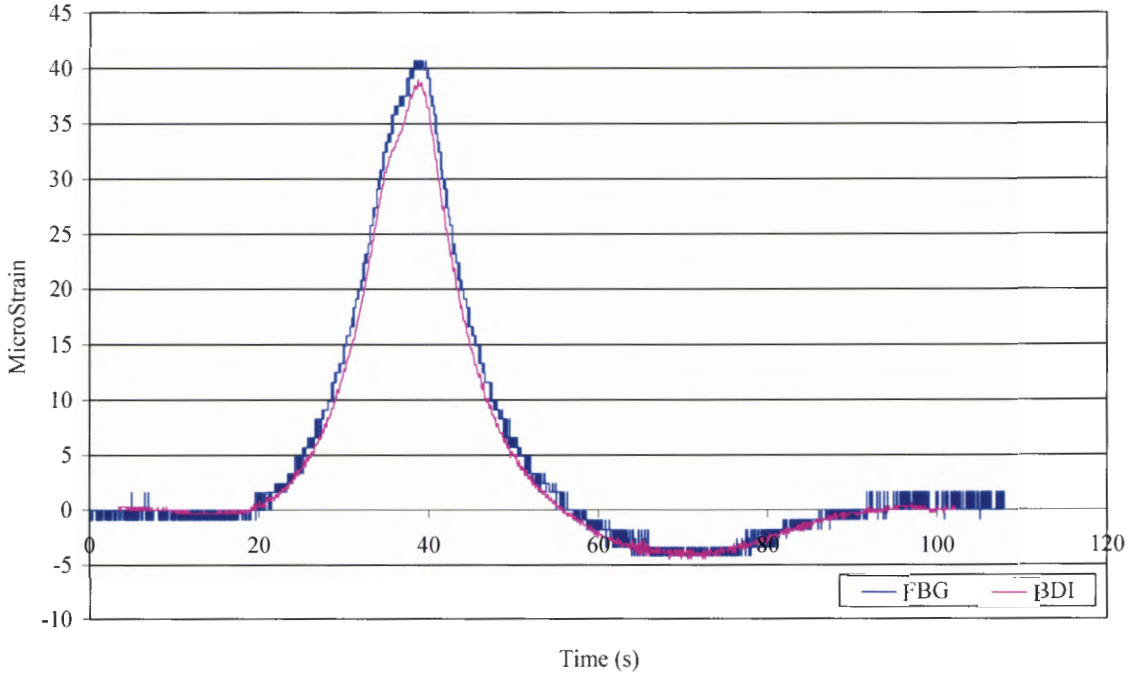

Figure 5.5. FBG and BDI strain comparison from the bottom flange of Girder 4 at the North midspan from the controlled load test Run 3.

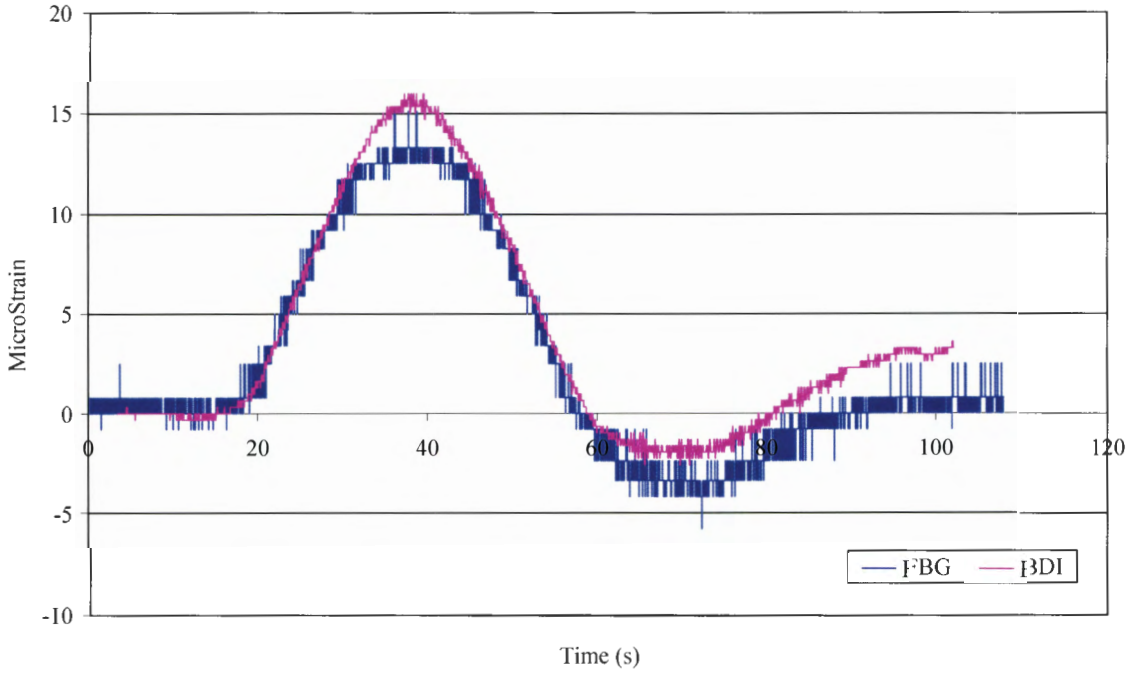

Figure 5.6. FBG and BDI strain comparison from the bottom flange of Girder 6 at the North midspan from the controlled load test Run 3.

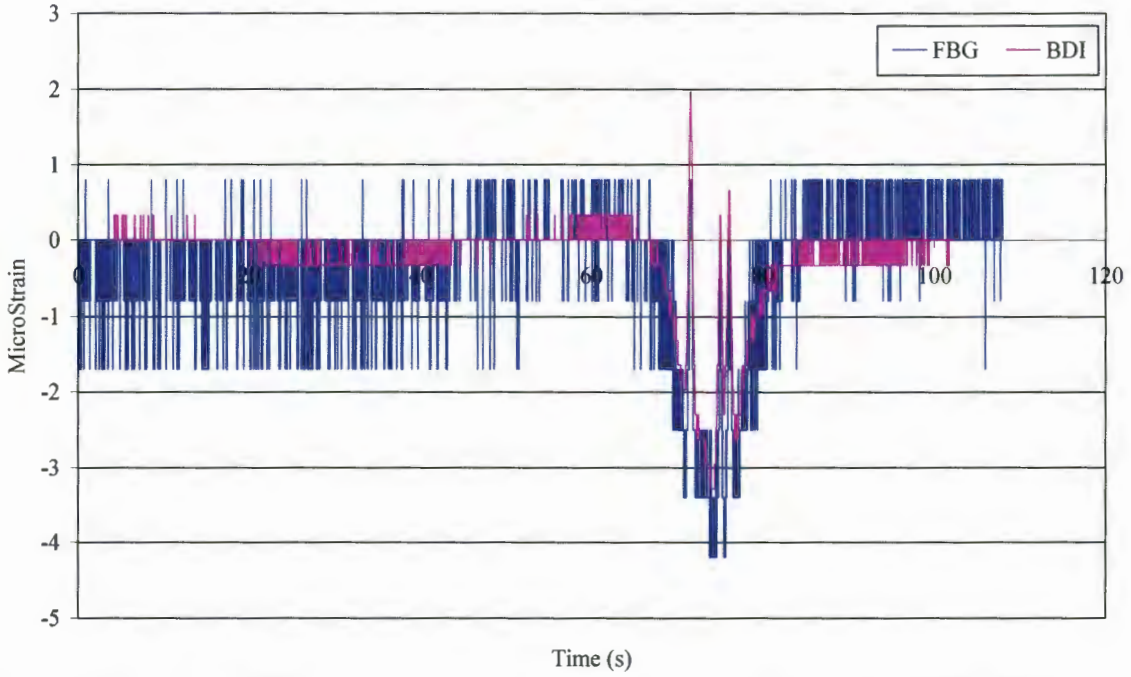

Figure 5.7. FBG and BDI strain comparison from the top flange of Girder 4 at the South midspan from the controlled load test Run 3.

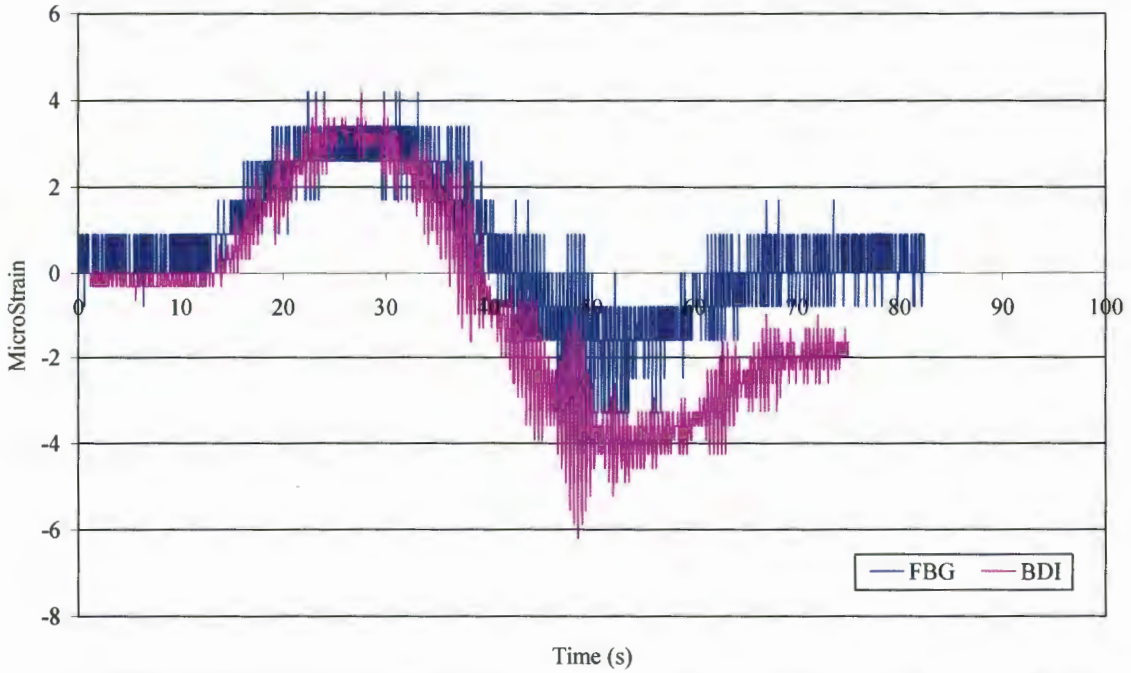

Figure 5.8. FBG and BDI strain comparison from the bottom flange of Girder 1 at the North midspan from the controlled load test Run 6.

5.1.3 FBG Sensor Performance Issues

Although the sensors were shown to perform well under short-term loading, several problems have appeared which could be related to the performance of the sensors. These issues include:

- Optical Loss
- Interference between Sensors
- Large Strain Range of Sensors
- Large Compressive Drops
- Backscatter

5.1.3.1 Optical Loss

When the instrumentation scheme for the bridge was designed, Channel 1 had 14 sensors. After all 14 sensors were installed, the system was powered on and initially only 13 sensors responded. The fusion splice between Sensor 13 and 14 was completed again to ensure that the splice provided a quality connection between the two cables. With still only 13 sensors appearing, Sensor 14 was replaced, but Sensor 14 still could not be found by the interrogator. Sensor 14 was then considered non-existent, but was left intact with the rest of the Channel 1 sensors.

On several occasions when the temperature rose to approximately 50°F above the installation temperature (80 to 90°F), data from Sensor 13 were also not obtained. This phenomenon leads the research team to believe optical loss in the system is the cause of the initial and subsequent problems with Sensors 13 and 14. The hypothesis is that when the temperature rises and the bridge experiences thermal expansion, the fiber is tightened. In some places where the fiber needed to be "curved", the fiber is then pulled too tight creating too small of a radius. This prevents the higher wavelengths of light from reaching the end of the FO cable on Channel 1.

5.1.3.2 Interference between Sensors

The data collected from the bridge have been problematic at various times (starting less than a month after the system was functional) with two adjacent sensors interfering with each other. The problem occurs when the wavelengths from at least two sensors are so close together that the Si425-500 can not distinguish between the sensors. This seems to occur when the difference approaches approximately 0.5 nm, and at that point only one wavelength reading is returned. A 3.0 nm center wavelength spacing was used for adjacent sensors for Channels 1 and 2. The problem is indicated when a data set has a column of data missing and large differences in subsequent sequential readings from a sensor (approximately a magnitude of 3000 $\mu\varepsilon$).

Another issue related to this problem is the wavelengths of two adjacent sensors crossing. In this case, two sensors' wavelengths converge, cross, and then diverge. Unfortunately in this case, the data from the two sensors become unusable if a distinguishable characteristic between the two sets of data cannot be found.

5.1.3.3 Large Strain Range of Sensors

Some of the sensors (from Channel 1 and Channel 2) on the bridge had larger strain ranges (difference between daily maximum and minimum strains) than did other sensors. The ranges for these sensors have also increased since the system was installed. Possible reasons for this include:

- Change in the global physical properties of the bridge
- Change in the local physical properties of the bridge in the area of the sensor
- Locations of sensors are more susceptible to temperature change
- Localized effect on the sensor (Sensor not fully adhered to bridge)
- Sensor malfunction

At this time the source of the problem has not been fully determined by the research team. The most likely cause is thought to be a localized effect on the sensor, such as epoxy loosening its bond with the bridge. Causes of this phenomenon could be the result of unsatisfactory installation, faulty adhesive, or insufficient sealing of sensors which could allow moisture into the sensor area.

5.1.3.4 Large Compressive Change

A large compressive change in strain was noticed at differing points in time from several of the various sensors on Channel 1 and Channel 2. One of the decreases was of a magnitude of 400 $\mu\varepsilon$. These sharp decreases could be due to:

- Change in the global physical properties of the bridge
- Change in the local physical properties of the bridge in the area of the sensor
- Localized effects on the sensor (e.g. epoxy bond failure)
- Sensor malfunction

The cause of the decrease is yet to be isolated, but a localized effect on the sensor is currently thought to be the cause. The effect could be due to the loosening of the epoxy bond with the bridge, and thus, causing a residual force from the epoxy to be transferred from the attached surface to the sensor.

5.1.3.5 Backscatter

At various times through the monitoring period extra data have been recorded. This situation would indicate that the interrogator is detecting sensors which do not exist. The problem has generally occurred on Channel 1. The research team believes this problem is due to backscatter. Backscattering generally occurs from an inadequate termination of the fiber optic cable at the end of the channel. Recall that 14 sensors were installed on Channel 1 but only 13 sensors were recognized by the interrogator. These two issues may be related, however, a visual verification of the problem and repair have not been performed due to access limitations.

5.1.3.6 Summary

Although problems have occurred, which could be the result of installation defects or performance of the bare FBG sensors, a system has been created, through programs developed by the research team, to verify the accuracy of the data and output only valid data for each sensor. It is important to note the short-term accuracy of the majority of the sensors is still acceptable (this was verified by the controlled load test). Due to the sensor problems discussed above, the long-term accuracy of some of the sensors maybe unreliable.

The Surface-Mountable Sensors (i.e. the FBG sensors bonded by FRP) have performed excellently and the research team has very high confidence in their performance (both short-term and long-term). The FRP sensors are highly recommended by the research team due to their ease of installation, robustness, and accuracy.

5.2 Bridge Performance

The performance of the bridge under live load events is evaluated in this section in several different ways. The first is by examination of the strain data from random ambient traffic on the bridge as well as the controlled load test strain data. The second is by presentation of the bridge indices discussed earlier (Distribution Factor, Neutral Axis, and End Restraint), which are calculated by the Data Processing Program. The indices are shown for both a short-term event (i.e. the controlled load test) and also for long-term data from ambient traffic data from the monitored life of the bridge. Strain cycle counting results for ambient traffic are also presented.

5.2.1 Bridge Response to Ambient Traffic Events

The data collected and processed from ambient traffic events on the bridge occured over a four month period (and is continuing). The real-time data and video from the bridge were helpful for the research team to become familiar with the general response of the bridge and the general vehicle

population. Because the video was not recorded, the size and position of the vehicle were unknown in most instances, therefore the information collected from the events had to be analyzed and studied to find information that was useful to the research team about the bridge's general performance under ambient traffic.

5.2.1.1 Strain Plots from Ambient Traffic Event

Presented in Figs. 5.9 and 5.10 are strain plots from a typical ambient traffic event. These plots are shown to illustrate the format of the data that are obtained for each vehicle crossing of the bridge. The strain plots in Fig. 5.9 are shown for all sensors on the six girders for measuring the global bridge behavior (i.e. flexure). Figure 5.10 shows sensor strain data from girders near the pier region that measure localized effects (i.e. connection details). In many of the strain plots there are "apparent" gaps of data with strains of 0.0 $\mu\varepsilon$ (see Figure 5.9e). This occurs from the data processing in which the temperature strain and live load strain are separated; in this process the data points which are between ±1.6 $\mu\varepsilon$ (i.e. the noise band) are set to 0.0 $\mu\varepsilon$ to eliminate that noise band and other insignificant strain data. The color coding represents the different sensor locations on the bridge.

More detailed discussion of these and other data is presented in the following subsections to describe the bridge's live load performance. Two arbitrarily selected ambient traffic events are referred to in this section: for reference, they will be known as Ambient Traffic Event 1 and Ambient Traffic Event 2. Ambient Traffic Event 1 data are shown in Figs. 5.9 and 5.10.

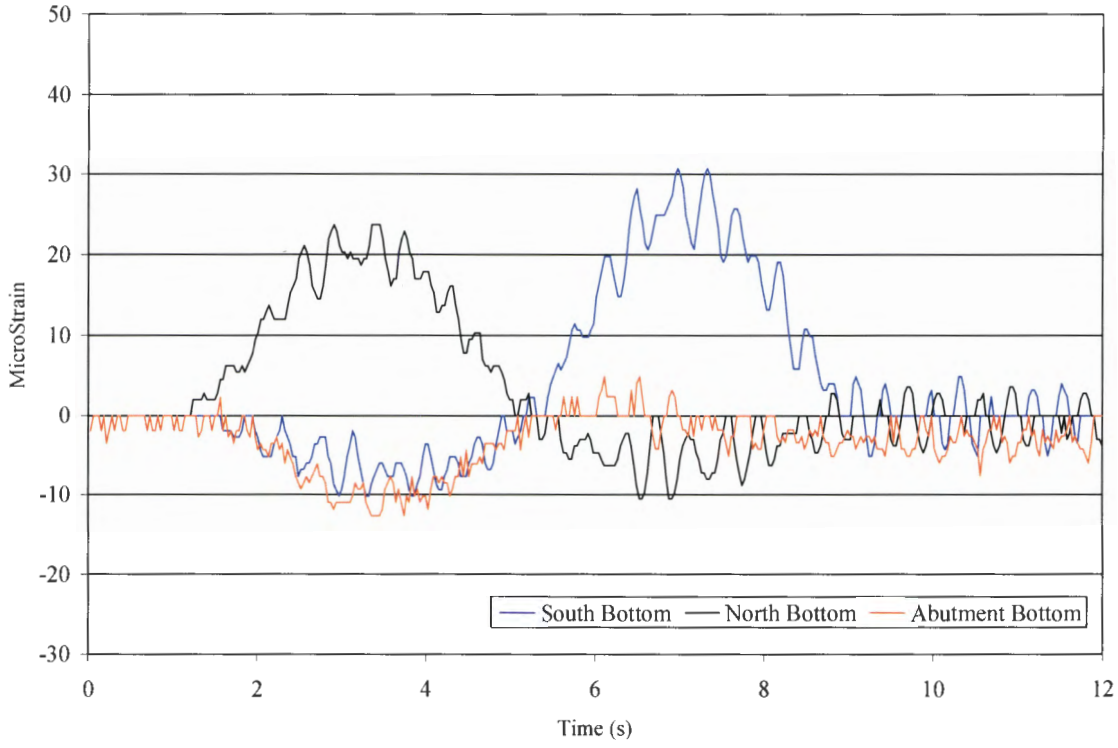

a. Girder 1.

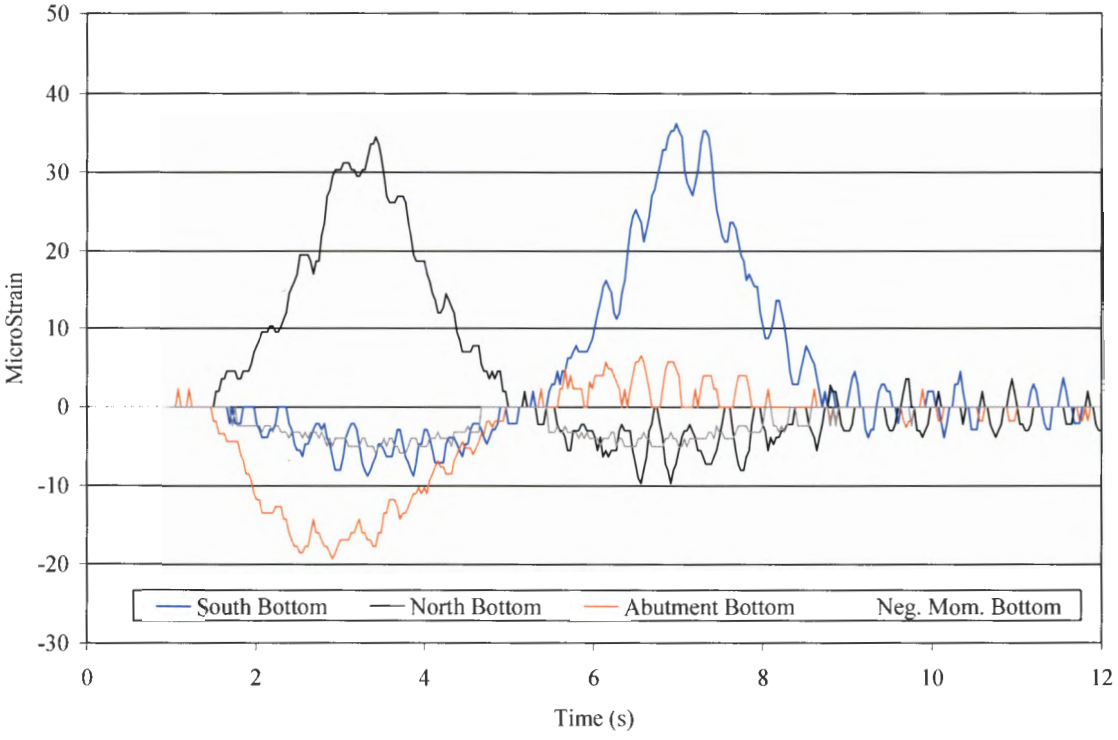

b. Girder 2.

Figure 5.9. Strain plot from an ambient traffic event.

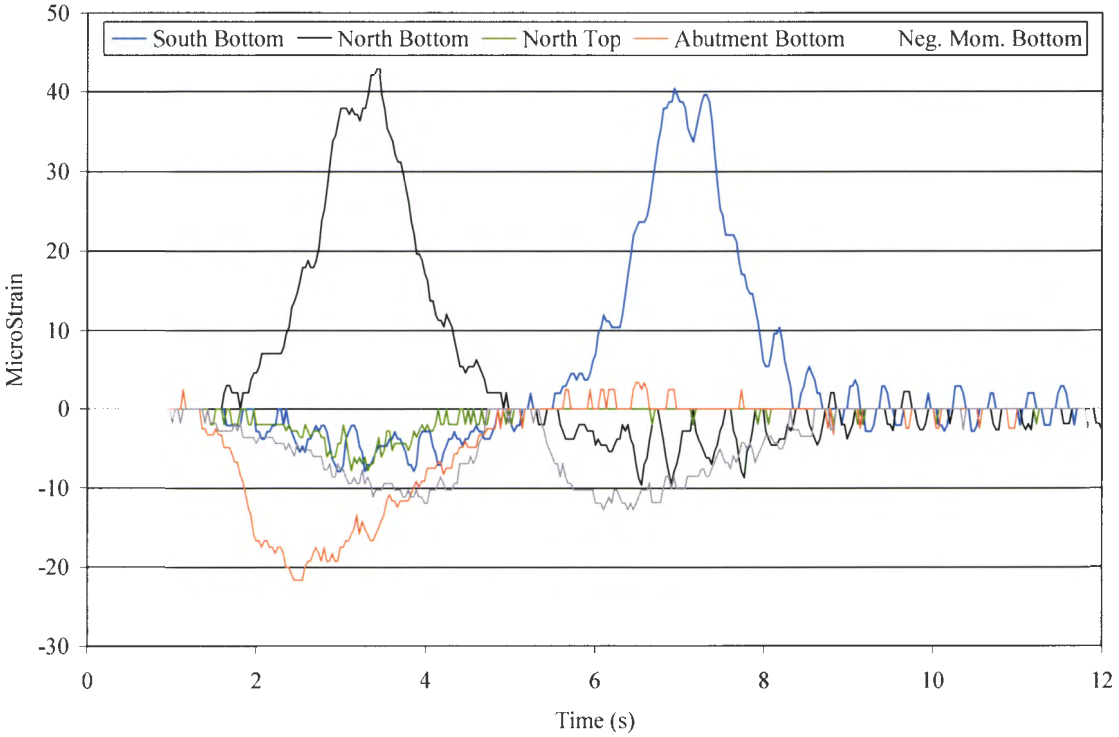

c. Girder 3.

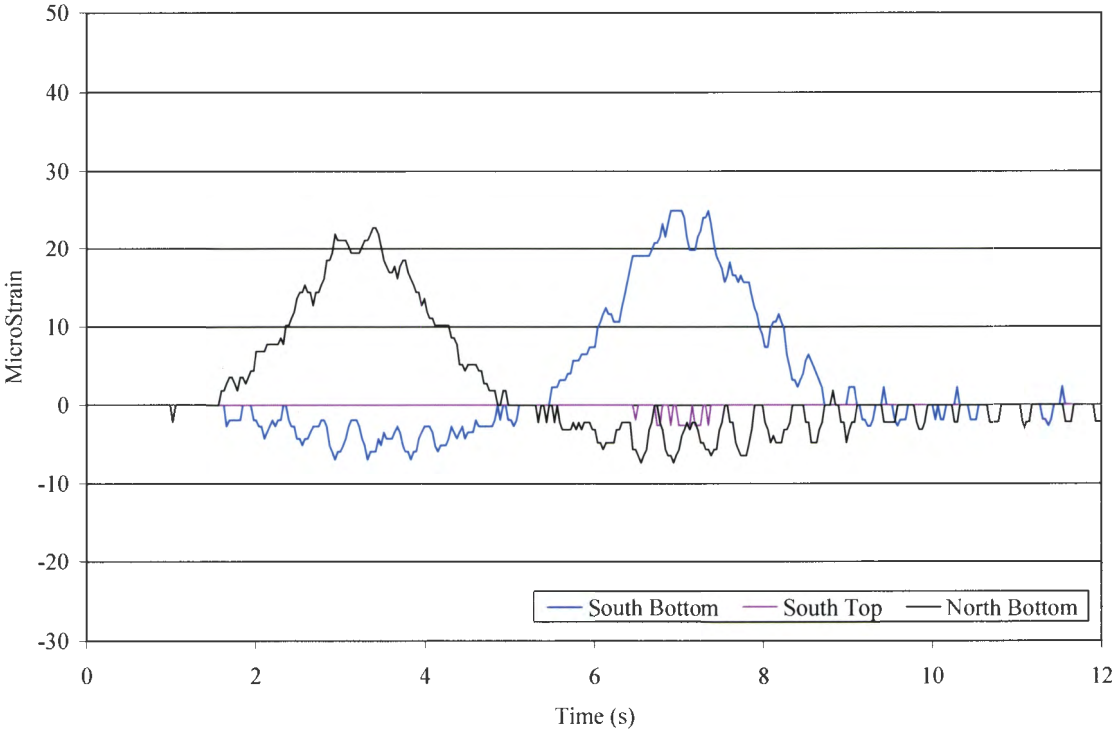

d. Girder 4.

Figure 5.9. Strain plot from an ambient traffic event (Continued).

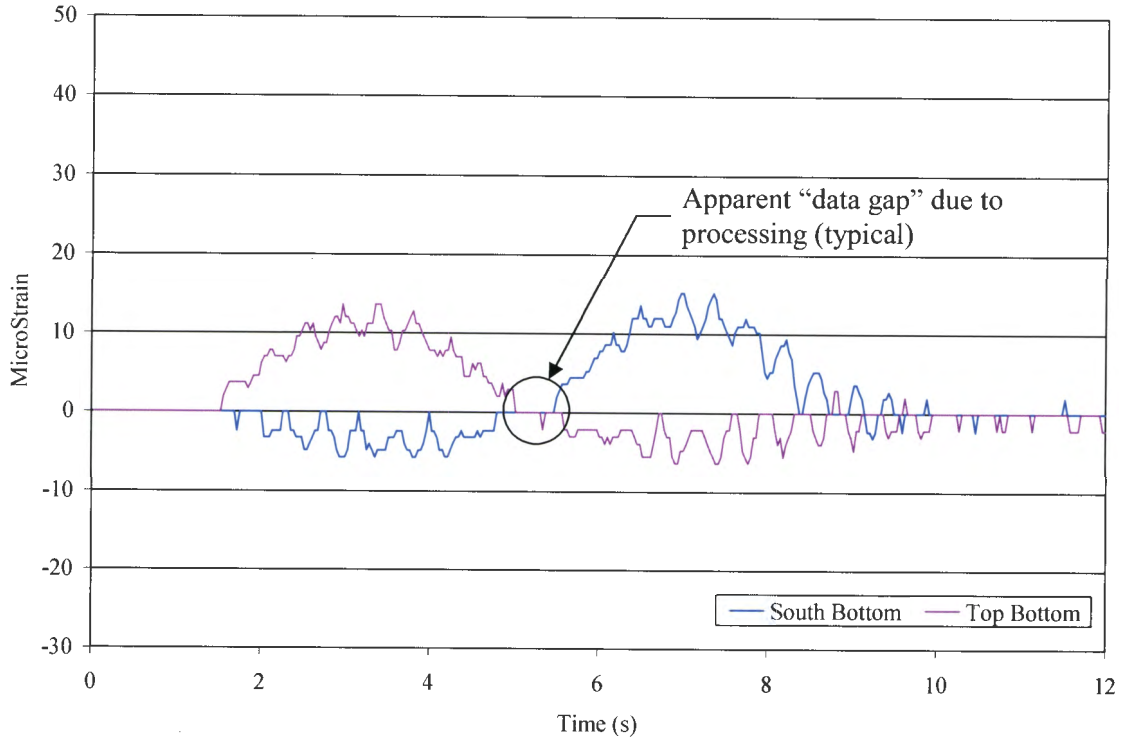

e. Girder 5.

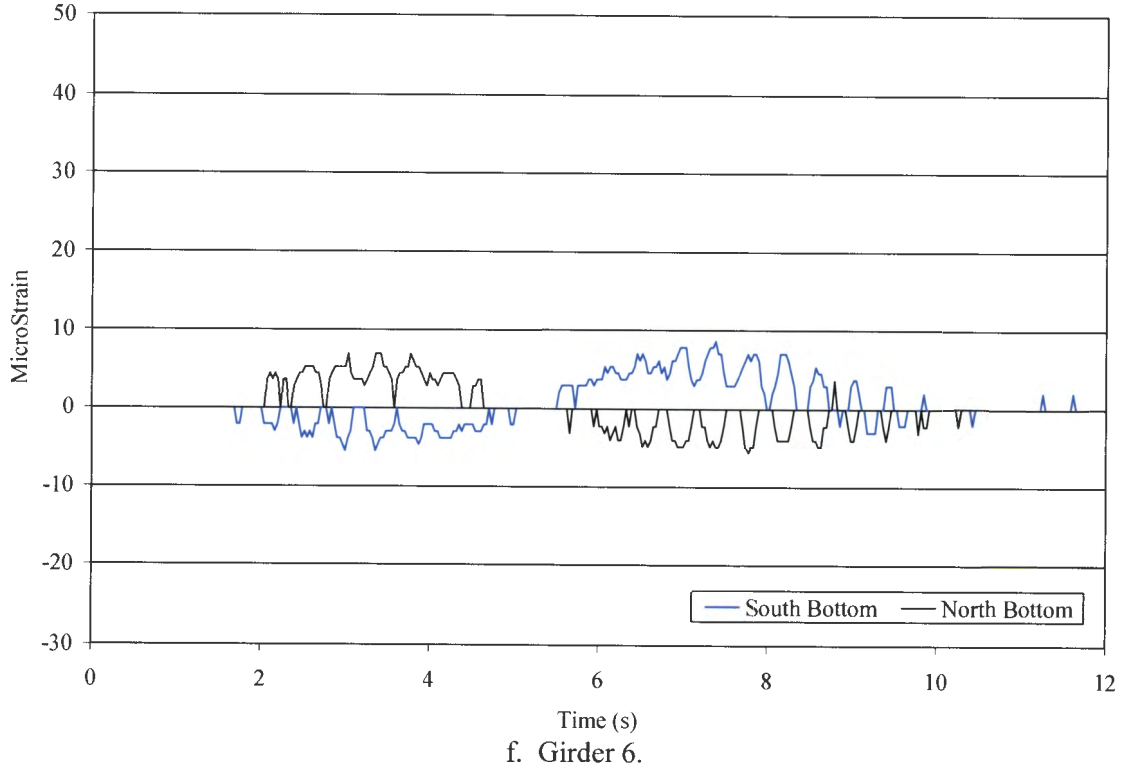

f. Girder 6.

Figure 5.9. Strain plot from an ambient traffic event (Continued).

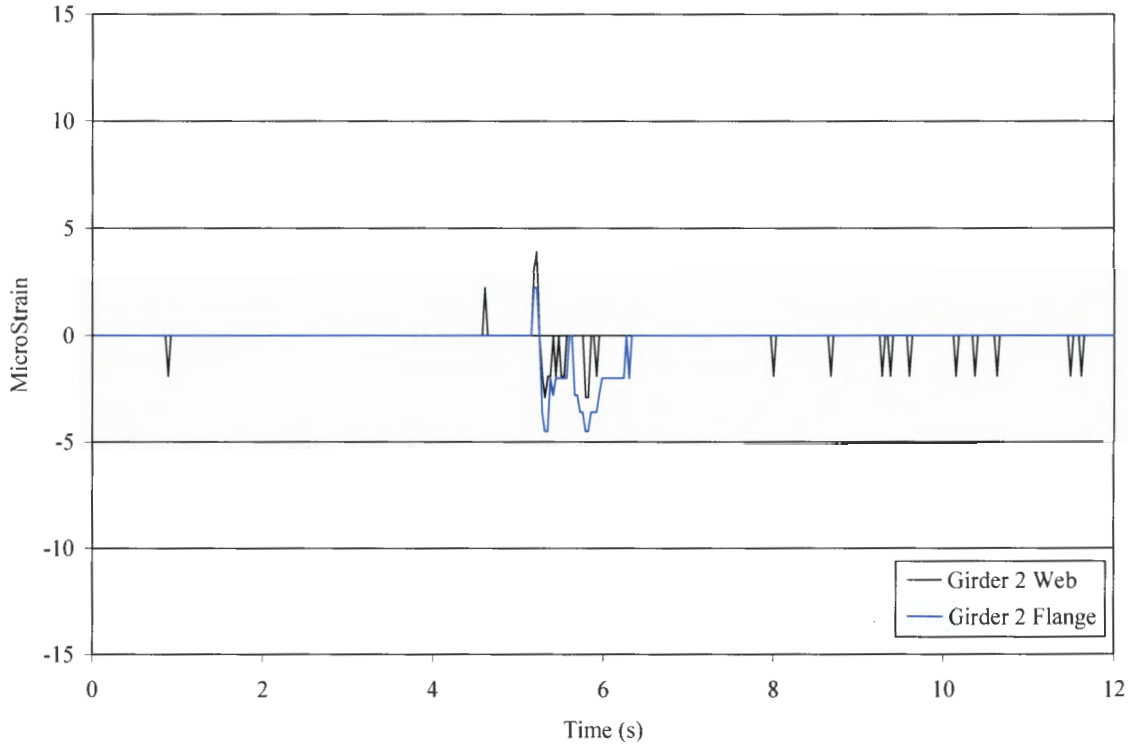

a. Welded plate splice in web and flange.

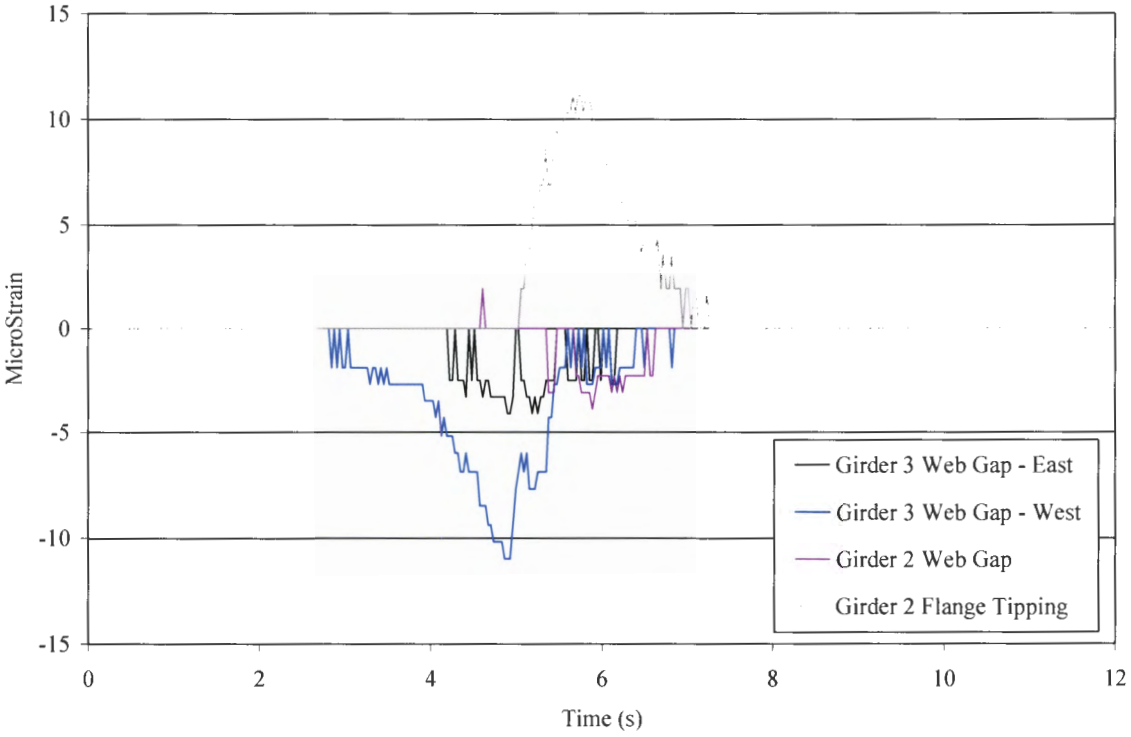

b. Web gap region.

Figure 5.10. Localized fatigue detail strain data from an ambient traffic event.

5.2.1.2 Qualitative Bridge Performance Characteristics

Basic qualitative observations of the bridge performance due to live loading are summarized below to verify that the bridge generally responds as expected. The observations are based on fundemental structural principles for a two span continuous bridge with restrained ends and a vertical support at the pier.

- Bottom Flange – Midspan:
  Positive strain when the loading is on the same span as the sensor and negative strain when the loading is on the opposite span of the sensor.
- Bottom Flange – Abutment:
  Negative strain when the loading is on the same span as the sensor and positive strain when the loading is in the opposite span of the sensor. Lower strains when compared to the bottom flange strains at the midspans.
- Bottom Flange – Negative moment region near the pier:
  Negative strains are recorded throughout the loading period. The strain goes to 0.0 $\mu\varepsilon$ when the loading nears the pier.
- Top Flange – Midspan:
  Negative strain when the loading is on the same span as the sensor, positive when the loading is in the opposite span of the sensor. Lower strains occur compared to the bottom flange strains at the midspans. This would be expected since the neutral axis of the effective girder depth due to the composite concrete deck is near the top flange.
- Localized Fatigue Details:
  Low levels of strain are recorded. The largest strain recorded at any of the details is equivalent to a stress of less than 1.3 ksi.

5.2.1.3 Vehicle Direction

The events recorded by the E. 12th St. Bridge SHM system can be characterized as Northbound or Southbound vehicle events through two methods. The first is by observation of the strain value (compression or tension) from the bottom flange midspan sensors. Southbound events are represented by initial positive bottom flange strains at the North midspan. The opposite is true for Northbound events, with initial positive bottom flange strain at the South midspan. The second is by comparing the magnitude of the strain at the bottom flange midspan sensors. If Girder 2 and 3 strains are larger than Girder 4 and 5 strains, the vehicle can generally be assumed to be traveling Southbound and vice-versa for a Northbound event.

Figure 5.11 shows Girder 3 bottom flange strain from Ambient Traffic Event 1. Based on the general observations given above, the vehicle direction associated with this event is Southbound. Figure 5.12 shows the same ambient traffic event; in this case the strain from the bottom flange

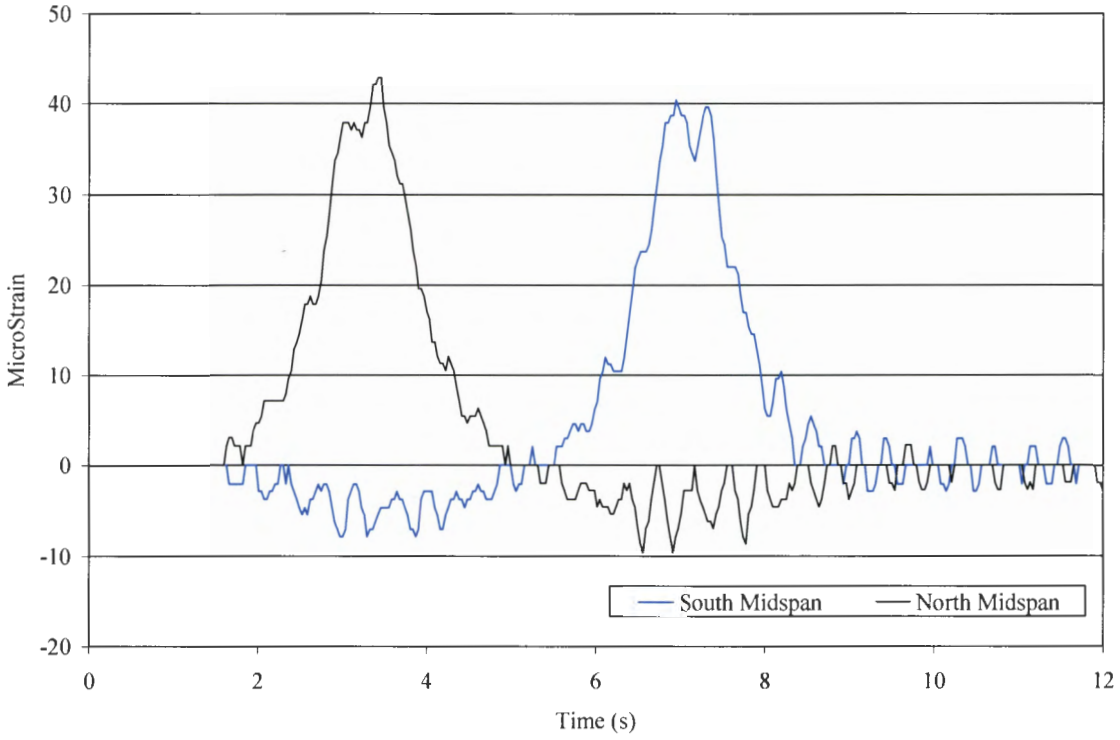

Figure 5.11. Strain plots of Girder 3 bottom flange sensors (North and South midspan) from Southbound Ambient Traffic Event 1.

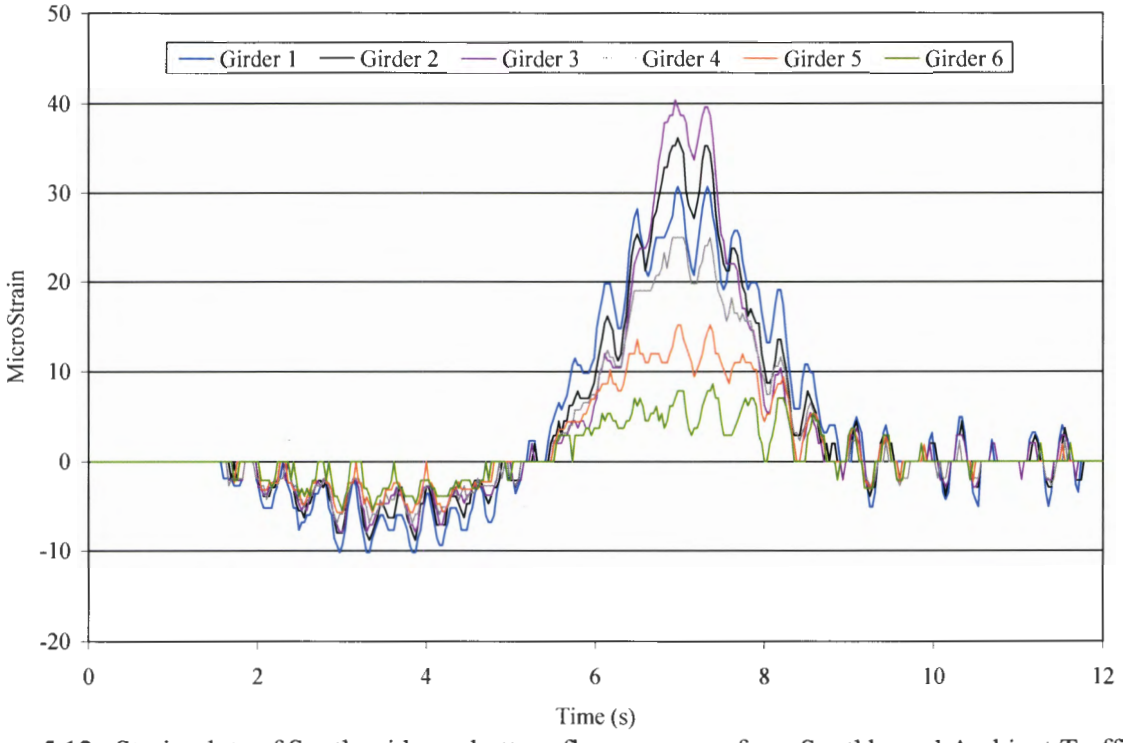

Figure 5.12. Strain plots of South midspan bottom flange sensors from Southbound Ambient Traffic Event 1.

sensor for each girder at the South midspan is presented. Girder 3 has the highest strain magnitude followed by Girders 2, 1, 4, 5, and 6, respectively. This also supports the observation that Ambient Traffic Event 1 is a Southbound event. Figure 5.13 shows the strain for each North midspan bottom flange girder for the same ambient event. Since Girder 4 has the highest strain followed by Girders 5, 3, 6, 2, and 1, the ambient event in Fig. 5.13 is a Northbound event. This is also evident by the initial negative strain from the North midspan bottom flange sensors.

Although the direction and a general transverse position (West or East lanes of the bridge) can be identified for ambient traffic using the strain magnitudes from the bottom flange sensors, this method can't be accurately used to determine a more precise transverse position of a vehicle on the bridge due to the unknown properties of the vehicles (i.e. relative weight of each wheel line, the dynamic properties of the vehicle, and the vehicle geometry).

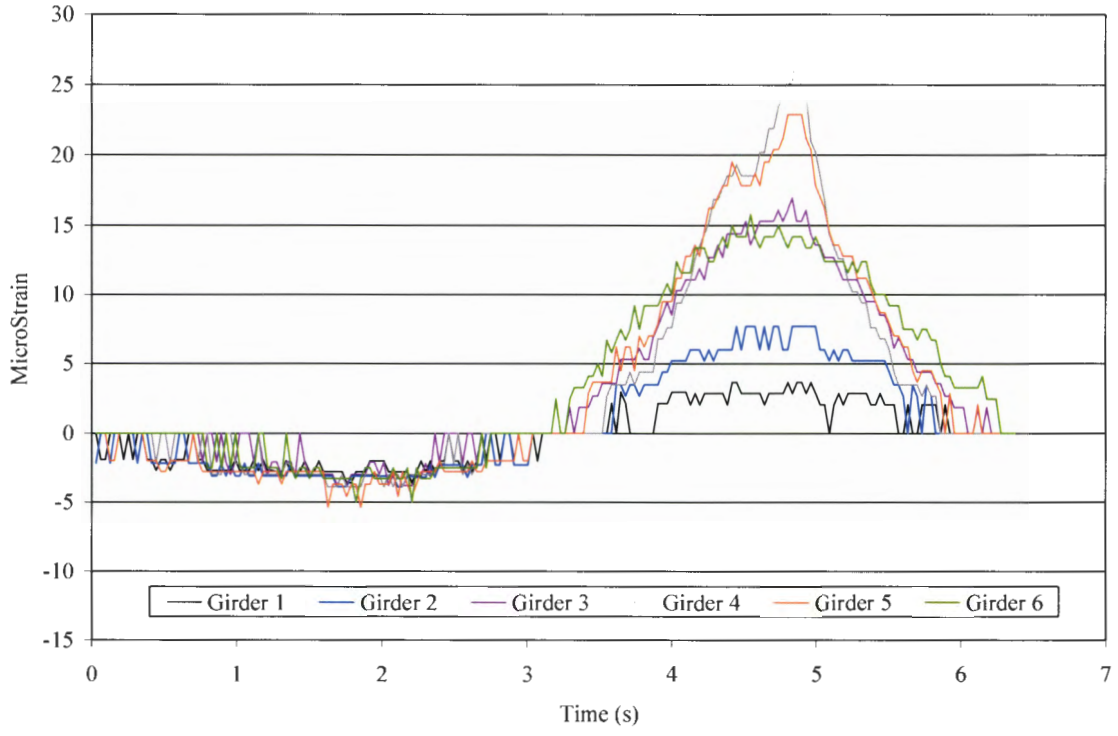

Figure 5.13. Strain plots of North midspan bottom flange sensors from Northbound Ambient Traffic Event 2.

5.2.1.4 Dynamic Response

The oscillations seen in Fig. 5.14 represent the dynamic response of the bridge. Dynamic patterns are noticeable in the ambient traffic data but the sample rate (i.e. 31.25 Hz) is not sufficient

to fully characterize the dynamic response. Further, evaluation of the dynamic behavior of the structure was beyond the scope of this study.

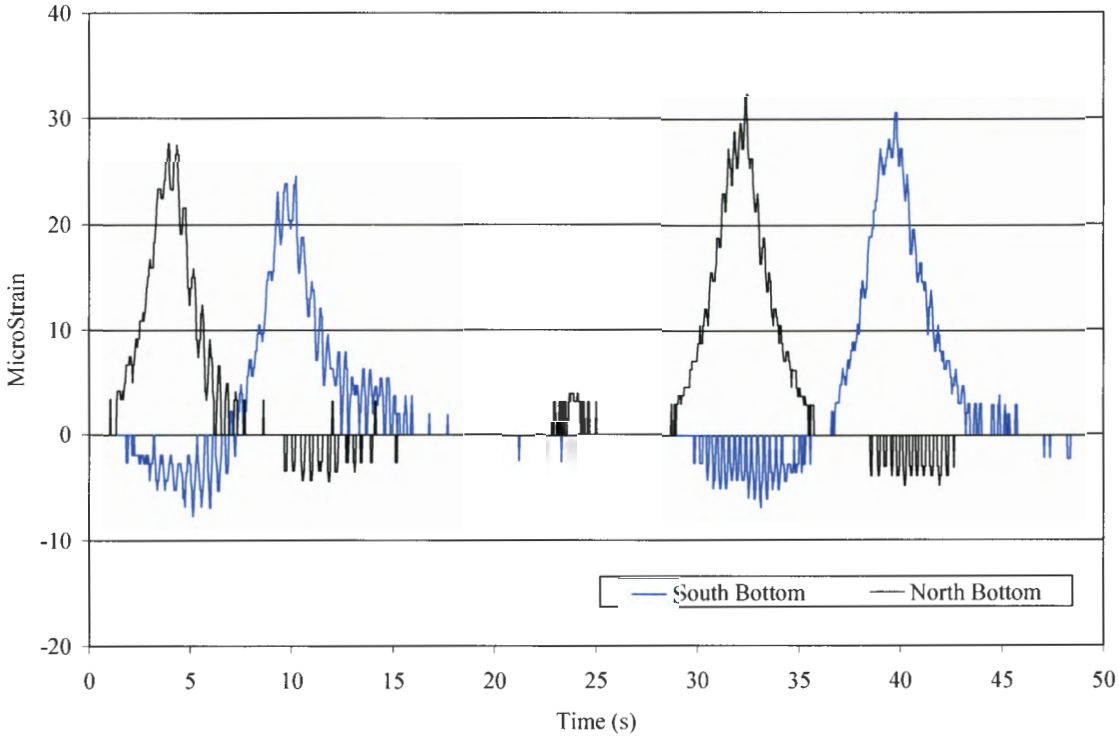

Figure 5.14. Strain plot of Girder 2 bottom flange sensors from Northbound Ambient Traffic Event 3.

5.2.2 Bridge Response due to Controlled Load Tests

The strain data from the controlled load tests provide additional information that can not be obtained from the ambient traffic data since the position of the truck and the truck geometry and weight are known. As discussed previously, the load tests were performed by driving the load truck from North to South.

5.2.2.1 Strain Plots from Controlled Load Test

Strain plots from the controlled load test Run 2 are presented in Fig. 5.15 (global performance sensors) and Fig. 5.16 (fatigue detail sensors). During Run 2 the test truck drove near the West barrier rail (see Fig. 5.2 for test truck position), therefore creating a loading condition similar to the ambient traffic condition resulting in the response shown in Figs. 5.9 and 5.10.

The bridge's live load performance is presented in the following subsection using data from Runs 2, 4, and 6. Not all of the data from the load tests are presented, but the data shown are representative of all of the data collected.

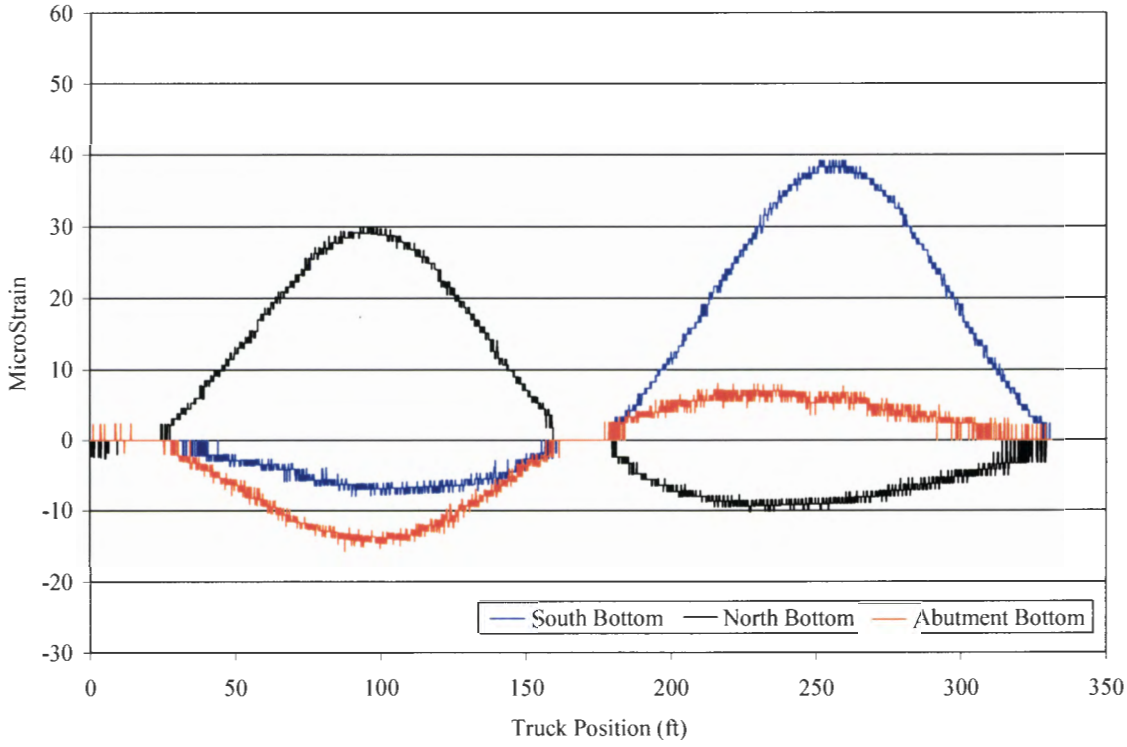

a. Girder 1.

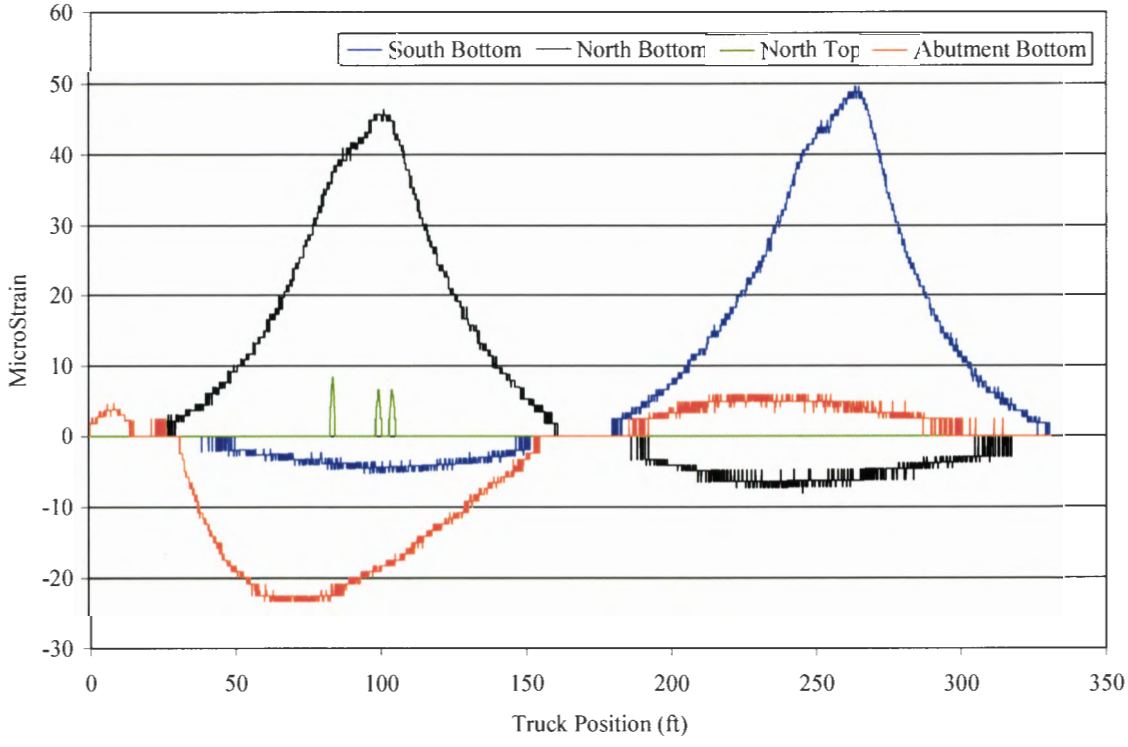

b. Girder 2.

Figure 5.15. Strain plot from controlled load test Run 2.

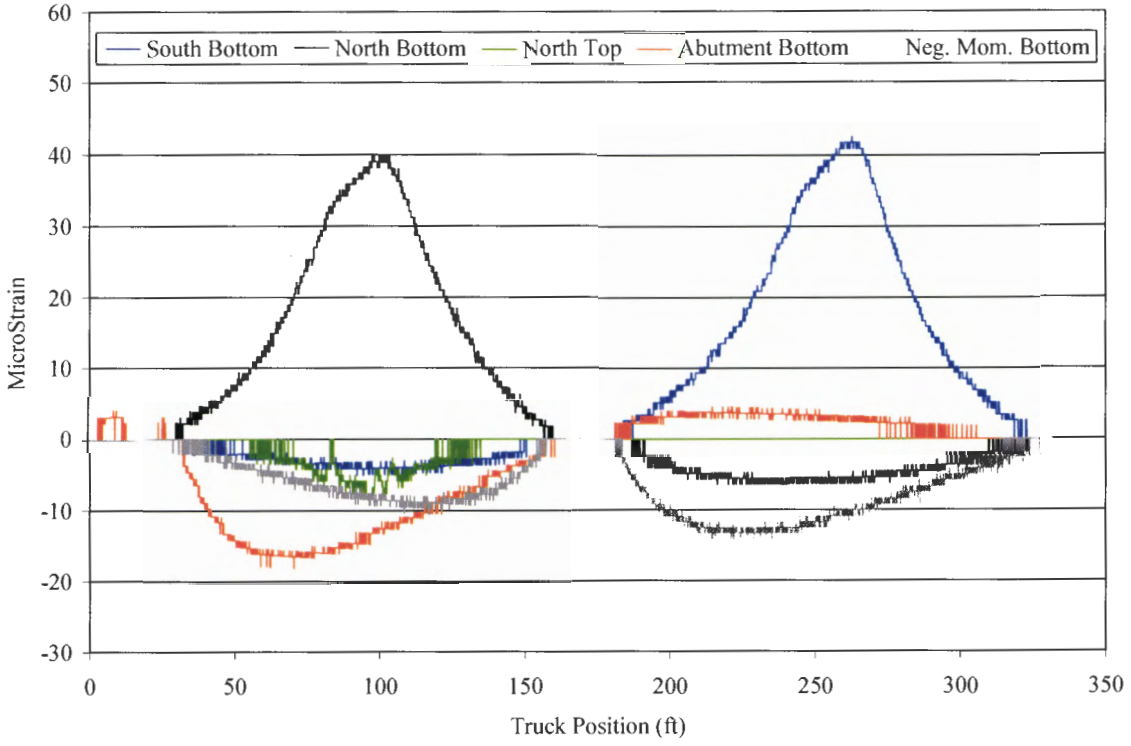

c. Girder 3.

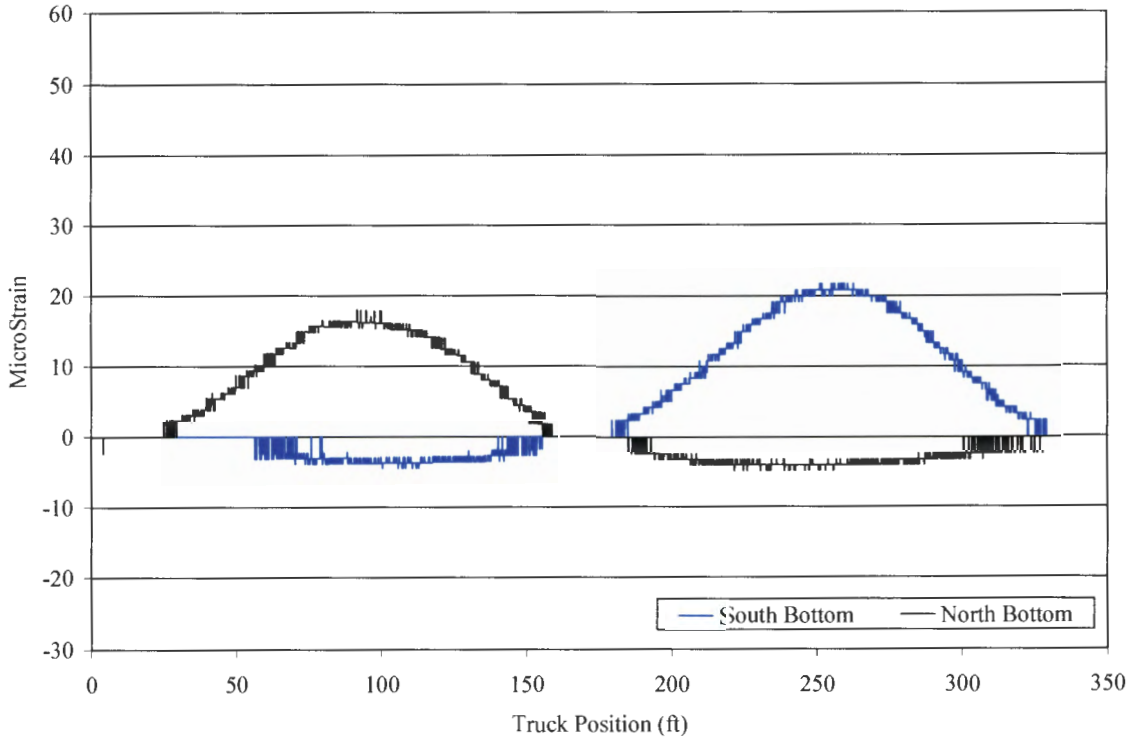

d. Girder 4.

Figure 5.15. Strain plot from controlled load test Run 2 (Continued).

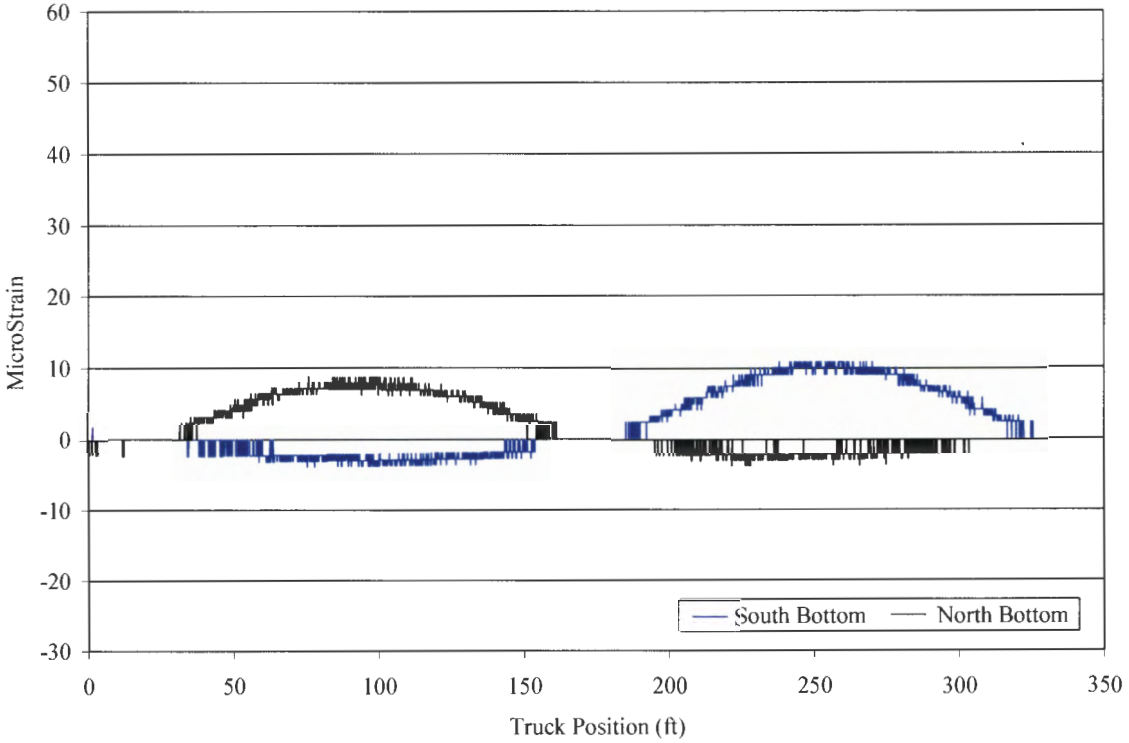

e. Girder 5.

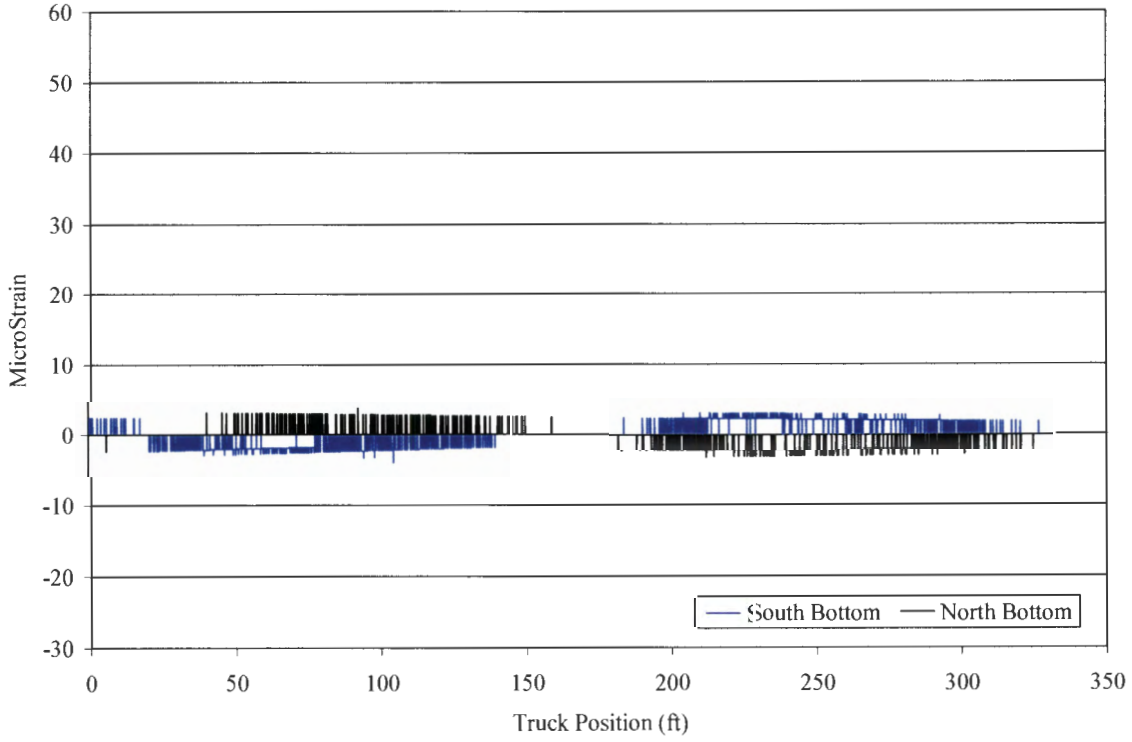

f. Girder 6.

Figure 5.15. Strain plot from controlled load test Run 2 (Continued).

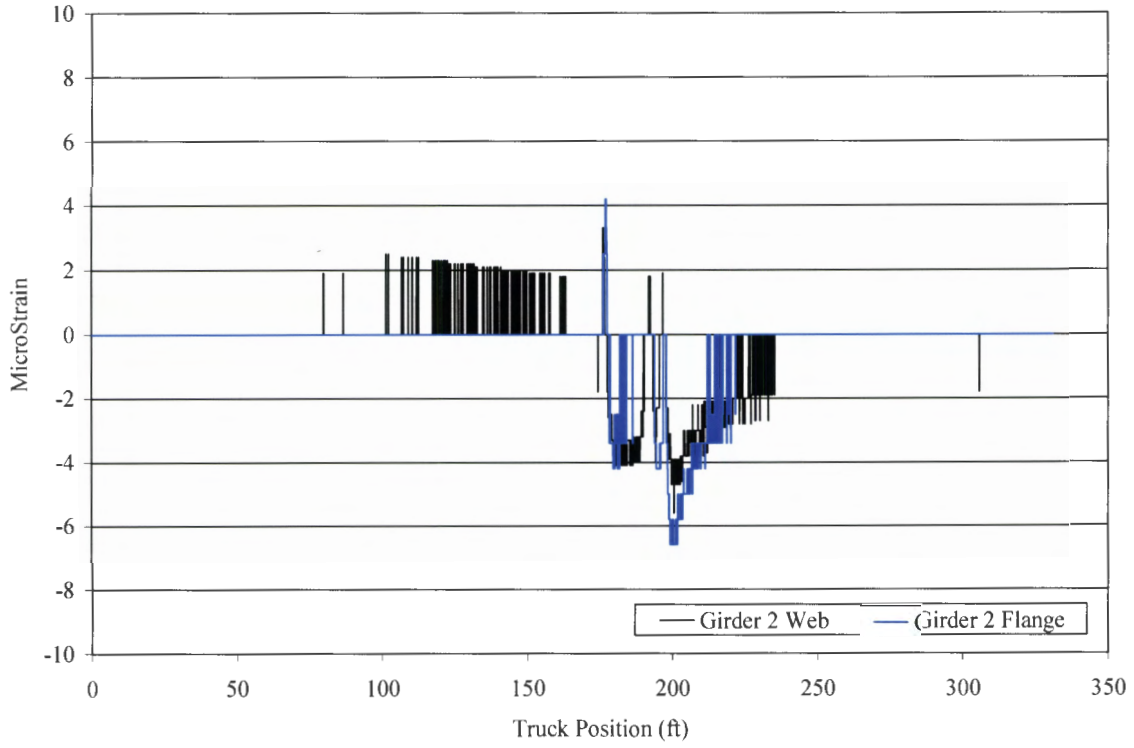

a. Welded plate splice in web and flange.

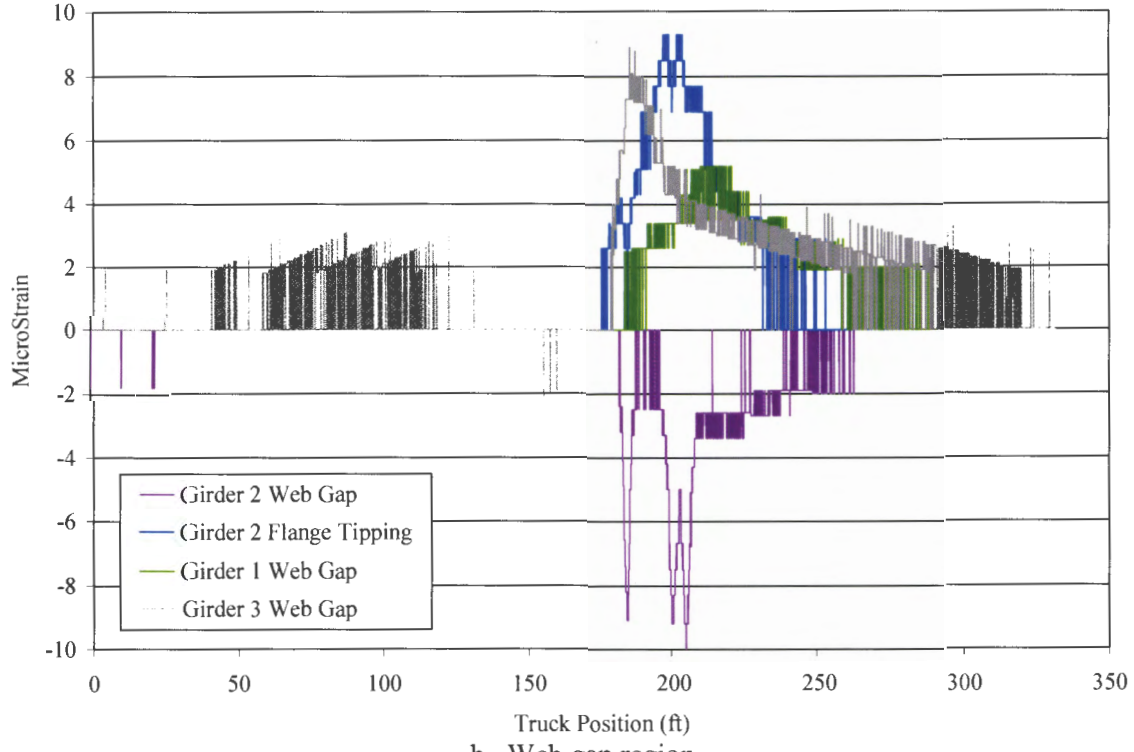

b. Web gap region.

Figure 5.16. Strain plots of localized fatigue details from controlled load test Run 2.

5.2.2.2 Comparison between North Midspan and South Midspan Strain

When the strain from the North and South midspan bottom flange sensors from each girder are compared in Fig. 5.15, especially for Girder 1, it is noted that the South midspan strains are larger than the North midspan strains. Primary reasons for this may include the difference in the live load positive moments generated in each span due to the load truck geometry with respect to the fixed ends and roller support as the truck crosses the bridge in one direction and the differing inertia values between the North and South spans. Other possible issues that could contribute to this situation are:

- Slightly different span lengths (North – 145.37 ft and South – 153.24 ft)
- Differing as-built conditions of the concrete barrier and deck across the bridge transversely and longitudinally, therefore creating different stiffness between each girder and the North and South spans.
- Boundary conditions at each end of each girder causing different stiffnesses in the girders

5.2.2.3 Localized Fatigue Detail Response

Figure 5.16 shows the response from the localized details during Run 2 of the controlled load test. The strain magnitudes measured at the instrumented fatigue sensitive details are relatively low. In Fig. 5.17 welded plate splice strain data from Ambient Traffic Event 1 and Run 2 are compared. The strain profile is the same for both, a positive spike is followed by multiple negative spikes. This demonstrates the behavior of the weld as the vehicle approaches the area is a positive spike, followed by negative spikes as the vehicle crosses over the area. Similarly, in Fig. 5.18 the web gap region strain data from Ambient Traffic Event 1 and Run 2 are compared. The profiles are similar with positive flange tipping strains and negative web gap strains. The positive flange tipping strains may be caused by the weld between the flange and the vertical stiffener being placed under tensile strains as the cross-frames act to pull stiffener away from the flange. The negative strain in web gap region may be from the compressive axial forces placed on the region as the vehicle crosses the instrumentation location. Three spikes can be seen which are most likely due to the axles as they cross the region. The magnitudes are different, although this is not surprising since the size of the ambient traffic event is unknown, and also this region would be affected by the exact transverse vehicle position which can't be verified for the ambient traffic event. It is important to note the strains in these details are very small, and the behavior in these regions is caused by very localized effects of the vehicle on the region. Therefore the above explanations of the behavior are only basic observations and engineering judgments.

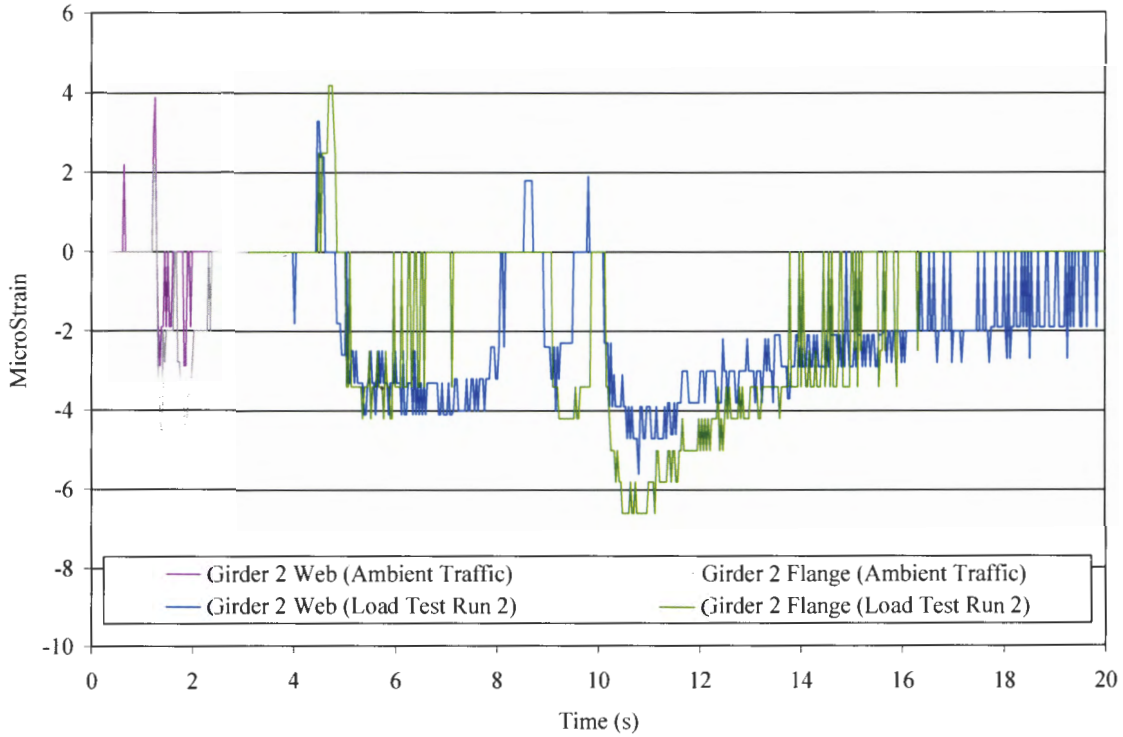

Figure 5.17. Girder 2 welded plate splice comparison for Ambient Traffic and Run 2.
Note: The time in which the events occur is different since Run 2 was conducted at crawl speed.

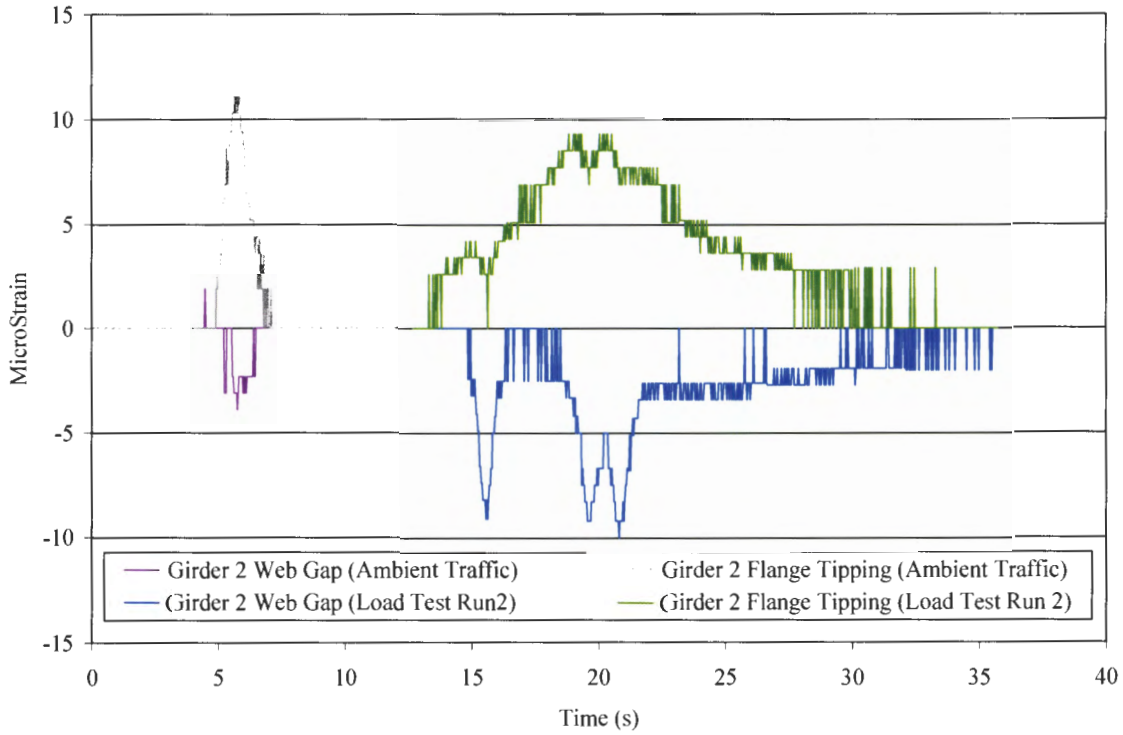

Figure 5.18. Girder 2 web gap comparison for Ambient Traffic and Run 2.
Note: The time in which the events occur is different since Run 2 was conducted at crawl speed.

5.2.2.4 Localized Top Flange Strain

The top and bottom flange response at the North midspan for Run 2 are shown in Fig. 5.19. Three positive strain spikes occur in the top flange as the truck crosses the top flange sensor location. These spikes represent localized strain effects on the top flange caused by the truck tires driving directly across the Girder 2 instrument location.

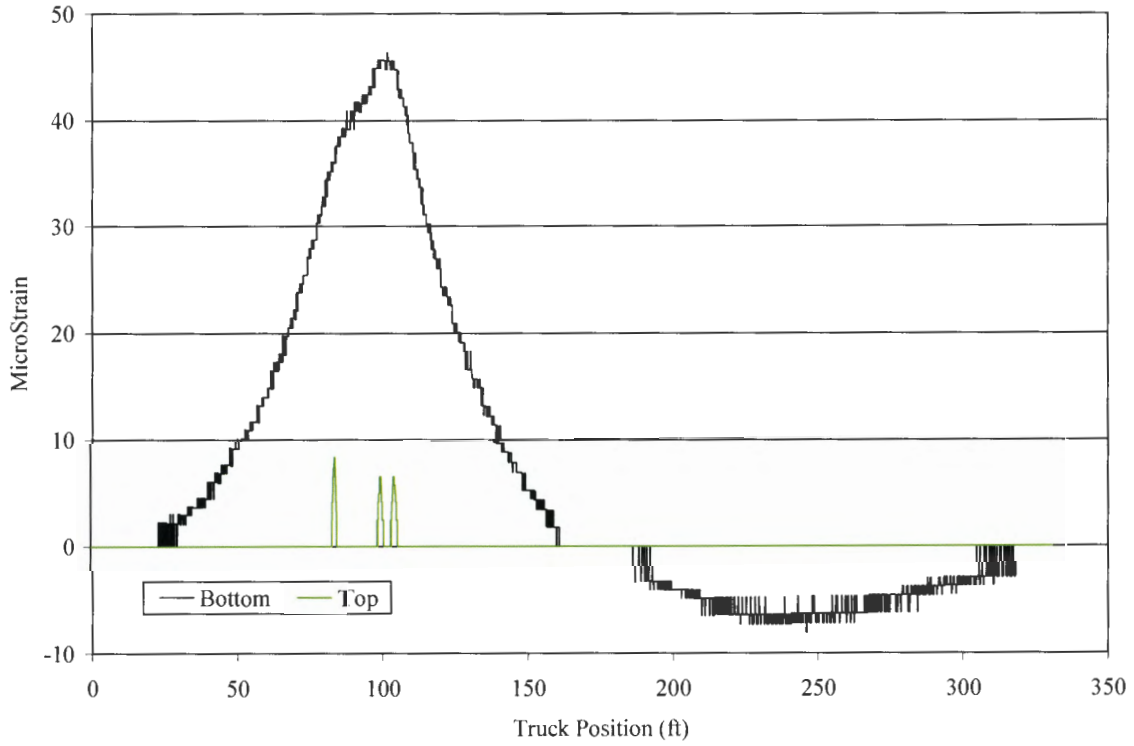

Figure 5.19. Strain plots of Girder 2 top and bottom flange sensors at the North midspan from controlled load test Run 2.

5.2.2.5 Symmetry of Bridge Response

The bridge is symmetrical about its longitudinal centerline as shown previously in the bridge description section (3.1). The symmetry of the bridge response from a symmetrical test truck position (Run 4) can be seen in Fig. 5.20, which shows the North midspan bottom flange strain. This is shown through the similar strain histories for Girders 1 and 6, Girders 2 and 5, and Girders 3 and 4, which are transversely symmetrical. The bridge's symmetry can also be seen in Fig. 5.21 which shows bottom midspan strain for Runs 2 and 6 from Girders 2 and 5, respectively. In this case the strain histories, which are similar for both girders, are from girders which have a wheel line almost directly above them in the respective Controlled Load Test runs.

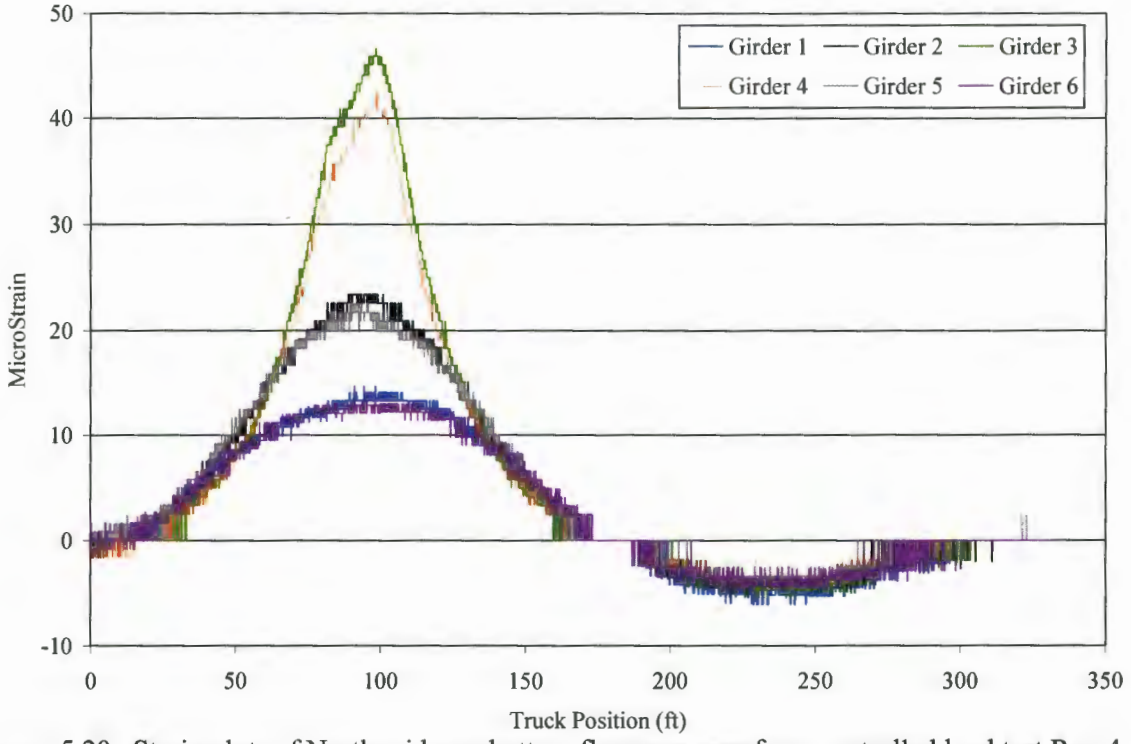

Figure 5.20. Strain plots of North midspan bottom flange sensors from controlled load test Run 4.

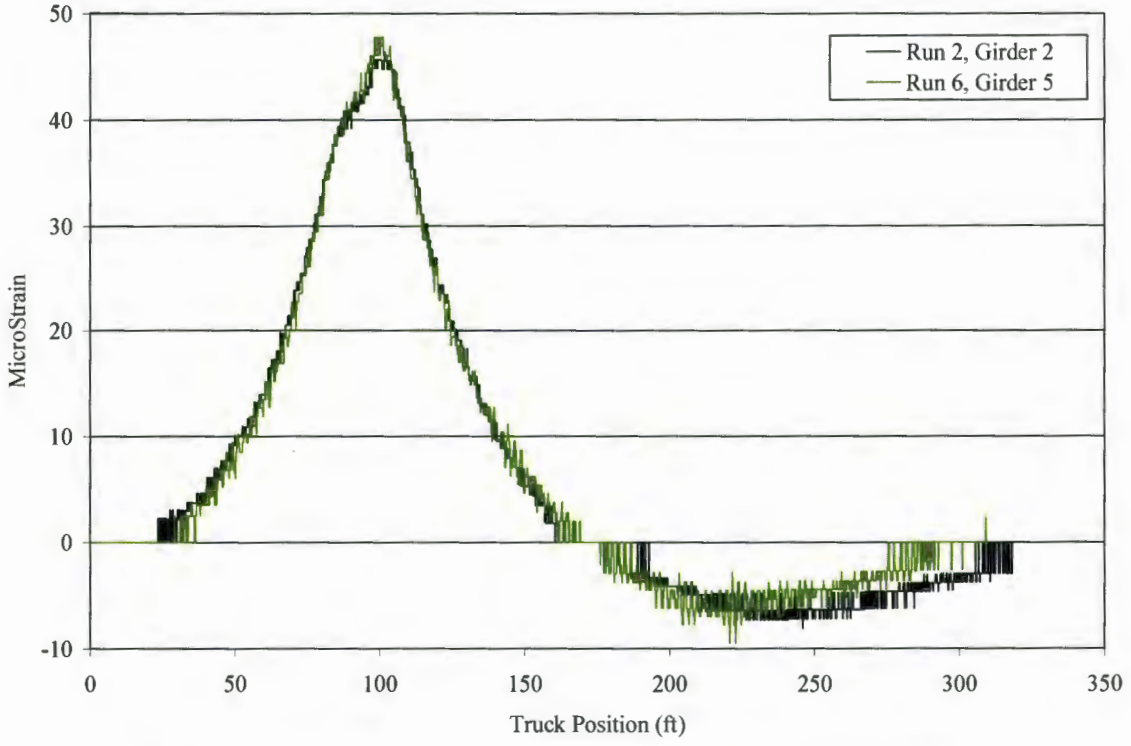

Figure 5.21. Strain plots of North midspan bottom flange sensors.

5.2.3 Bridge Performance Indices

As stated previously, the FBG strain data are processed with the DPP program, which calculates several bridge performance indices. The indices include the distribution factor (DF), neutral axis (NA), and end restraint ratio (ER) which can potentially be used to evaluate the performance of the bridge during the controlled load test as well as for the bridge's performance over time.

5.2.3.1 Distribution Factor (DF)

The amount of load distributed to each girder (as a percentage or fraction of total strain on the bridge cross-section) is presented subsequently. This distribution is calculated from data at the North and South midspans using the recorded bottom flange strains. The DF at each midspan will be referred to as either North or South.

DF from Controlled Load Tests - The DF for each girder for Runs 2, 4, and 6 are presented subsequently. Since the sum of the bottom flange strain at the particular cross section must be greater than the threshold set by the user (45 $\mu\varepsilon$ in this case), the DFs at the North midspan were computed only while the load truck was in the middle of the North span and the DFs at the South midspan were computed only while the load truck was in the middle of the South span.

Figure 5.22a shows the DFs for Run 2 of the load test. The magnitudes of the DFs for Girders 2 and 3, the two most heavily loaded girders, increase as the truck nears the middle of each span and decrease as the truck passes midspan. The DFs for the other girders generally have magnitudes that are proportional to the distance the truck is from the girder. When comparing the North and South midspan DF data, several things can be observed. Girders 2 and 3 (the most heavily loaded girders) have a larger DF at North midspan than the South. Girders 1, 4, 5, and 6 have a lower DF at the North midspan than the South. This indicates the South midspan is distributing the load better than the North. The maximum DF for any girder was approximately 0.34 for Girder 2.

The DFs for Run 4 of the load test are shown in Fig. 5.22b. The shapes of the individual DF plots for each girder are similar to Run 2, where the girders that are more heavily loaded (i.e. Girders 3 and 4) have concave down shapes, while the other girders have concave up shapes. Once again, the symmetrical behavior of the bridge is demonstrated as girders that are transversely symmetric exhibit similar DR profiles. The same behavior that was discussed for Run 2 can be seen in Run 4, in which the South midspan distributes the load slightly better than the North (it is not as significant in Run 4 as Run 2). The maximum DF is less than 0.30.

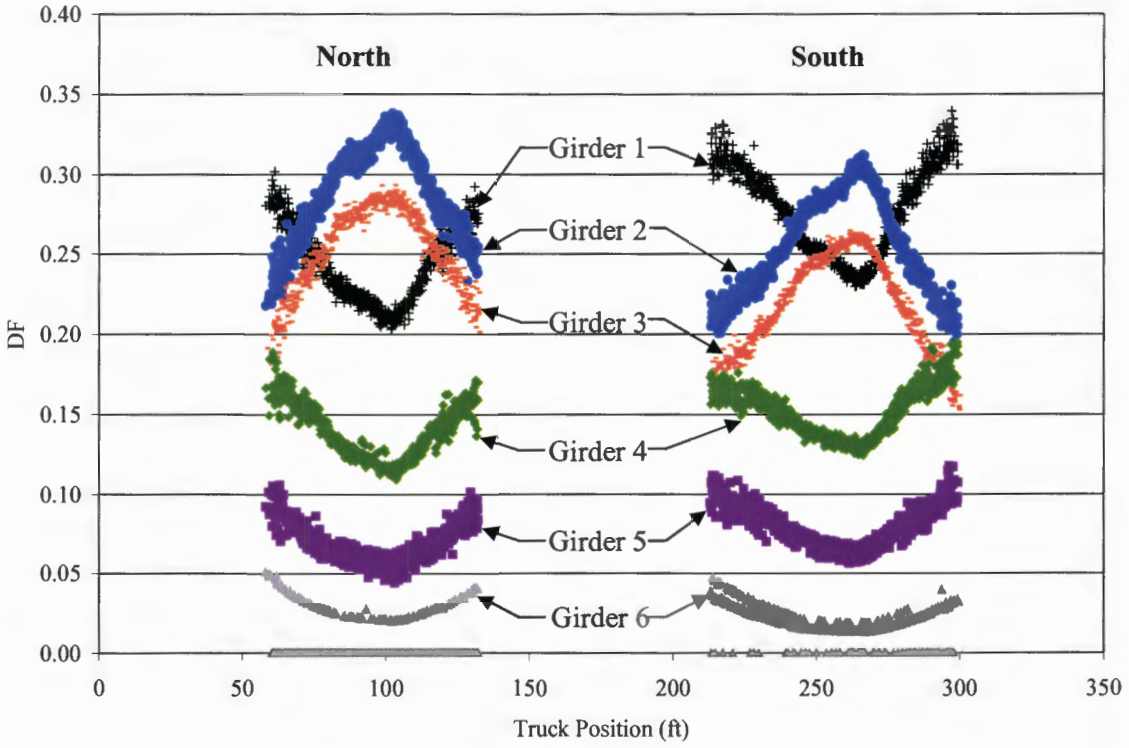

a. Run 2.

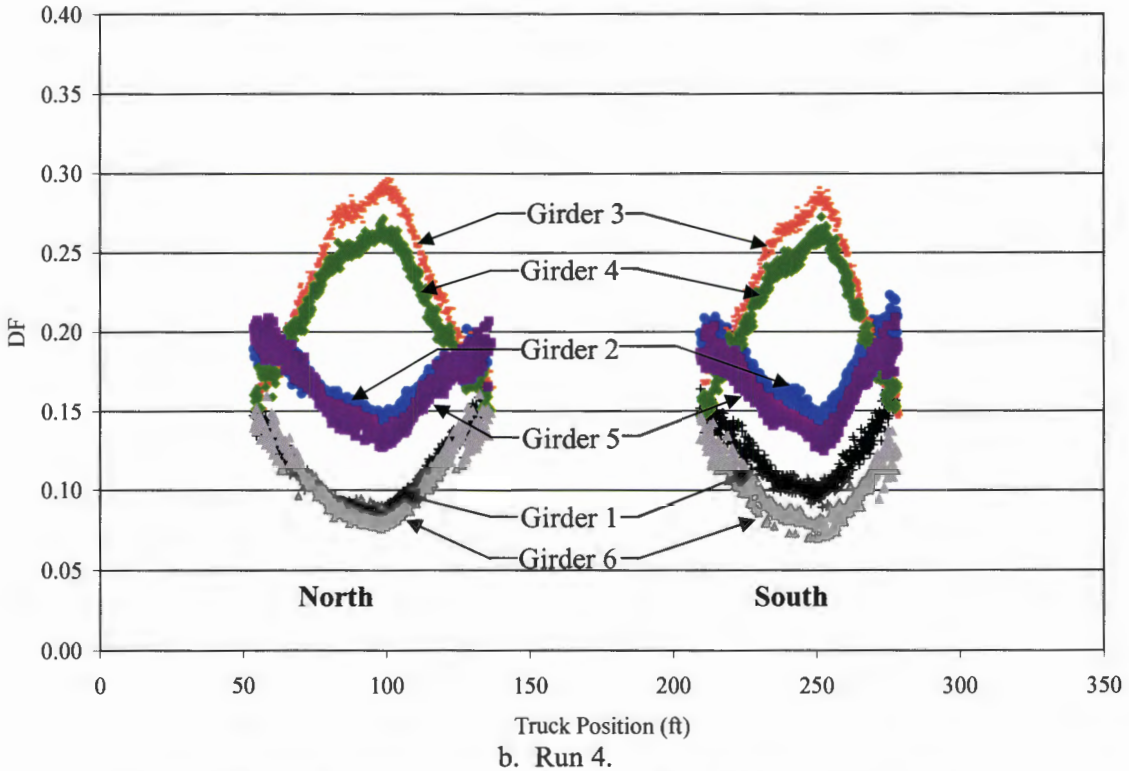

b. Run 4.

Figure 5.22. DF at North and South midspan for the Controlled Load Test.

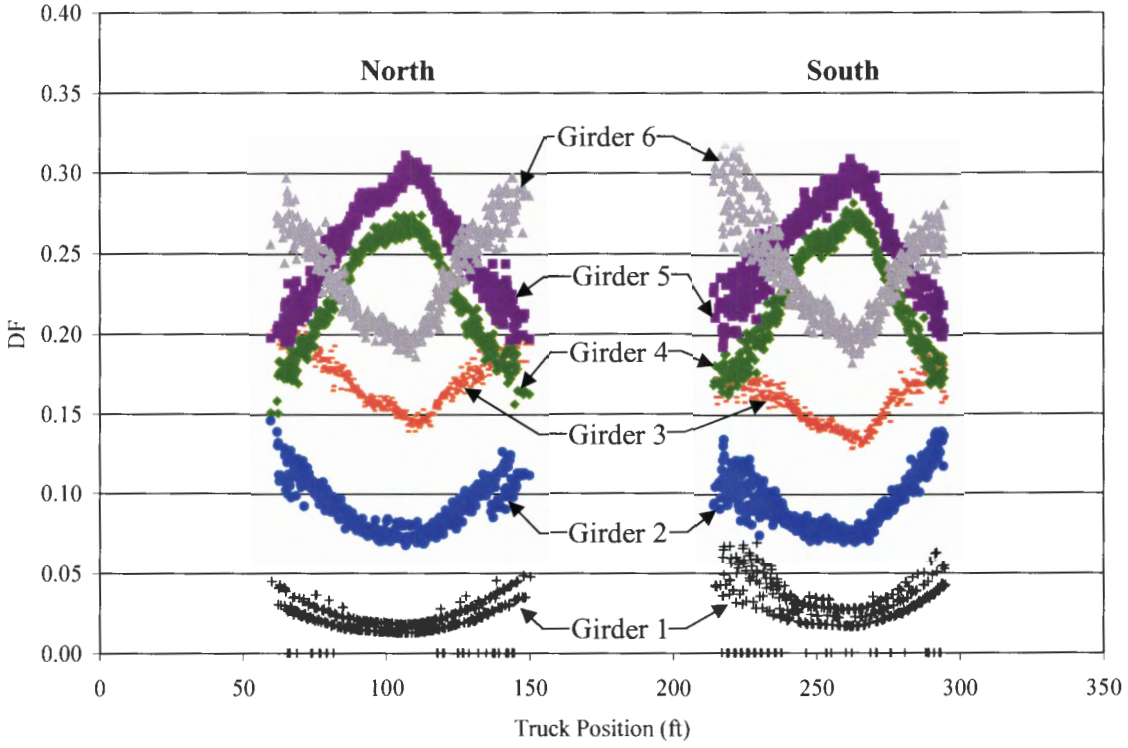

c. Run 6.

Figure 5.22. DF at North and South midspan for the Controlled Load Test (Continued).

The DF values for Run 6, shown in Fig. 5.22c, have similar shapes and magnitudes to the corresponding transversely symmetrical girders associated with the DF values from Run 2. However, unlike the Run 2 data, there is much better agreement in the North and South DF for the more heavily loaded girders. Girder 5 has the largest DF, which is 0.31, which is just slightly less than the DF for Girder 2 for Run 2 (0.34).

The general profiles of the data in Fig. 5.22 show the DF for the most heavily loaded girders increase as the vehicle approaches the midpoint of each span and then decrease as the vehicle moves past the midpoint of the span. Conversely, the DF for the lesser loaded girders decrease as the vehicle approaches the midpoint of each span and then increase as the vehicle moves past the midpoint of the span. This behavior is easily validated by considering St. Venant's Principle, the longitudinal and transverse flexibility of the bridge, and the change in load paths through the bridge resulting from dynamic loads.

In Fig. 5.22 the heavier loaded girders show that the DF for the North midspan is slightly higher than the South midspan. These differences could be due to the stiffness differences between the girders in the North and South spans.

DF Time History from Ambient Traffic - Presented subsequently is the DF for each girder over time using ambient traffic data that exceed the DF threshold discussed previously. Each data point represents the average daily DF for the particular girder for one day. The graphs are presented with a linear best fit trend line for the North and the South midspan. As stated previously, the sensors at the North midspan were installed before the South midspan sensors, therefore more data are shown for the North midspan. The DF data for all of the girders presented subsequently have outliers much higher and lower than the rest of the data set. This can be attributed to days with low volumes of traffic in which one event can skew the results. On a particular Sunday, for example, only one event was large enough for the DF to be calculated, therefore the data would be skewed for that day.

Figure 5.23 shows the DF for all six girders for the North and South midspan. The South DF for Girders 2, 4, 5, and 6 is nearly equal to or lower than the North DF. For Girder 1 the South DF is slightly higher than the North DF. This agrees with the strain data shown in Fig. 5.15 and the DF load test data shown in Fig. 5.22. The North DF is higher than the South DF for Girder 3; this agrees with what was found in the controlled load test. With the exception of North span of Girder 3, the trend lines are slightly decreasing or nearly constant for each Girder. The trend line for the North span of Girder 3 shows an increase in the DF with time. Near day 30 the North Girder 3 DF starts to rise. A possible reason for this is a change in traffic patterns (i.e. seasonal traffic change, change in the number of vehicles traveling in each direction, the size of the vehicles in each direction, etc.).

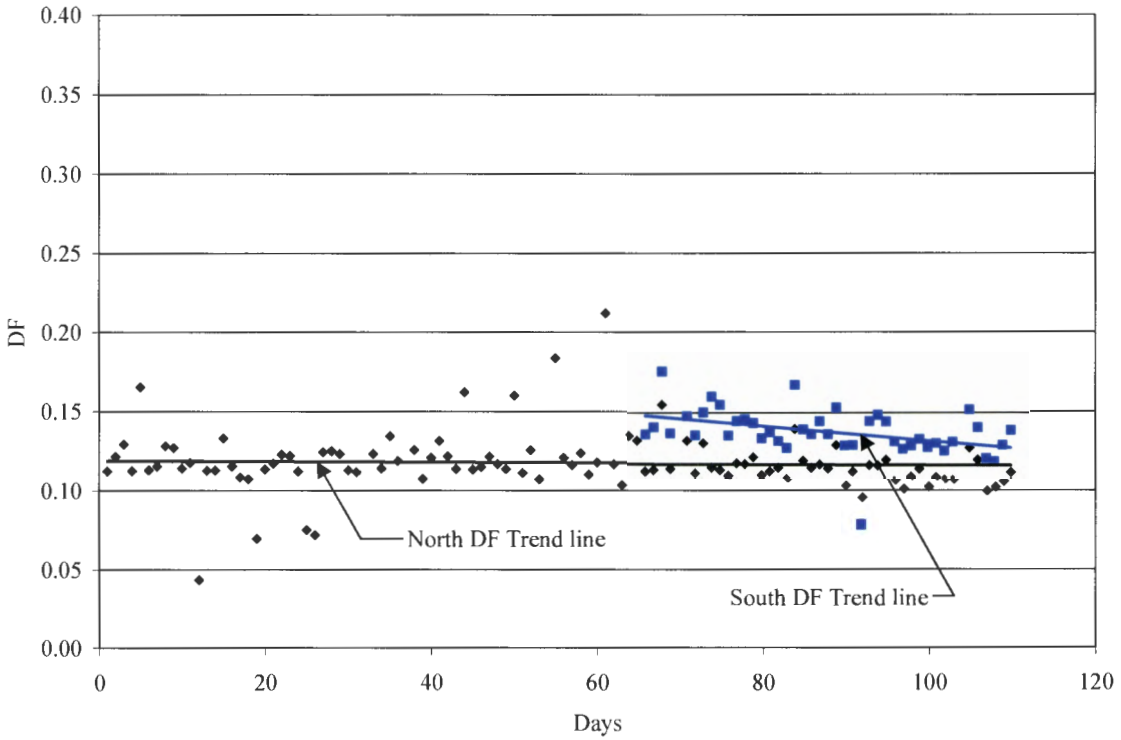

a. Girder 1.

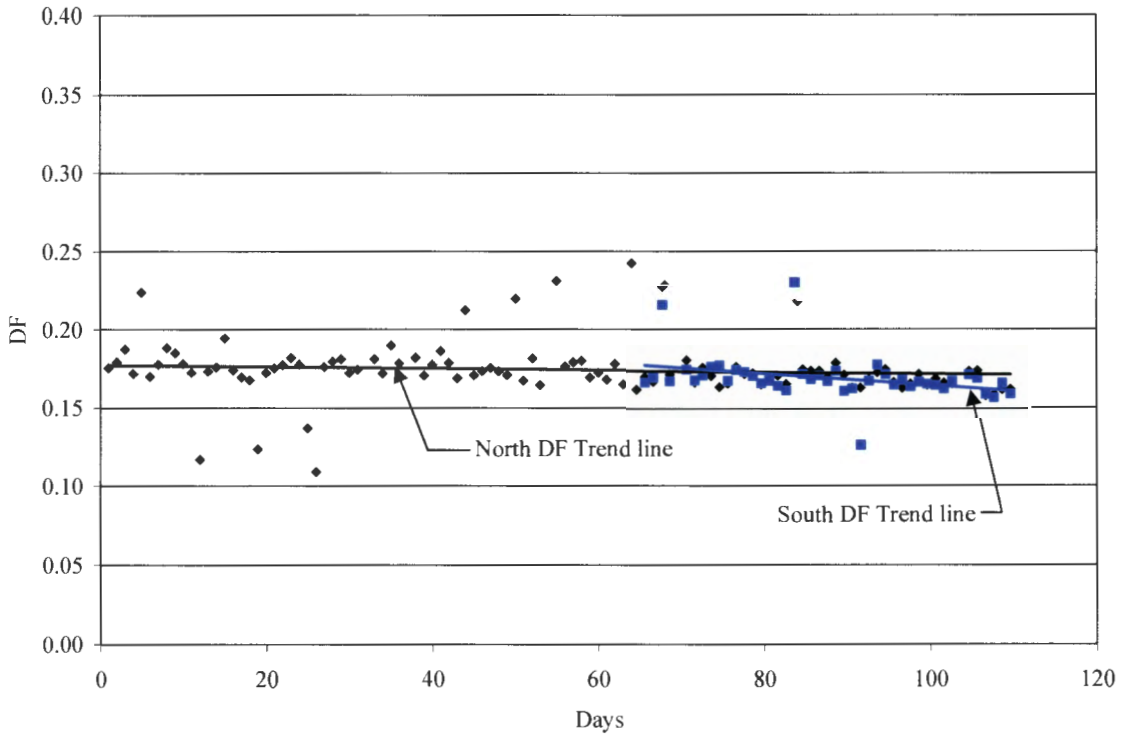

b. Girder 2.

Figure 5.23. Average DF per day over time.

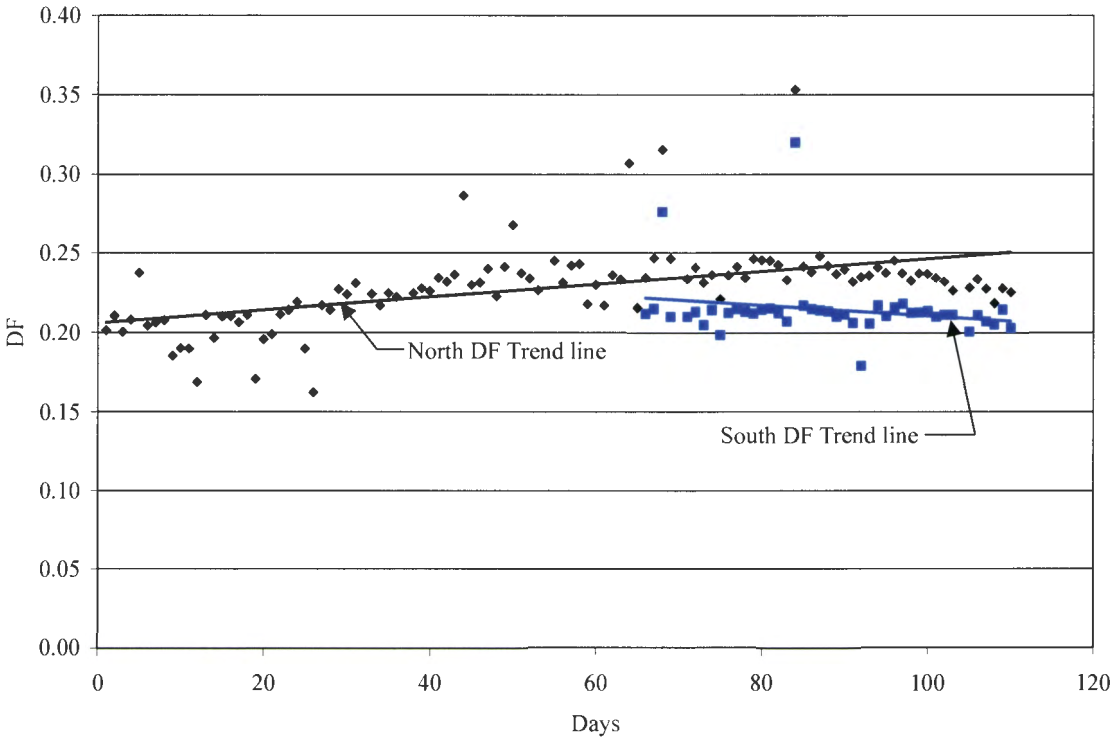

c. Girder 3.

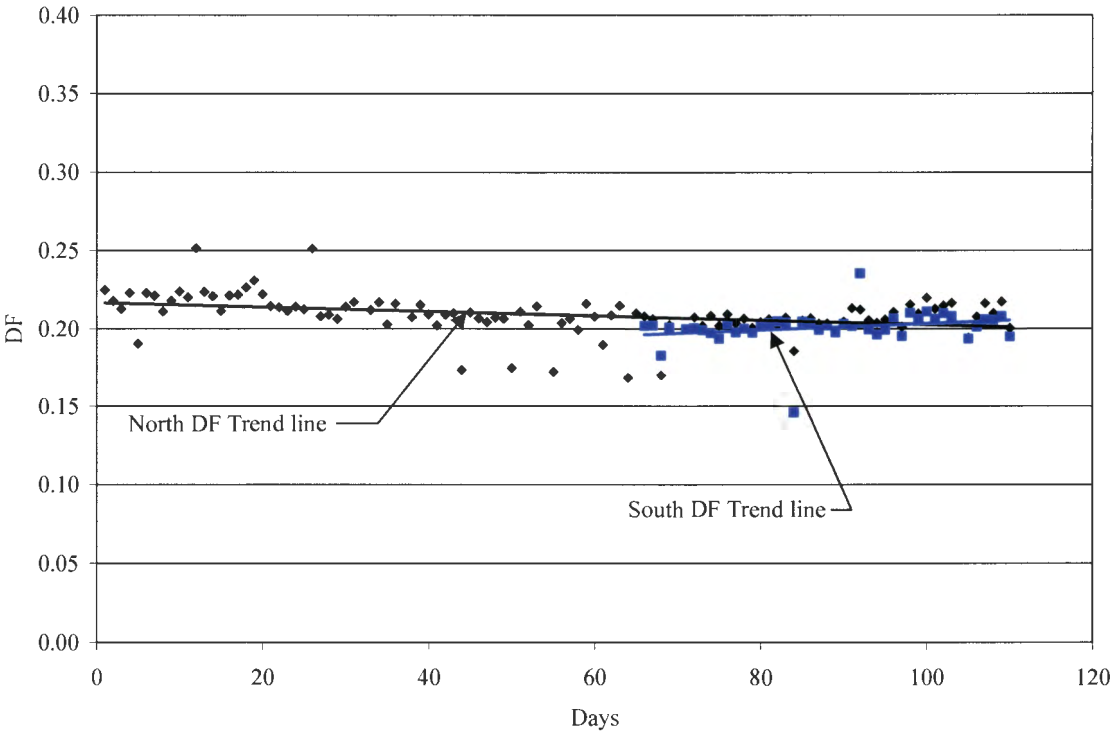

d. Girder 4.

Figure 5.23. Average DF per day over time (Continued).

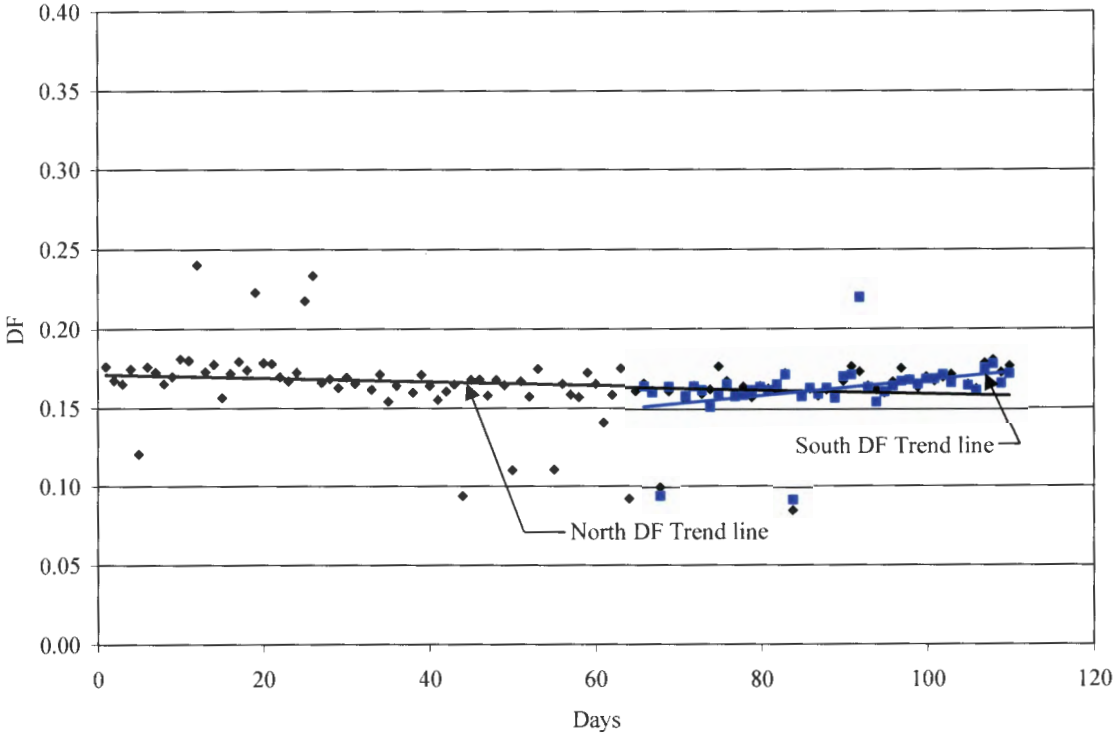

e. Girder 5.

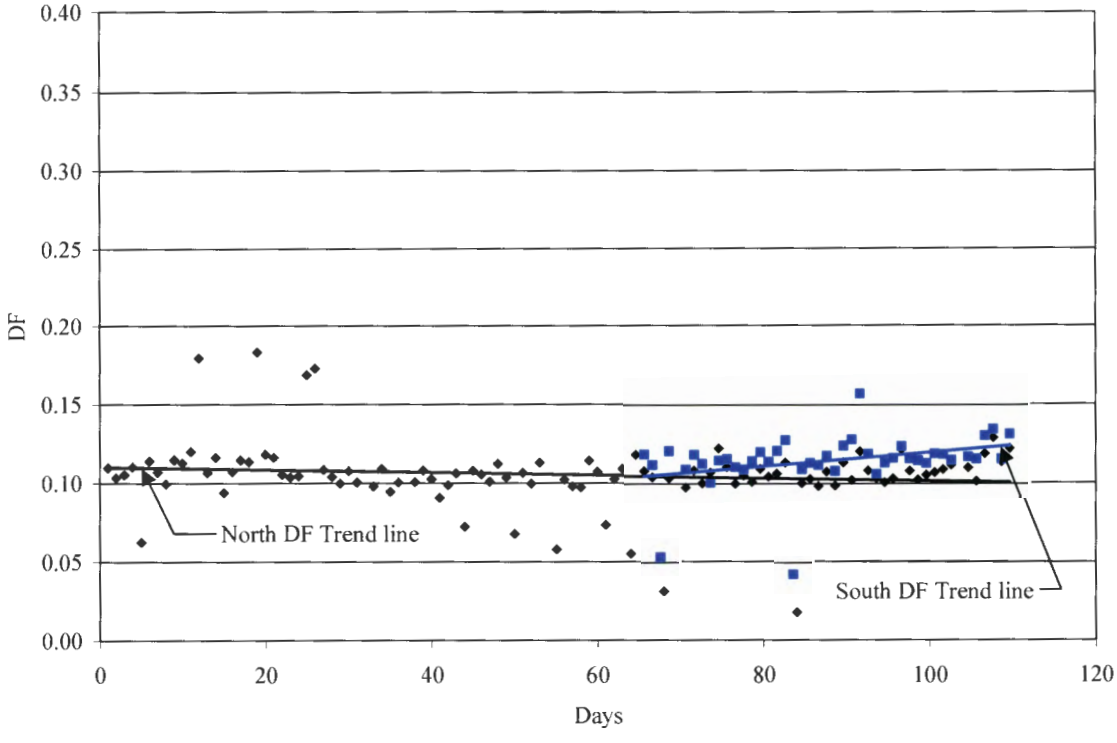

f. Girder 6.

Figure 5.23. Average DF per day over time (Continued).

The DF trend lines may not accurately represent the data shown. As mentioned above, the outliers adversely affect the slope of the trend line. As more data are collected this problem should be minimized and a more statistically significant and accurate representation developed.

The RMS for each DF has more statistical significance and minimizes data outliners. Table 5.3 and Fig. 5.24 shows the long term and load test DF RMS values for each girder for both the North and South spans. The difference in the long term and load test DF RMS can be expected since the load test DF is based on a specific vehicle configuration (the load truck) and the long term DF results from ambient traffic which the vehicle configuration, location, nor direction can be determined. The difference between the North and South span RMS for the long term and the load test can be attributed differences in the stiffnesses of the girders with respect to the different spans, which would affect the load path for each span.

Table 5.3. DF RMS data from long term ambient traffic and Controlled Load Test.

	Girder 1	Girder 2	Girder 3	Girder 4	Girder 5	Girder 6
	Long term DF RMS data					
North	0.12	0.18	0.23	0.21	0.17	0.11
South	0.14	0.17	0.22	0.20	0.16	0.12
	Load test DF RMS data					
North	0.13	0.18	0.22	0.21	0.19	0.16
South	0.17	0.18	0.20	0.20	0.19	0.15

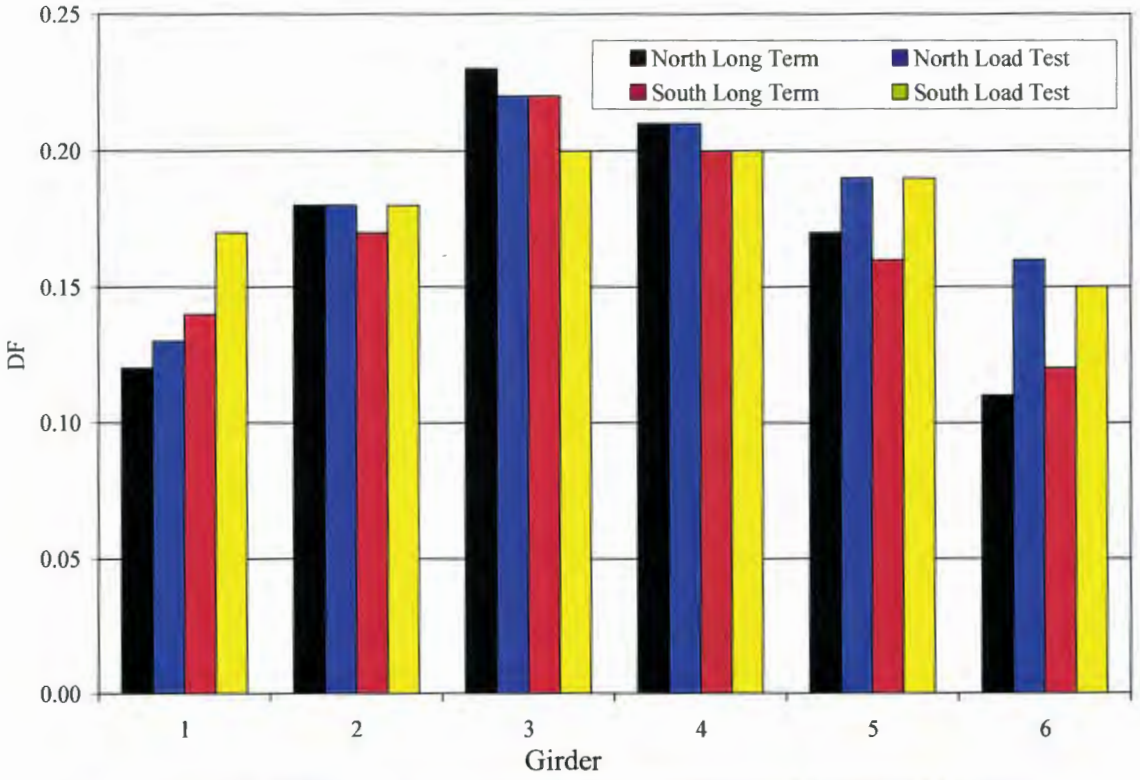

Figure 5.24. DF RMS data from long term ambient traffic and Controlled Load Test.

The American Association of State Highway and Transportation Officials (AASHTO) Standard Specifications for Highway Bridges [32] specifies that the single lane lateral distribution factor DF for interior girders is determined by S/7.0 (where S is defined as the spacing of girders in ft). For this bridge the DF for the interior girders would be 1.23 wheel lines per girder or 0.62 vehicles per girder. For comparison, the largest measured DF from the ambient traffic data was 0.35 vehicles/girder, but the typical DF values for interior girders were much less (approximately 0.20 to 0.25). It must be noted that the ambient traffic lane position may not cause the worst case DF values as inferred by the AASHTO values. And that the experimental DF values only represent a single vehicle on the bridge which is not what the AASSHTO values are meant to represent. They, rather, are intended to represent the local results from multiple vehicles.

5.2.3.2 Neutral Axis Location (NA)

The NA location is calculated at seven different positions on the bridge. Table 5.4 shows the relationship between the seven positions, labeled by an NA designation, and the girder number and span location. The NA location is referenced from the bottom of the girder and all dimensions are in inches.

Table 5.4. Location on bridge of NA designations

NA Designation	Girder Number	Cross-Sectional Location
G1N	1	North Midspan
G2N	2	North Midspan
G3N	3	North Midspan
G1S	1	South Midspan
G4S	4	South Midspan
G5S	5	South Midspan
G6S	6	South Midspan

NA from Controlled Load Tests - Figure 5.25 shows the NA location for Run 2 of the controlled load test. Data from all of girders expect Girder 6 are presented. The NA was not calculated at G6S during Run 2 due to insufficient strain in the bottom flange of Girder 6 (i.e. the bottom flange strain did not meet the threshold of 25 $\mu\varepsilon$). The NA location on all of the plots can be characterized by three different conditions: 1) NA location predominantly at top flange, 2) NA location predominantly below the top flange, and 3) NA location at least partly above the top flange.

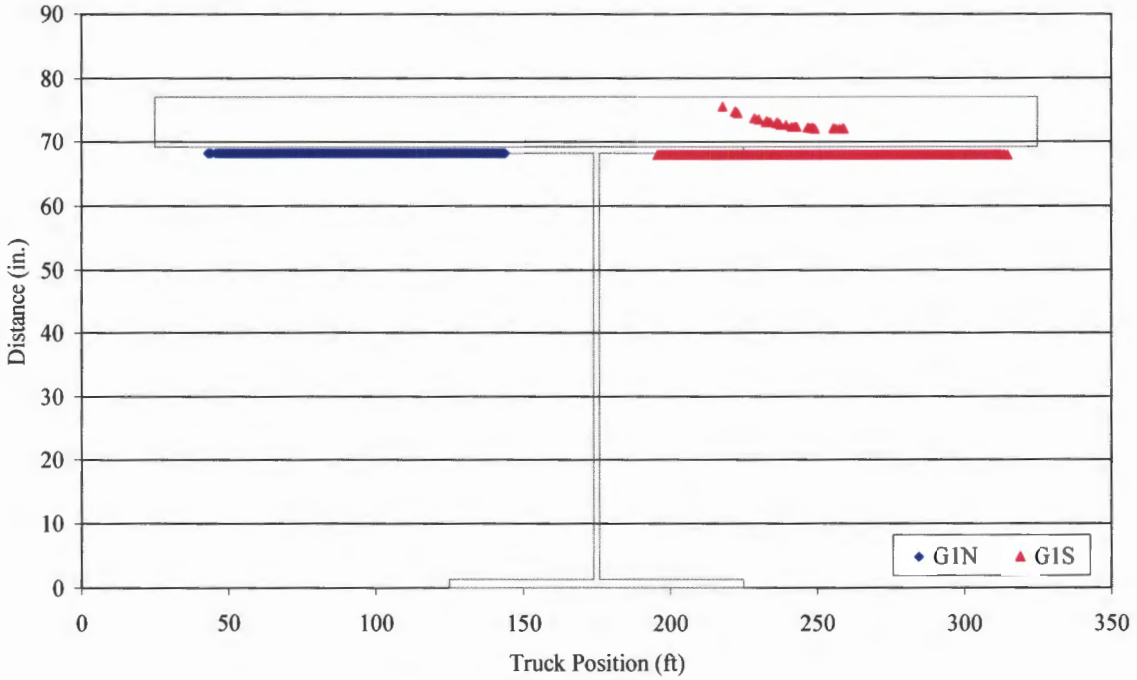

a. G1N and G1S.

Figure 5.25. NA location from the Controlled Load Test Run 2.

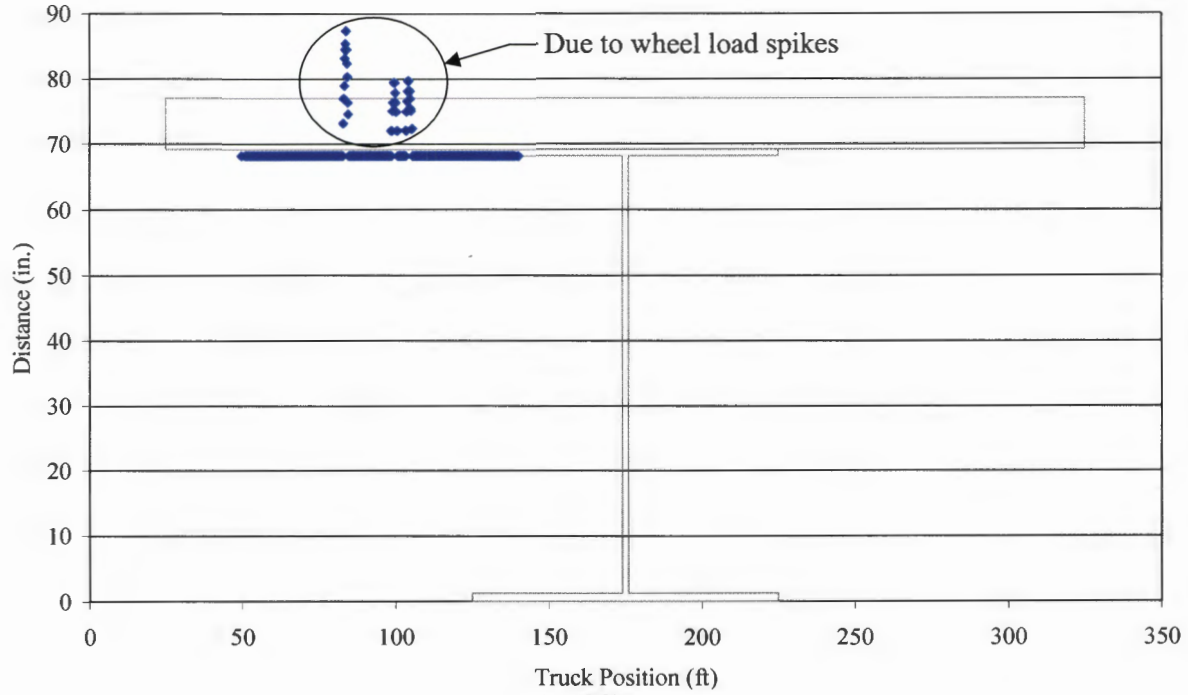

b. G2N.

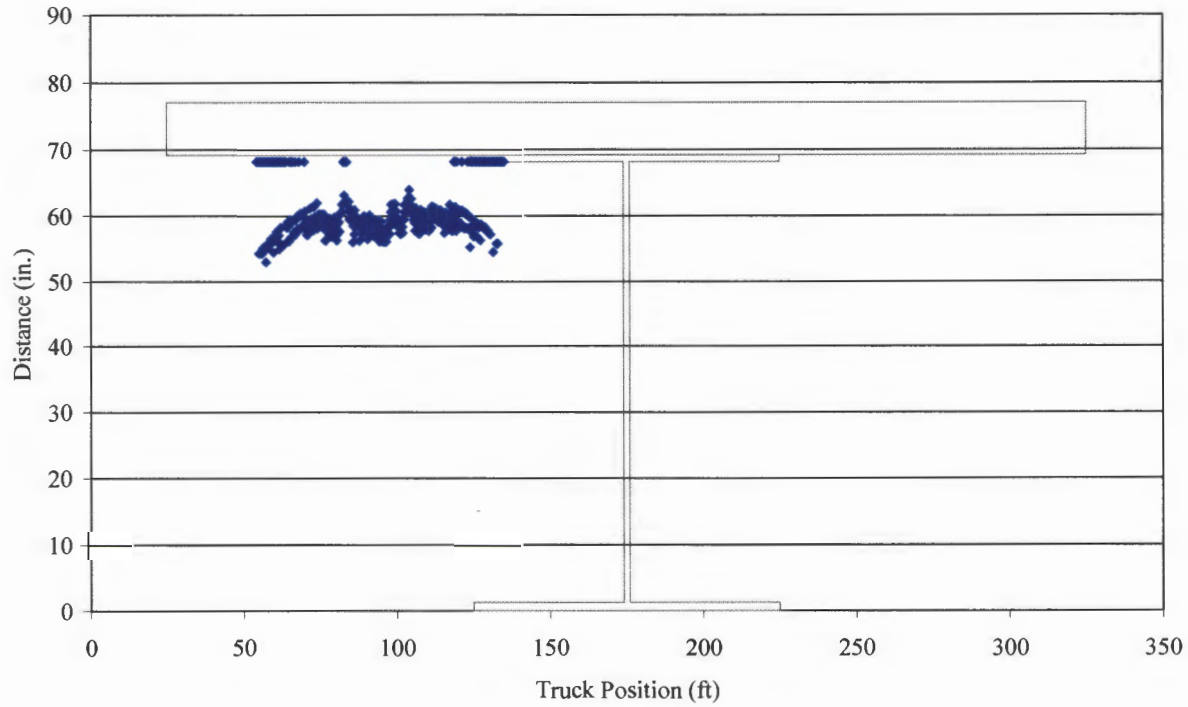

c. G3N.

Figure 5.25. NA location from the Controlled Load Test Run 2 (Continued).

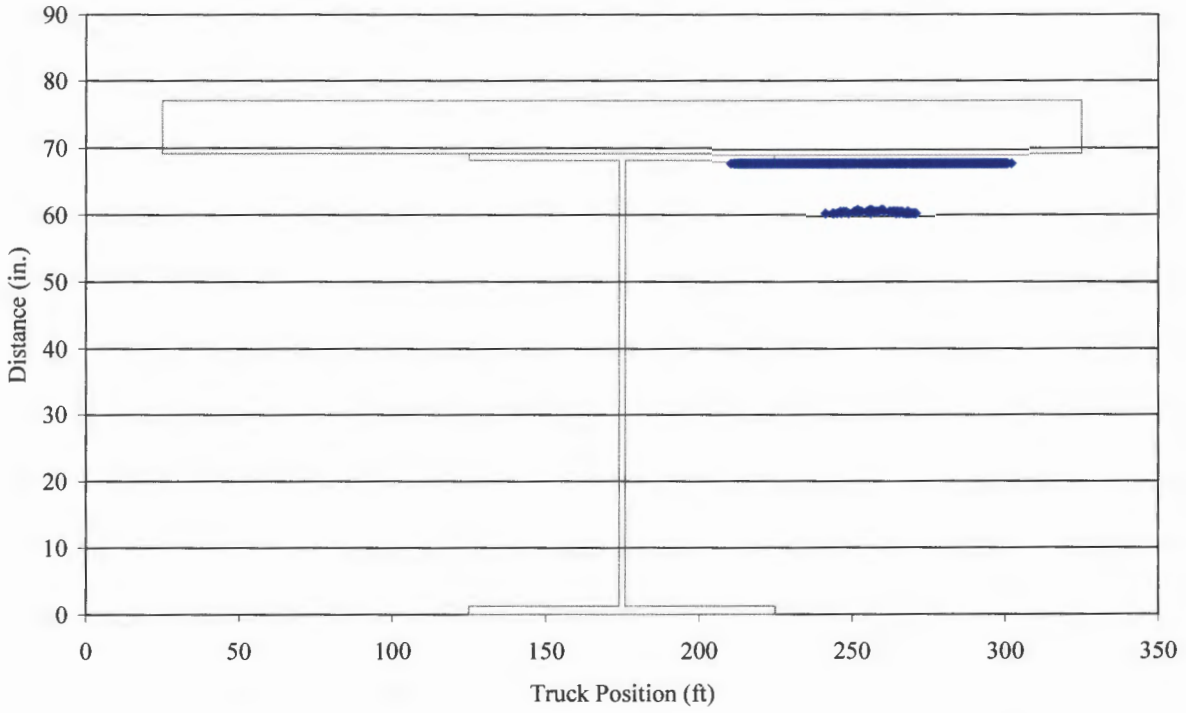

d. G4S.

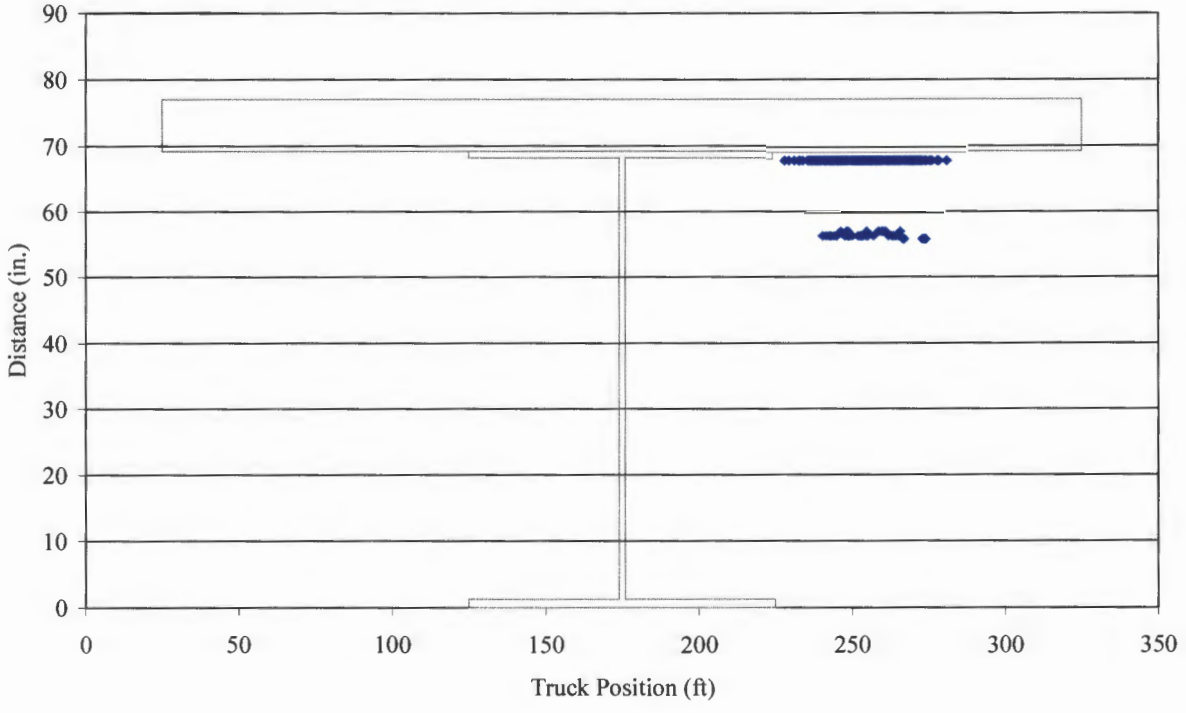

e. G5S.

Figure 5.25. NA location from the Controlled Load Test Run 2 (Continued).

NA location predominantly at top flange - Figure 5.25a and Fig. 5.25b show Girder 1 and 2 NA data, respectively for Run 2, in which the NA location at G1N and G2N is predominantly at the top flange location. The NA is calculated at two positions on Girder 1, the North (G1N) and South (G1S) midspans. The NA at G1S rises above the top flange several times, unlike the data for G1N. This anomaly will be discussed subsequently. Figure 5.25b shows the NA data from Girder 2 (G2N) where the NA location is at the top flange for the essentially the entire run. The few spikes in the data in which the NA location is above the top flange can be attributed to localized effects. As shown in the previous sections, when the load truck axles cross directly over, or extremely close to, the location where the top flange FBG is located, a positive (tensile) spike in the strain occurs in the top flange. Figure 5.26 shows the location of the West load truck wheels for Run 2 of the Controlled Load Test in relation to the Girder 2 top flange sensor.

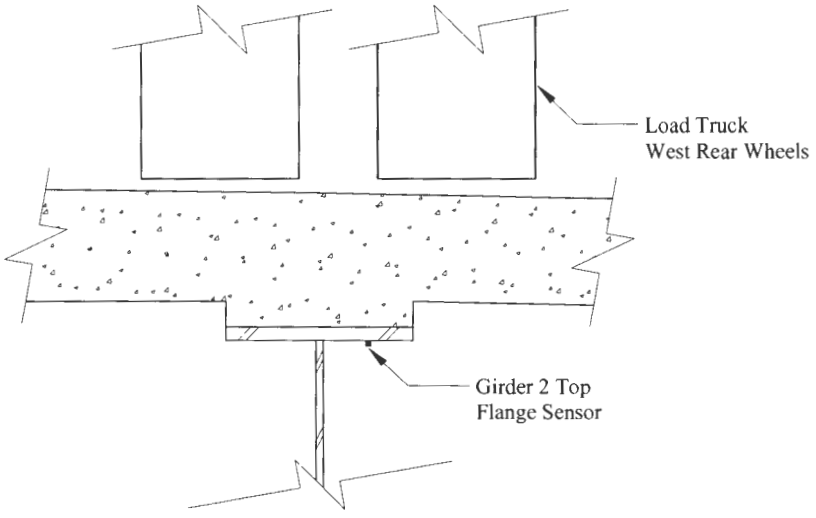

Figure 5.26. Sketch of load truck wheels in relation to Girder 2 top flange sensor for Run 2.

NA location predominantly below the top flange - Girder 3 (G3N) and Girder 4 (G4S) NA data from Run 4 are shown in Fig. 5.27. The NA location goes down when the load truck approaches the location of the sensor. Notice when the NA is below the top flange there are no transition data points between the points when the NA is at the bottom of the top flange and when it is well below the top flange. This is an anomaly caused by the DSP, since strain values less than $\pm 1.6\ \mu\varepsilon$ are set

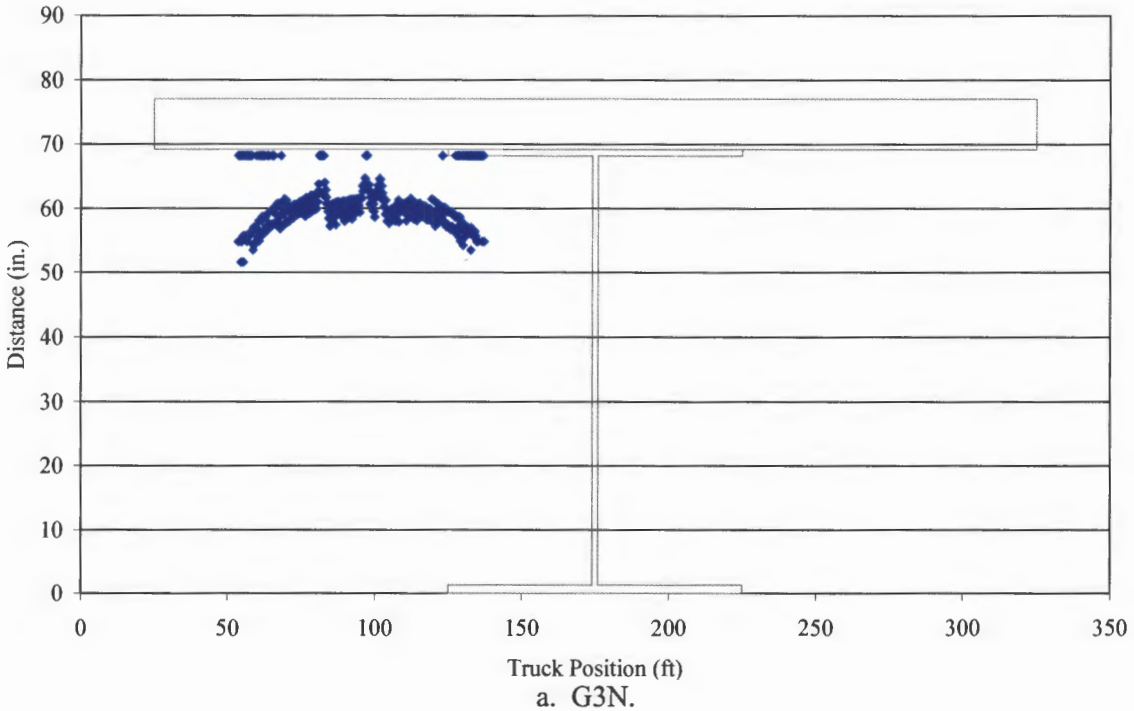

a. G3N.

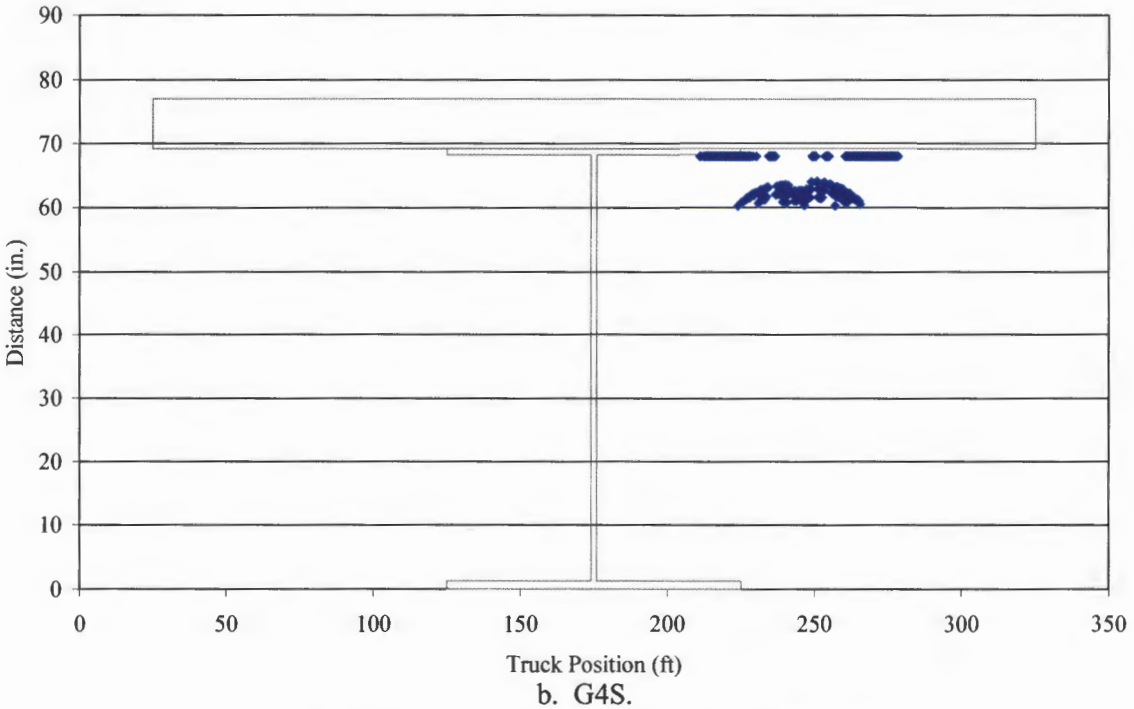

b. G4S.

Figure 5.27. NA location from the Controlled Load Test Run 4.

equal to 0.0 $\mu\varepsilon$. Consequently the NA is shown at the top flange when it may actually be slightly below the top flange. Since Run 4 provides symmetric truck loading to Girders 3 and 4, the NA locations should be similar for the two positions, assuming the North and South span lengths are similar (true) and the girder stiffnesses are similar (not true). G3N has a lower NA location which is below the top flange more often than for G4S. This is likely due to the lower girder stiffness in relation to the deck stiffness in the South span than in the North span.

NA location at least partly above the top flange - Figure 5.28 shows several conditions in which the NA is at least partly above the top flange. The same anomaly discussed previously occurs when the NA is above the top flange also. Therefore NA is forced (through the DSP) to be at the top flange when it maybe slightly above the top flange. The Girder 5 (G5S) NA is above the deck (the barrier near Girder 5 in compression) at several points, some of which are most likely due to localized effects from the truck axle (the three peaks near the center). Note the localized effects on G5S from the truck axle occurred during a situation which is symmetric to the localized effects on G2N discussed previously. Girder 6 (G6S) has more data points above the top flange than does Girder 5 (G5S). This signifies a higher deck stiffness in Girder 6 than Girder 5, which is most likely due to degree of contribution of the barrier rails near Girders 5 and 6.

The NA location for G1S from Run 2 and G6S from Run 6 (symmetrical loading on transversely symmetrical girders) are shown together in Fig. 5.29. Notice how the data points have the same magnitude and trend. Although exact reason for the shape of the anomaly is unknown, note the consistency and transverse symmetry behavior exhibited by Girders 1 and 6 at the South midspan. The NA location above the top flange can be attributed to positive (tensile) strains on the top flange.

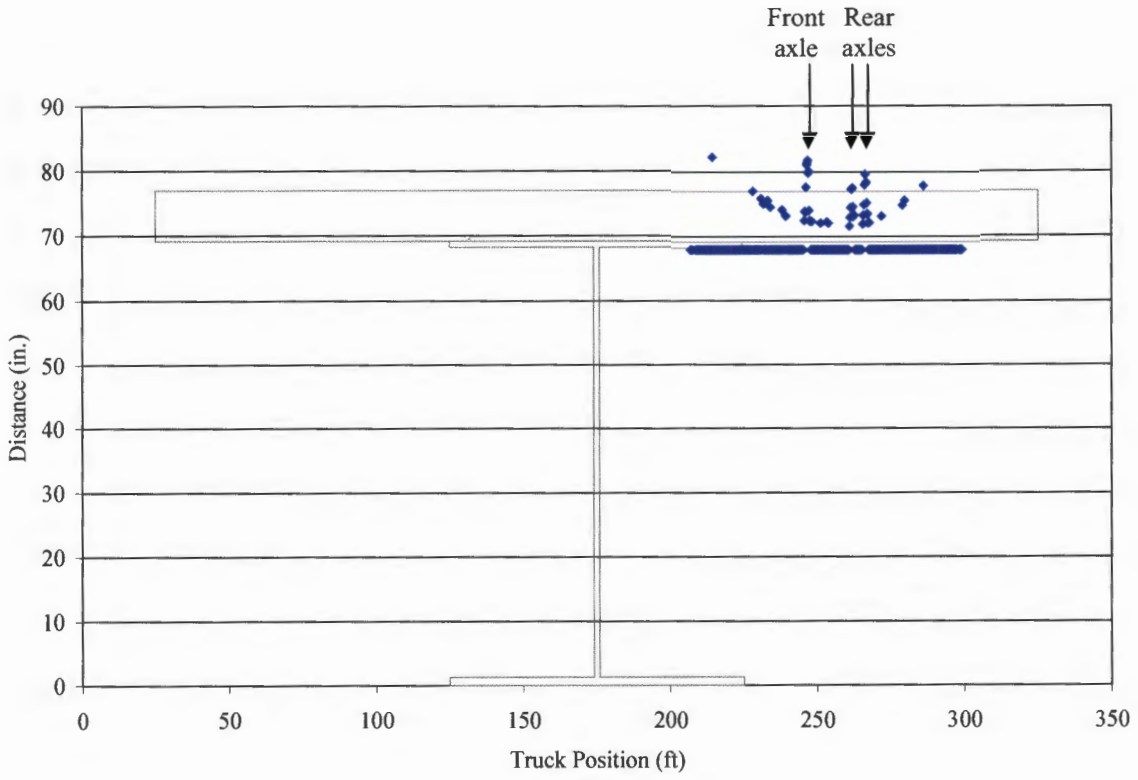

a. G5S.

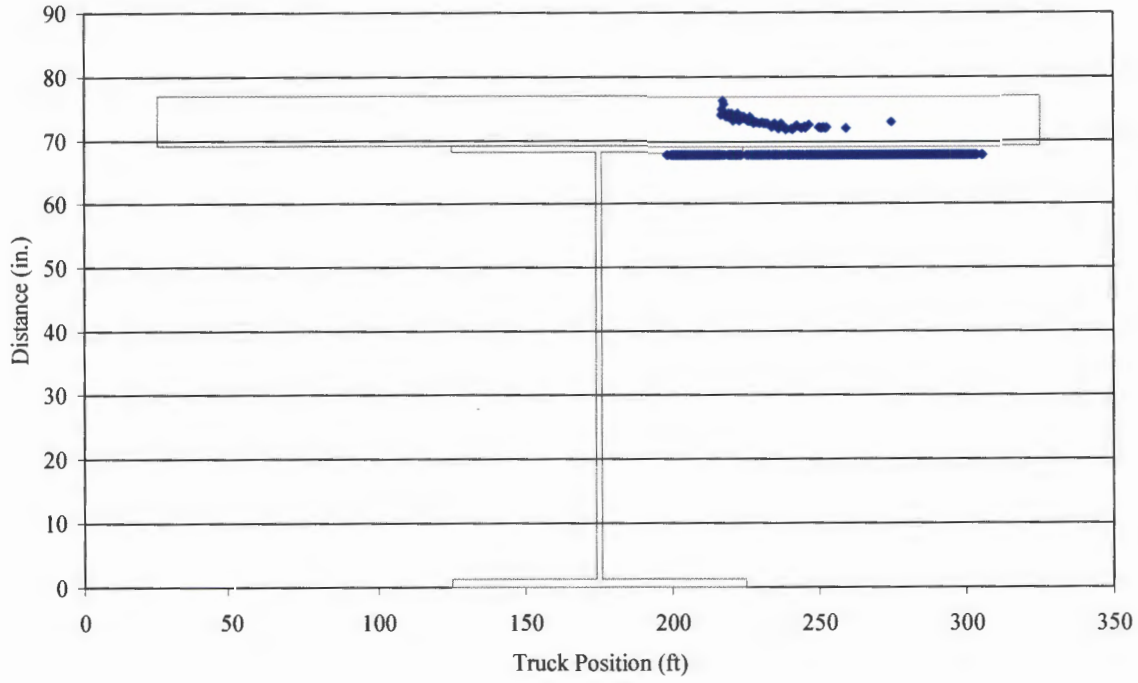

b. G6S.

Figure 5.28. NA location from the Controlled Load Test Run 6.

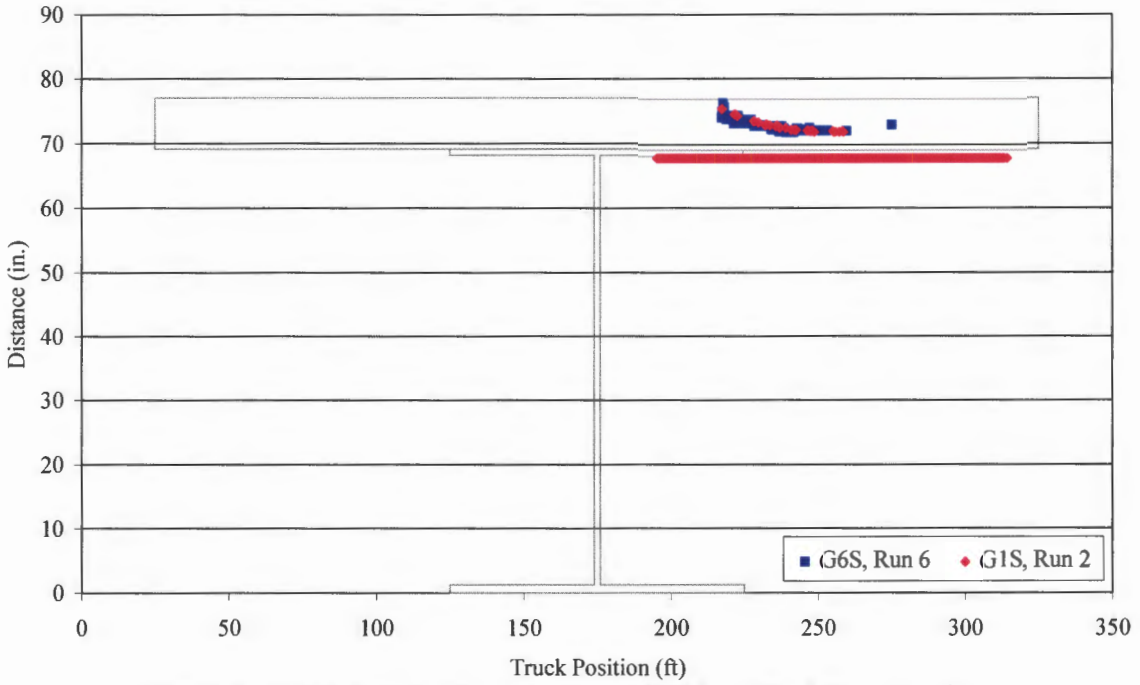

Figure 5.29. NA location from the Controlled Load Test Runs 2 and 6.

NA Time History from Ambient Traffic - The NA location for each girder is shown subsequently. Each data point represents the average NA location for a particular day in the monitored life of the bridge. If a point is not shown, the NA was not calculated at that position for a particular day due to no traffic events satisfying the minimum strain threshold. The RMS of the NA location time history is also provided.

The G1N, G1S, G2N, G5S, and G6S long term data (Fig. 5.30) show that the NA location is very near the top flange. This is consistent with the Controlled Load Test data for the girders near the barrier rails (i.e. Girders 1, 2, 5, and 6). Also note there are fewer G1N, G1S, and G6S data points than for the other girders. This validates the DF data presented earlier in which Girders 1 and 6 had lower DF than the other girders. Since the load distributed on Girders 1 and 6 is lower, the strain in Girders 1 and 6 may not be large enough for the NA to be calculated. When G3N and G4S are compared, the NA location for G3N is lower and more varied than the NA location for G4S. Indicating G4S has a higher deck stiffness in relation to the girder stiffness than G3N. The same observation was made for the Controlled Load Test data.

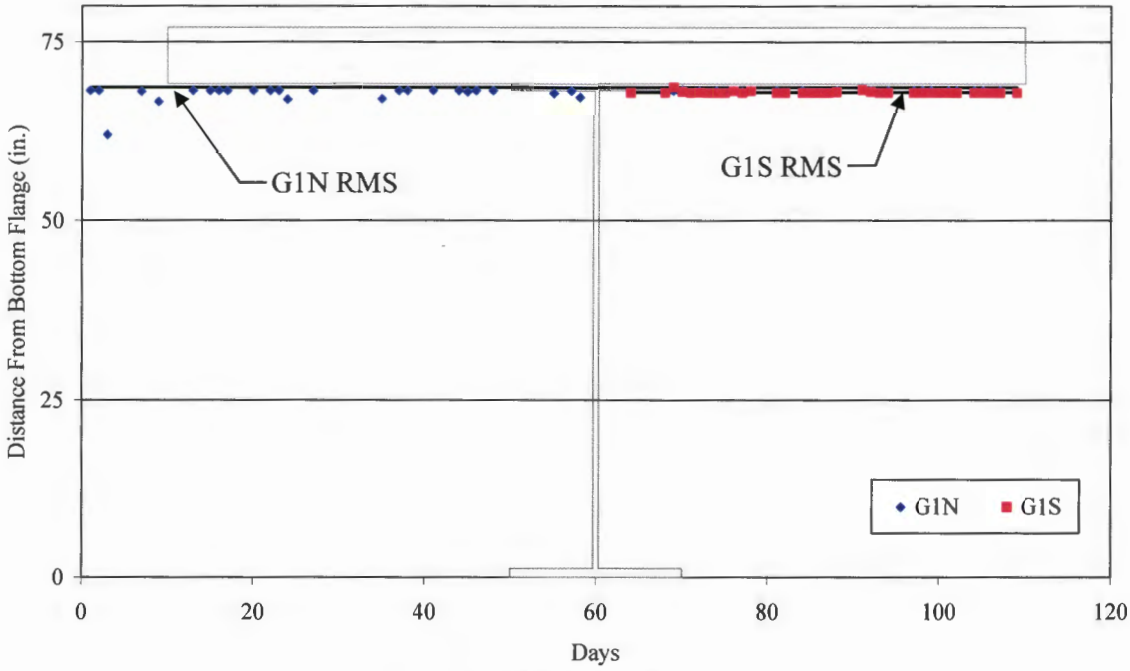

a. G1N and G1S.

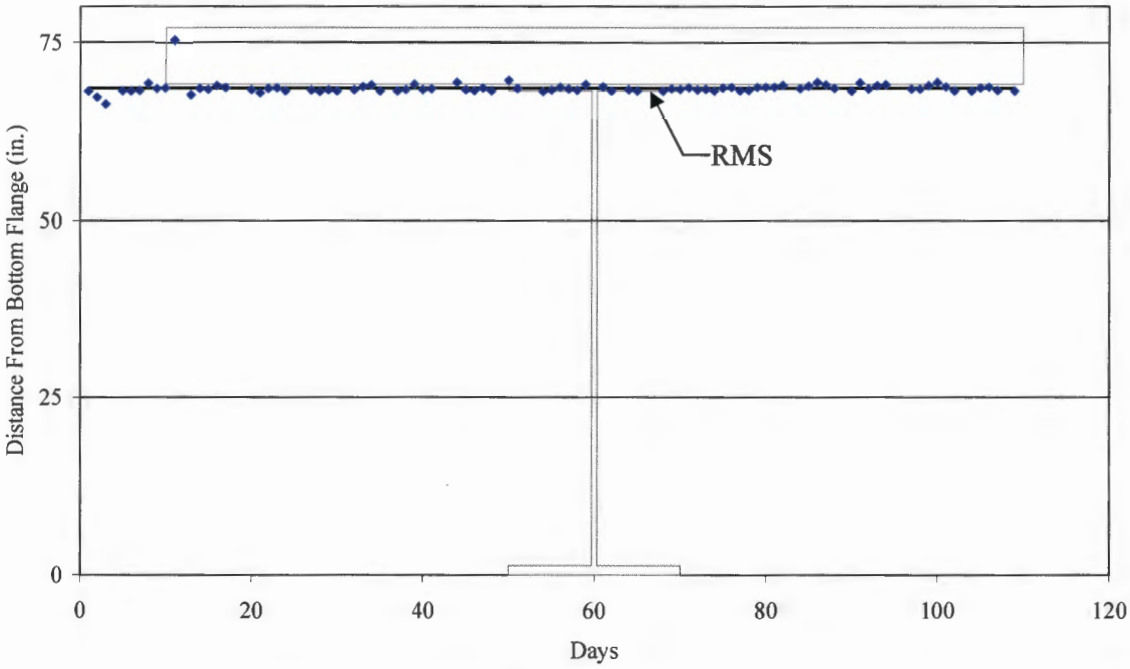

b. G2N.

Figure 5.30. Average NA location per day over time.

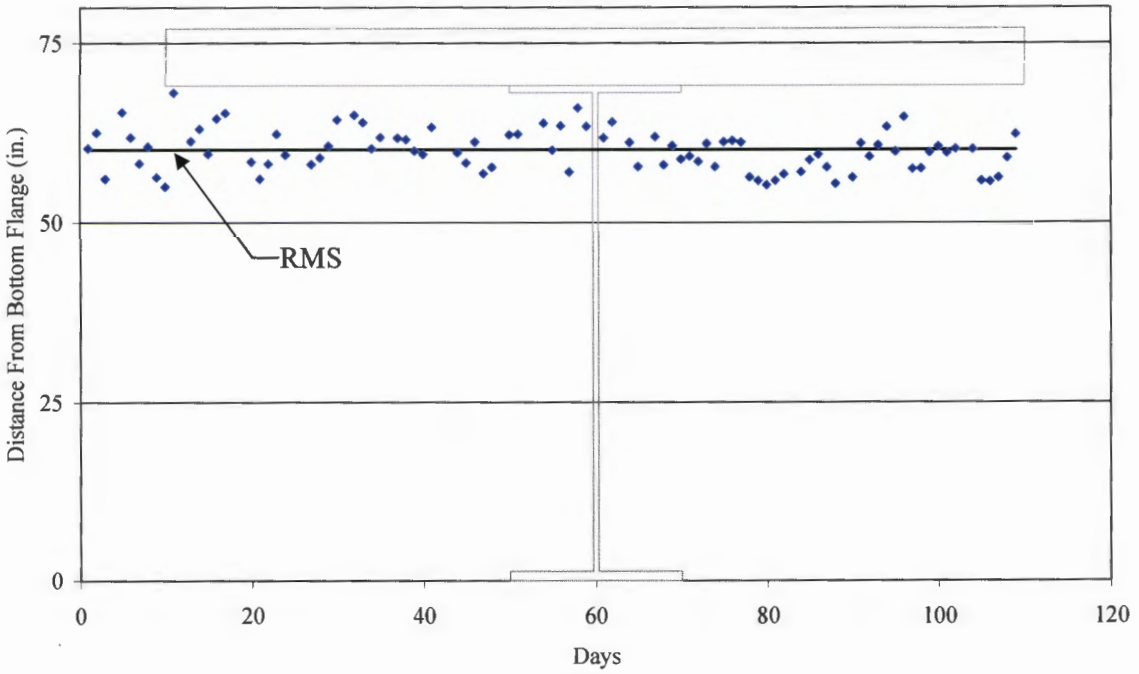

c. G3N.

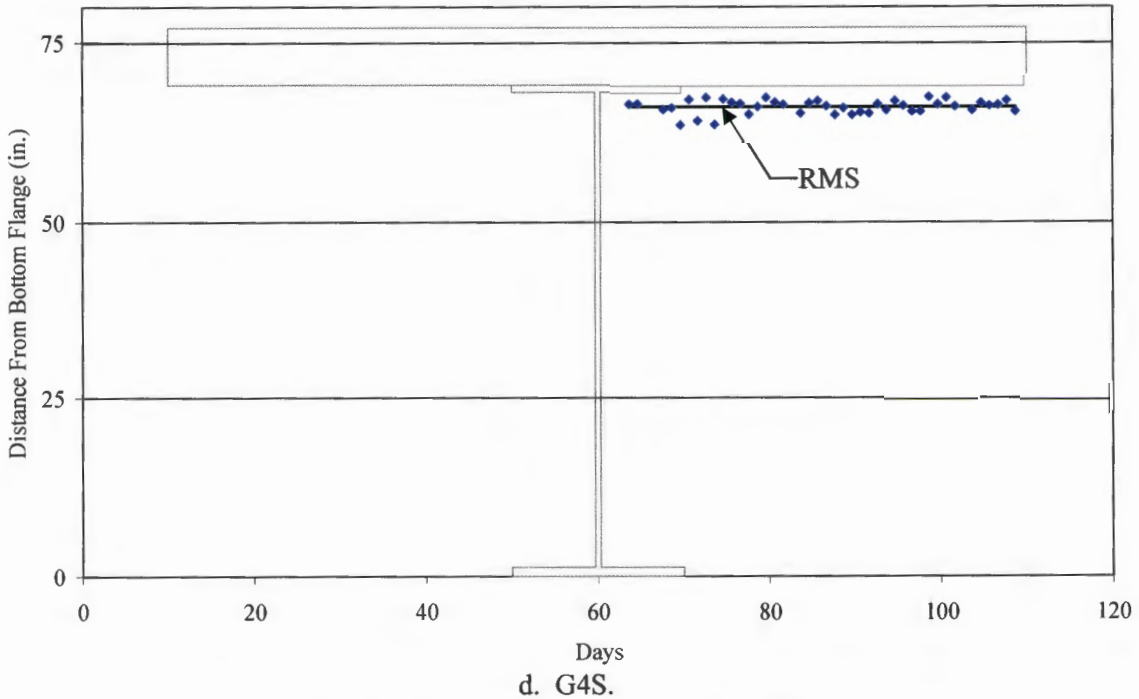

d. G4S.

Figure 5.30. Average NA location per day over time (Continued).

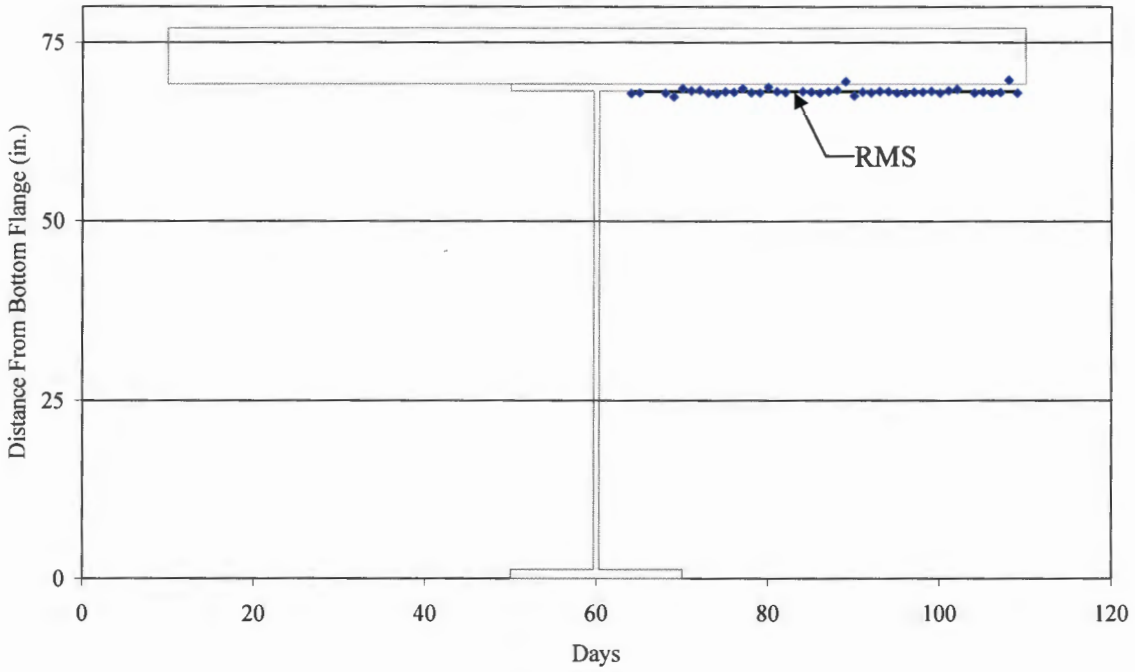

e. G5S.

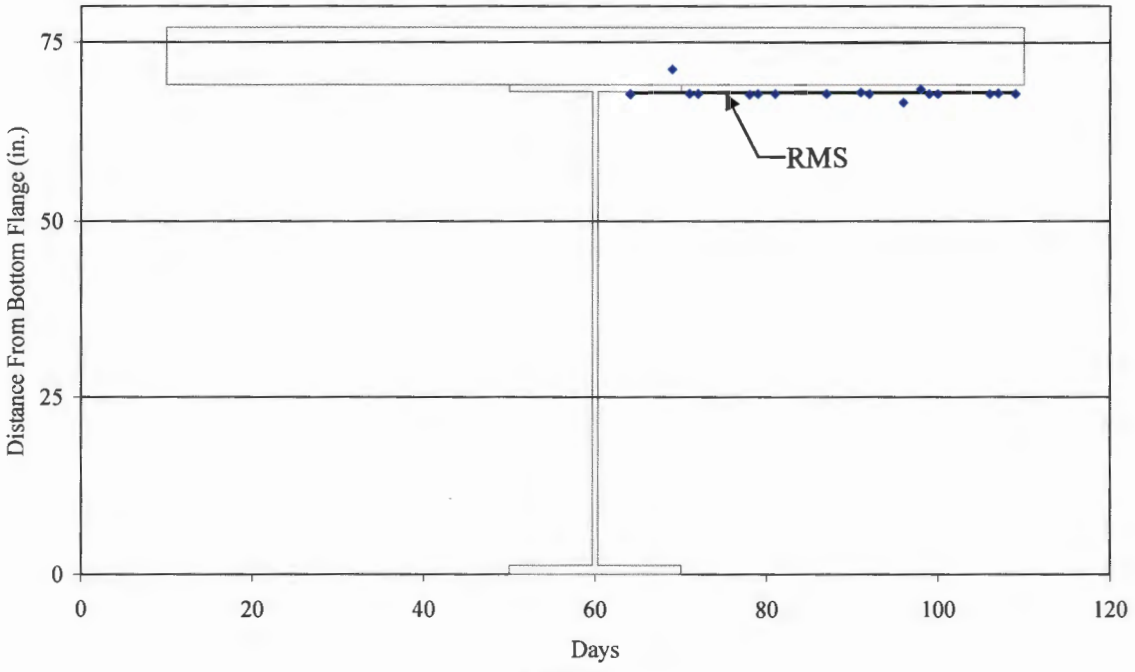

f. G6S.

Figure 5.30. Average NA location per day over time (Continued).

A summary of the long term and controlled load test NA RMS data for each girder is shown in Table 5.5 and Fig. 5.31. The long term and load test RMS data are close for each girder except Girder 3. This could be due to the difference in the geometry of the load truck compared to the ambient traffic (Girder 3 may be affected by this more than the other girders for reasons discussed subsequently). Comparisons can be made between transversely symmetric girders (although the symmetrical indices are not in the same span in most cases). Girders 3 and 4 show the largest difference of the symmetric girders as one would expect from the previous discussion. The difference in Girders 3 and 4 could be due to the stiffness difference (due to differing cross-sectional properties and boundary conditions) between the North and South spans. Since Girders 3 and 4 have the lowest stiffness (Girders 1, 2, 5, and 6 have the concrete barriers and sidewalks above them), the differences in the stiffness resulting from different cross-sections of the North and South girders would affect the NA location on Girders 3 and 4 more than Girders 1, 2, 5, and 6. Table 5.6 compares the inertia (which is related to the stiffness) of the composite sections and theoretical NA location at the North and South midspan of Girders 3 and 4 for several different assumed f'_c values (since concrete continues to gain strength after the specified 28 days, the actual f'_c is unknown). The NA is about 1 in. higher in the South span than the North span for each calculation. Table 5.6 implies that the different cross-section between the North and South midspan is most likely not the main factor in the difference between the NA location for Girders 3 and 4.

Table 5.5. NA RMS data from long term ambient traffic and Controlled Load Test.

	Girder1 (G1N/G1S)	Girder 2 (G2N)	Girder 3 (G3N)	Girder 4 (G4S)	Girder 5 (G5S)	Girder 6 (G6S)
Long Term RMS	68.61/67.97	68.58	60.16	66.31	68.12	68.09
Load Test RMS	68.19/67.98	68.01	62.33	66.75	67.99	68.37

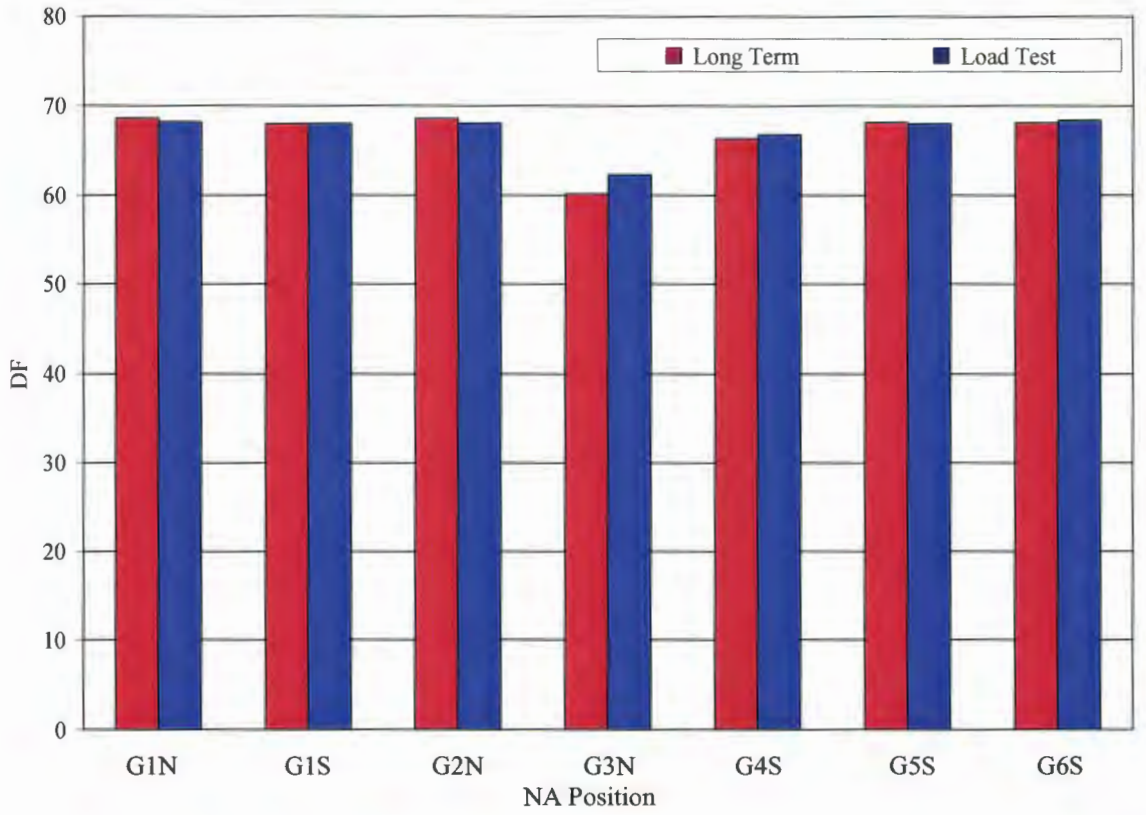

Figure 5.31. NA RMS data from long term ambient traffic and Controlled Load Test.

Table 5.6. Girders 3 and 4 theoretical composite I and NA location at the North and South midspans.

	North Midspan		South Midspan	
Assumed f'c of deck	Composite I	NA Location	Composite I	NA Location
5 ksi	134,152 in.^{4}	57.81 in.	117,040 in.^{4}	58.90 in.
7 ksi	138,819 in.^{4}	59.36 in.	120,955 in.^{4}	60.38 in.
9 ksi	144,076 in.^{4}	61.09 in.	125,326 in.^{4}	62.03 in.

After observing the controlled load test and long-term ambient data, an argument could be made that the threshold for the DPP to calculate the neutral axis (25 $\mu\varepsilon$ on the bottom flange) is too low since most of the data are concentrated near the top flange. This would cause smaller traffic events, which occur more frequently than larger events and are not as significant in terms of potentional damage or deterioration of the bridge when compared to larger events, to skew the results of the NA data.

5.2.3.3 End Restraint Ratio (ER)

The ER presented subsequently correlate the ratio of the midspan bottom flange strain to the abutment bottom flange strain (on the same girder) as a vehicle crosses the bridge. The ratio is intended to be used as a qualitative measure of changes in the longitudinal stiffness characteristics of the girders over time. It is important to note that the results from Girder 1 are dependant on the bottom flange abutment sensor on Girder 1, which is the sensor that was found to be unreliable in short-term loading conditions. Therefore, the Girder 1 ER is not shown for the Controlled Load Tests.

ER from Controlled Load Tests – Perhaps the most significant source of information from the ER is given from Run 2 for Girders 2 and 3 (see Fig. 5.32). As shown in these figures, the strain magnitude at the midspan increases more rapidly than at the abutment as the vehicle approaches the midspan. Figure 5.33 shows the Girder 2 ER for Run 6, to illustrate a typical plot for a girder far away from the applied load. Note that the ER is approximately 50% less than the ER close to the applied load and also a significantly different shape. The plots shown and the results noted are typical for all data from the controlled load test.

ER Time History from Ambient Traffic - The average daily ER for the girders which were instrumented to calculate the ER (Girder 1, 2, and 3) over time are presented in this section. The ER is plotted with both a linear trend line and the long term RMS. There is a slight decreasing trend over time for all three girders. This trend could be caused by events similar to those that are listed for the change of the DF over time. The ER data for Girder 1 is "shifted" significantly after about 60 days unlike the gradual change in Girders 2 and 3. The Girder 1 bottom flange sensor at the abutment started to perform unusually and is thought to be performing unreliably under both live and long term temperature loads (as was discussed previously). The time at which the sensor is thought to have begun performing unreliably is shown on the plot. The RMS of the long term ER data was found for each girder, which is also shown in Table 5.7 and in Fig. 5.34. By definition, the RMS is a positive number, but the vast majority of the ER data are negative. Therefore, for plotting convenience a negative value is assigned to the RMS.

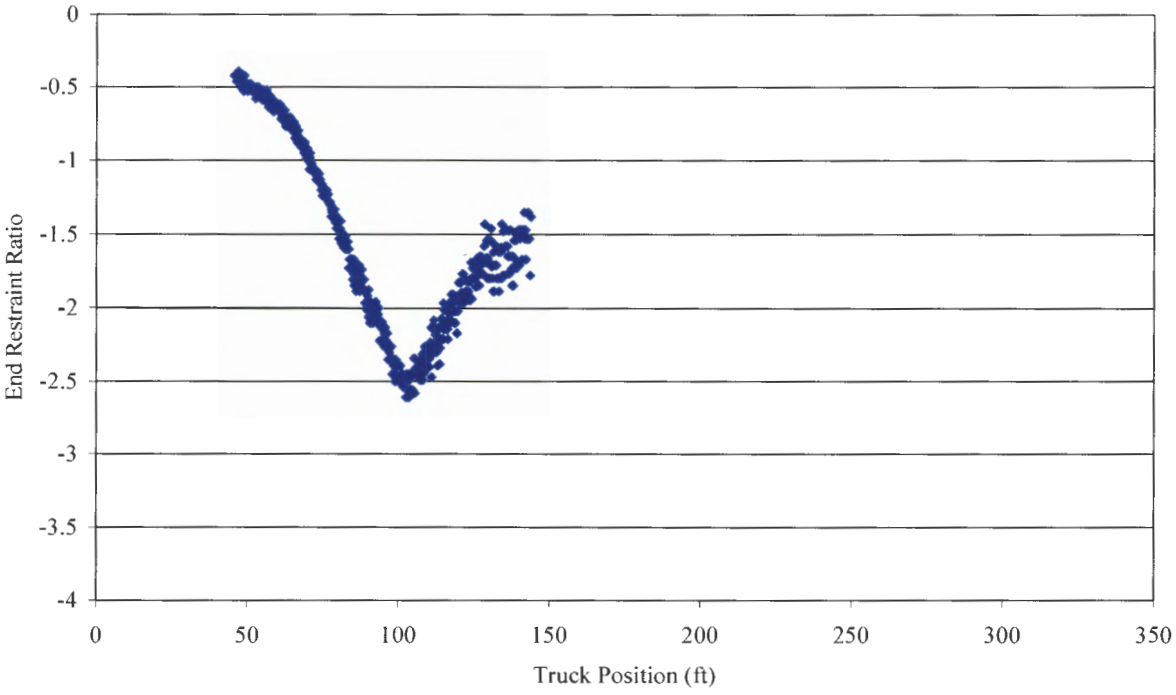

a. Girder 2.

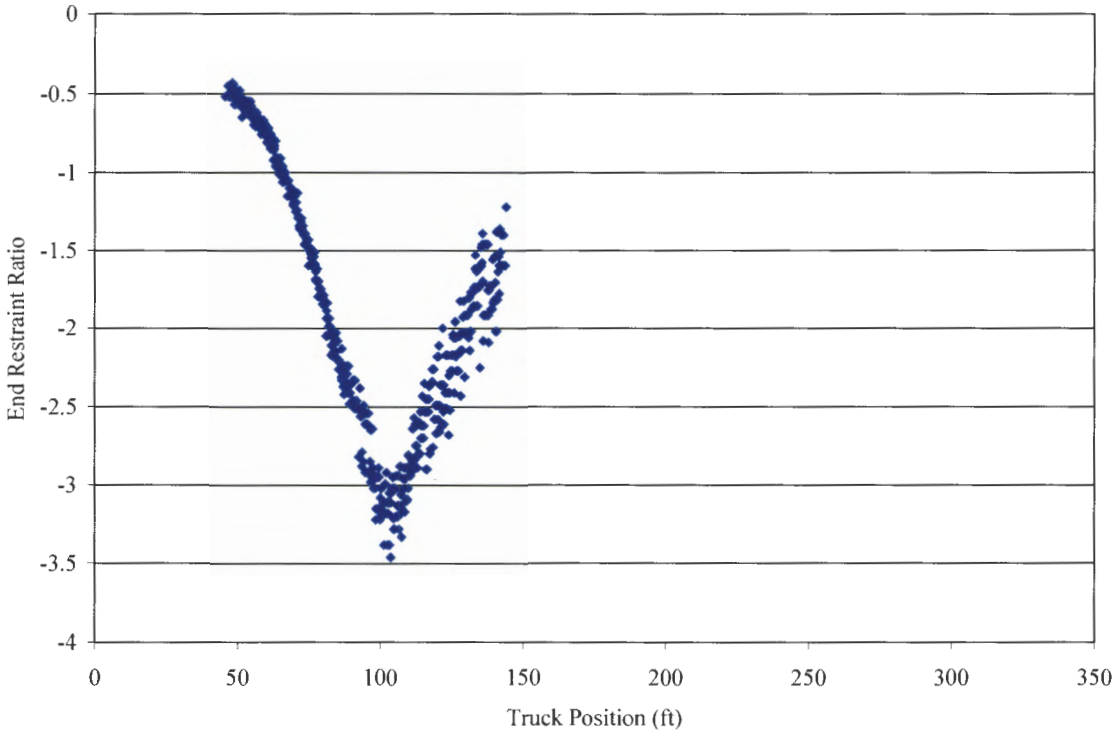

b. Girder 3.

Figure 5.32. ER from the Controlled Load Test Run 2.

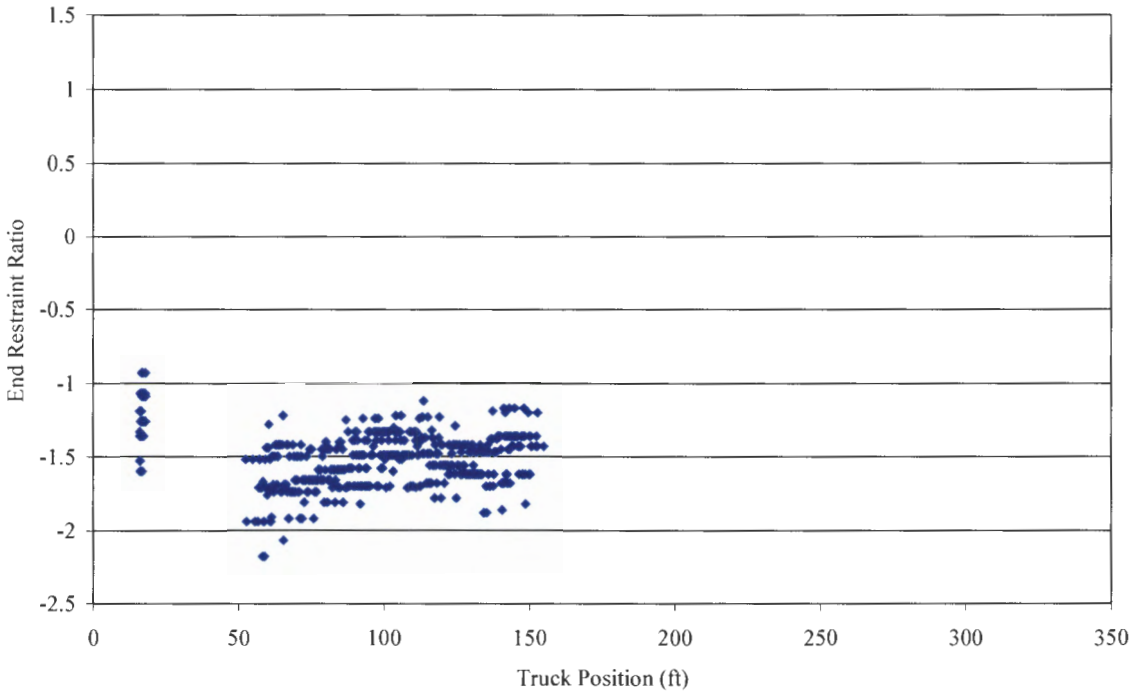

Figure 5.33. ER for Girder 2 from the controlled load test Run 6.

Table 5.7. Long term ER - negative RMS values.

	Girder 1	Girder 2	Girder 3
RMS	-2.31	-2.01	-2.68

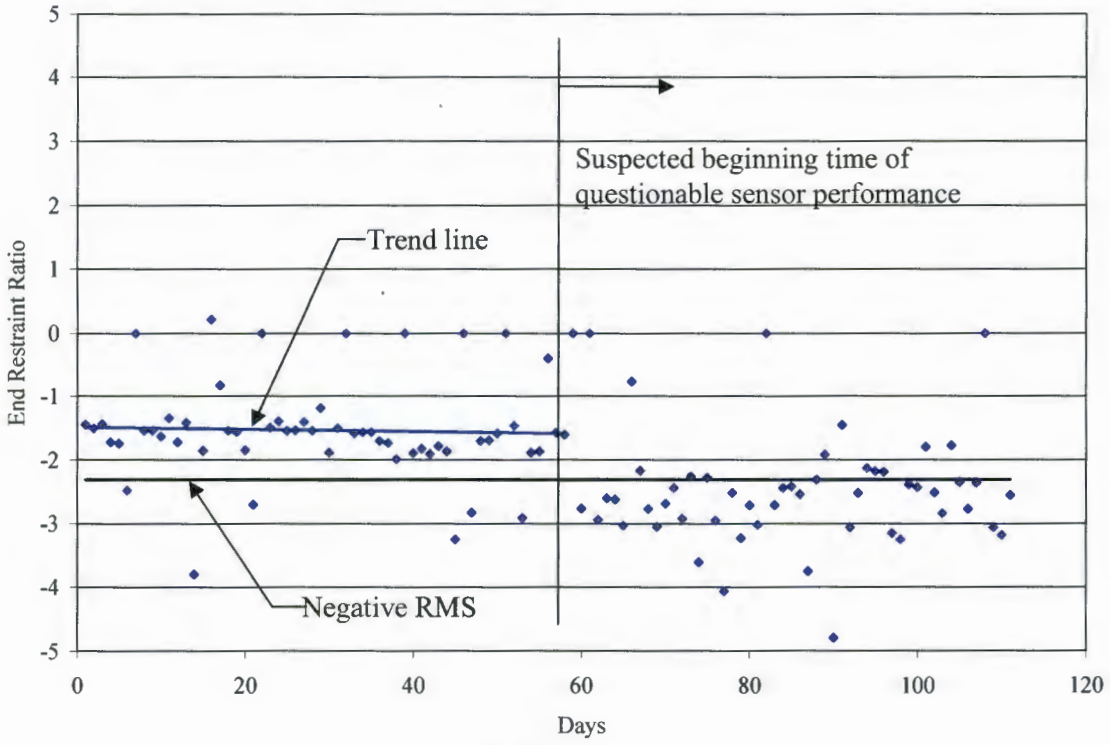

a. Girder 1.

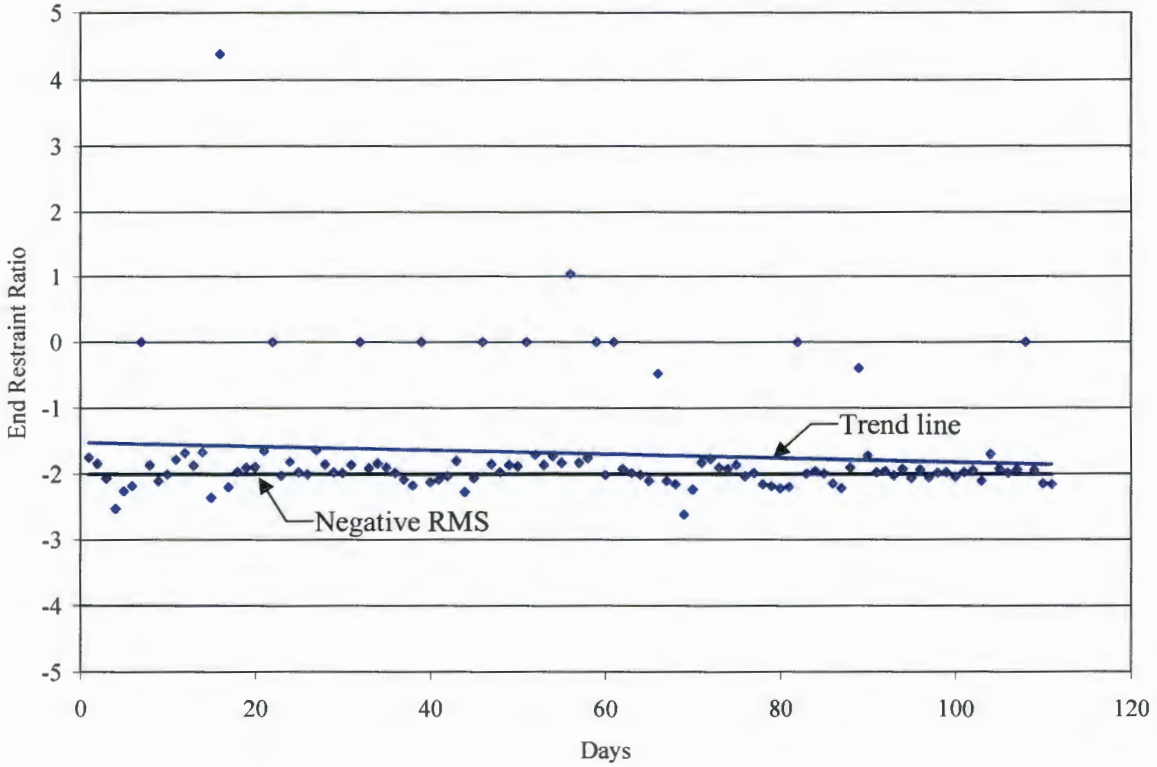

b. Girder 2.

Figure 5.34. Average ER per day over time.

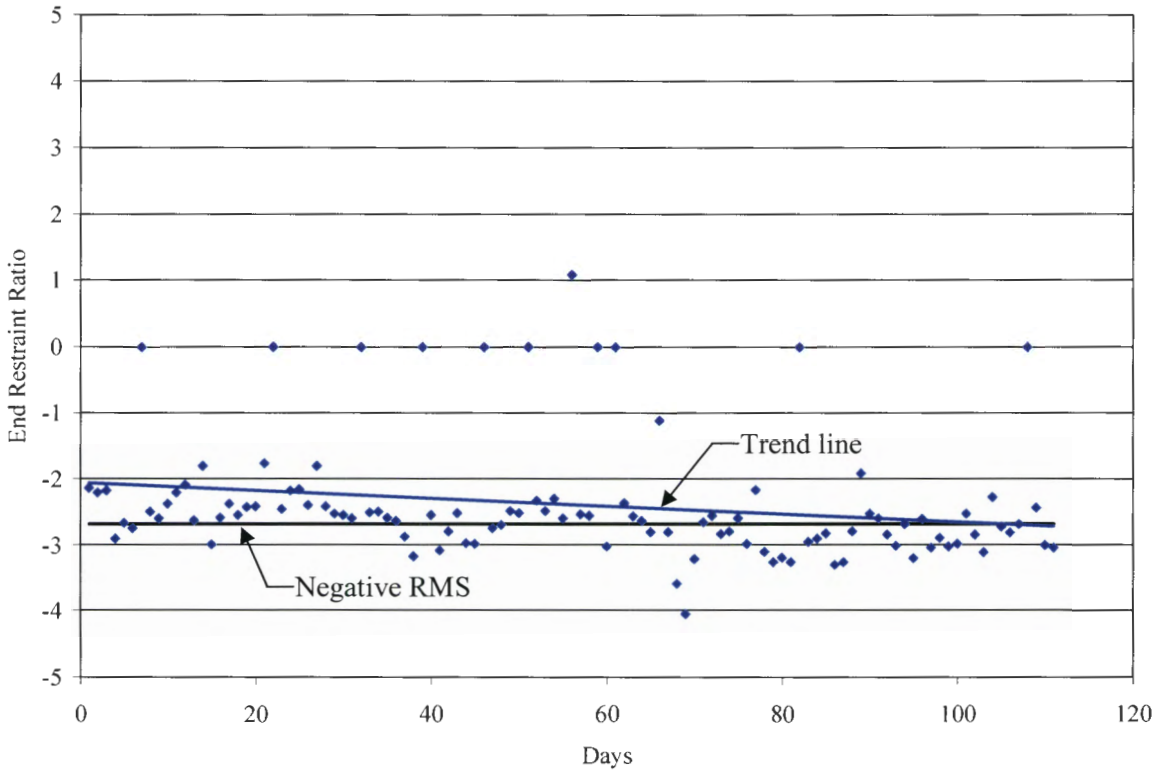

c. Girder 3.

Figure 5.34. Average ER per day over time (Continued).

As stated before, with the limited amount of data collected at this time, the trend lines shown for the long term data may not adequately represent the trends in the data. The RMS data provide a better basis than the trend line to monitor the changes of the bridge indices over time.

5.2.4 Strain Cycle Counting

Strain cycle counting using the rainflow counting method is used to quantify behavior from ambient traffic in two ways: 1) to monitor the number of strain cycles due to individual ambient traffic events at different locations on the bridge, and 2) to approximate the number of vehicles that use the bridge on a daily basis.

5.2.4.1 Ambient Traffic Event Strain Cycles

The results from the rainflow counting process are shown subsequently. The sensors are grouped by their location on the bridge. Data are presented for 110 days of monitoring for the North midspan sensors, the South midspan sensors were installed later and thus the results of the cycle counting from the South are only for 35 days. The term "bin strain" on the figures refers to the average of the bin range (the bin range is 10 $\mu\varepsilon$). For example, a 15 $\mu\varepsilon$ "bin strain" would contain strain cycles ranging from 10 to 20 $\mu\varepsilon$.

Figure 5.35 shows the distribution of cycles for the North midspan bottom flange sensors. For all bin sizes except 25 $\mu\varepsilon$, Girders 1 and 6 typically record the least number of cycles, followed by Girders 2 and 5, and Girders 3 and 4 report the most. This is as would be expected due to the proximity of these girders to the live loads. Possible reasons for the difference in the 25 $\mu\varepsilon$ bin include Girders 1, 2, 5, and 6 have cycles recorded in the 25 $\mu\varepsilon$ bin that were recorded for Girders 3 and 4 in the 35 $\mu\varepsilon$ bin (since Girders 1, 2, 5, and 6 are loaded less than Girders 3 and 4 the cycles from a particular event may not appear in the same bin for each girder), and the size of the vehicles which use the bridge may not be a normal distribution (i.e., there are small vehicles which would register strain in the 15 $\mu\varepsilon$ bin and larger vehicles which would register strain in the 35 $\mu\varepsilon$ bin, but no medium sized vehicles which register in the 25 $\mu\varepsilon$ bin). For the 15 $\mu\varepsilon$ bin, Girder 3 shows significantly more cycles than Girder 4, suggesting more Southbound traffic than Northbound. With the exception of the first bin, the sensors which are transversely symmetric on the bridge to each other have nearly the same number of cycles.

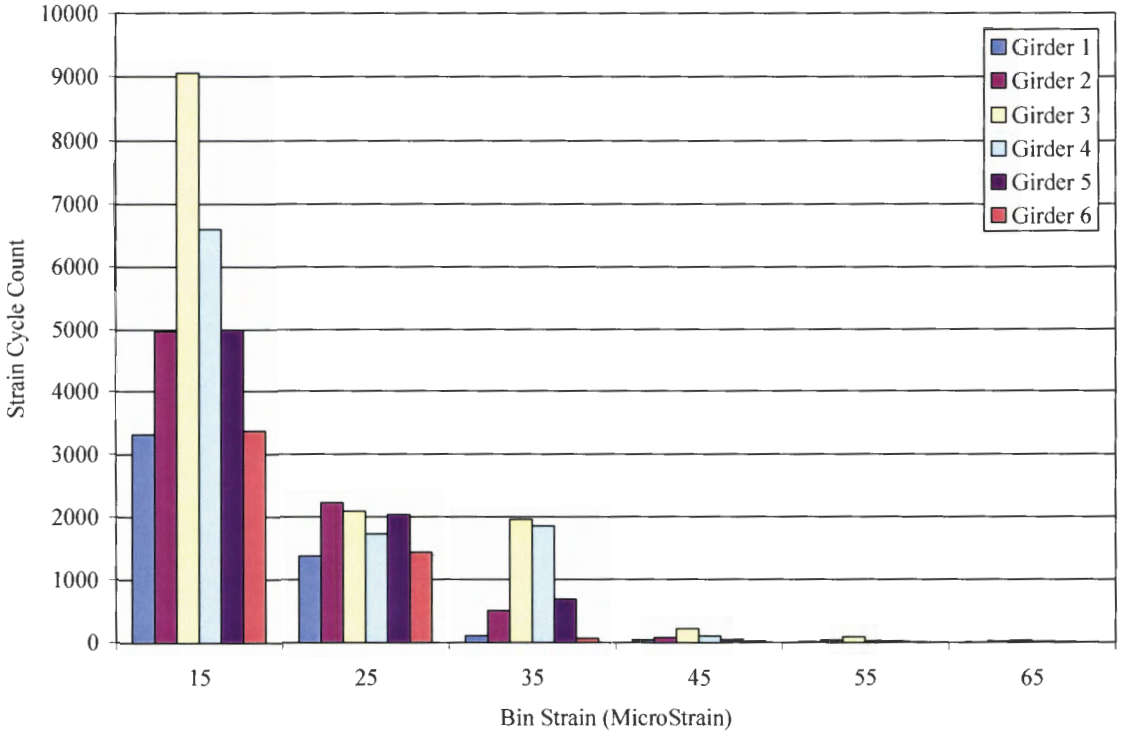

Figure 5.35. Rainflow counting results from bottom flange sensors at the North midspan.

Figure 5.36 shows North midspan top flange sensor data for Girders 1, 2, and 3. Note that the Girder 3 data are significantly larger than the other two girders. Note that Girder 3 also had significantly more 15 $\mu\varepsilon$ bin cycles at the bottom flange of the North midspan. Girders 1 and 2 have a smaller number of strain cycles due to the larger stiffness (due to the sidewalk and barriers rails near Girders 1 and 2). Girder 3 also likely has a larger number of strain cycles due to the localized effects of the vehicles passing directly over the top flange sensor locations (this has been previously shown).

The South midspan bottom flange sensors shown in Fig. 5.37 have a similar distribution to the North midspan bottom flange sensors (Fig. 5.35). Girder 3, once again, has a larger number of cycles indicating more Southbound traffic than Northbound. Note that the distribution of the 25 $\mu\varepsilon$ bin is similar to North midspan bottom flange sensors, indicating the trend was seen in both spans and is not an anomaly due to sensor or data processing issues. The South midspan top flange sensors (Fig. 5.38) have a similar distribution to the North midspan sensors in which Girder 4 has more cycles than Girders 1, 5, and 6.

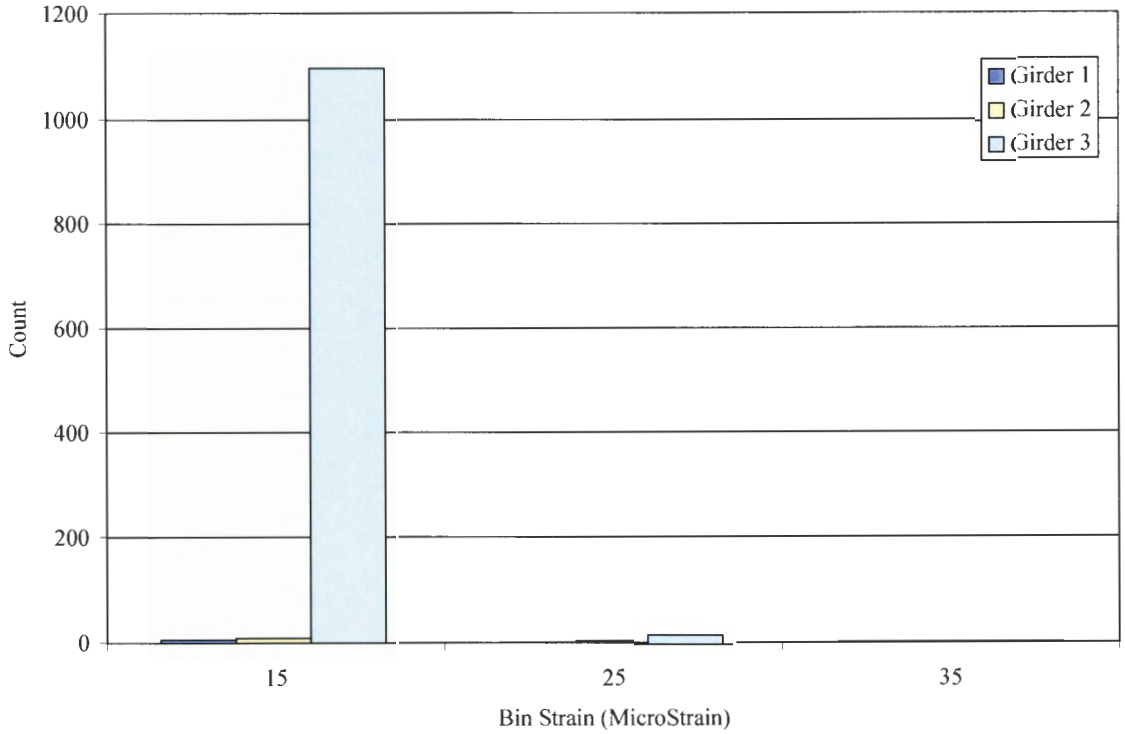

Figure 5.36. Rainflow counting results from top flange sensors at the North midspan.

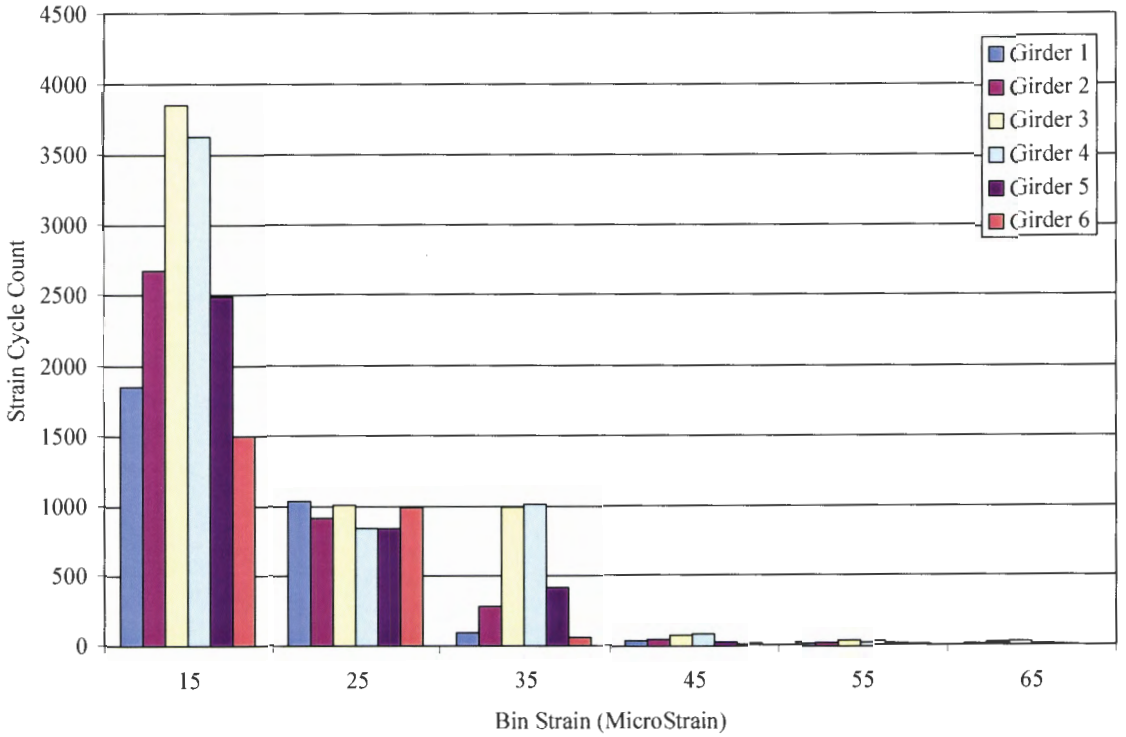

Figure 5.37. Rainflow counting results from bottom flange sensors at the South midspan.

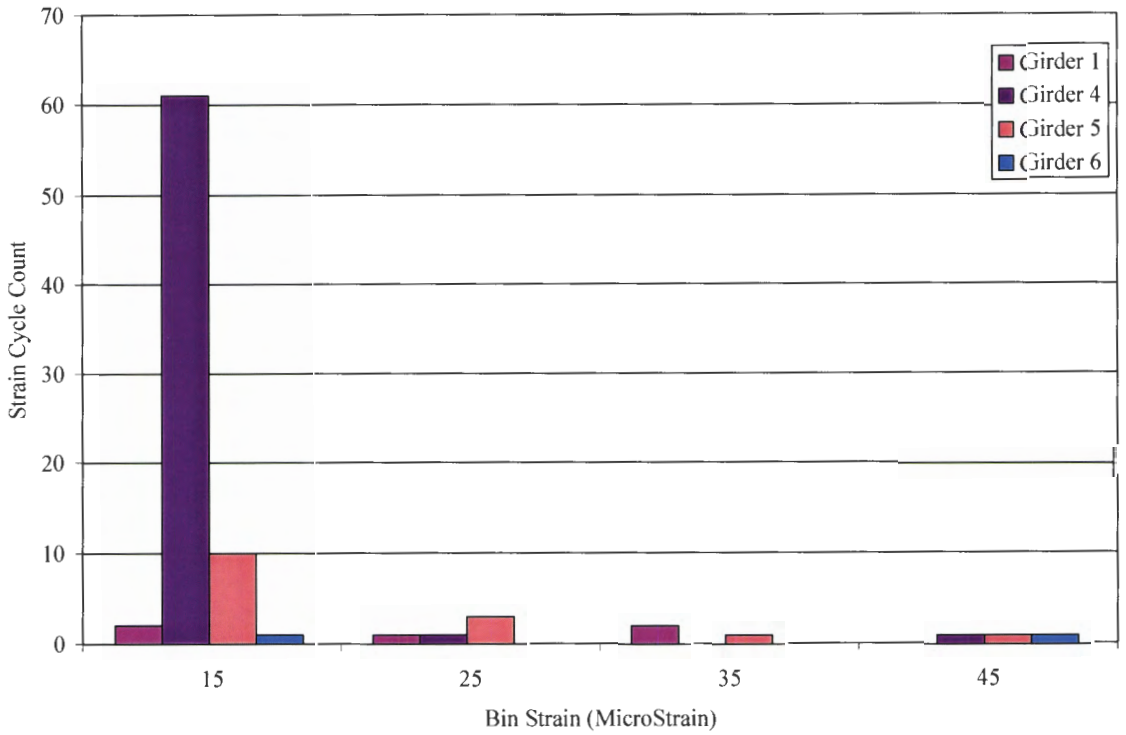

Figure 5.38. Rainflow counting results from top flange sensors at the South midspan.

The number of cycles for the abutment sensors in Fig. 5.39 is reasonable since the bottom flange strain at the abutment was shown to have smaller strain ranges than the North midspan bottom flange. The smaller strain ranges would lead to less strain cycles meeting the minimum bin size requirement. Girder 3 (bottom flange) has by far the largest number of cycles. Girder 1 is not shown due to its irregular performance for short-term events.

The rainflow counting of the weld stress concentrations, shown in Fig. 5.40, shows the flange splice on Girder 1 has the most cycles followed by the web splice on Girder 1, then the flange splice on Girder 2 and the fewest cycles are on the web splice on Girder 2. The flange splice was shown to have slightly larger strains than the web splice as was shown in Fig. 5.17. The splices in Girder 1 showed less strain than Girder 2 in the events presented previously (the strains from Girder 1 were so small they were not shown on Fig. 5.10a and 5.16a). Therefore, some of the data presented in Fig. 5.40 are supported by the strain plots shown previously (flange splice higher cycles than plate splice) but other data are not (Girder 1 higher cycles than Girder 2).

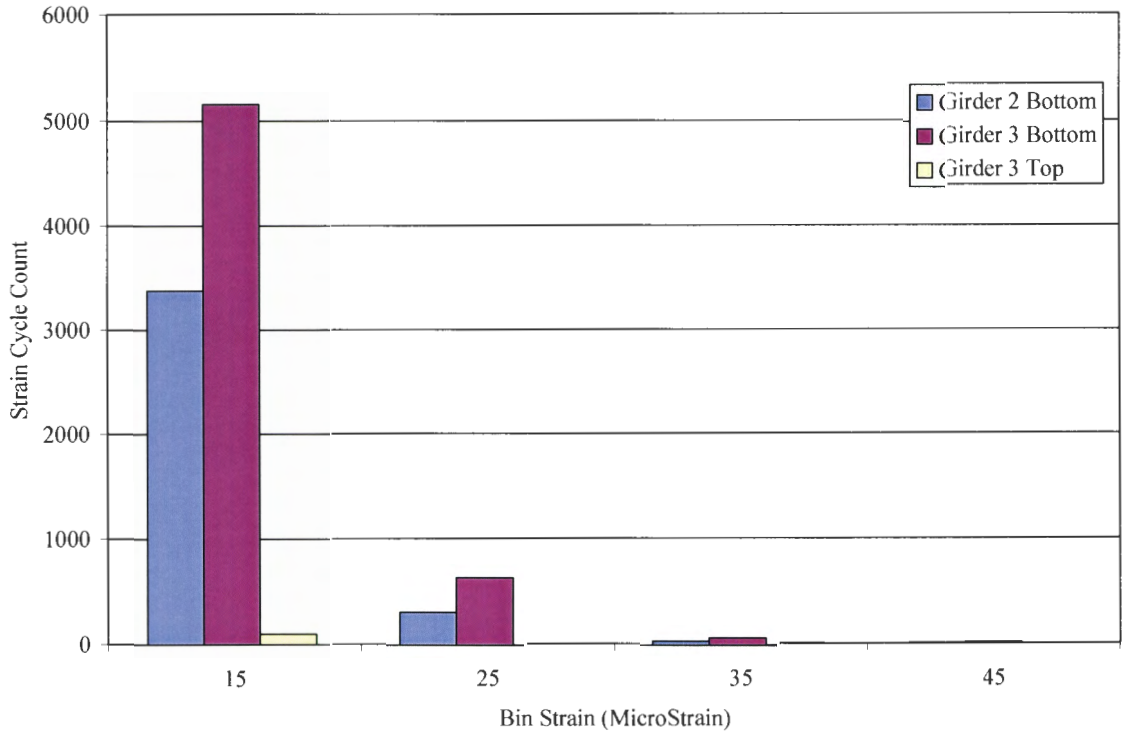

Figure 5.39. Rainflow counting results from abutment sensors.

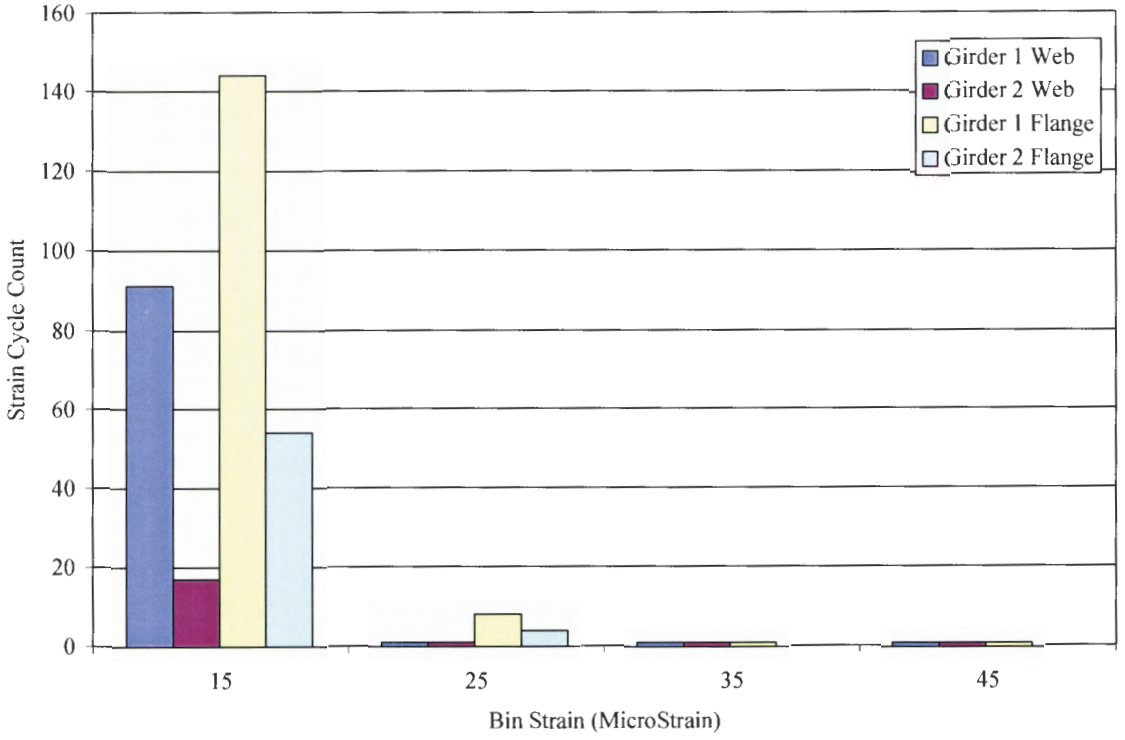

Figure 5.40. Rainflow counting results from weld splice stress concentration sensors.

Figure 5.41 shows the web gap region sensors. The Girder 2 flange tipping has more cycles than the Girder 2 web gap and the Girder 1 flange tipping and web gap. This information agrees with what was shown in the strain data plots (Fig. 5.10, 5.16, and 5.18). The web gap sensors on Girder 3 are not shown due to a lack of data due to sensor problems described previously.

The fatigue details which were monitored include the weld between the flange and the web (flange and web weld splice sensors and the web gap sensors). Also included is the weld between the transverse diaphragm stiffener and the flange (flange tipping sensor). The maximum recorded stress in the weld between the flange and web on the bridge is 1.3 ksi (assuming uniaxial state of stress and using Hooke's Law), which is less than the design stress of 2 ksi and the AASHTO allowable stress of 15 ksi. The AASHTO allowable stress in the weld between the flange and the stiffener is 21 ksi, which is well above the maximum stress recorded on the bridge (0.73 ksi); the calculated design stress was 12 ksi.

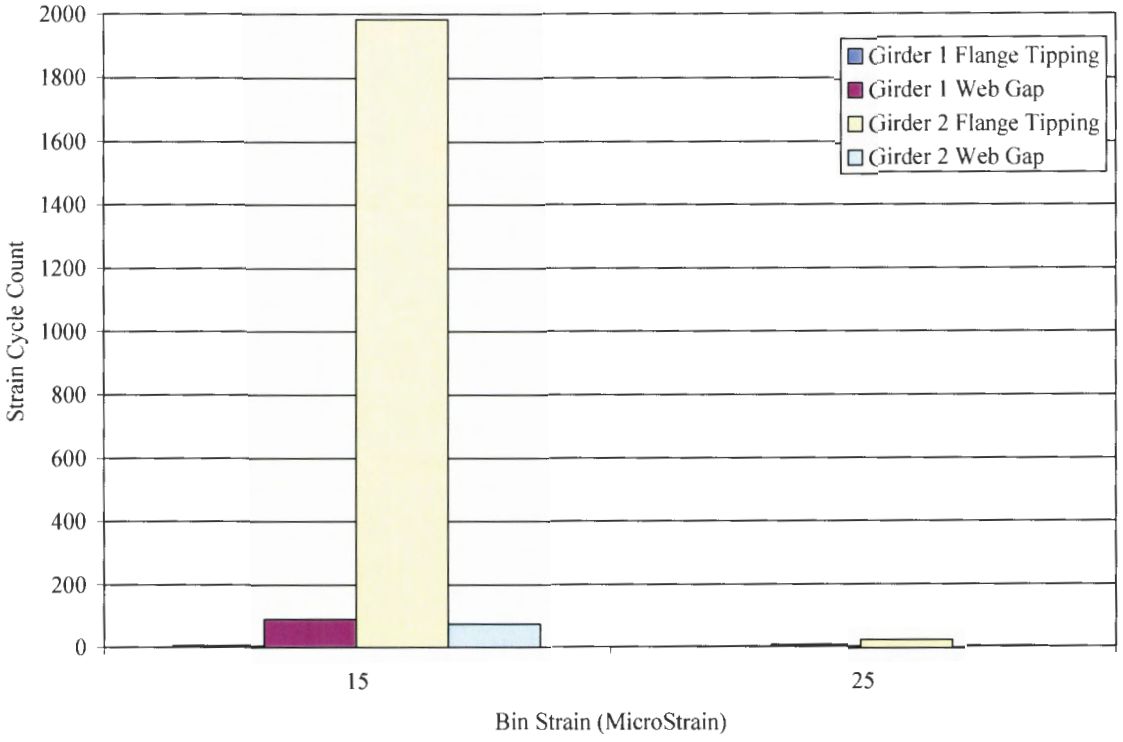

Figure 5.41. Rainflow counting results from web gap region sensors.

5.2.4.2 Traffic Monitoring

A sample of what can be observed relative to traffic engineering is shown in Figs. 5.42 and 5.43, which show the bottom flange strain cycles at the South mid-span for the weeks of Jul. 26 to Aug. 1, 2004 and Sept. 9 to Sept. 15, 2004, respectively. It is interesting to note the increase in strain cycles in the fall relative to the summer. The traffic volume difference is most likely due to the close proximity of the bridge to a high school as well as a lower number of people traveling to and from work in the summer months due to vacations. The dramatic drop in number of events on the weekends compared to weekdays is also noticeable. Although this information in this form is not directly applicable to the structural analysis of the bridge, it could provide insight on changes of the bridge performance related to changes in traffic patterns. Being able to extract traffic pattern information from the same data set as structural performance provides opportunities to further the understanding of how traffic patterns affect the behavior of a bridge over time.

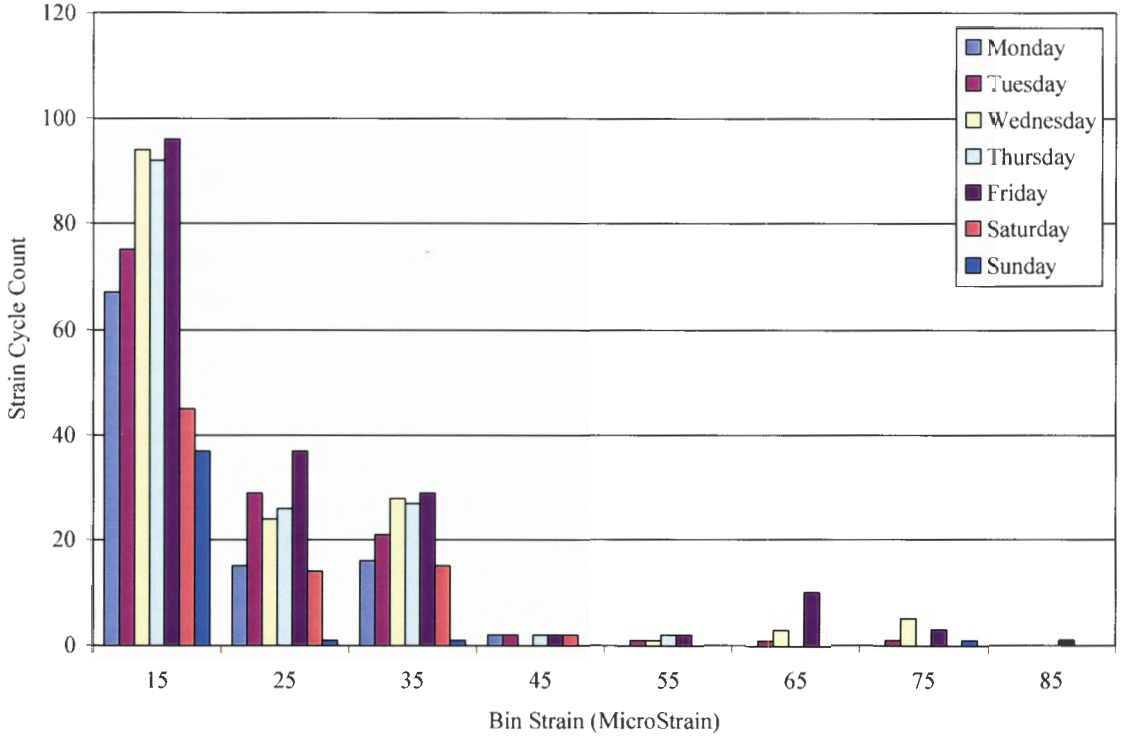

Figure 5.42. Strain cycles from July 26 to August 1, 2004 at the South midspan bottom flange for Girder 3.

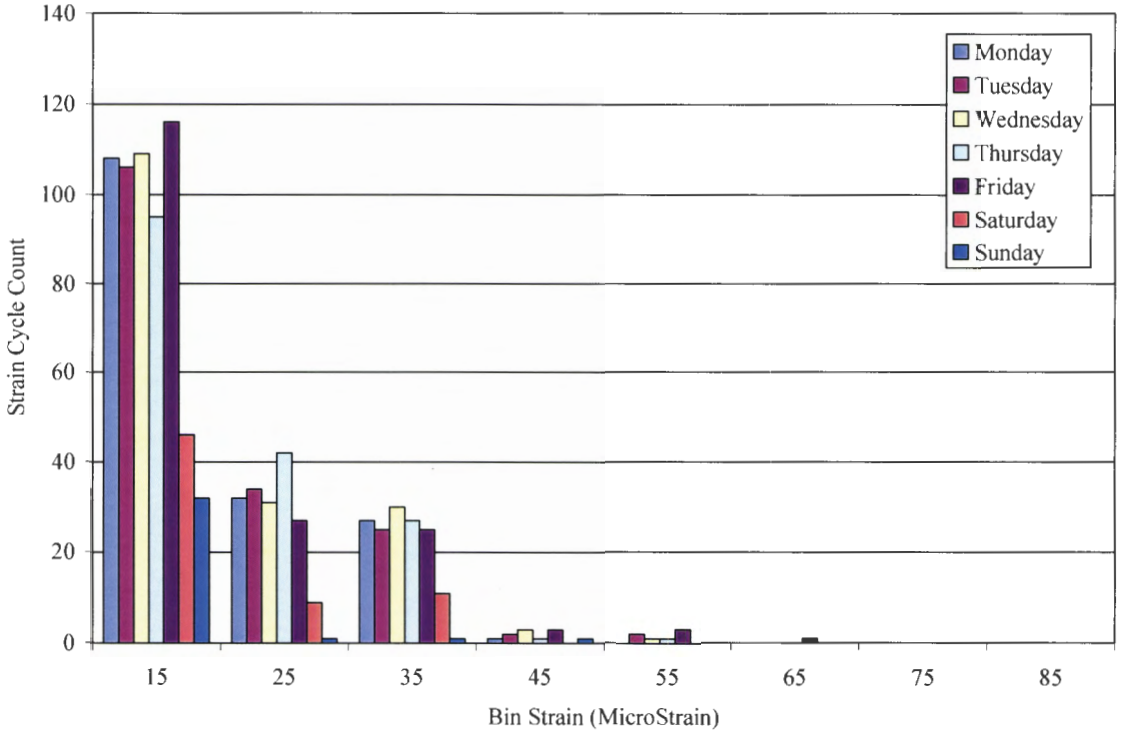

Figure 5.43. Strain cycles from September 9 to September 15, 2004 at the South midspan bottom flange for Girder 3.

6. CONCLUSIONS AND RECOMMENDATIONS

6.1 Conclusion

The intent of this project was to investigate the use and performance of High Performance Steel (HPS) in bridge applications using a Structural Health Monitoring (SHM) system. The objectives of the E. 12th St. Bridge SHM project were stated in Chapter 1. The objectives are outlined in the following summary discussion of the project.

6.1.1 Design and Construction Documentation of the E. 12th St. Bridge

As Iowa's first HPS Bridge, the E. 12th St. bridge allowed the Iowa DOT examine the relatively new material in terms of design, fabrication, and construction. The design of the bridge utilized the material strength, toughness, and fatigue characteristics of HPS. The construction documentation of the subject bridge was provided in Chapter 3. One challenging aspect of the bridge construction was coordination with traffic on the major roadway (I-235) over which it spans. This limited the times when certain construction activities, which mandated lane closures of I-235, could be performed.

6.1.2 E. 12th St. Bridge Structural Health Monitoring System

The SHM system that was designed for and installed on the E. 12th St. Bridge generally met the objectives established for the project. This project provided an opportunity to evaluate and assess a remote, continuous, fiber optic SHM system. The following are major overall accomplishments:

- Given the location of the DASS equipment and the lack of accessibility of the equipment due to traffic, methods were developed to control the equipment from remote locations.
- Readily available technology was used and met the expectations for the objectives of the project to be achieved.
- The monitoring system successfully acquired data continuously.
- A SHM data processing system was developed that provides the bridge performance in a format that is consistent with design and evaluation parameters typically used by bridge engineering practitioners.
- While the website developed has been a useful part of the SHM system, there have been continued problems. User interaction with the website has, on occasion, disrupted with the data collection.

6.1.2.1 Sensors

Strain readings from 23 of the 36 Fiber Bragg Grating (FBG) sensors used on the bridge were validated with respect to Bridge Diagnostics, Inc. (BDI) strain transducers during the Controlled Load

Test. Twenty-two of the 23 sensors proved to be accurate under live loading. Two types of FBG sensors were used, 1) Bare FBG and 2) Surface-Mountable Sensors (Bare FBG embedded in FRP). Several problems were encountered with the long-term strain readings of several Bare FBG. These problems were:

- Optical loss
- Interference between sensors
- Large strain range of sensors
- Large compressive drop
- Backscatter

The Surface-Mountable Sensors performed well under long term and short term loading conditions.

6.1.2.2 Data Processing

To adequately deal with the vast amount of data that were collected, check the integrity of the data, extract the reliable data (portions of the data were unreliable due to the problems previously discussed), and provide useful information, several programs were developed. These programs included the Data Correction Program (DCP), Data Sorter Program (DSP), and the Data Processing Program (DPP). Each of these programs must be started by a user who must load the data into the programs. This process, although simple and redundant, does require time and the user to be actively involved in data processing. Since the programs are performed in a post-processing mode, rather than in real-time, the results from the processing are not readily available to the research team.

6.1.3 Monitoring Performance Changes Using Bridge Indices

The bridge performance indices mentioned previously are calculated from the processed live load strain data. Monitoring changes in these indices may provide information regarding the health and performance of the bridge over time. The data can provide insight into the deterioration rates, possible reasons for deterioration, the extent of deterioration, and how the performance is affected. The following observations were based on the bridge indices calculated from ambient traffic and the Controlled Load Test:

- Distribution Factor (DF)
  - The South midspan load distribution is better than the distribution in the North midspan.
  - The typical average DF per day for an interior girder is between 0.20 and 0.25; the AASHTO single lane design DF is 0.62.
  - Monitoring the DF from ambient traffic over time may provide a useful tool to bridge engineers, since the data collected have shown slight changes.

- Neutral Axis (NA)
  - The theoretical NA location for Girder 4 at the South midspan differed significantly from the experimental NA location.
  - The theoretical NA location for Girder 3 at the North midspan matched the experimental NA location well.
  - There were noticeable differences between the NA location of Girder 3 at the North midspan and Girder 4 at the South midspan (laterally symmetrical girders).
  - As the trends of the NA are examined over time, conclusions about the performance of the bridge should be apparent since the NA has been fairly consistent over time at each location the NA is calculated.
- End Restraint (ER)
  - The data collected has provided a baseline of bridge performance.
  - The value of the ER is still undetermined, as more data are collected the significance will be evaluated.

In addition to monitoring each of the indices individually, examining them together over time may provide insight into the bridge performance since the indices are based on interrelated properties of the bridge.

6.1.4 Fatigue Sensitive Detail Performance

The strain plots of the ambient traffic and load tests show very low levels of strain in the localized fatigue details. This is verified by the magnitudes and number of stress cycles in the Cycle Counting section. The largest stress in the weld between the flange and web due to a live load event is 1.3 ksi; this is less than the design stress (2 ksi) and significantly less than the AASHTO allowable stress (15 ksi). The stress recorded between the flange and the stiffener (0.73 ksi) is considerably less than the design stress (12 ksi) and the AASHTO allowable stress (21 ksi).

6.2 Recommendations

6.2.1 Sensors

As stated in the Sensor Performance section, several problems were encountered with the fiber optic sensors. For future work with continuous health monitoring and fiber optic sensing the research team recommends the following:

- Use Surface Mountable Sensors
- Use at least a 3mm jacket on the cable
- Use mechanical splices to splice adjacent fiber strands
- If bare FBGs are used, test different types of epoxy for best adhesion
- Separate the wavelengths of adjacent sensors by at least 5 nm

- Cover sensors and splices so they would be accessible for visual inspection (only necessary if access to sensors will be available after installation. In this project future access is unobtainable)

After completion of this project, the research team recommends that continuous monitoring be continued and a revised plan for instrumentation location has been developed. This plan involves replacing some of the Bare FBGs with Surface Mountable Sensors, removing some sensors completely, and supplementing the existing sensors with more Surface Mountable Sensors. The plan calls for placing top and bottom flange sensors on every girder at the North midspan, installing bottom flange sensors on Girders 2, 3, 4, and 5 at the North abutment, monitoring the flange and web plate splice weld on Girder 2, installing sensors in the web gap near the pier on Girders 1 and 2, installing bottom flange sensors on Girders 3 and 4 near the pier in the negative moment region, and leaving the Surface Mountable sensors located at the South midspan. This will allow the bridge indices to be further developed and studied, while eliminating some of the fatigue detail sensors due to low strain levels. This instrumentation scheme should improve the research team's ability to monitor the use of High Performance Steel on the E. 12th St. Bridge using a remote, continuous, fiber optic structural health monitoring system.

6.2.2 Data Processing

To simplify user intervention and repetitive involvement required in processing the data, it is recommended that a system which combines the programs used for data processing be developed. Along with that, it may be beneficial to automate the processing and perform it in real time. Performing the data processing in real time would require a change in the algorithms currently used. A data collection and processing system that requires little user intervention but still provides the beneficial information of the current system would enhance the capabilities of the current system. Such a system that requires low levels of involvement in the collection and processing of the data would be advantageous in expanding the use of SHM to more bridges.

7. REFERENCES

1. Bethlehem Lukens Plate. Bethlehem Lukens Plate High Performance Steels for Bridges: HPS-70W. http://www.bethsteel.com/customers/pdfs/bridges.pdf, January, 2002 (last accessed April, 2005).
2. Federal Highway Administration (FHWA). High Performance Steel Designers' Guide. http://www.fhwa.dot.gov/download/hpsguide.pdf, April 2002 (last accessed April, 2005).
3. Wilson, A. D. Production of High Performance Steels for U.S.A. Bridges. http://www.nabro.unl.edu/articles/20002012/download/wilson.pdf (last accessed April, 2005).
4. American Society for Testing and Materials (ASTM) International. *Annual Book of ASTM Standards 2002,* West Conshohocken, PA, 2002.
5. Texas Measurements, Inc. Strain Gage Series List. http://straingage.com/strain_gage/list/index.php (last accessed April, 2005).
6. Roctest. Vibrating-Wire Strain Gage. http://www.roctest.com/modules/AxialRealisation/img_repository/files/documents/C-110.pdf (last accessed April, 2005).
7. Casciati, F., L. Faravelli, F. Borghetti, and A. Fornasari. Future trends in infrastructure monitoring. *Proceedings of the First International Conference on Structural Health Monitoring and Intelligent Infrastructure,* Tokyo, Japan, November 2003, pp. 997-1002.
8. Trans-Tek, Inc. Linear Variable Differential Transformer. http://www.transtekinc.com/lvdt.htm (last accessed April, 2005).
9. PCB Piezotronics, Inc. Products. http://www.pcb.com/products/ (last accessed April, 2005).
10. Ansari, F. Fiber optic health monitoring of civil structures. *Proceedings of the First International Conference on Structural Health Monitoring and Intelligent Infrastructure,* Tokyo, Japan, November 2003, pp. 19-30.
11. Glisic, B., D. Inaudi, S. Vurpillot, E. Bu, and C.-J. Chen. Piles monitoring using topologies of long-gage fiber optic sensors. *Proceedings of the First International Conference on Structural Health Monitoring and Intelligent Infrastructure,* Tokyo, Japan, November 2003, pp. 291-298.
12. Inaudi, D. State of the art in fiber optic sensing technology and EU structural health monitoring projects. *Proceedings of the First International Conference on Structural Health Monitoring and Intelligent Infrastructure,* Tokyo, Japan, November 2003, pp. 191-198.
13. Liu, D.H., W.L. Jin, E.Y. Zhang, and J.W. Shao. Applying Brillouin health monitoring network for civil engineering. *Proceedings of the First International Conference on Structural Health Monitoring and Intelligent Infrastructure,* Tokyo, Japan, November 2003, pp. 237-240.
14. Inaudi, D., and B. Glisic. Combining static and dynamic deformation monitoring with long-gage fiber optic sensors. *Proceedings of the Second International Conference on Bridge Maintenance, Safety, Management and Cost*, Kyoto, Japan, October 2004, pp. 543-544.
15. Todd, M.D., G.A. Johnson, and B.L. Althouse. A novel Bragg grating sensor interrogation system utilizing a scanning filter, a Mach-Zehner interferometer and a 3x3 coupler. *Measurement Science and Technology*, Vol. 12, No. 7, 2001, pp. 771-777.
16. Micron Optics. Si425. http://www.micronoptics.com/si425.htm (last accessed April, 2005).

17. Roctest. Products. http://www.roctest.com/index.php?module=CMS&id=73 (last accessed April, 2005).

18. Luna Innovations. Fiber Optic Systems at Luna Innovations. http://www.lunainnovations.com/products/systems.htm (last accessed April, 2005).

19. Blue Road Research. Blue Road Products. http://www.blueroadresearch.com/ (last accessed April, 2005).

20. Microsoft. What Is a Wired Network? http://www.microsoft.com/hardware/broadbandnetworking/10_concept_what_is_wired.mspx (last accessed April, 2005).

21. Indiana University Knowledge Base. What are some common networking terms? http://kb.indiana.edu/data/ahpn.html?cust=450662.53156.30 (last accessed April, 2005).

22. Center for the New Engineer. Asynchronous Transfer Mode (ATM) Tutorial. http://www.cne.gmu.edu/modules/atm/Texttut.html (last accessed April, 2005).

23. Froehlich, J. Internet Bandwidth Technologies. http://www.msdn.microsoft.com/archive/default.asp?url=/archive/en-us/dnarntpro00/html/wnp0095.asp (last accessed April, 2005).

24. University of Tennessee, Technology Consulting and Support. Overview of Wireless Technologies. http://oit.utk.edu/helpdesk/section/Wireless/38 (last accessed April, 2005).

25. Dummies.com. Storing Data with PHP – Flat File or Database? http://www.dummies.com/WileyCDA/DummiesArticle/id-2402.html (last accessed April, 2005).

26. Webopedia. Flat-file database. http://webopedia.internet.com/TERM/f/flat_file_database.html (last accessed April, 2005).

27. Webopedia. Database. http://webopedia.internet.com/TERM/d/database.html (last accessed April, 2005).

28. Kulcu, E., X. Qin, R.A. Barrish Jr., and A.E. Aktan. Information Technology and Data Management Issues for Health Monitoring of The Commodore Barry Bridge. *The International Society for Optical Engineering,* Vol. 3995, 2000, pp.98-111.

29. Seim, J., E. Udd, and W. Schulz. Health monitoring of an Oregon historical bridge with fiber grating strain sensors. *The International Society for Optical Engineering*, Vol. 3671, 1999, pp. 128-134.

30. Tennyson, R.C., A.A. Mufti, S. Rizkalla, G. Tadros, and B. Benmokrane. Structural health monitoring of innovative bridges in Canada with fiber optic sensors. Smart Materials and Structures, Vol. 10, No. 3, 2001, pp. 560-573.

31. Bannantine, J.A., J.J. Commer, and J.L. Handrock. *Fundamentals of Metal Fatigue Analysis.* Prentice Hall, Englewood Cliffs, N.J., 1990.

32. American Association of State Highway and Transportation Officials, Inc. (AASHTO). *Standard Specifications for Highway Bridges, Sixteenth Edition, 1996,* Washington D.C., 1996.

APPENDIX A. BRIDGE INDICES VERIFICATION AND SENSITIVITY STUDY

A.1 Distribution Factor (DF)

A.1.1 DF Calculation Verification

The distribution factor (DF) of a bridge (see Equation 1) is measure of the lateral distribution of a load between primary resisting elements. It the percent of the total load that a particular element resists (since the E. 12th St. Bridge has six girders, the equations presented herein represent a bridge with six girders)..

$$DF = \frac{L_n}{L_1 + L_2 + L_3 + L_4 + L_5 + L_6} \quad (1)$$

Where: L_n = Load from Girder of Interest
L_1 = Load from Girder 1
L_2 = Load from Girder 2
L_3 = Load from Girder 3
L_4 = Load from Girder 4
L_5 = Load from Girder 5
L_6 = Load from Girder 6

When gathering experimental data from a bridge, the load on each girder is not known. For bridges, the load can generally be directly related to the bending resistance. The resistance can be related to strain through basic mechanics (equations 2 and 3) resulting in equation 4. Note that this assumes plane sections remain plane and that the material is linear elastic. Equations 1 and 4 can be combined (modulus of elasticity is cancelled since it can be assumed to be constant for each girder with the section modulus substituted for I/c [equation 5]) resulting in equation 6. The terms used in equation 6 (hereafter also referred to as the exact equation) are terms which can usually be obtained when gathering experimental data from a bridge and measurement of the bridge elements.

$$\sigma = \frac{Mc}{I} \quad (2)$$

Where: σ = Stress
M = Moment
c = Distance from the neutral axis to the point of interest
I = Moment of inertia

$$\sigma = E\varepsilon \tag{3}$$

Where: E = Modulus of elasticity
ε = Strain

$$\varepsilon = \frac{Mc}{IE} \tag{4}$$

$$S = \frac{I}{c} \tag{5}$$

Where: S = Section modulus

$$DF = \frac{\varepsilon_n S_n}{\varepsilon_1 S_1 + \varepsilon_2 S_2 + \varepsilon_3 S_3 + \varepsilon_4 S_4 + \varepsilon_5 S_5 + \varepsilon_6 S_6} \tag{6}$$

Where: ε_n = Strain at girder of interest
S_n = Section modulus of girder of interest
ε_1 = Strain from Girder 1
S_1 = Section modulus of Girder 1
ε_2 = Strain from Girder 2
S_2 = Section modulus of Girder 2
ε_3 = Strain from Girder 3
S_3 = Section modulus of Girder 3
ε_4 = Strain from Girder 4
S_4 = Section modulus of Girder 4
ε_5 = Strain from Girder 5
S_5 = Section modulus of Girder 5
ε_6 = Strain from Girder 6
S_6 = Section modulus of Girder 6

A task within this project was to monitor the DF over time as a potential technique for identifying damage. If a change in DF occurs, it was postulated that deterioration or damage of the bridge may have also occurred.

For the E. 12th St. Bridge, the strain is measured at the bottom flange of each girder near the North and South midspans. Theoretically, there are three different section moduli at each midspan of the bridge, exterior girder plus a barrier rail (G1 and G6), interior girder plus a barrier rail (G2 and G5), and interior girder (G3 and G4). If the section moduli of the girders are adequately equal,

equation 6 could be reduced to equation 7 (hereafter referred to as the approximate equation). The section modulus, assuming composite action of the deck and portions of the barrier rails (for the exterior girders), for each girder at each midspan is presented in Table A.1, along with the percent difference of the section modulus from the average section modulus of all the girders.

$$DF = \frac{\varepsilon_n}{\varepsilon_1 + \varepsilon_2 + \varepsilon_3 + \varepsilon_4 + \varepsilon_5 + \varepsilon_6} \tag{7}$$

Table A.1. Section modulus and percent difference between girders at the North and South midspans.

	Girder 1	Girder 2	Girder 3	Girder 4	Girder 5	Girder 6
			North Midspan			
S (in^3)	2443.99	2475.93	2320.57	2320.57	2475.93	2443.99
Percent difference	-1.26%	-2.59%	3.85%	3.85%	-2.59%	-1.26%
			South Midspan			
S (in^3)	1987.1	2130.92	2101.19	2101.19	2130.92	1987.1
Percent difference	4.15%	-2.79%	-1.36%	-1.36%	-2.79%	4.15%

To determine the impact of using the approximate versus the exact equation, the DF at the North and South midspans was calculated using equations 6 and 7 for two different load cases from the Controlled Load Test (maximum values at each midspan for Runs 4 and 6). The results are presented in Tables A.2 and A.3. As can be seen, the results are very similar for each case. Thus it is felt that the DF calculated using the approximate equation can be used to adequately determine the DF.

Table A.2. Actual and approximate DF at the North and South midspan from Controlled Load Test Run 4.

	Girder 1	Girder 2	Girder 3	Girder 4	Girder 5	Girder 6
			North Midspan			
Actual	0.08	0.15	0.28	0.25	0.14	0.09
Estimated	0.08	0.14	0.29	0.26	0.13	0.09
			South Midspan			
Actual	0.11	0.16	0.29	0.26	0.12	0.07
Estimated	0.10	0.15	0.29	0.27	0.12	0.07

Table A.3. Actual and approximate DF at the North and South midspan from Controlled Load Test Run 6.

	Girder 1	Girder 2	Girder 3	Girder 4	Girder 5	Girder 6
			North Midspan			
Actual	0.02	0.08	0.14	0.26	0.31	0.19
Estimated	0.02	0.08	0.15	0.27	0.30	0.19
			South Midspan			
Actual	0.02	0.08	0.13	0.26	0.31	0.20
Estimated	0.02	0.08	0.13	0.27	0.30	0.20

A.1.2 DF Sensitivity Study

To provide insight on how changing the properties of the bridge (mainly the stiffness of the girders) would affect the DF, a sensitivity study was performed using a computer-based stiffness model. The flexural stiffness of each girder has an impact on the distribution of load within the system. By changing the stiffness, the load path changes, as well as the strain induced by a unit load.

The simplified computer model used in this study is shown in Fig. A.1. In the model the deck of the bridge was represented by a beam and the girders are represented by vertical axial members which can be thought of as springs. Since the moment of inertia in flexural stiffness is comparable to the area in axial stiffness, the axial stiffness was used to simulate the flexural stiffness. The axial members have a pinned base and a hinge where the member connects to the horizontal beam element. A horizontal restraint was placed on the beam to make the structure stable. The point loads, which were 23.4 kips each (representing the weight of the load truck), were placed in accordance with the actual position of the load truck during Run 6 of the Controlled Load Test.

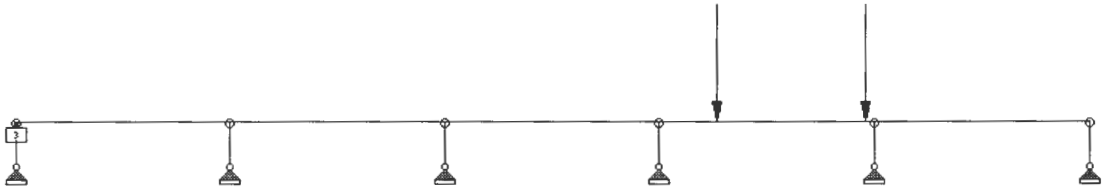

Figure A.1. Computer model used in DF sensitivity study (looking North).

The properties of the members (beam and vertical axial members) within the model were established such that the DF from the model were as close as possible to the DF from Run 6 of the Controlled Load Test. The areas of the axial members were then changed individually by increments of 5% from 100% to 75% to represent a change in the stiffness of the girders on the bridge (the

stiffness of Girder 1 was not changed since the model showed negative strains in Girder 1 and Girder 1 is significantly away from the loading).

Figure A.2 shows the results of the study. Because it was proven to be adequate, the estimated DF equation was used in the calculation of the DF. Notice when the stiffness changes for a particular girder the DF increases at some point in the deterioration. This is especially noticeable in Girder 6, Fig. A.2e. This would indicate the percent of reduction of load taken by the reduced member is less than percent reduction in area of the member, thereby raising the DF. Notice regardless of which girder's stiffness is changed, the Girder 6 DF changes by at least as much as, if not more than, the DF for the other girders. The data also shows Girder 3 changes more significantly than Girders 4 and 5 in most instances. This would mean Girders 3 and 6 the girders, which don't take the heaviest loads but the 3rd and 4th largest loads, are more affected by a change in stiffness than the most heavily loaded girders, Girders 5 and 6.

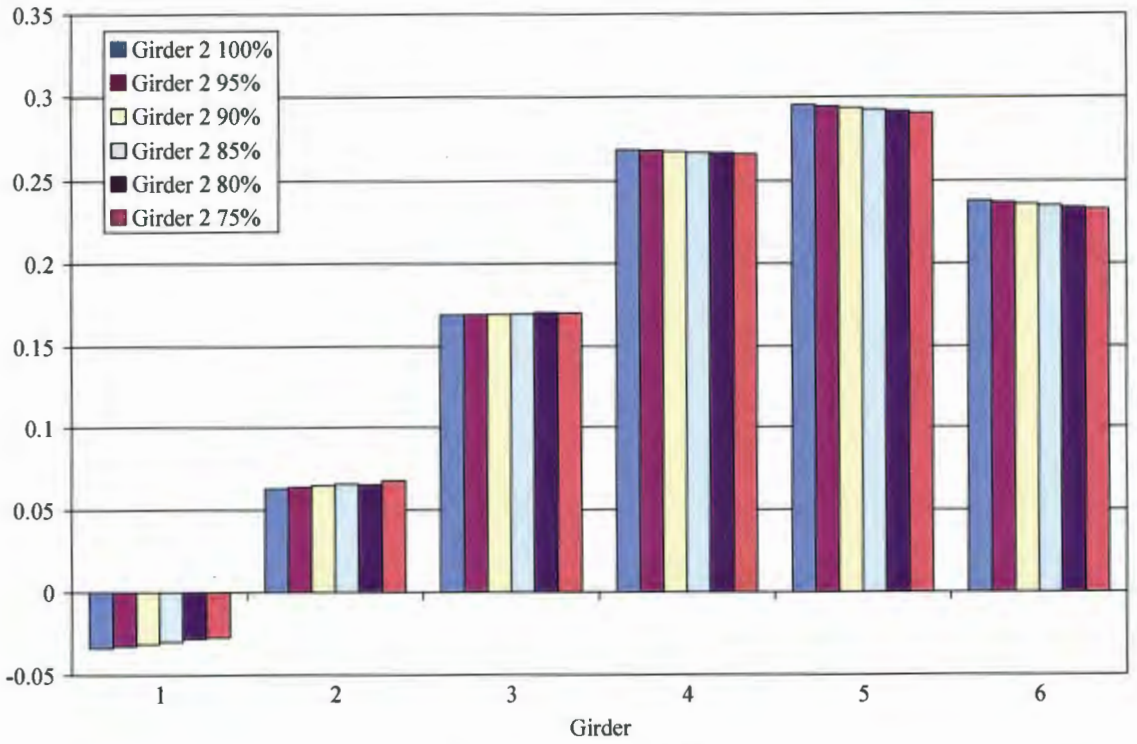

a. Reduction of Girder 2.

Figure A.2. DF when girder stiffness is reduced.

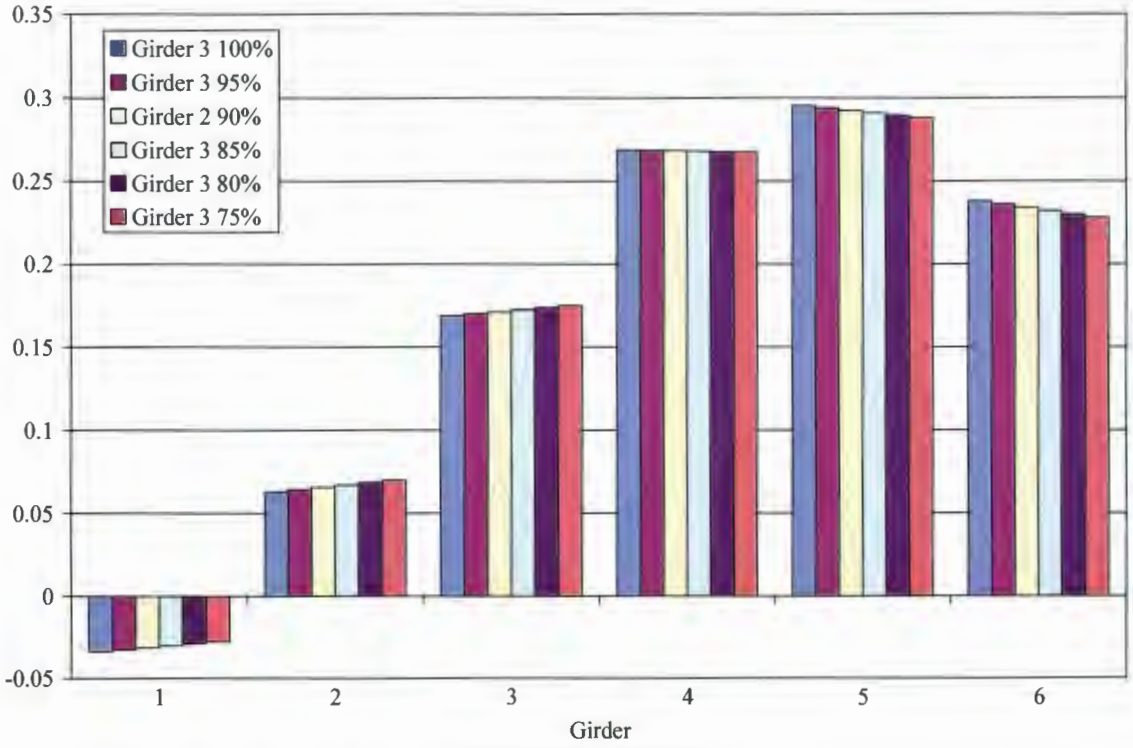

b. Reduction of Girder 3.

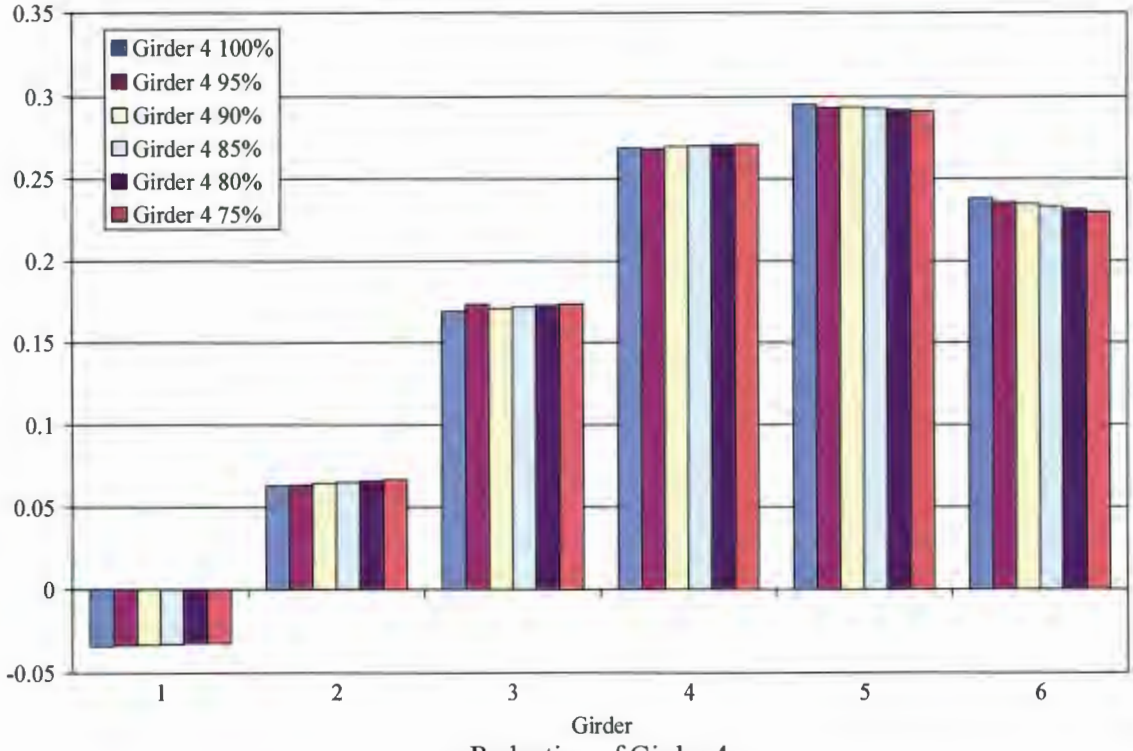

c. Reduction of Girder 4.

Figure A.2. DF when girder stiffness is reduced (Continued).

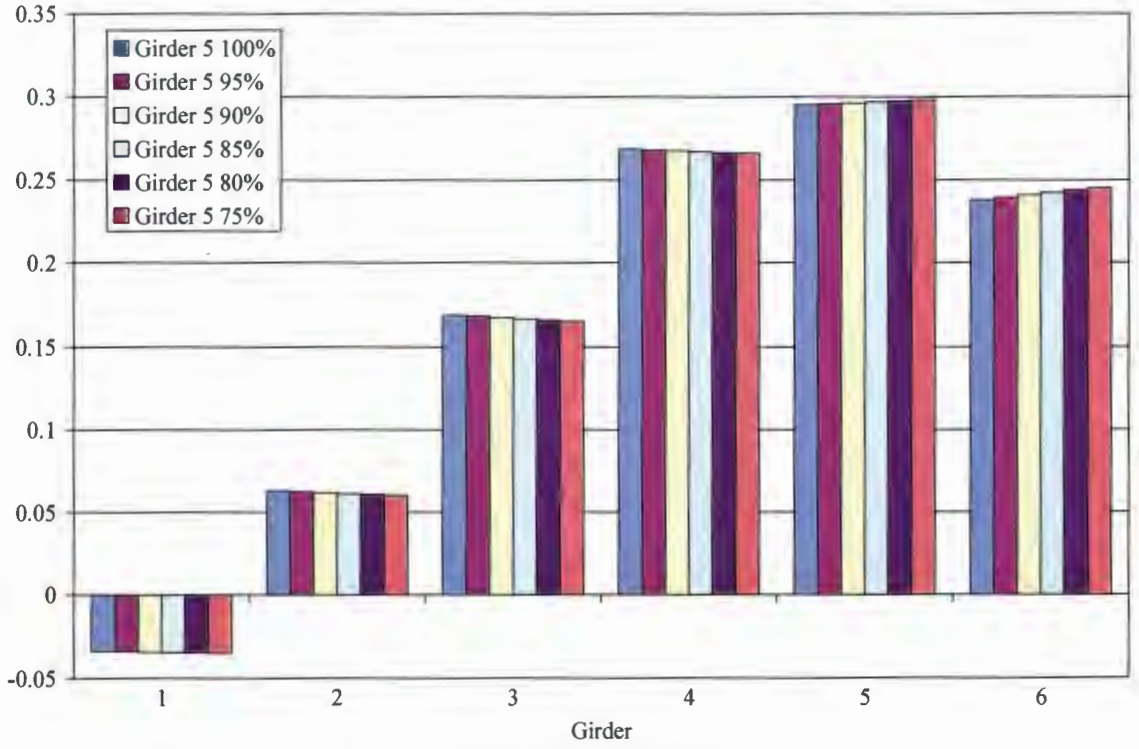

d. Reduction of Girder 5.

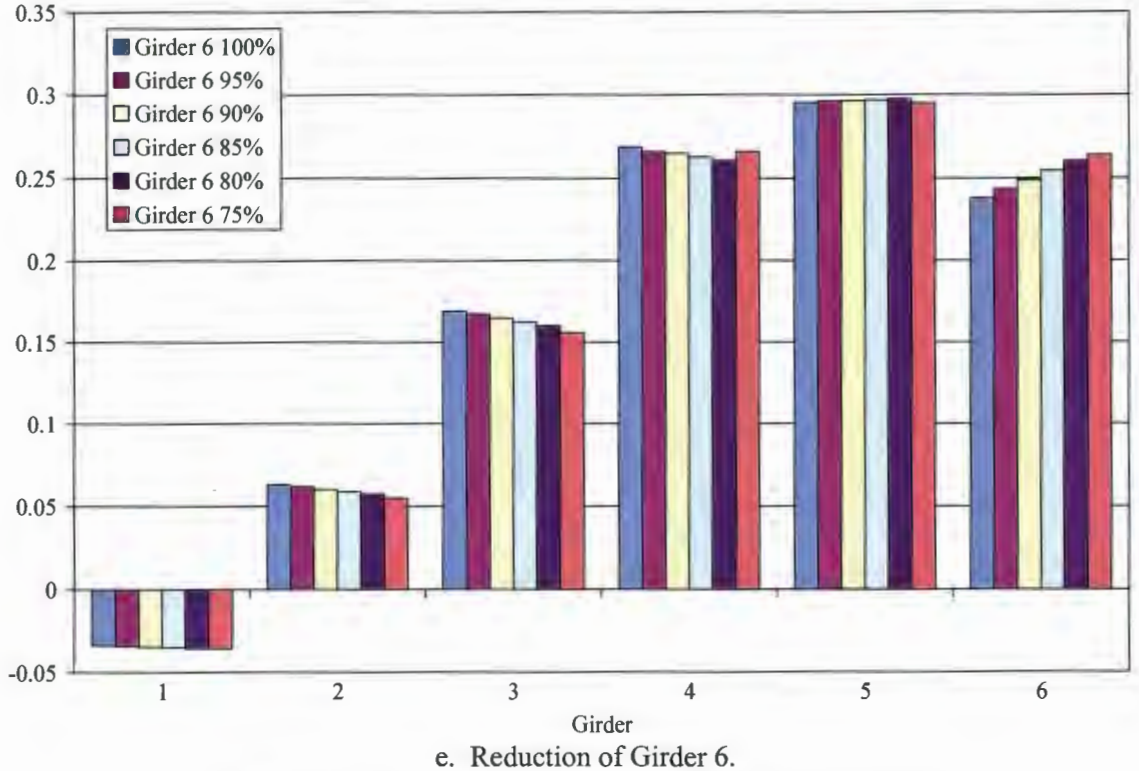

e. Reduction of Girder 6.

Figure A.2. DF when girder stiffness is reduced (Continued).

This sensitivity study concludes that changes in the DF will most likely take place when the stiffness of a girder changes. How obvious the change in DF would most likely depend on which girder the stiffness is changed, how much it is changed, and the position of that girder to the loading position.

A.2 Neutral Axis (NA)

When an element is placed in positive bending, the top part of the beam is in compression and the bottom part is in tension. Since the elements in the top of the beam are shortened and the elements in the bottom of the beam are lengthened, there is a transition point in between where there is no change in length. This point is referred to as the neutral surface of a beam. The location of the neutral surface in a cross-section is commonly referred to as the neutral axis (NA). Since there is no change in length of the fibers which makeup the element at the NA, the strain is zero. The NA of an element can be found by equation 8, which is equal to equation 9 if the element is under a pure bending load.

$$c = \frac{\sum_i y_i A_i}{\sum_i A_i} \tag{8}$$

Where: y_i = The distance from a reference point (consistent for all objects) to the centroid of an object
A_i = The area of an object
c = Distance from the reference point to the centroid

$$NA = \left(\frac{\varepsilon_{BF}}{\varepsilon_{BF} - \varepsilon_{TF}}\right) d_w + t_{BF} \tag{9}$$

Where: ε_{BF} = Bottom flange strain
ε_{TF} = Top flange strain
d_w = Web depth
t_{BF} = Bottom flange thickness

Note: NA distance is taken from the bottom of the bottom flange.

As shown in Equation 8, when the cross-sectional properties of a member change the NA of the member may also change. Changes to the bridge could result in a change in the cross-sectional area. Examples of such changes include section loss (girder and concrete deck), fracture which

causes part of the section to no longer bear stress (i.e., crack in the weld between the bottom flange and web which limits the amount of stress distributed to the bottom flange), reduction in the composite action of the bridge, and a change in the deck performance which changes the effective width of the deck.

A.2.1 NA Sensitivity Study

A sensitivity study was performed to determine the change in the NA when the cross-sectional properties of the girders on the E. 12th St. bridge were changed. The three cross sections mentioned previously (G1 and G6, G2 and G5, and G3 and G4 [represented by G1, G2, and G3 respectively in Fig. A.4]) at the North midspan were changed by reducing either the bottom flange area (reducing the thickness from the bottom side of the flange) or the total area of the girder cross-section (reducing the bottom flange thickness from the bottom side of the flange, reducing the web thickness from both sides, and the top flange thickness from the bottom side of the flange) to study the resulting change in the NA location. The results are presented in Table A.4. Table A.4 shows a change in the area of the bottom flange also can be more significant than a change in the area of the entire section. It is also shown the change in the NA is the largest for the interior girders for both the bottom flange and the total area reduction.

Table A.4. NA location (in.) after reduction of bottom flange or total area.

Percent of Area	G1 NA (BF Area)	G1 NA (Total Area)	G2 NA (BF Area)	G2 NA (Total Area)	G3 NA (BF Area)	G3 NA (Total Area)
100	60.36	60.36	61.02	61.02	57.81	57.81
95	60.81	60.62	61.47	61.28	58.26	58.09
90	61.32	60.94	61.97	61.59	58.77	58.43
85	61.81	61.21	62.45	61.85	59.19	58.71
80	62.31	61.49	62.93	62.12	59.77	59.01
75	62.86	61.79	63.48	62.41	60.33	59.33

From this sensitivity study it is shown that a change in the area of a cross-section results in a change in the NA location. If the cross-sectional properties of a girder change, the change should be noticed by monitoring the NA location over time using equation 9. The change in the NA may not be noticeable with a small change in the area, but a significant loss of area may be noticeable over time.

A.3 End Restraint (ER)

The E. 12th St. Bridge is a two-span bridge with integral abutments at both ends, a vertical support with a horizontal restraint at the center pier, and three different girder cross-sections (North

Region, Center Region, and South Region). Since the system is indeterminate to the third degree, changing the rotational restraint of the abutments and/or changing the stiffness of each of the girder sections changes how the bridge responds to loading. To monitor change in the longitudinal girder stiffness overtime, the end restraint ratio (ER) was developed as given in equation 10.

$$ER = \frac{\varepsilon_{MS}}{\varepsilon_{AS}} \tag{10}$$

Where: ε_{MS} = Midspan bottom flange strain

ε_{AS} = Abutment bottom flange strain

A.3.1 ER Sensitivity Study

To determine how changing the rotational restraint at the abutments and changing the stiffness of the girders affects the ER, a computer based stiffness model was developed of a single beam line. Figure A.5 shows a screenshot of the model used. One interior girder (Girder 3 since instrumentation is in place to allow the ER to be calculated for Girder 3) was modeled as a continuous beam with three different segments, each having a constant cross-sectional area and inertia as determined from plan dimensions. The abutments were modeled by a condition which provided vertical support and a rotational restraint that could be modified. The boundary conditions induced on the bridge at the center pier were represented by a pin. The model had 6 different nodes with beams (numbers shown in Fig. A.3) between each of them. Table A.5 gives the important properties for each region of the model. This includes the beam numbers which makeup each region, moment of inertia for the region, and the cross-sectional area for each region. A load vertical load of 46.8 kips, which represents the weight of the load truck used in the Controlled Load Test, was applied at a node which was located 100 ft from the North abutment.

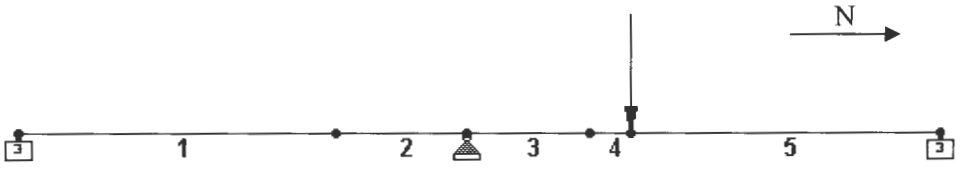

Figure A.3. Stiffness model used in the ER sensitivity study.

Table A.5. Specifications for regions in stiffness model.

	Beam Number	I	Area
South Region	1	116,951 in^4	58.36 in^2
Center Region	2, 3	147,267 in^4	85.72 in^2
North Region	4, 5	134,162 in^4	67.50 in^2

To determine how the rotational restraint of the abutments affects the ER, the rotational restraint of the abutments was changed (simultaneously for both abutments). The rotational restraint was modeled at various stiffnesses ranging from a pin condition to a fixed condition, with a special emphasis in the range that was determined from field conditions (long term RMS for Girder 3 is -2.68). Figure A.4 shows a log-plot of the ER as the rotational restraint at the abutments change. For a rotational restraint of 1,000,000, which approximately represents the fixed condition, the ER is 0.83 and for a pin condition the ER is 10.6. Interestingly, when the rotational restraint approaches a pinned condition, an inflection point develops near the sensor located near the abutment. This creates the discontinuity seen in Fig. A.4a. Figure A.4b shows the region of the plot of most interest. The ER calculated during the load test during when the load truck was approximately 100 ft from the North abutment was about -3. The exact rotational restraint of the abutments can't be determined from this study but from the brief analysis done the bridge seems to respond closer to a pinned end condition than a fixed end condition.

Changing the moment of inertia for each region was also studied to determine the impact on the ER. The I was changed for each region separately from 100% to 75% of the composite I. A rotational restraint value of 9,000 (with 100% I for all regions), provides the ER closest to the long-term RMS and was therefore used. The results are shown in Fig. A.5. When the moment of inertia of the South Region is changed, the ER changes very little. A slight change in ER occurs when the moment of inertia of the Center Region is changed. As expected, the largest change in ER is due to a change in the North Region moment of inertia. This is the region where the strains that are used to calculate the ER are located. The change in the ER due to the change in the moment of inertia is almost linear.

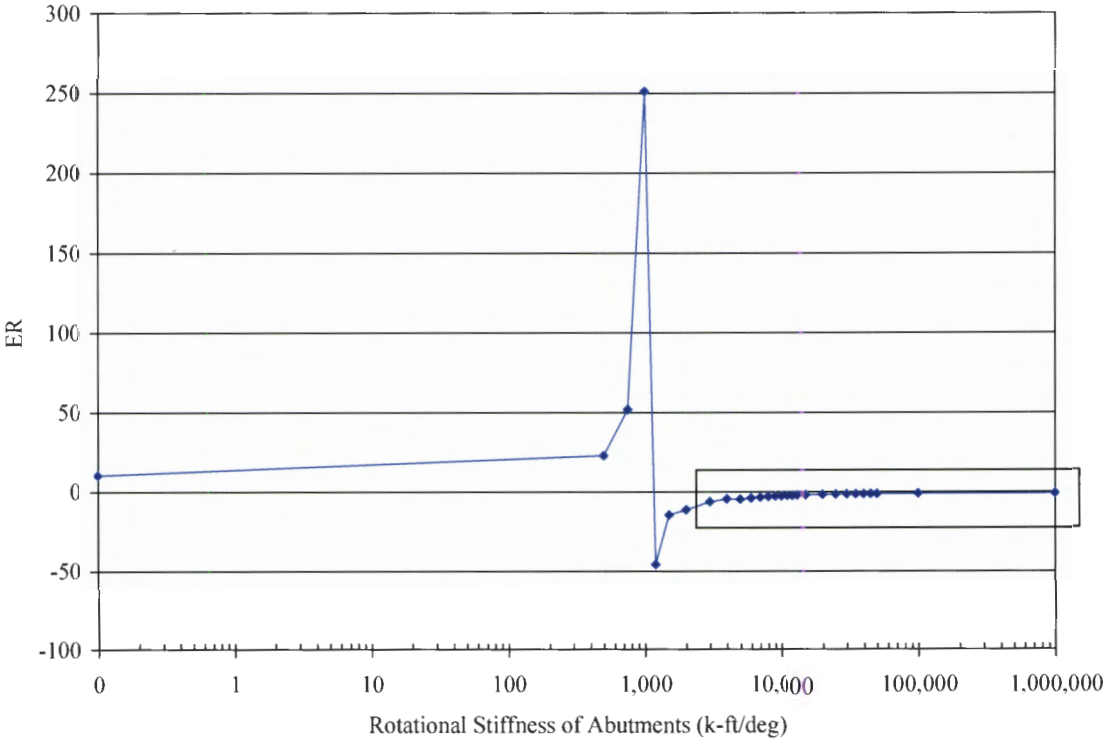

a. Range of rotational restraint between 0 and 1,000,000 k-ft/deg.

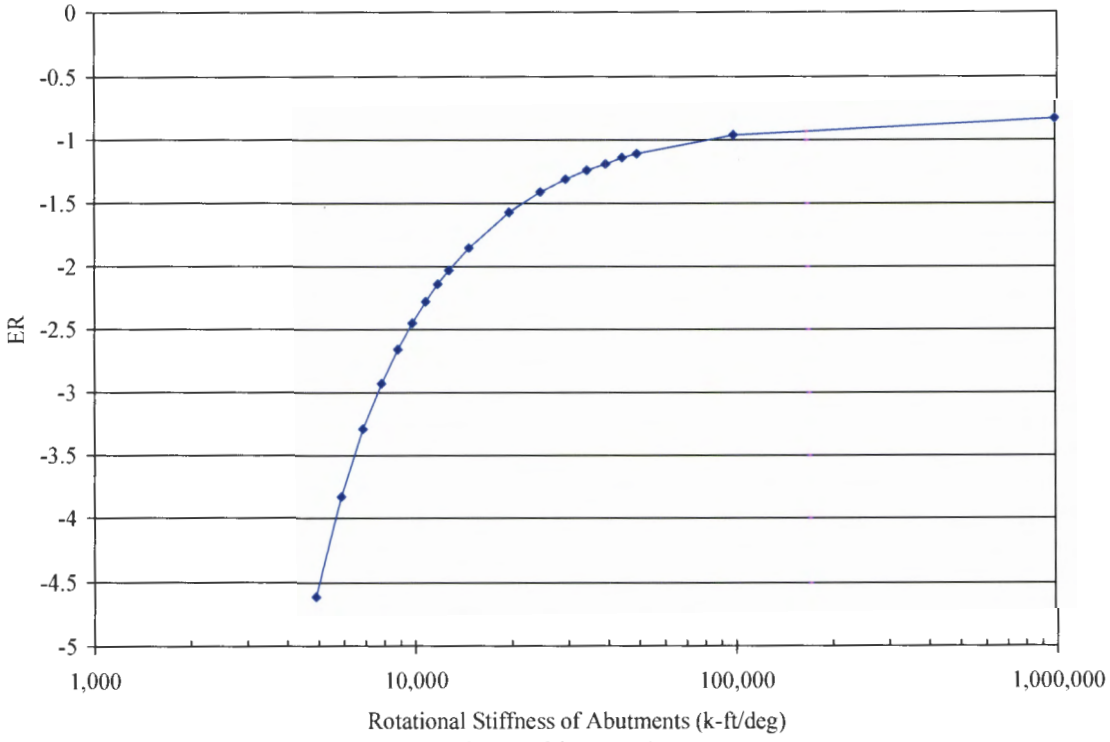

b. Area denoted by box in part a.

Figure A.4. ER as the abutment rotational restraint is changed.

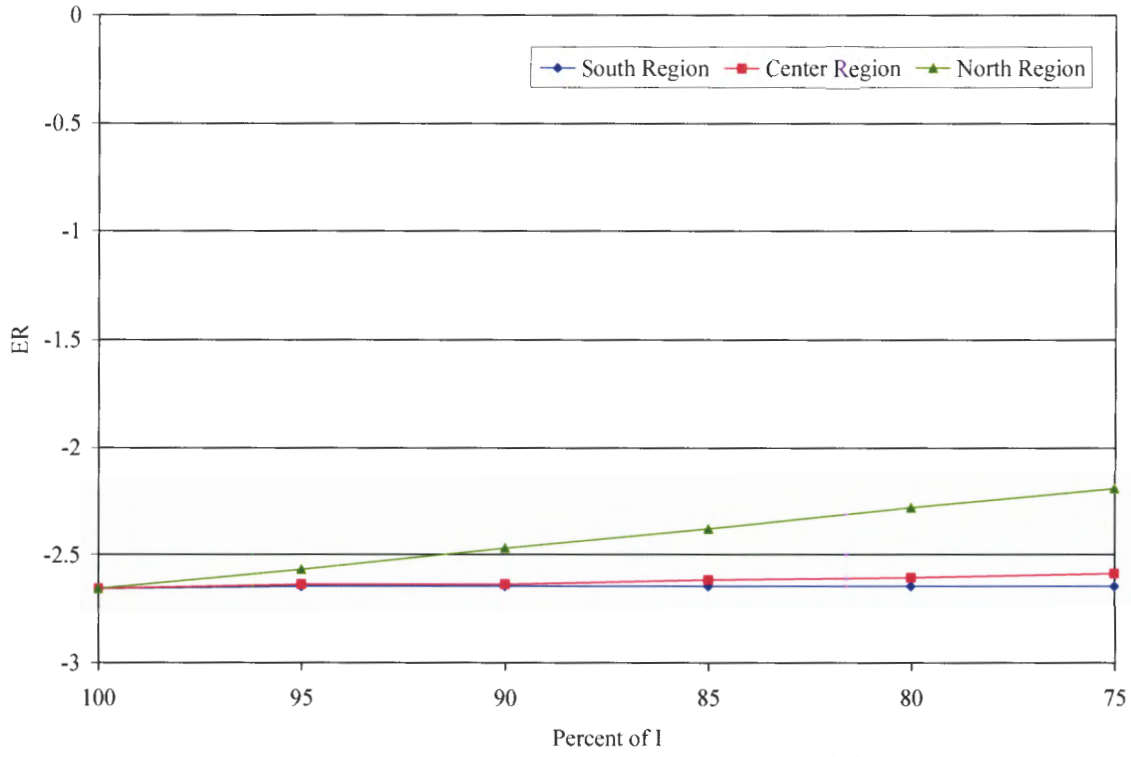

Figure A.5. ER as the I of each region is changed.

As the trends of the ER are monitored over time, changes in the stiffness of the bridge or rotational restraint may be apparent. A noticeable change in the ER would probably not occur until the moment of inertia is reduced by at least 90% to 85%. The change in the rotational restraint could be caused by a negative change in the bridge (deterioration or damage) or by a natural cause such as a change in the pile-soil interaction due to seasonal temperature changes.

A.4 Using the Bridge Indices

As shown in the previous sections, the bridge indices are sensitive to changes in the properties of the bridge. None of the three indices are highly sensitive to the changes which were tested in this study. Since many of the bridge properties impact all of the indices in different forms, if the indices are monitored over time independently and as a collection for changes, deterioration or damage to the bridge may be noticeable with such a redundant system of calculations.

APPENDIX B. LONG-TERM TEMPERATURE STRAIN

As discussed previously, the girder strain from short-term loading and long-term loading are separated in the DSP. Long-term strain induced on the bridge can be attributed to such things as settlement and temperature. The strain caused by a change in temperature can be due to expansion and contraction of the bridge. Stress can be induced if the induced strain is not constant through the depth of the cross-section, causing bending. Stresses can also be induced if the bridge is not allowed to expand and contract freely (i.e., due to restraint from the abutments). In most cases the majority of the long-term strain is due to changes in temperature which can affect the strain on the bridge in different ways including: expansion and contraction of the superstructure and change in boundary conditions (i.e. change in soil-pile interaction and soil-abutment concrete interaction). The collected data are characterized and presented based on different periods of time including: 1) seasonal temperature changes, 2) short-term temperature changes (cold or warm fronts that change the temperature for several days at a time), and 3) daily temperature changes.

B.1 Seasonal Temperature Change

Due to the limited time over which the data presented in this report were collected (Early May to Early September), the seasonal temperature data are limited. Figure B.1 shows the long-term strain data for a North midspan bottom flange, North abutment bottom flange, and North midspan top flange. The gaps seen in the long-term strain data are due to periods of time in which data are not available (i.e. system problems or upgrades). The general trend and magnitude of the strain data shown at these locations are representative of the strain data seen at other locations on the bridge. The locations respond in the same manner with respect to the cyclic trends of the data (i.e. the strain data increases and decreases similarly).

Figures B.1ds through B.1h show the long-term strain data of the top and bottom flange at the North and South midspan (note the South midspan has less data due to the later sensor installation date). The cyclic trends of the top and bottom flange strains are similar. With the exception of Girder 1 at the North midspan, the ranges of the top and bottom flange strains are similar. These trends will be discussed further subsequently. A difference in the absolute strain of the top and bottom flanges of Girder 3 (Fig. B.1f) starts to appear around day 70. Trends of increasing and decreasing strain represent daily cycles due to warming or cooling. It is apparent the strain ranges due to temperature changes are much larger than the strain ranges induced by live-load events.

The long-term temperature strain at the North and South midspans on the bottom flange of Girder 3 is shown in Fig. B.2 for the monitoring period of the South midspan. The trend of the data is similar for both locations but the absolute strains are higher for the North than the South. Notice that the North strains are positive while the South strains are negative. This is because the North sensors were installed during March and April, 2004 and had accumulated strain to day 100. The South sensors were installed on July 19 and 20, 2004 and recording began on day 100 soon after. The data shown for Girder 3 in Fig. B.2 is representative of the North and South bottom flange data of all of the girders.

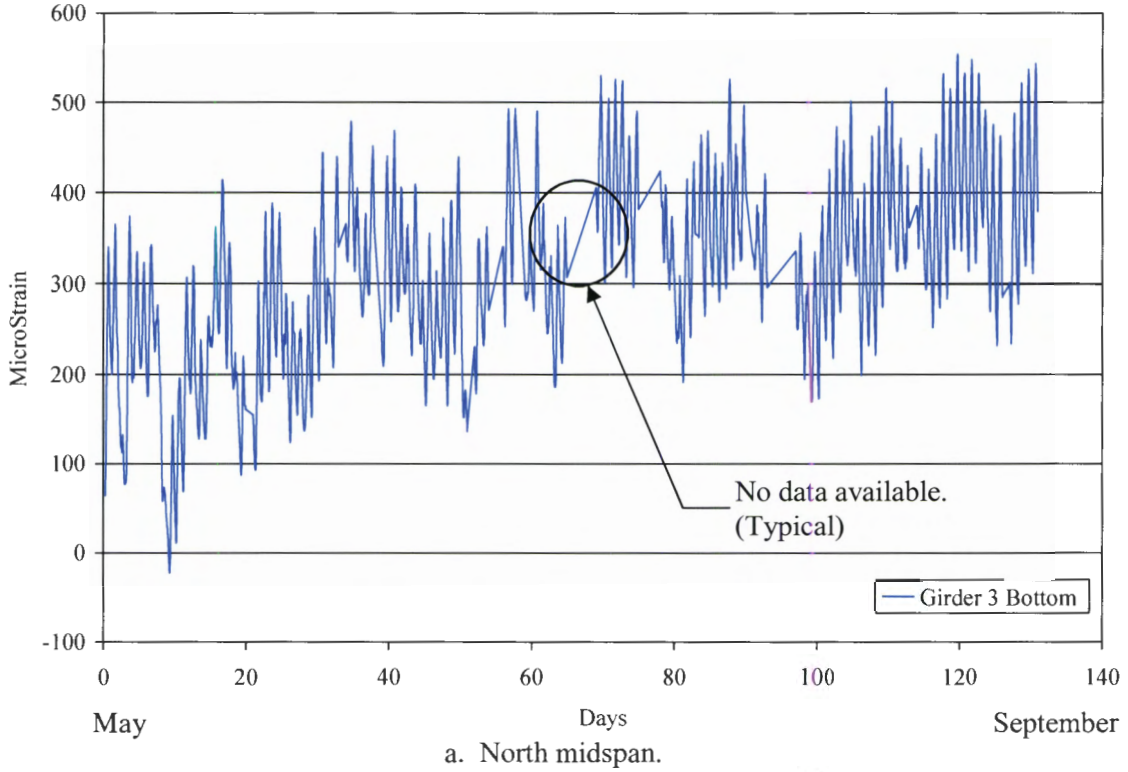

a. North midspan.

Figure B.1. Long-term temperature strain over monitoring period.

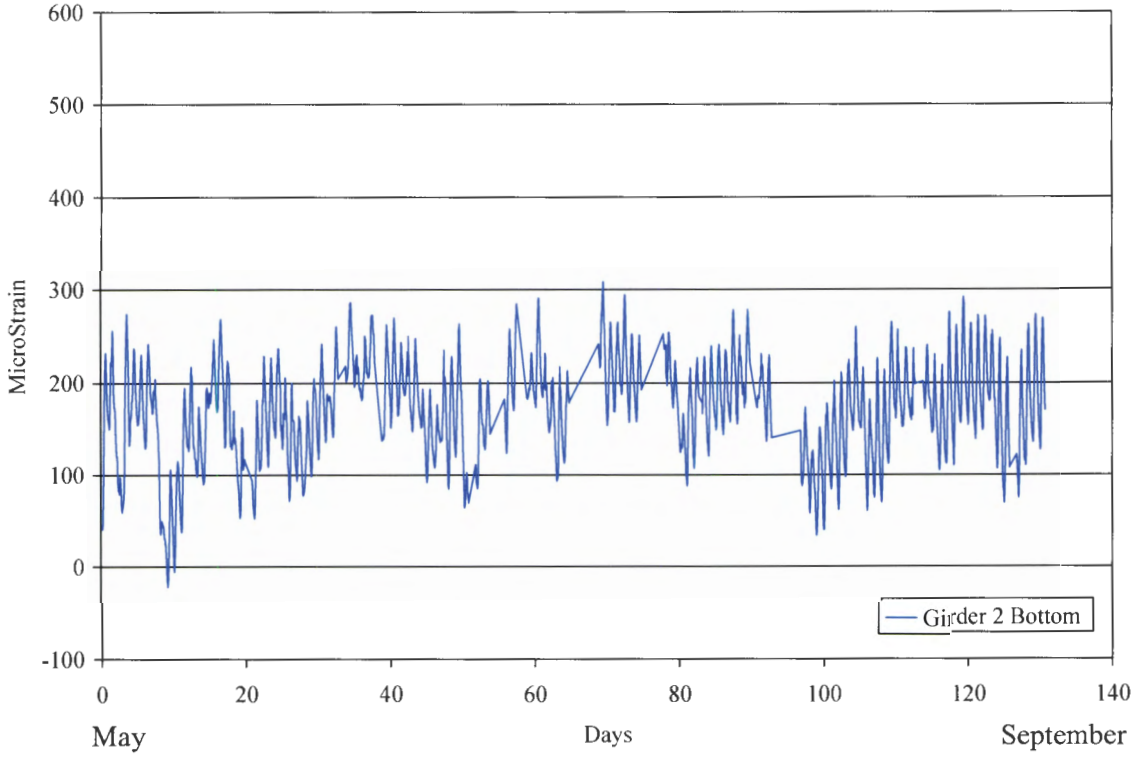

b. Abutment.

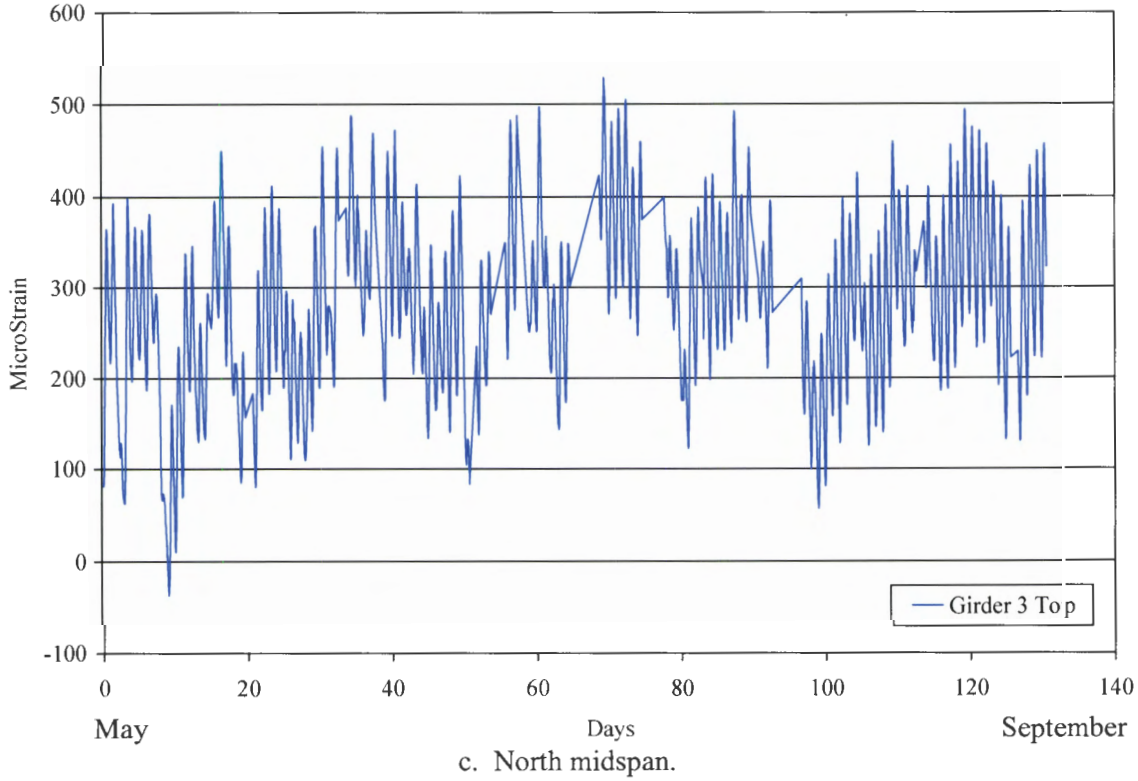

c. North midspan.

Figure B.1. Long-term temperature strain over monitoring period (Continued).

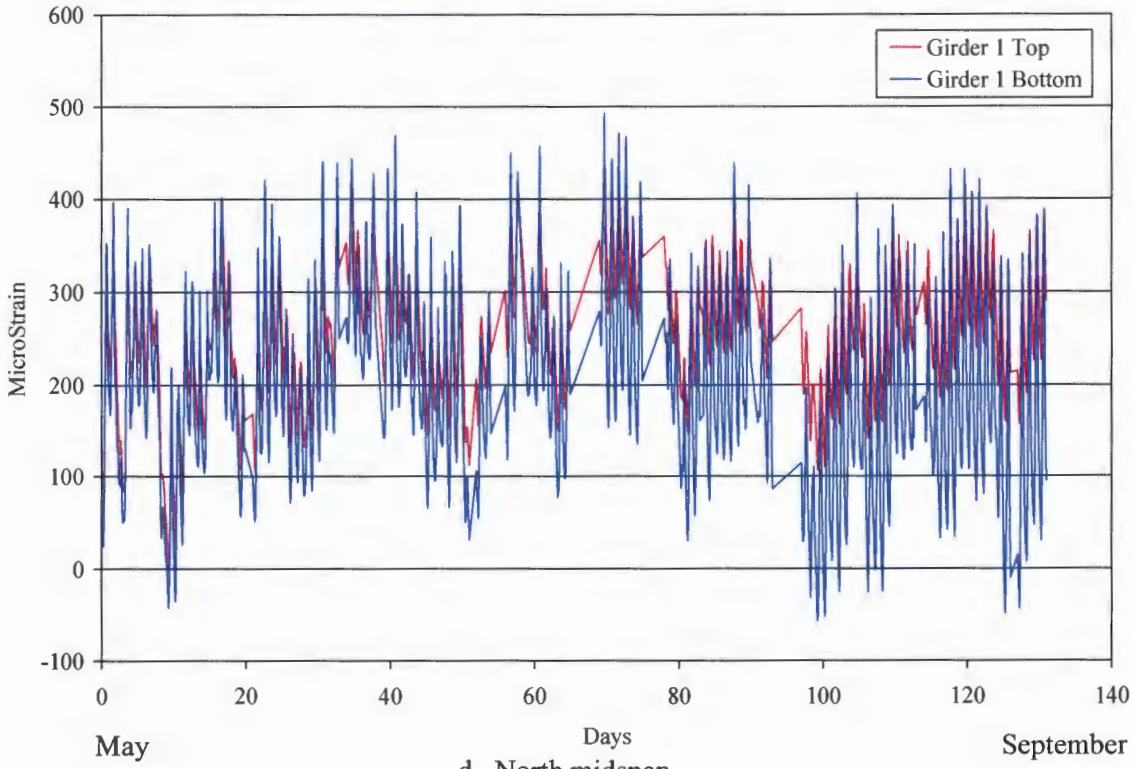

d. North midspan

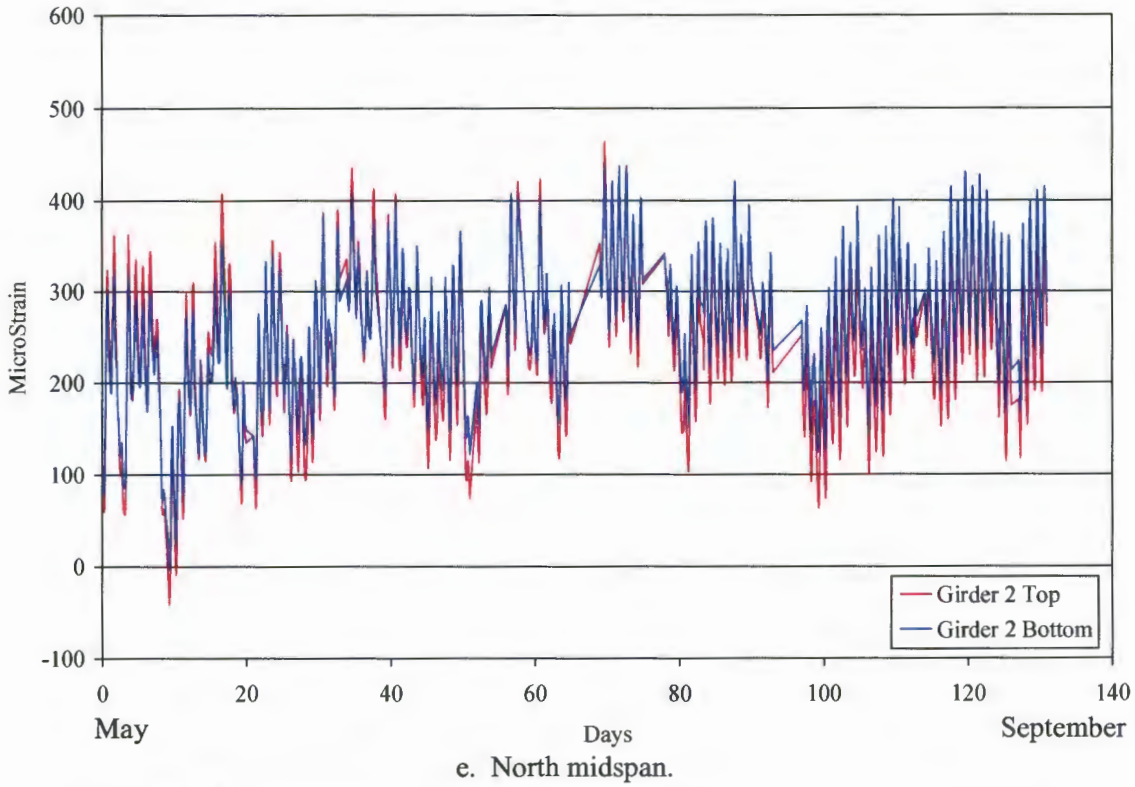

e. North midspan.

Figure B.1. Long-term temperature strain over monitoring period (Continued).

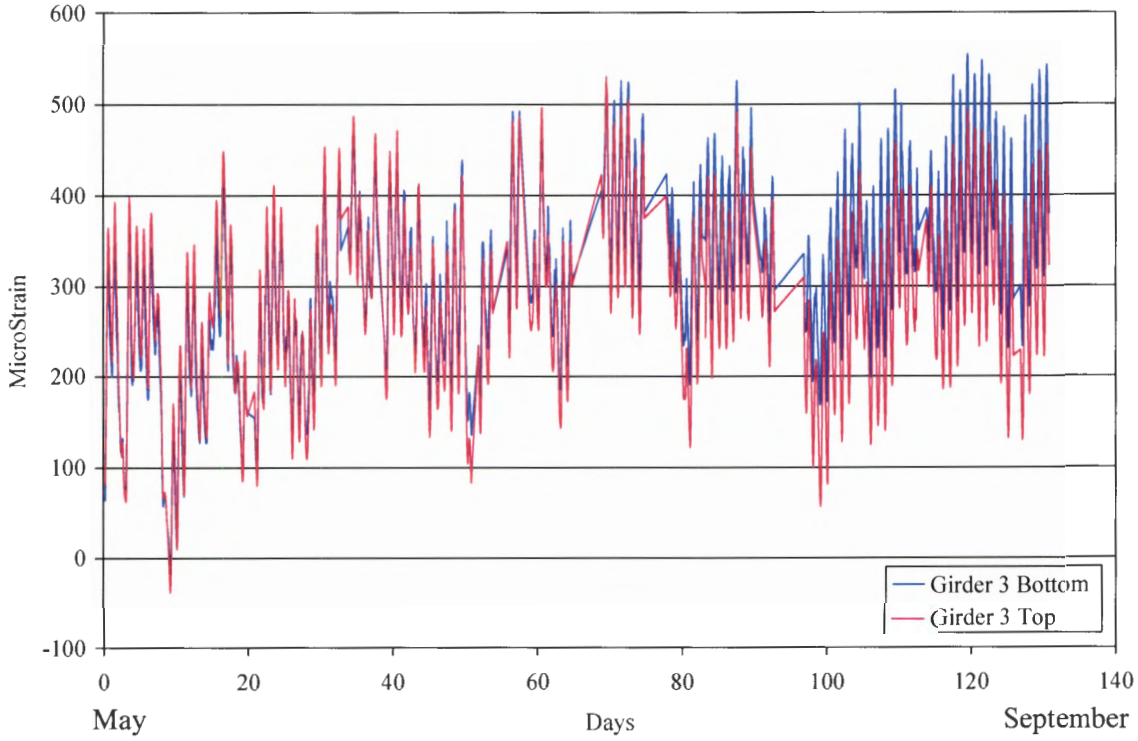

f. North midspan.

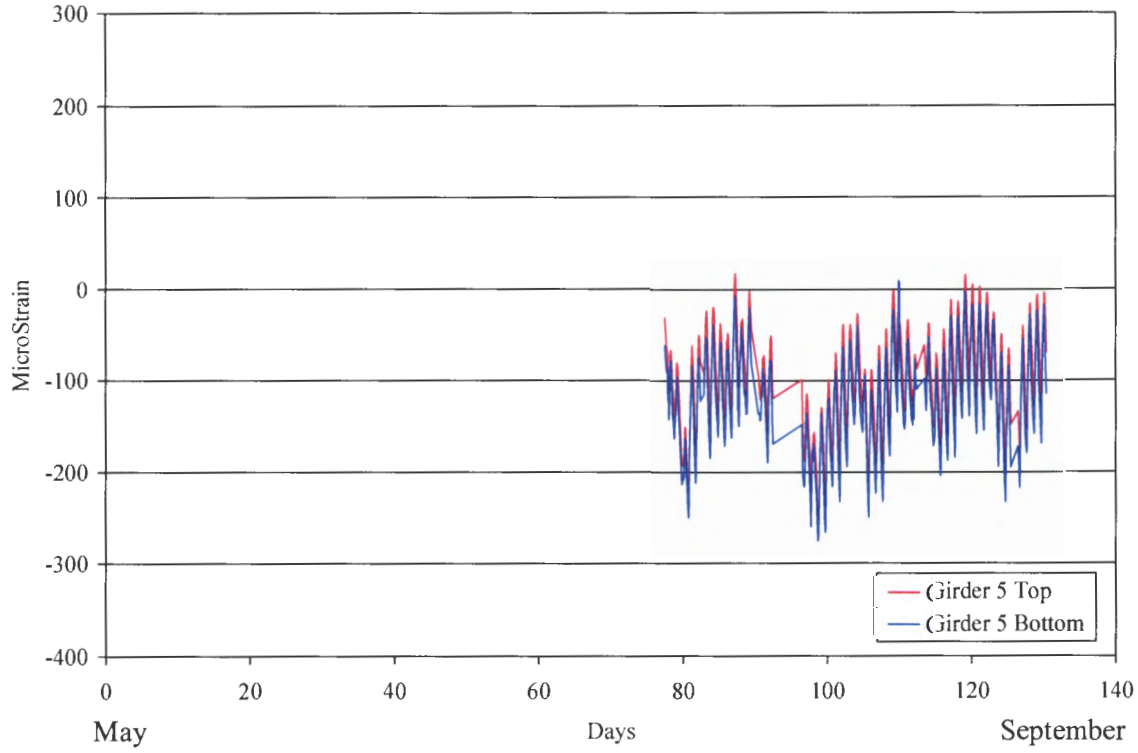

g. South midspan.

Figure B.1. Long-term temperature strain over monitoring period (Continued).

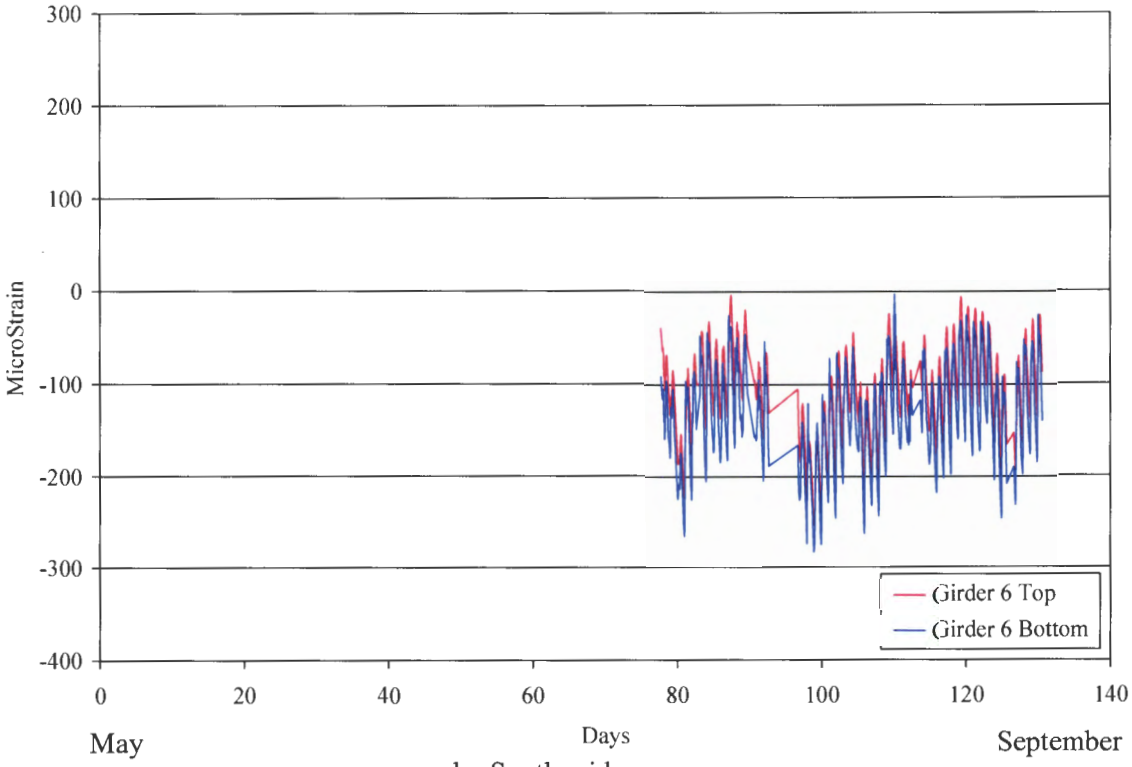

h. South midspan.

Figure B.1. Long-term temperature strain over monitoring period (Continued).

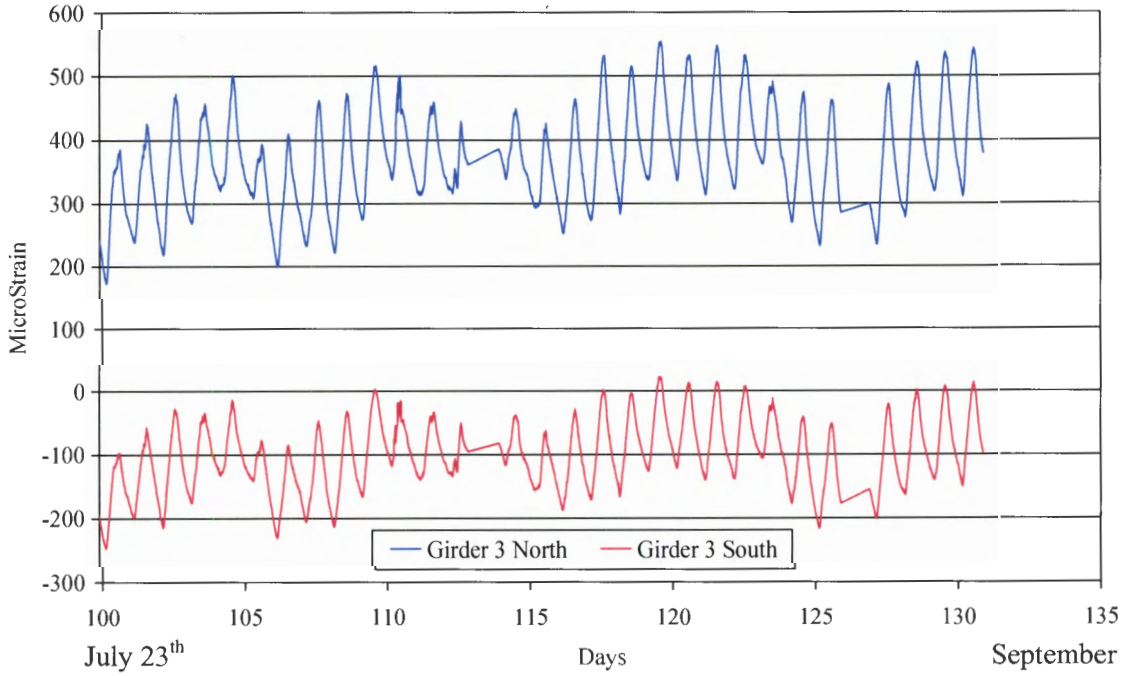

Figure B.2. North and South bottom flange temperature strain.

B.2 Short-term Temperature Change

Strain data for approximately a 30 day period is provided along with strain data presented in weekly time frames. Figure B.3 shows strain data for a 30 day period for strain data at a South midspan top and bottom flange and an abutment bottom flange. As with the seasonal temperature data, increasing and decreasing trends can be seen in the data. The daily strain ranges are on the order of 100 to 150 $\mu\varepsilon$ for each location.

Figure B.4 compares the strain collected from the bottom flange sensors at the North midspan and the temperature sensors located near the North midspan sensors. The trends of the sensors are the same but the magnitudes are different, since one measures the strain in the steel and the other measures the change in the FBG due to temperature. The "temperature sensor" is not fastened to the bridge; it is housed in a black plastic tube which provides environmental protection. It is assumed that the temperature sensor measures the change in strain due to the change in the steel girder temperature.

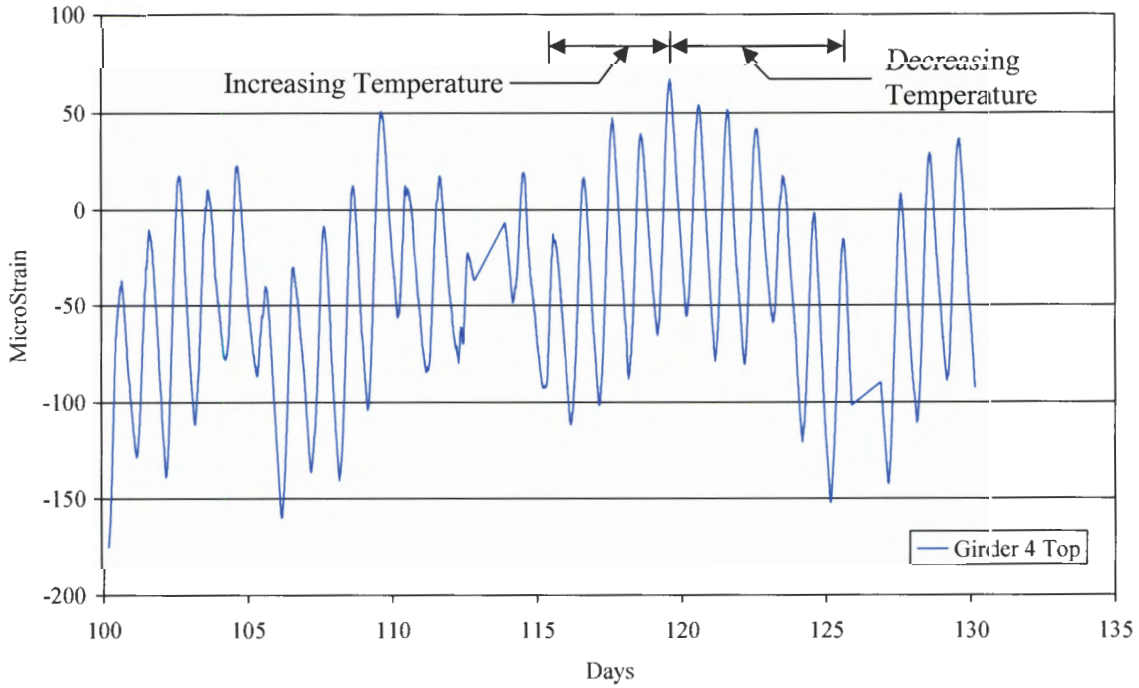

a. South midspan.

Figure B.3. Temperature strain from a 30 period.

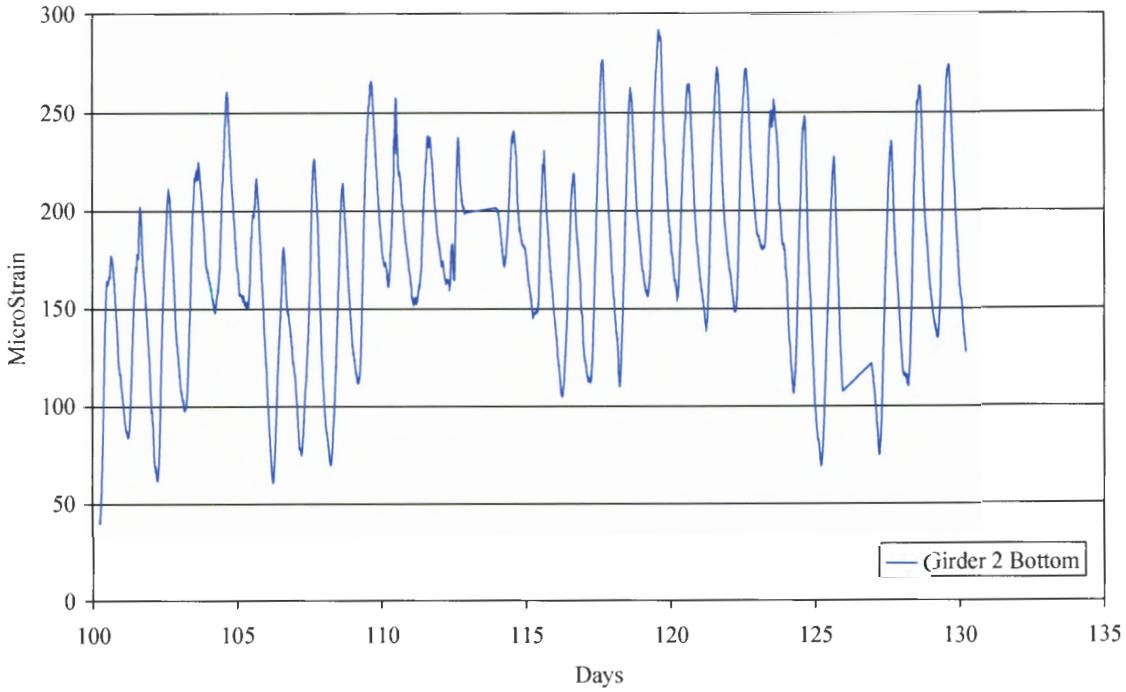

b. Abutment.

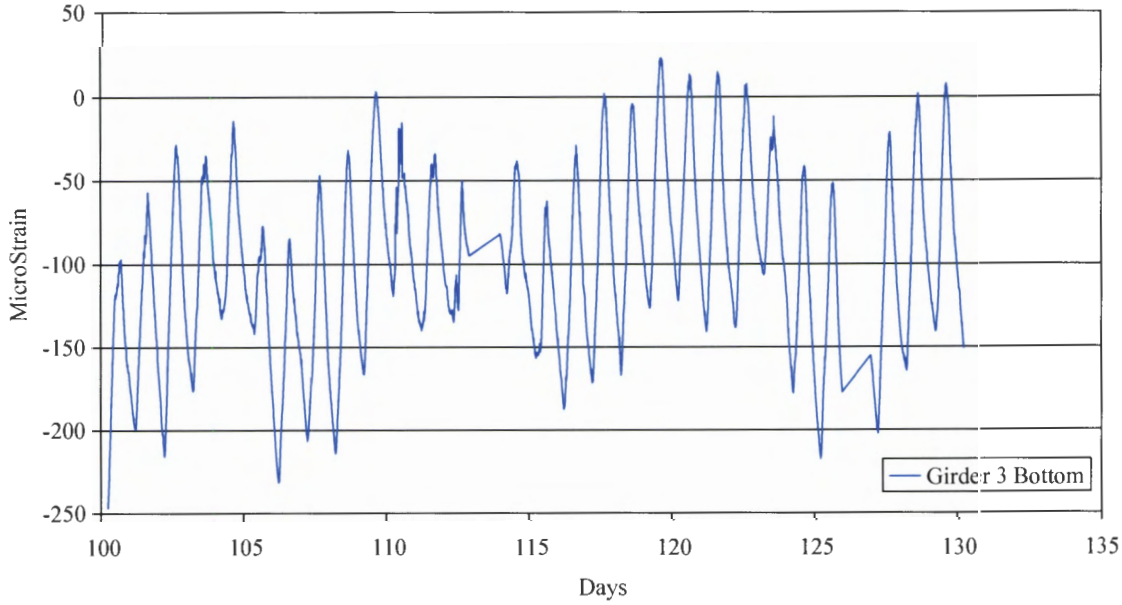

c. South midspan.

Figure B.3. Temperature strain from a 30 period (Continued).

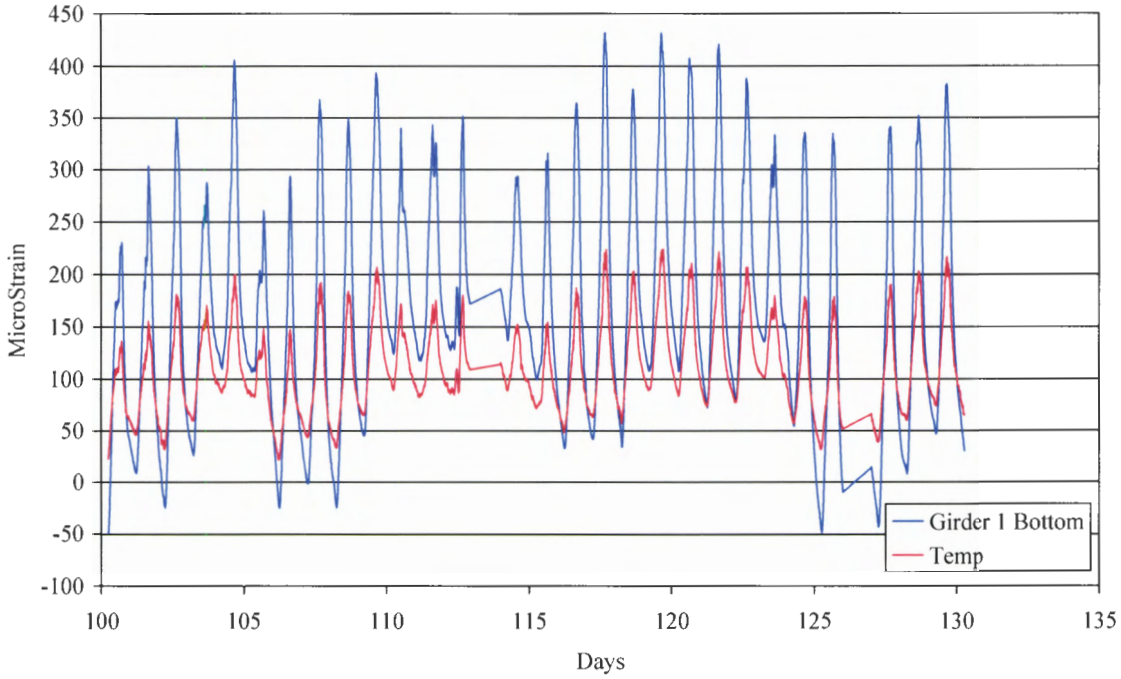

a. Girder 1

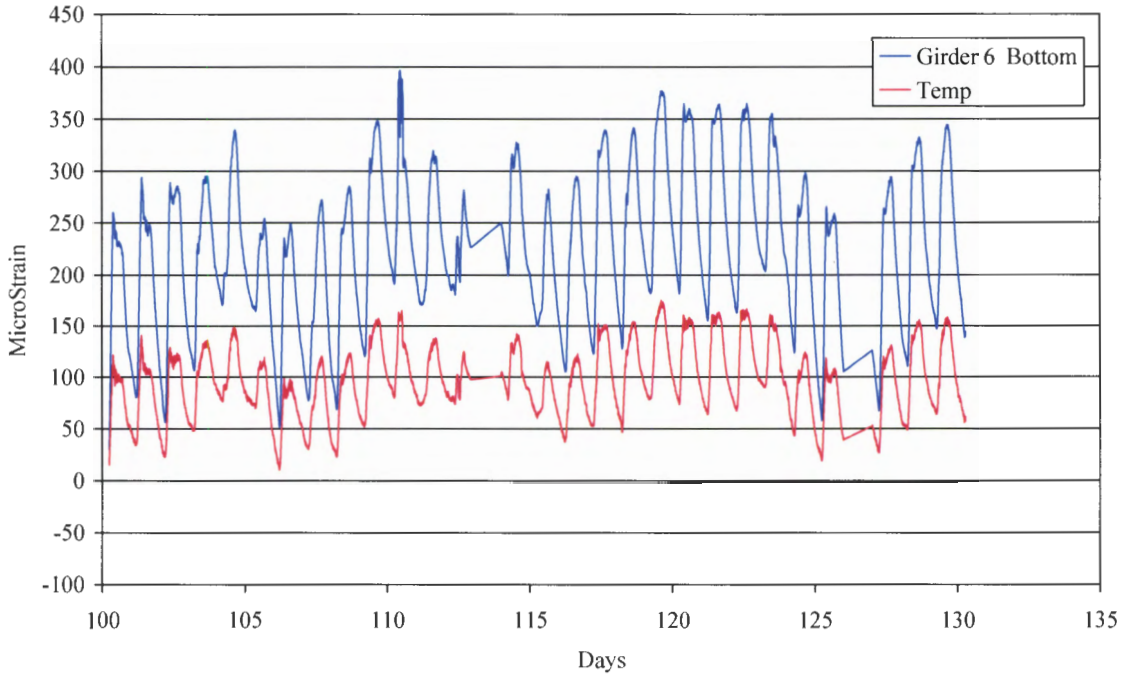

b. Girder 6

Figure B.4. Temperature strain from a 30 period at the North midspan.

Weekly strain plots are presented in Fig. B.5. Several different combinations of sensor strains are compared.

Figure B.5a compares the localized detail strains and top flange strain. Three different sensors are shown: longitudinal sensors (i.e. top flange and welded plate splice), lateral sensors (i.e. flange tipping), and vertical sensors (i.e. web gap). The response is similar for all of the sensors in terms of magnitude and trends. The temperature strains for a one week at the abutment and bottom flange of Girder 2 are shown in Fig. B.5b. The two locations have similar magnitudes and general trends. Figures B.5c and B.5d are plots of the temperature strain for the bottom flange of all six girders at the North and South midspans, respectively. The general trend of the strain change is similar for all six girders at both the North and South midspan. The relationship between the change in strain between the girders will be examined subsequently in the daily temperature sub-section.

Three anomalies are identified in Figs. B.5c and B.5d. Anomilies 1 and 3 are similar in that they show a sudden decrease in strain and the sharp rise while anomaly 2 is a sudden decrease which then levels out. These anomalies are most likely due to sudden weather induced temperature changes.

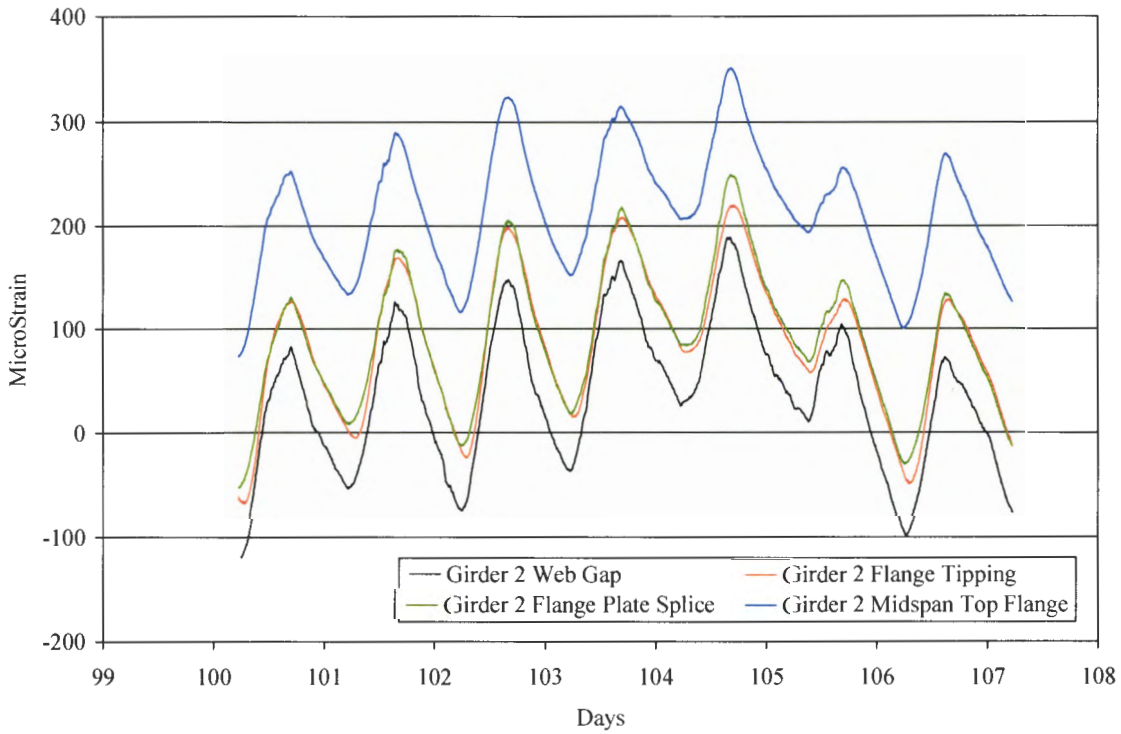

a. Localized fatigue details.

Figure B.5. Temperature strain for weekly periods.

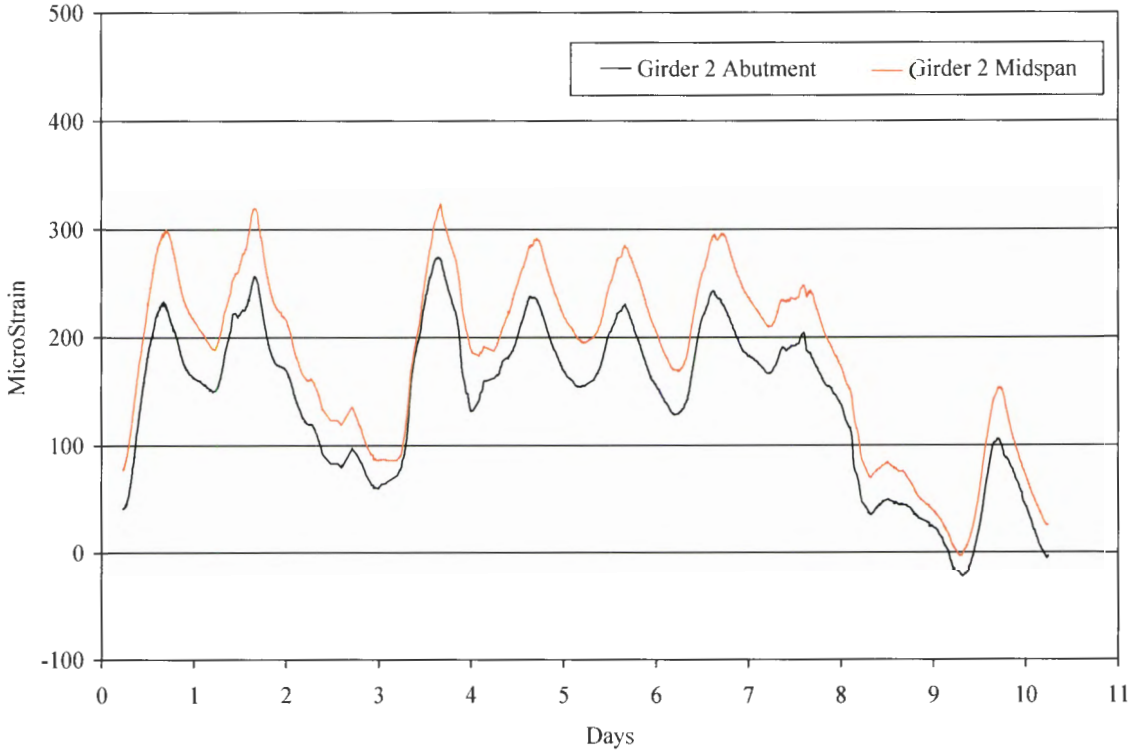

b. Girder 2 bottom flange at the midspan and abutment.

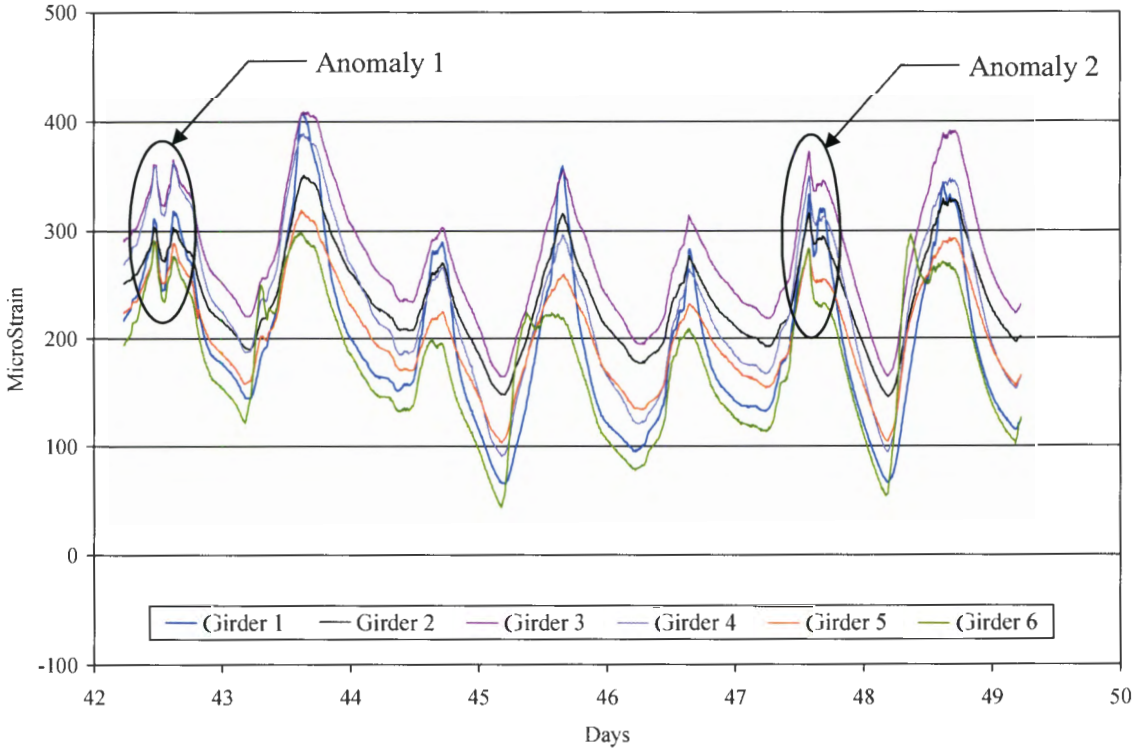

c. Bottom flange at the North midspan.

Figure B.5. Temperature strain for weekly periods (Continued).

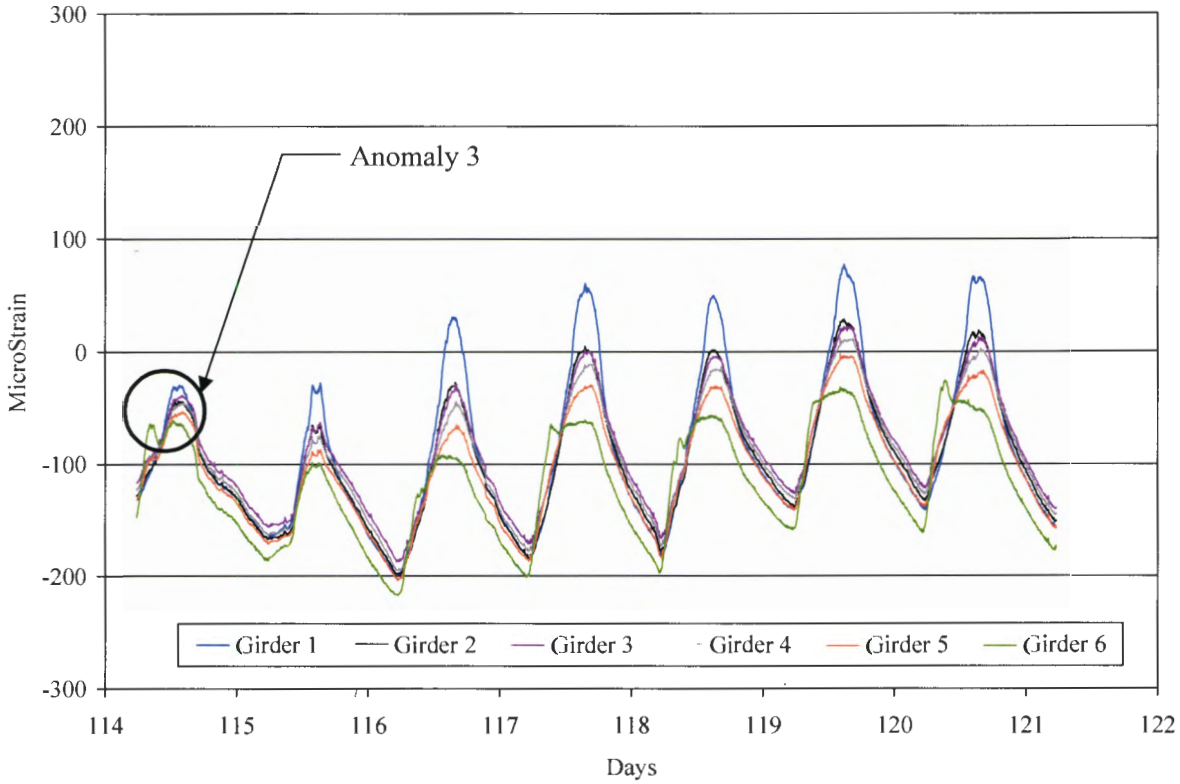

d. Bottom flange at the South midspan.

Figure B.5. Temperature strain for weekly periods (Continued).

B.3 Daily Temperature Change

The daily change in temperature results in a daily strain cycle. This cycle is usually on the order of 100 to 200 $\mu\varepsilon$. Figure B.6 compares the daily temperature strain data for the top and bottom flange of interior and exterior girders at the North and South midspans. The exterior girder at the North midspan is on the West side of the bridge, while the exterior girder at the South midspan is on the East side of the bridge. The South midspan (Fig. B.6a) shows the exterior bottom flange has a sharp rise in strain which is explained by the sun shining directly on it in the morning. The top flange on the exterior girder does not increase as sharp which would be expected since the mass of concrete from the deck (which is in contact with the top flange) takes more time to heat up than the bottom flange. The top flange on the interior girder has the largest strain range, which for the day shown is approximately 160 $\mu\varepsilon$.

At the North midspan in Fig. B.6b, the bottom flange of the exterior girder has the highest strain range. The top flange of the exterior girder has the lowest. The strain profiles at all of the locations have the same slope until approximately hour 7 (or 1 pm), when the bottom flange of the

exterior girder rapidly rises. This would be the approximate time in which the afternoon sun would be shining directly on Girder 1. The bottom flange of Girder 1 would heat up rapidly since sun is shining directly on it and there is no large mass to provide a heat sink which would slow the warming and cooling of a location (as is the case with the top flange).

Figure B.7 compares the bottom flange strain for the six girders at the North and South midspans. The same trends of the exterior girders on the West and East sides of the bridge that were previously discussed are apparent in Fig. B.7. Girder 1 (the exterior girder on the West side of the bridge) has the highest strain range. The interior girders have the same trend through the day. It is interesting to note, although slight, the girders on the West side of the bridge have a larger strain range than the girders on the East side of the bridge.

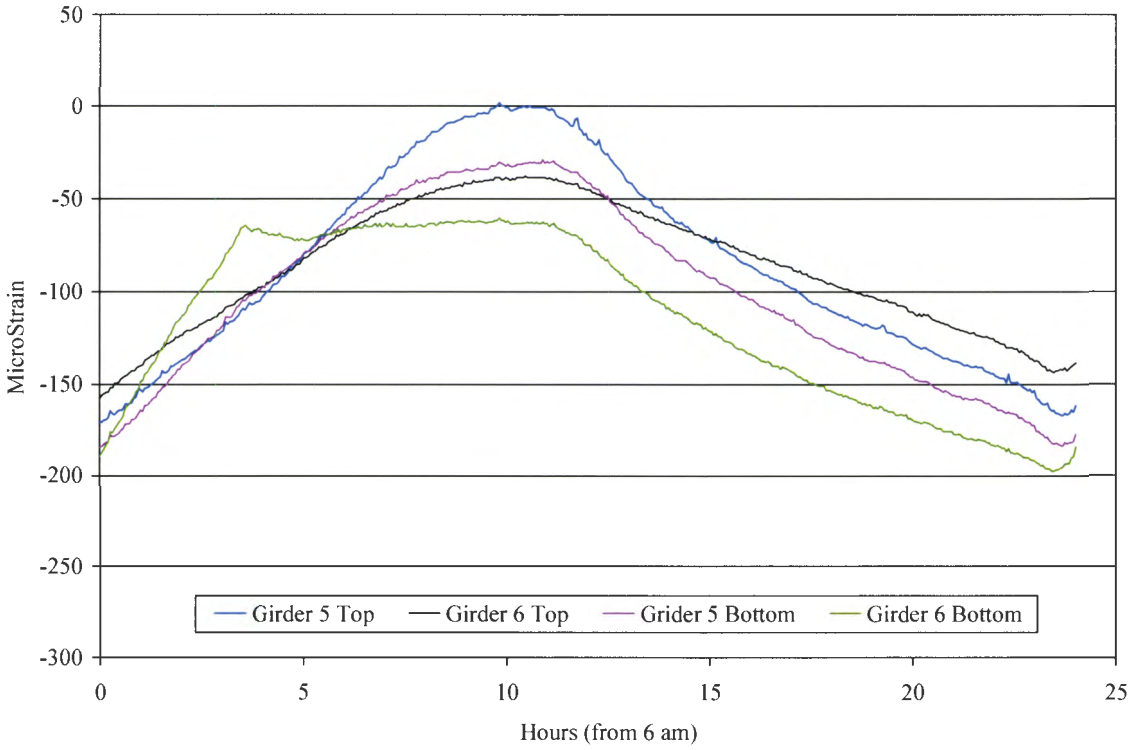

a. South midspan - East side.

Figure B.6. Daily temperature strain at top and bottom flange for interior and exterior girders.

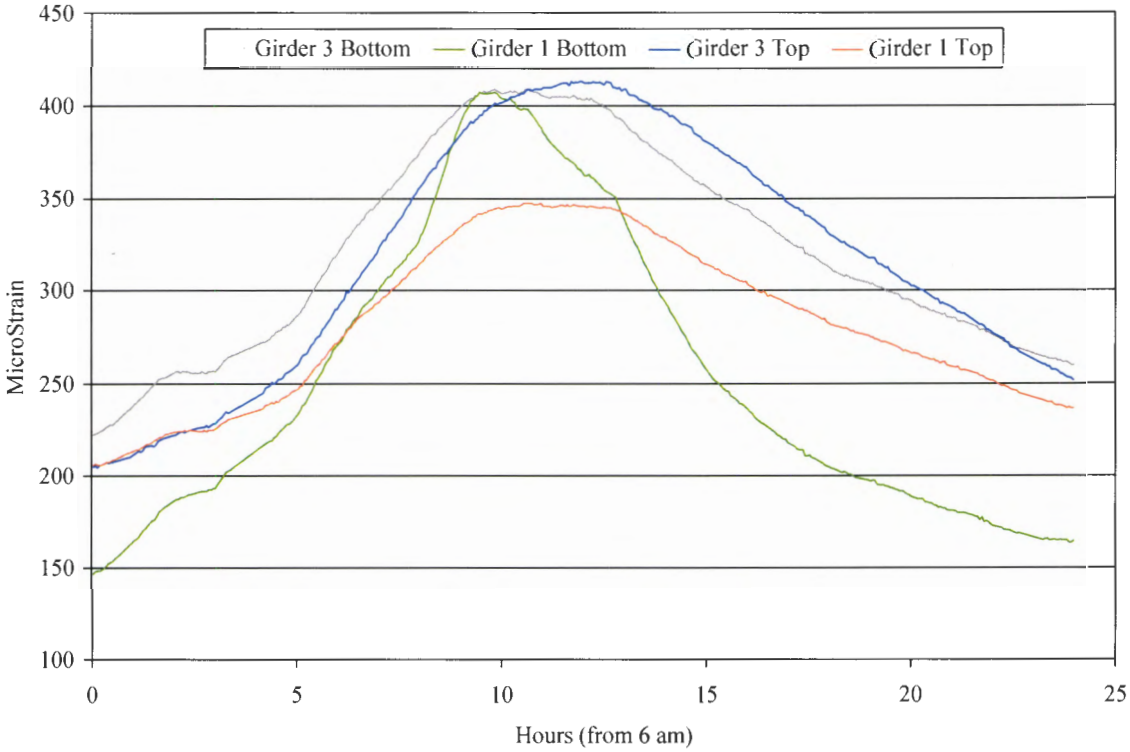

b. North midspan - West side.

Figure B.6. Daily temperature strain at top and bottom flange for interior and exterior girders (Continued).

Another noticeable difference between the North and the South strain plots is the difference in the range of the starting and ending strain of each girder. Notice how the strains from the South midspan are closer together than the North. It is important to note the sensors at the South midspan are the Surface Mountable Sensors and the sensors at the North midspan are the Bare FBG Sensors. It has been noticed by the research team the Surface Mountable Sensors seem to stay within a smaller range of one anther than the Bare FBG Sensors. This may be due to the fact the Surface Mountable Sensors were installed over a two-day period while the North midspan sensors were installed on several days over approximately 30 days.

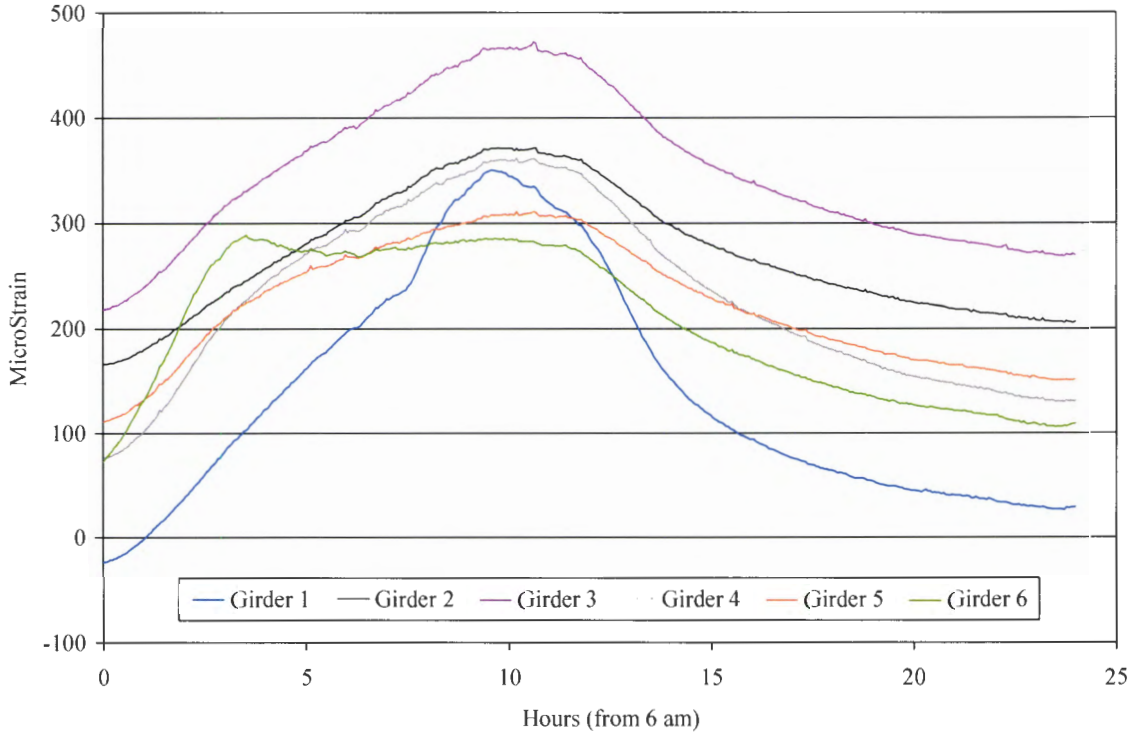

a. North.

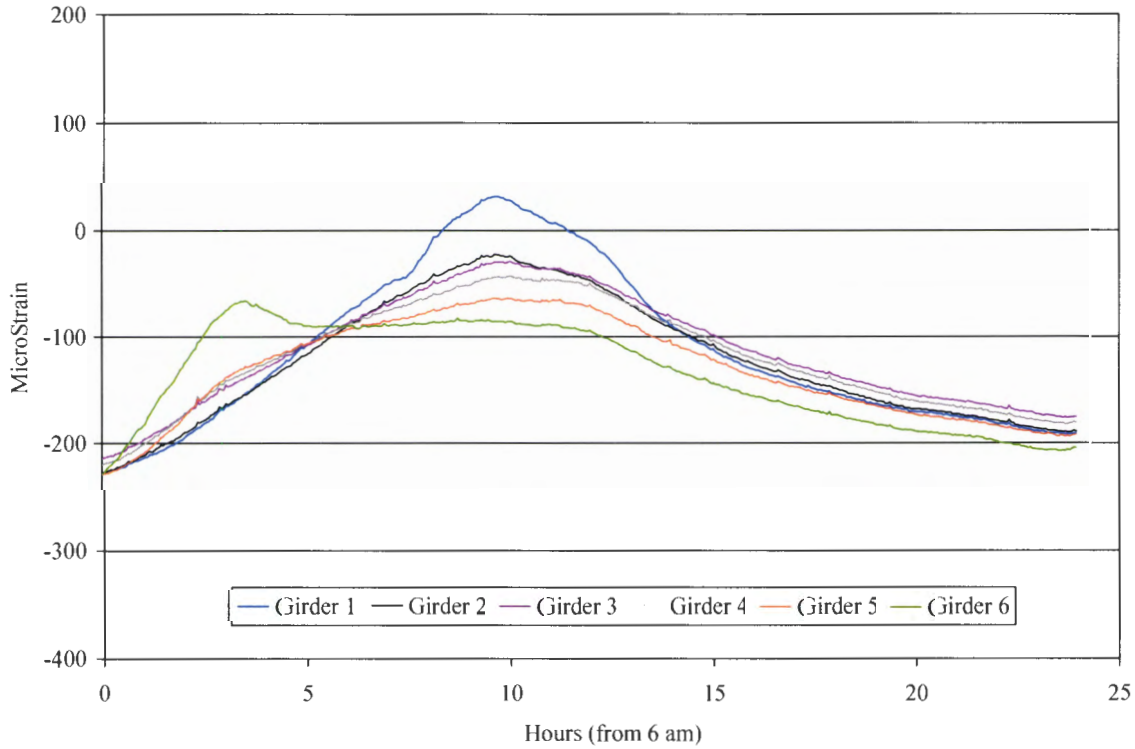

b. South.

Figure B.7. Daily temperature strains at bottom flange at midspan.

Figure B.8 compares the top and bottom flange daily temperature strains at midspans for Girders 1, 4, and 6. The bottom flange strain range in Girder 1, shown in Fig. B.8a, is approximately 175 $\mu\varepsilon$ more than the top flange strain range. The temperature sensor is also plotted for Girder 1. The strain trend is similar for the bottom flange and the temperature sensor. The slopes change at nearly the same times, although the slopes are different (but once again a direct comparison in magnitudes can't be made). The strain ranges for Girder 4 and 6 are nearly equal for the top and bottom flange. When the trends of the temperature strains for the exterior girders were discussed previously, it was noted the bottom flange of Girder 1 is exposed to direct sunlight during the warmest part of the day and is not near a heat sink as the top flange is. This would indicate the bottom flange would have a higher range than the top flange.

When the top and bottom flange have the same strain range, the bridge strain would be characterized as purely axial (i.e., no flexure). This would qualitatively indicate the abutment allows movement and little axial restraint is provided (this was also discussed in Appendix A, ER section). Since the strain ranges in the top flange and the bottom flange on Girder 1 are different, a combination of flexural and axial strains would be induced in the girder. The purely axial strains shown in Girders 2 through 6 indicate that these girders are expanding and contracting without lateral end restraint. In that case, these strains would not create stress in the girder. If lateral end restraint is present, stress would be induced in the girder and a change in length would not occur due to the restraint. In this case the strain would be zero.

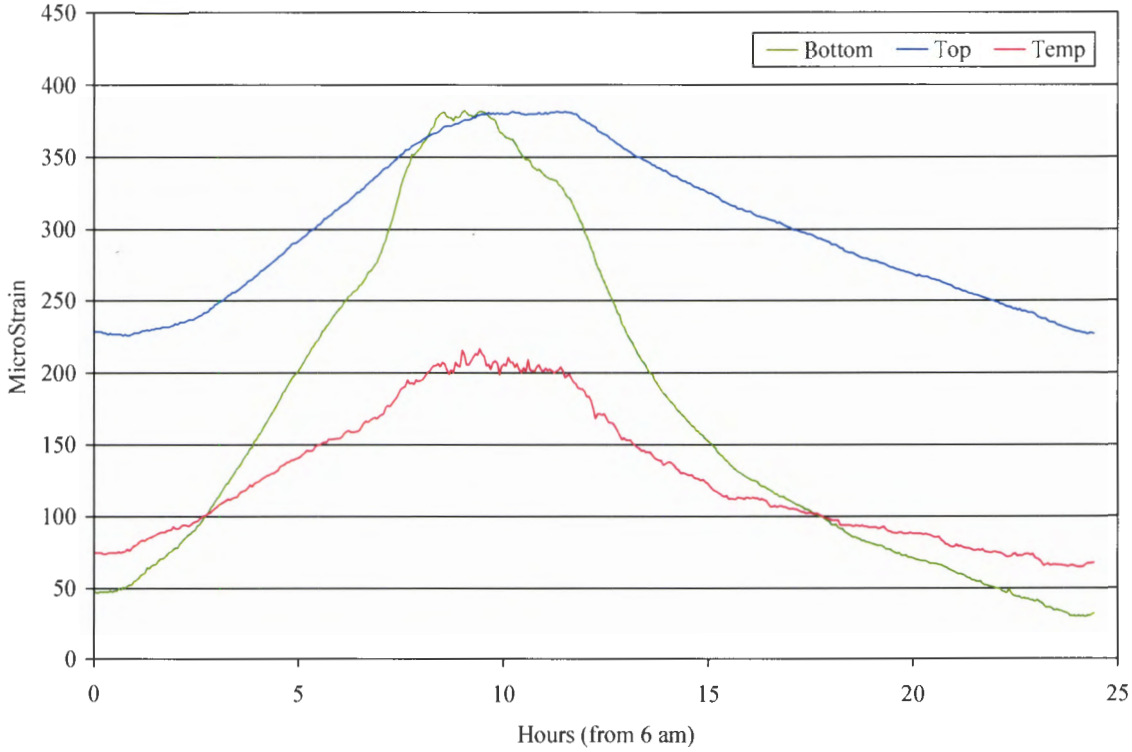

a. Girder 1 North midspan.

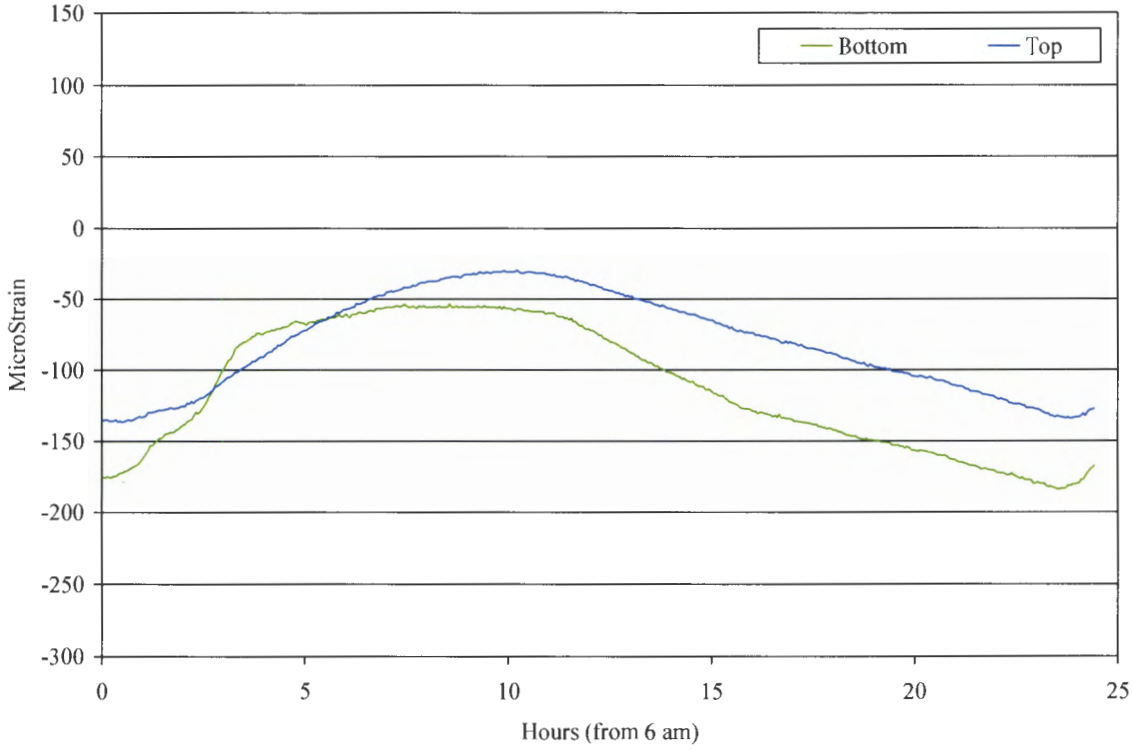

b. Girder 6 South midspan.

Figure B.8. Daily temperature strains at top and bottom flange.

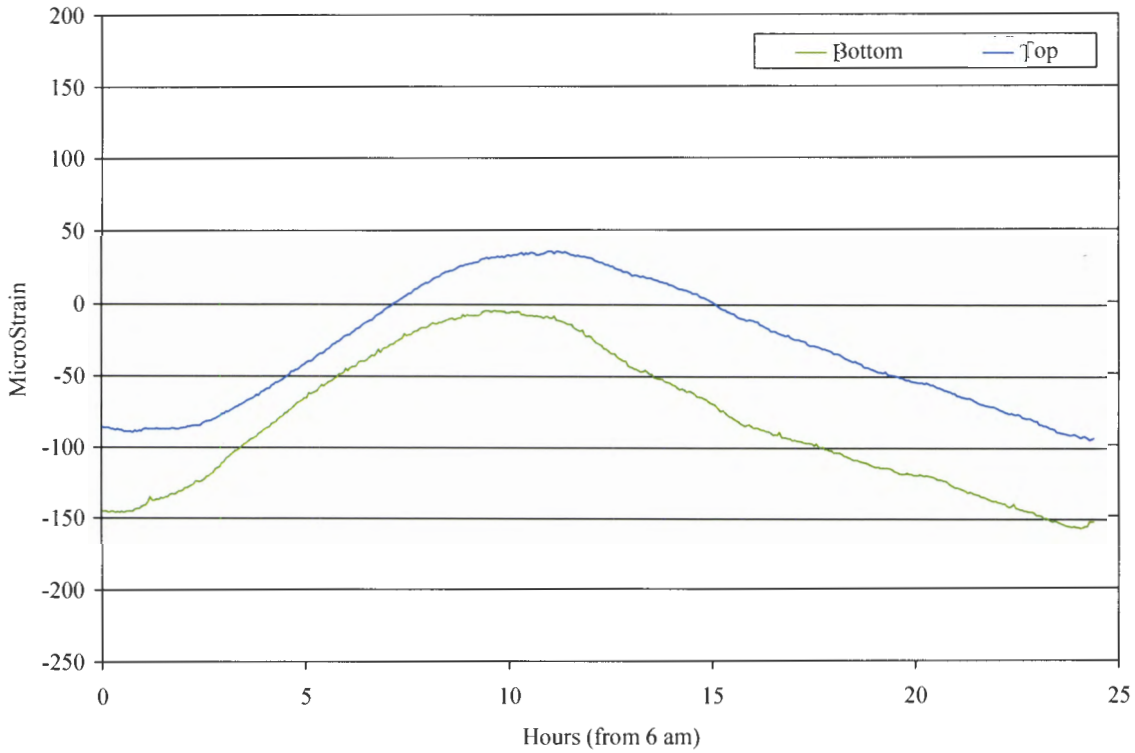

c. Girder 4 South midspan.

Figure B.8. Daily temperature strains at top and bottom flange (Continued).

The temperature strain plots presented previously indicate several strain cycles exist which are induced by temperature changes: seasonal, short-term, and daily. The strains induced on the bridge by temperature are much more significant than that of the live-load strains recorded. This does not mean the stress induced in the bridge is of the magnitude relative to the strain. Since the ratio of the difference between the ranges of the top and bottom flange strain to the range of the top or bottom flange strain is small, the majority of the strain is due to the bridge expanding and contracting without restraint. Therefore, little moment is induced and the stress level induced in the bridge is small. The bridge seems to react in a similar fashion at many locations with the exception of exterior girders which are exposed to direct sunlight at different periods throughout a day.